



HAL
open science

On the radiative properties of passive and active subwavelength mid-infrared devices

Loubnan Abou-Hamdan

► **To cite this version:**

Loubnan Abou-Hamdan. On the radiative properties of passive and active subwavelength mid-infrared devices. Optics / Photonics. Université Paris sciences et lettres, 2023. English. NNT : 2023UPSLS007 . tel-04106283

HAL Id: tel-04106283

<https://pastel.hal.science/tel-04106283>

Submitted on 25 May 2023

HAL is a multi-disciplinary open access archive for the deposit and dissemination of scientific research documents, whether they are published or not. The documents may come from teaching and research institutions in France or abroad, or from public or private research centers.

L'archive ouverte pluridisciplinaire **HAL**, est destinée au dépôt et à la diffusion de documents scientifiques de niveau recherche, publiés ou non, émanant des établissements d'enseignement et de recherche français ou étrangers, des laboratoires publics ou privés.



THÈSE DE DOCTORAT

DE L'UNIVERSITÉ PSL

Préparée à l'École Supérieure de Physique
et de Chimie Industrielles de la ville de Paris
en collaboration avec l'ONERA

**On the radiative properties of passive and active
subwavelength mid-infrared devices**

**Sur les propriétés radiatives des dispositifs passifs et
actifs dans l'infrarouge moyen sub-longueur d'onde**

Defended by

Loubnan Abou-Hamdan

February 10, 2023

Doctoral School n°564

**Ecole Doctorale Physique
en Ile-de-France**

Speciality

Physics

Prepared at

Institut Langevin and ONERA

Jury:

M. Thierry Taliercio
IES, Univ. Montpellier

Président du jury

Mme. Natalia Del Fatti
Institut Lumière Matière, Univ. Lyon

Rapporteur

M. Nicolas Bonod
Institut Fresnel, Marseille

Rapporteur

M. Jérémie Drevillon
Institut Pprime, Univ. Poitiers

Examineur

M. Emmanuel Baudin
LPENS, Paris

Examineur

M. Yannick De Wilde
Institut Langevin/ESPCI

Directeur

M. Patrick Bouchon
ONERA

Co-directeur

Acknowledgments

I would like to begin this acknowledgments section by thanking my wonderful mother, father, brother, and sister for their infinite love and support, without which none of the work presented in these pages would have been possible. I would like to also thank my family across the pond, my two lovely aunts and their husbands, and all my amazing cousins, who were kind enough to host me and provide me with the perfect environment for me to continue my work during a forced stay of over two months in Canada during the final months of my Ph.D. I am deeply grateful for all their love and generosity and, although my time in Canada was troublesome, I am glad things turned out the way they did as I got the chance to reconnect with them. I thank as well my brother-in-law who always believed in me and gave me the confidence and drive to push myself further. He is truly an inspiration and I thank him for his great help and support.

Many thanks to my two exceptional directors Yannick De Wilde and Patrick Bouchon, who have been rather two father figures to me. It was truly a pleasure working with both of them over the past three or so years. I am genuinely honored and privileged to have conducted my doctoral research under their direction and I am extremely proud of the work that we have accomplished together. Special thanks also to Riad Haidar and Valentina Krackmalnicoff who co-supervised the thesis. I thank as well our two brilliant collaborators Emmanuel Baudin and Aurélien Schmitt who were the masterminds behind the study presented in chapter 5 of this manuscript. I would like to also thank Sébastien Bidault and Rémi Carminati for many fruitful discussions.

I would like to express my deepest thanks to the jury members for reading the thesis and participating in my thesis defense. I would like to particularly thank the two reviewers, Pr. Natalia Del Fatti and Pr. Nicolas Bonod, for their detailed and thoughtful reports and their insightful comments and inquiries.

I would like to express as well my warmest thanks to all the lovely and wonderful people from Institut Langevin and ONERA, whom I had the pleasure to interact with over the past three years, particularly, Camilo Pérez, Samer Al Haddad, Anwesh Bhattacharya, Bart van Dam, Jeanne Heintz, Maximilian Lengauer, Laura Paggi, Baptiste Fix, Clément Verlhac, Cyprien Brulon, Tomasz Matthia, and Denis Langevin.

I would like to also express my infinite gratitude to Pr. Michel Kazan who has been a great mentor and dear friend and the catalyst to my scientific career.

In closing, I would like to thank Dr. Thomas Pernin, a wonderful medical practitioner who has been instrumental in maintaining my sanity over the past three nerve-racking years.

To Lina, Anwaar, Firas, and Fouad

Abstract

Infrared metamaterials have been used in a wide range of applications, such as radiative cooling, photo-detection, and solar cell design. The building blocks of these materials are subwavelength structures that exhibit many interesting antenna effects, namely, directional emission, spectral selectivity, and high field confinement. The study of the intrinsic radiative properties of these subwavelength structures is a crucial step toward the optimization of the optical response of large-scale metasurfaces. Traditionally, investigating the radiative properties of individual subwavelength structures has, for the most part, been rather elusive due to their inherently weak electromagnetic radiation. In the mid-infrared spectral range, one is also met with overwhelming background radiation.

In this thesis, we push the limits of various highly sensitive techniques, such as infrared spatial modulation spectroscopy, and scattering-scanning near-field optical microscopy, to probe the intrinsic mid-infrared electromagnetic radiation of single- or few-element subwavelength structures. A potpourri of subwavelength devices is examined and discussed, spanning a broad continuum, from passive dielectric and plasmonic antennas to electrically biased graphene field-effect transistors. The fundamental properties and interactions associated with these structures are elaborated, with special emphasis being placed on the influence of geometrical and material properties on the near- and far-field response. The results presented in this thesis and the discussion therein are of particular interest to light applications in which a tailoring of the mid-infrared spectrum at the subwavelength scale is required.

Keywords: Subwavelength, mid-infrared, antennas, near-field, far-field, surface polaritons

Résumé

Les métamatériaux infrarouges ont été utilisés dans un large éventail d'applications, telles que le refroidissement radiatif, la photodétection et la conception de cellules solaires. Les éléments constitutifs de ces matériaux sont des structures de taille sub-longueur d'onde qui présentent de nombreux effets d'antenne intéressants, à savoir une émission directionnelle, une sélectivité spectrale, ainsi qu'une exaltation du confinement du champ. L'étude des propriétés radiatives intrinsèques de ces structures sub-longueur d'onde est une étape cruciale vers l'optimisation de la réponse optique des métasurfaces à grande échelle. Traditionnellement, l'étude des propriétés radiatives des structures individuelles sub-longueur d'onde est extrêmement difficile en raison de leur rayonnement électromagnétique intrinsèquement faible. Dans la gamme spectrale du moyen infrarouge, le rayonnement du fond est dominant.

Dans cette thèse, nous repoussons les limites de diverses techniques hautement sensibles, telles que la spectroscopie à modulation spatiale infrarouge et la microscopie optique en champ proche à pointe diffusante, pour sonder le rayonnement électromagnétique intrinsèque dans le moyen infrarouge de structures sub-longueur d'onde composées d'un ou plusieurs éléments. Un pot-pourri de dispositifs sub-longueur d'onde est examiné et discuté, couvrant un large spectre allant, des antennes diélectriques et plasmoniques passives aux transistors à effet de champ en graphène polarisés électriquement. Les propriétés fondamentales et les interactions associées à ces structures sont élaborées, avec un accent particulier mis sur l'influence des propriétés géométriques et des matériaux sur la réponse en champ proche et lointain. Les résultats présentés dans cette thèse et la discussion associée sont d'un intérêt particulier pour les applications photoniques dans lesquelles une adaptation du spectre moyen infrarouge à l'échelle sub-longueur d'onde est requise.

Mots clés : Sub-longueur d'onde, moyen infrarouge, champ proche, champ lointain, antennes, polaritons de surface

Contents

Acknowledgments	i
Abstract	iii
Résumé	iv
Contents	iv
List of figures	viii
List of Tables	xxvii
1 Introduction	1
2 Fundamentals of surface polaritons in bulk materials and subwavelength heterostructures	16
2.1 Local dielectric continuum theory of polar dielectrics and metals	17
2.1.1 The dielectric function of polar semi-conductors: the Drude-Lorentz model	18
2.1.2 The dielectric function of metals: the free electron gas	20
2.2 Surface polaritons within the local dielectric continuum theory	22
2.2.1 Surface polaritons in a semi-infinite medium	22
2.2.2 Surface polaritons in thin films	29
2.2.3 Virtual modes in a polar dielectric sphere	33
2.3 Surface polaritons in anisotropic media	36
2.3.1 Hyperbolic phonon-polaritons in an anisotropic semi-infinite medium . . .	36
2.3.2 Surface plasmon-polaritons in free-standing graphene	38
2.4 Hexagonal boron nitride (hBN)/graphene heterostructures	40
2.4.1 hBN thin film on a substrate	40
2.4.2 Graphene on hBN	43
2.4.3 Encapsulated graphene	44
2.5 Conclusion	46
3 Experimental study of surface polaritons in dielectric media	50
3.1 Near-field microscopy techniques	50
3.1.1 Scattering-scanning near-field optical microscopy (s-SNOM) setup	54
3.1.2 Modeling s-SNOM	59
3.1.3 Determining the local thickness and dielectric properties of hBN flakes with s-SNOM	65
3.2 Near-field spectroscopy of surface polaritons with scattering disks	70

3.2.1	Infrared spatial modulation spectroscopy: a far-field technique	70
3.2.2	Near-field spectroscopy of a SiC substrate with a gold disk	78
3.2.3	Near-field spectroscopy of hBN thin films with local scatterers	82
3.3	Far-field thermal radiation of a subwavelength polar dielectric sphere on a gold substrate	84
3.3.1	Infrared spatial modulation spectroscopy of single SiO ₂ spheres on an Au substrate	85
3.3.2	Thermal radiation of sub- λ PTFE spheres	92
3.4	Conclusion	93
4	Properties of mid-infrared plasmonic antennas: from single to multi-element subwavelength cavity antennas	98
4.1	Metal-insulator-metal (MIM) cavities	98
4.2	Single MIM antennas in the near- and far-field	100
4.3	Far-field thermal radiation of a coupled patch MIM antenna pair: thermally excited hybrid plasmonic modes	105
4.3.1	Far-field thermal radiation of a single asymmetric dimer MIM antenna	106
4.3.2	Polarized thermal emission measurements of a single MIM antenna pair	108
4.3.3	Asymmetric vs symmetric MIM antenna pair	109
4.4	Shaping the optical properties of MIM cavities through multi-element surface patterning: the case of a 3×3 -patch MIM cavity antenna	110
4.4.1	Mapping the near-field of a 3×3 -patch MIM antenna	110
4.4.2	Microscope reflectivity measurements of a 3×3 -patch MIM antenna: angularly dependent antenna response	113
4.4.3	3×3 -patch MIM antenna with a missing element	116
4.5	Conclusion	118
5	Mid-infrared emission of high-mobility hBN/graphene/hBN field-effect transistors under large bias: electroluminescence and radiative cooling	121
5.1	Ultra-fast and ultra-hot incandescent graphene in the visible to ultra-violet spectral range	124
5.2	Transport properties of high-mobility graphene field-effect transistors (HGFETs) under large bias	125
5.2.1	Electrostatic doping	126
5.2.2	Electron mobility	127
5.2.3	Contact resistance	128
5.2.4	I-V Transfer Curve	128
5.2.5	Bias doping	130
5.2.6	Zener-Klein tunneling	130
5.3	Electron gas cooling in graphene under large bias	133
5.3.1	In-plane and out-of-plane heat transfer	133
5.3.2	Radiative near-field cooling: Planckian emission of hyperbolic phonon-polaritons	134
5.3.3	Beyond Planckian emission: radiative cooling due to Electroluminescence of HGFETs under large bias	136
5.3.4	Mid-infrared signature of electroluminescence cooling in HGFETs by phonon-polaritons	141
5.4	Mid-infrared electroluminescence of graphene	143
5.4.1	What is electroluminescence?	143
5.4.2	Can a metal be electroluminescent?	144

5.4.3	Experimental observation of electroluminescent emission from HGFETs under large bias	144
5.4.4	Shaping the mid-IR emission of electroluminescent HGFETs under large bias	146
5.5	Conclusion	150
Conclusions and perspectives		154
List of communications		158
Appendix		i
A	Finite-element method simulations	i
B	Finite-difference time-domain simulations	ii
C	Single microspheres on an Au substrate: sample preparation	iii
D	Heat transfer simulation: sphere on a heated substrate	iii
E	Angle resolved cross-section spectra of a sphere on an Au substrate	iv
F	Absorption in a BiMIM structure with an SiO ₂ insulator layer vs absorption in SiO ₂ alone	v
G	Metal-insulator-metal antennas: sample fabrication	vi
H	Simulations of a 3 × 3-patch MIM antenna consisting of the layers sketched in Fig. A7 (c)	viii
I	s-SNOM: miscellaneous	ix
i	Approch curves	ix
ii	Mapping the near-field of plasmonic nanostructures: metallic vs dielectric tips	ix
J	Microscope reflectivity measurements of 3 × 3-patch MIM antennas	x
K	Fabrication of high-mobility graphene field-effect transistors (HGFETs)	xi
L	Transport properties of electroluminescent HGFETs	xii
M	Determining the temperature increase of an HGFET with an SiO ₂ back-gate from mid-infrared measurements	xiii
N	Measurements of the absorptivity of an HGFET as a function of electrical bias	xiv
O	Stokes-anti-Stokes Raman thermometry of HGFETs	xv

List of figures

1.1	Scanning electron microscope (SEM) images of various examples of nanostructures, fabricated via lithography techniques. (a) Hollow out-of-plane nanostructures (ref. [2]). (b) & (c) Planar nanostructures (panel (b), ref. [3]; panel (c), ref. [4]). (d-h) Commercially available tips used in scanning-probe techniques. Courtesy of <i>Nanosensors</i> TM (panels (d-f)) and <i>NanoWorld AG</i> (panels (g) and (h)).	2
1.2	Diagram illustrating characteristic length scales as compared with the wavelength of the electromagnetic spectrum. Reproduced from ref. [28].	5
1.3	Schematic illustration of the enhancement in the transmission efficiency from a transmitter (dipole \mathbf{p}_1) to a receiver (dipole \mathbf{p}_2) via an antenna. Reproduced from ref. [19].	6
1.4	(a) Image of a radio-frequency Yagi-Uda antenna. (b) Schematic illustration of the dimensions of the various elements of a Yagi-Uda antenna with respect to the operating wavelength of the antenna λ (reproduced from ref. [47]). In general, a Yagi-Uda antenna consists of 5 or more half-wave antennas, which are detuned with respect to each other. A feed element of length $L_f = \lambda/2$ is driven so that it emits electromagnetic radiation, while smaller director elements (length $L_d < L_f$) passively direct (scatter) the radiation in the forward direction (to the right of panel (b)). A larger reflector element (length $L_r > L_f$) suppresses any back-scattered radiation. The resulting emission of this antenna configuration is, thus, highly directional. (c) SEM image of an optical Yagi-Uda antenna, whose feed element is coupled to a quantum dot, enabling uni-directional emission at $\lambda \sim 800$ nm [48]. (d) Angular radiation pattern in the polar angle (θ) for the Yagi-Uda antenna of panel (c), showing a narrow emission lobe.	8
1.5	Depiction of the atomically thin van der Waals materials graphene and hexagonal boron nitride (hBN). Graphene consists of a single sheet of carbon atoms (represented as black spheres) in a honeycomb lattice and is characterized as a semi-metal with no band-gap. hBN is a polar dielectric made up of boron and nitride atoms (red and blue spheres) also in a honeycomb lattice. Typically, graphene is assembled as mono-, bi-, or tri-layer graphene, while hBN is exfoliated on a substrate, forming a flake that is a few hundred atomic layers thick.	9

2.1	Real (ϵ') and imaginary (ϵ'') parts of the dielectric function vs wavenumber ($1/\lambda$) for SiC (panels (a) and (b)), and SiO ₂ (panels (c) and (d)), calculated from the Drude-Lorentz model Eq. (2.9). For SiC: $\omega_{\text{TO}} = 793 \text{ cm}^{-1}$, $\omega_{\text{LO}} = 969 \text{ cm}^{-1}$, $\epsilon_{\infty} = 6.7$, and $\gamma = 4.76 \text{ cm}^{-1}$. For SiO ₂ : $\omega_{\text{TO}} = 1075 \text{ cm}^{-1}$, $\omega_{\text{LO}} = 1250 \text{ cm}^{-1}$, $\epsilon_{\infty} = 1.97$, and $\gamma = 69 \text{ cm}^{-1}$. Optical constants taken from ref. [6]. The shaded regions indicate the material's <i>Reststrahlen</i> band between ω_{TO} and ω_{LO} , in which the real part of the dielectric function is negative.	18
2.2	(a) Infrared reflectivity of SiC and crystalline quartz measured using Fourier transform infrared (FTIR) spectroscopy with an integrating sphere. The integrating sphere is sketched in panel (b). The integrating sphere consists of a gold-coated sphere, which collects both diffuse and specularly reflected light off the sample surface. Both SiC and crystalline SiO ₂ have substantial reflectivity in their <i>Reststrahlen</i> bands (shaded regions), with the reflectivity of SiC reaching values close to 100%.	19
2.3	(a) Real (ϵ') and imaginary (ϵ'') parts of the dielectric function of gold based on Eq. (2.19). $\lambda_p = 159 \text{ nm}$ and $\Gamma = 0.0048$. (b) Reflectivity of a gold surface (black curve), calculated from the Fresnel reflection coefficient at normal incidence: $R = (\tilde{n} - 1)/(\tilde{n} + 1) ^2$, where $\tilde{n} = \sqrt{\epsilon' + i\epsilon''}$. The Au interface maintains a high reflectivity of $\sim 99 \%$ over the entire plotted infrared spectral range.	21
2.4	Sketch of the half-space geometry. Surface polaritons can propagate along the interface between the active and inactive media.	23
2.5	(a) Real (ω vs k') and (b) imaginary (ω vs k'') parts of the dispersion curves of the normal modes for a vacuum/SiC half-space (red curves) and a vacuum/SiO ₂ half-space (blue curves). The modes corresponding to the SPhPs are given by the portion of the curves in the material's <i>Reststrahlen</i> band (shaded regions) between ω_{TO} and ω_{LO} , where the real part of the dielectric function is negative (see Figs. 2.1 (a) and (c)).	25
2.6	(a) Dispersion relation of SPhPs in a vacuum/SiC half-space in the absence of damping ($\gamma = 0$ in Eq. (2.11)) obtained from solving Eq. (2.42) and plotted as a function of dimensionless frequency $\omega/\omega_{\text{TO}}$ and dimensionless wavevector k/k_{TO} . For SiC $\omega_{\text{LO}}/\omega_{\text{TO}} = 1.22$. (b) & (c) Dimensionless penetration depths of SPhPs $(\alpha d)^{-1}$ in SiC (panel (b)) and $(\alpha_I d)^{-1}$ in vacuum (panel (c)), where $d = 5 \text{ \AA}$ is the mean interionic spacing.	26
2.7	Dimensionless penetration depth $\delta_z/\lambda = \alpha ^{-1}/\lambda$, in the boundary-active medium, and $\delta_z^I/\lambda = \alpha_I ^{-1}/\lambda$, in the boundary-inactive medium (for $\epsilon_I = 1$), where $\lambda = 2\pi c/\omega$ is the wavelength in vacuum, for SPhPs at (a) a vacuum/SiC interface and (b) a vacuum/SiO ₂ interface. (c) and (d) Dimensionless propagation length L_p/λ of SPhPs, at the surface of SiC and SiO ₂ , respectively.	28
2.8	Geometry and notation of a thin film of thickness $L = 2a$ and dielectric function $\epsilon(\omega)$. The film is sandwiched between two inactive media of dielectric constants ϵ_t and ϵ_b , from the top and bottom, respectively. All media are considered to be non-magnetic, <i>i.e.</i> , $\mu = 1$	29

2.9	A physical representation of the real part of the surface polariton electric fields within a thin film (thickness L such that $k_{\text{TO}}L \ll 1$) as obtained from the fields for the surface polariton in a half-space. (a) and (b) Electric fields of the two half-spaces having the same sign of the amplitude factor. (d) and (e) Electric fields of the two half-spaces having the opposite sign of the amplitude factor. The sign of the amplitude factor is specified by the arrows in each case. (c) (resp. (f)) Resultant field from the superposition of panels (a) and (b) (resp. panels (d) and (e)).	30
2.10	Sketch of the dispersion curves of SPhPs corresponding to the thin film geometry of Fig 2.8 for (a) $\varepsilon_t = \varepsilon_b = \varepsilon_I \geq 1$ and (b) $\varepsilon_b > \varepsilon_t \geq 1$	31
2.11	Dispersion curves for normal modes for which $k^2 = \varepsilon\omega^2/c^2$, for a SiC film of thickness L on a metallic backplate.	33
2.12	Geometry and notation of the sphere problem, in which a sphere of dielectric function $\varepsilon(\omega)$, occupying the region $r \leq r_o$, is surrounded by an inactive medium of dielectric constant ε_I ($r > r_o$). Both media are considered to be non-magnetic.	34
2.13	(a) Real part (ε') of the dielectric function of hBN, obtained by applying Eq. (2.11) for the parallel and perpendicular directions. The purple-shaded regions indicate the two <i>Reststrahlen</i> bands of hBN. The optical constants appropriate for hBN are: $\varepsilon_\infty^\parallel = 2.95$, $\varepsilon_0^\parallel = 3.57$, $\omega_{\text{TO}}^\parallel = 746 \text{ cm}^{-1}$, $\omega_{\text{LO}}^\parallel = 820.65 \text{ cm}^{-1}$, and $\gamma^\parallel = 4 \text{ cm}^{-1}$, for the perpendicular direction, and $\varepsilon_\infty^\perp = 4.87$, $\varepsilon_0^\perp = 6.71$, $\omega_{\text{TO}}^\perp = 1372 \text{ cm}^{-1}$, $\omega_{\text{LO}}^\perp = 1610.5 \text{ cm}^{-1}$, and $\gamma^\perp = 5 \text{ cm}^{-1}$ for the parallel direction [13] (b) Real dispersion curve (ω vs k') of an hBN half-space bound by vacuum. (c) & (d) Dimensionless penetration depth δ_z/λ , where λ is the wavelength in free space, of type I and II HPhPs in hBN. (e) & (f) Dimensionless propagation length L_p/λ of type I and II HPhPs on the hBN surface.	37
2.14	(a) sketch of a monolayer graphene encapsulated between two semi-infinite media of dielectric constants ε_1 and ε_2 . (b) Dispersion curves of free-standing graphene in vacuum for various Fermi energies (E_F) for electron mobility $\mu_e = 10^4 \text{ cm}^2/\text{V.s.}$	39
2.15	(a) Dimensionless penetration depth δ_z/λ of surface plasmons of a free-standing graphene in vacuum for $0.08 \leq E_F \leq 0.64 \text{ eV}$. The curves for different Fermi energies are overlapping so that a single curve appears in panel (a). (b) Dimensionless propagation length L_p/λ of SPPs in free-standing graphene in vacuum for various Fermi energies. The value for the electron mobility is taken to be $\mu_e = 10^4 \text{ cm}^2/\text{V.s.}$	40
2.16	Sketch of an hBN thin film of thickness d placed on an SiO_2 substrate.	41
2.17	(a) Color map of the imaginary part of the reflection coefficient ($\text{Im}(r_p)$) given by Eq. (2.76) for $d = 135 \text{ nm}$. The branches resulting from the maxima of $\text{Im}(r_p)$ correspond to the various dispersion curves of the HPhP modes of the hBN thin film. (b) and (c) Zooms of the two <i>Reststrahlen</i> bands of hBN, marked by the white dashed lines in panel (a). The blue dashed lines in panel (b) were obtained by solving Eq. (2.79) for multiple values of l	42
2.18	Sketch of the geometry and notation of the vacuum/graphene/hBN/ SiO_2 heterostructure.	43
2.19	(a) Dispersion branches of a 60 nm hBN thin film on SiO_2 (b) Dispersion branches of the graphene/hBN heterostructure of Fig. 2.18 for $d = 60 \text{ nm}$, $E_F = 0.37 \text{ eV}$ and $\mu_e = 10^4 \text{ cm}^2/\text{V.s.}$ The dashed white lines enclose the two <i>Reststrahlen</i> bands of hBN.	44
2.20	Sketch of a graphene layer encapsulated between two hBN thin films of thicknesses d_1 and d_2	45

2.21	Dispersion curves of the hBN/graphene/hBN heterostructure, with hBN thickness $d_1 = 50$ nm and $d_2 = 30$ nm, for $\mu_e = 60,000$ cm ² /V.s at three different values of the Fermi energy E_F . The dashed white lines enclose the two <i>Reststrahlen</i> bands of hBN.	46
3.1	Schematic illustration of different scanning near-field optical microscopy (SNOM) techniques reproduced from ref. [6]. (a) Aperture on an opaque plate. (b) Aperture at the end of a coated optical fiber. (c) Apertureless- or scattering-SNOM with a laser-illuminated metallic tip. The opening or the tip is much smaller than the wavelength λ . The electric field is highly collimated in the near-field within a distance of λ and diverges as the distance increases.	51
3.2	Finite-difference time-domain (FDTD) simulations of the electric field enhancement, $ \mathbf{E} / \mathbf{E}_{in} $, in the near-field of a scattering tip illuminated by a laser beam with an incident field amplitude $ \mathbf{E}_{in} $. The laser beam is considered to be a monochromatic Gaussian beam with $\lambda_{\text{Laser}} = 10.6$ μm that is focused onto the tip with a focusing objective of numerical aperture, $\text{NA} = 0.46$. The incident field \mathbf{E}_{in} is polarized along the z -axis and the wavevector k_{in} giving the direction of propagation of the field is angled at 60° from the z -axis. The tip apex is assumed to have a radius of curvature $a = 30$ nm. Panel (a) shows the simulation result for a platinum (Pt) tip with $\varepsilon_{\text{Pt}} = -1450.7 + 1051i$ and panel (b) shows the result for a silicon (Si) tip with $\varepsilon_{\text{Si}} = 11.7$. Further details on the FDTD simulations presented in this figure can be found in Appendix B.	52
3.3	(a) Geometry and definitions for the discussion of light scattering from the tip-sample region. The tip and sample are illuminated by an incident field \mathbf{E}^i and a scattered wave \mathbf{E}^s is produced so that the total field after scattering is given by $\mathbf{E} = \mathbf{E}^i + \mathbf{E}^s$. The tip and sample are described by the dielectric susceptibilities $\chi(r)$ and $\eta(r)$, respectively. (b-e) Different types of nanoscale microscopy techniques categorized according to the leading term in the Born series. Reproduced from ref. [7].	53
3.4	(a) Image of the commercial <i>NeaSpec</i> s-SNOM setup. All the optics are enclosed within a compact box setup in order to minimize perturbations that can be introduced to the tip from the environmental conditions of the experimental room. The particular configuration that is shown here has two modules: a near-field imaging module (left side) and a near-field spectroscopy module (right side), also known as nano-FTIR. (b) Sketch of the optical setup of the s-SNOM in the back-scattering configuration. Depending on which module is used, either a single wavelength tunable quantum cascade laser (QCL) or a broadband laser is used as the light source. The abbreviations used in panel (b) are: beam splitter (BM) and reference mirror (RM). Courtesy of <i>NeaSpec GmbH</i>	55

- 3.5 (a) Sketch of a beam of length L and diameter $2R$ fixed at one end and allowed to oscillate freely on the other. (b) A diagram representing the feedback loop employed in scanning probe microscopy such as s-SNOM to establish and maintain contact with the sample surface. This is done by measuring an *interaction signal* that is compared to an externally defined setpoint. Ideally, the measured interaction signal should correspond to the externally defined setpoint when the tip is in contact. The speed and stability of the feedback loop depend on the parameters of the controller $G(\omega)$. (c-f) Resonance of a vibrating beam. The amplitude $x_0(\omega)$ (panel (c)) and phase $\varphi(\omega)$ (panel (d)) of a beam driven at a frequency ω . As the beam-end starts to interact with a sample surface, the resonance shifts and the amplitude drops. (e) and (f) show the amplitude and phase at frequency $\omega = \omega_0$ as functions of the distance d between the beam-end (tip) and the surface. The distance range over which the amplitude and phase vary depends on the interaction area (tip sharpness). Reproduced from ref. [7]. 56
- 3.6 Nano-FTIR spectroscopy of SiC. (a) amplitude, (b) phase, (c) real part, and (d) imaginary part of the near-field signal on SiC, $S_3^{\text{SiC}} = s_3^{\text{SiC}} e^{i\phi_3^{\text{SiC}}}$, normalized to the signal of a reference Si substrate, $S_3^{\text{Si}} = s_3^{\text{Si}} e^{i\phi_3^{\text{Si}}}$. The detected signal is demodulated at the 3rd harmonic. Tapping parameters: tip oscillation frequency, $\Omega = 241$ kHz, and tapping amplitude, $\Delta z = 55$ nm. 58
- 3.7 (a) Schematic representation of the tip above a sample surface and its image in the sample. (b) and (c) Representation of the point dipole approximation [12], in which the tip and its image are replaced by two spherical particles of dipole moments p and p' , respectively, and radius a . The applied electric field, E_{in} , is assumed to be perpendicular to the sample surface in panel (b) and parallel to it in panel (c). 59
- 3.8 Effective polarizability amplitude at $\lambda = 10.6 \mu\text{m}$ for a platinum (Pt) tip of radius $a = 30$ nm, at a distance $z_{\text{tip}} = z$ above SiC and Au, normalized by that of a Si reference sample. Due to the polariton resonance of SiC, the near-field is highly enhanced (about ten times more) above SiC as compared to that of Au, which acts as a mirror in the mid-infrared (see Fig. 2.3 (b)). Solid lines correspond to field polarization perpendicular to the sample surface, while dashed curves correspond to parallel field polarization. For both SiC and Au, the amplitude ratio is larger for the perpendicular field polarization. 61
- 3.9 Absorption (C_{abs}) and scattering (C_{scat}) cross-sections at $\lambda = 10.6 \mu\text{m}$ of (a) a Pt tip and (b) a Si tip ($a = 30$ nm), above Au (green curves) and Si (blue curves). Solid lines correspond to electric field polarization perpendicular to the surface, while dashed lines correspond to the parallel polarization. Optical constants: $\epsilon_{\text{Pt}} = -1450.7 + 1051i$, $\epsilon_{\text{Au}} = -4680 + 1674.5i$, and $\epsilon_{\text{Si}} = 11.7 + 0.00084i$ 63
- 3.10 (a) Geometry of the finite-dipole model. Reproduced from ref. [21]. (b) Comparison between the normalized s-SNOM amplitude, $s_3^{\text{SiC}}/s_3^{\text{Si}}$, presented in Fig. 3.6 (a) above SiC and the corresponding fit result from the finite-dipole model (Eq. (3.20)). Fit parameters: $a = 20$ nm, $L = 300$ nm, and $g = 0.7e^{0.18i}$. The optical constants used for SiC are given in Fig. 2.1. 64

3.11	(a) Microscope image ($\times 10$ magnification) showing the exfoliated hBN flakes on the SiO ₂ substrate. The substrate consists of a 285 nm SiO ₂ layer on top of a bulk Si layer. (b) Normalized amplitudes of the nano-FTIR spectra measured on an hBN flake (such as the one encircled in panel (a)) and on the SiO ₂ substrate next to the flake, demodulated at the 3rd harmonic of the tip oscillation frequency. The amplitudes are normalized by the nano-FTIR amplitude of a reference Si sample.	66
3.12	(a) Sketch of the three-layer geometry used in the extension of the finite-dipole model to a multi-layer sample. Reproduced from ref. [21]. (b) Comparison between the normalized amplitude of the nano-FTIR spectrum measured on the SiO ₂ substrate and the corresponding amplitude obtained from the three-layer finite-dipole model (panel (a)) with $\epsilon_1 = 1$, $\epsilon_2 = \epsilon_{\text{SiO}_2}$, $\epsilon_3 = \epsilon_{\text{Si}} = 11.7$, and $d = 285$ nm. (c) and (d) Same as panel (b) but for hBN. Here the finite-dipole model result is obtained by taking $\epsilon_1 = 1$, $\epsilon_2 = \epsilon_{\text{hBN}}$, $\epsilon_3 = \epsilon_{\text{SiO}_2}$, and $d = 10$ nm. Panel (c) shows the fit result for $w_1 = 1$ and $w_1 = 5$ in Eq. (3.24), while panel (d) shows the result of the fit with $w_1 = w_2 = 1$	67
3.13	Dispersion curves of the HPhP modes of the air/hBN/SiO ₂ multi-layer structure of Fig. 3.12 (c) visualized from the maxima of the imaginary part of the reflection coefficient of the structure for p -polarized waves, given by Eq. (2.76). Panel (a) shows type I HPhP branches and panel (b) shows the type II branches. The black dashed lines show the limits of the two <i>Reststrahlen</i> bands of hBN.	69
3.14	(a) Schematic illustration of the IR-SMS technique. The inset on the left shows a microscope image of a sub- λ square patch antenna over a uniform background substrate. The antenna is optically conjugated with the active area of the detector and a piezoelectric translation stage is used to modulate its position in the detector's field of view (FOV). The field of view size is determined by the size of the active area of the detector ($250 \times 250 \mu\text{m}^2$ here) and the magnification, M , of the collection optics. (b) Confocal configuration equivalent to the optical setup of panel (a), consisting of a collection lens of focal length f_1 and a focusing lens of focal length f_2 . Three objects in the sample are depicted. Only the object (circle) on the optical axis lying in the conjugated detection plane in the object space reaches the center of the active area of the detector, producing a maximal detected signal. The other objects (triangle and square) are either focused to the sides of the active area (triangle) or arrive at the detector unfocused such that their signals are either minimal or suppressed. The magnification of the two-lens system shown here is given by $M = f_2/f_1$	71
3.15	(a) Scanning electron microscope (SEM) image of a square patch metal-insulator-metal (MIM) antenna of side $w = 2 \mu\text{m}$. MIM antennas will be discussed in greater detail in chapter 4. (b) and (c) Spatial scans of the signal of the single antenna of panel (a), demodulated at the 1st and 2nd harmonic, respectively.	73
3.16	(a) Uncalibrated spectra of the thermal emission of a reference blackbody sample at variable temperature T . (b) Spectral response function (r_ν) of the optical setup computed from Eq. (3.36). (c) Measured blackbody spectra of panel (a) after calibration ($L_\nu = \frac{C_\nu}{r_\nu} - L_\nu^0$) and (d) their corresponding Planck blackbody spectral radiance.	77
3.17	(a) Sketch representing the scattering of thermally excited surface polaritons by an Au disk at the surface. (b) Microscope images of Au disks that were patterned via optical lithography on the surface of a SiC substrate. The disks are 110 nm thick and are of varying diameters.	78

- 3.18 Finite-element method (FEM) calculations of the cross-sections of a gold disk in air. (a) & (d) Absorption cross-section (C_{abs}). (b) & (d) Scattering cross-section (C_{scat}). (c) & (f) Extinction cross-section ($C_{\text{ext}} = C_{\text{abs}} + C_{\text{scat}}$). The top panels correspond to the electric field incident upon the disk from the top and the bottom panels are for electric field incident upon the disk from the side (see insets of panels (a) and (d)). Details on FEM simulations can be found in Appendix A. 79
- 3.19 Far-field characterization of the near-field thermal radiation scattered by a single sub- λ Au disk (diameter, $d = 2 \mu\text{m}$) on a SiC substrate. The far-field signal is detected using the IR-SMS technique and normalized to the response of a reference blackbody sample. (b) IR-SMS spectra of the scattered near-field signal as a function of increasing disk diameter d . (c) Far-field absorption of a SiC substrate measured using three different techniques: IR-SMS at an Au/SiC substrate (black curve), optical chopping (green curve), and using an integrating sphere (blue curve). For the latter method, the absorptivity A was obtained from $A = 1 - R$, where R (red curve) is the sample's reflectivity (the sample was thick enough that the transmission was effectively zero). The optical chopper measurement was performed with the same optical setup as that of the IR-SMS technique except that the spatial modulation of the sample was replaced by the optical chopping of the signal by the blades of the chopper. The detected signal was demodulated at the frequency of chopping to improve the signal-to-noise ratio. To remove the signal coming from the blades of the chopper we performed a measurement on the bare SiC substrate and a reference measurement on a large Au pattern and took the difference of the two. The green-shaded regions mark the *Reststrahlen* band of SiC between ω_{TO} and ω_{LO} 80
- 3.20 (a) Microscope image ($\times 50$ magnification) showing two 50-nm-thick hBN flakes, each with a single sub- λ Au disk on top. The disks were fabricated via optical lithography. Each flake has a disk with a different diameter d . The disks shown here correspond to (1) $d = 2 \mu\text{m}$ and (2) $d = 3 \mu\text{m}$. The disks all have a thickness of 110 nm. (b) Normalized IR-SMS spectra of a single Au disk of diameter d placed on an hBN flake as in panel (a). The purple-shaded region marks the type II *Reststrahlen* band of hBN. 82
- 3.21 HPhP branches of the three-layer system sketched in the inset of panel (b), obtained from (a) the maxima of the imaginary part of Eq. (2.76) and (b) by solving Eq. (2.79) for mode number $0 \leq l \leq 6$. The purple-shaded region in panel (b) marks the *Reststrahlen* band corresponding to the type II HPhPs in hBN between $\omega_{\text{TO}}^{\perp}$ and $\omega_{\text{LO}}^{\perp}$ 83
- 3.22 (a) Schematic illustration of the optical setup used to perform far-field optical characterization with a chopper. The setup is equivalent to that shown in Fig. 3.14 (a), except that the lateral modulation of the sample is replaced by the optical chopping of the light that is collected from the sample by the blades of the chopper. (b) Normalized far-field spectra, measured with the setup of panel (a), of an hBN flake with multiple Au disks (blue curve) and an hBN flake in which multiple holes were etched (red curve). Each spectrum is the result of the difference of two measurements, one with the hBN flake in the detection plane, and the other with the bare SiO_2 in the detection plane. The second measurement serves as a reference to remove the signal coming from the blades of the chopper. 84

- 3.23 (a) Schematic illustration of an IR-SMS measurement of a single sub- λ sphere. (b-e) Measured IR-SMS thermal radiation spectra of single sub- λ SiO₂ spheres on a gold substrate (solid curves, left axis, normalized to 1), along with FEM simulations of their absorption cross-section (C_{abs} , dotted curves, right axis), for $r_o = 1, 1.5, 2,$ and $2.5 \mu\text{m}$. The dashed vertical line marks the spectral position of the transverse optical phonon resonance frequency (ω_{TO}) in SiO₂. The plotted FEM spectra correspond to the absorption cross-section (C_{abs}) of the sphere on gold, simulated with unpolarized light, averaged for incident angles from 10 to 30° (see Appendix A for more details). The insets show visible microscope images of the measured spheres, taken using a $\times 50$, NA=0.55 visible objective. The left inset of panel (b) shows the simulated electric field enhancement $|E|/|E_0|$, where $|E_0|$ is the amplitude of the incident electric field (incident at 20° from the normal), calculated at the peak of the absorption cross-section, in the xz -plane for a sphere with $r_o = 1 \mu\text{m}$ on a gold surface. The white dashed line indicates the intersection of the gold substrate with the sphere. 86
- 3.24 (a) Simulated distribution of the electric (\vec{E}) and magnetic (\vec{H}) fields inside an SiO₂ sphere of radius $r_o = 1 \mu\text{m}$, in vacuum (for electric field incident into the page and polarized along x) at the maxima of the peaks indicated by the markers in panel (c). They correspond to the electric dipole (star), magnetic dipole (circle), and electric quadrupole (asterisk) modes of the sphere. (b) Real (ϵ'_{SiO_2}), and imaginary ($\epsilon''_{\text{SiO}_2}$) parts of the dielectric function of SiO₂, taken from ref. [24]. The blue shaded region indicates the *Reststrahlen* band between the transverse (ω_{TO}) and the longitudinal (ω_{LO}) optical phonon frequencies in which the real part of the dielectric function is negative. (c-f) Mie theory calculation of the absorption cross-section of SiO₂ spheres in vacuum, of radii (c) $r_o = 1 \mu\text{m}$, (d) $r_o = 1.5 \mu\text{m}$, (e) $r_o = 2 \mu\text{m}$, and (f) $r_o = 2.5 \mu\text{m}$, along with the individual contributions of the first few electric and magnetic modes to the absorption cross-section. 89
- 3.25 (a) Sketch of the sphere and image sphere charges, induced by the gold substrate, for the electric dipolar and quadrupolar modes. (b) Simulated electric field enhancement ($|E|/|E_0|$), calculated at the electric quadrupolar mode frequency in the xz -plane for a sphere with $r_o = 2 \mu\text{m}$ in vacuum (top panel), and on an Au substrate (bottom panel), for normal incidence, $\theta = 0^\circ$. Due to the large field enhancement between the sphere and substrate, the color bar in the bottom panel is scaled to reveal the field features. The value in the top right inset in red indicates the maximal calculated field enhancement near the point of intersection between the sphere and the gold substrate. The white dashed line indicates the intersection of the gold substrate with the sphere. (c) Calculated absorption cross-section at the surface and low-frequency virtual modes of an SiO₂ sphere with $r_o = 2.5 \mu\text{m}$ on Au, for unpolarized light incident at various angles θ , as sketched in the inset. (d) Electric field enhancement plots of an SiO₂ sphere with $r_o = 2.5 \mu\text{m}$ on gold, for $\theta = 0$ and $\theta = 30^\circ$ 91
- 3.26 (a) Measured thermal radiation spectrum of a single PTFE sphere with $r_o = 1.5 \mu\text{m}$ on a gold substrate (solid curve, left axis) and its corresponding simulated absorption efficiency ($C_{\text{abs}}/\pi r_o^2$, dotted curve, right axis) for unpolarized light averaged over various angles of incidence from 10 to 30° from the normal. (b) Mie theory calculation of the absorption efficiency of PTFE spheres, in vacuum, of various radii r_o . (c) Real (ϵ'_{PTFE}) and imaginary (ϵ''_{PTFE}) parts of the dielectric function of PTFE, taken from ref. [56]. 93

- 4.1 (a) Sketch of a one-dimensional metal-insulator-metal cavity. The surface plasmon-polariton modes propagating at each interface (drawn in red) are weakly coupled for a thick cavity ($t_d \gg \lambda$, panel (b)) and are strongly coupled for a narrow cavity ($t_d \ll \lambda$, panel (c)). (d) Same as panel (c) except that one of the metallic layers has a finite length w . Reproduced from ref. [14]. 99
- 4.2 (a) Cross-sectional view of a square-patch MIM antenna, showing a p -polarized electric field of amplitude $|E^P|$, that is incident from the top at an angle θ . (b) Top view of the antenna. (c) Real (n_{ZnS}) and imaginary (k_{ZnS}) parts of the index of refraction of the insulator layer of the antenna, which consists of zinc sulfide (ZnS). The average value of the index of refraction of ZnS in the spectral range considered here is $\bar{n}_{\text{ZnS}} = 2.21 + 0.003i$. Optical constants taken from ref. [16]. (d) Fabry-Perot phase matching condition for the fundamental resonant mode ($m = 1$), $\lambda_1^{\text{res}} = 2\tilde{n}_{\text{eff}}w$ ($n_{\text{eff}} = \tilde{n}_{\text{eff}} + i\tilde{k}_{\text{eff}}$), of the antenna sketched in panels (a) and (b) with $w = 1.65 \mu\text{m}$. The fundamental resonance mode occurs at $\lambda_1^{\text{res}} = 8.88 \mu\text{m}$. (e) Finite-difference time-domain simulation of the electric field enhancement ($|E|/|E^P|$) in the near-field of the square patch MIM antenna with $w = 1.65 \mu\text{m}$, computed at one of the ends of the patch in the xz -plane at $\lambda = 8.88 \mu\text{m}$ for normal incidence ($\theta = 0^\circ$). (f) Electric field enhancement of the antenna in the xy -plane 30 nm above the patch at $\lambda = 8.88 \mu\text{m}$. Further details on the FDTD simulations presented here can be found in Appendix B. 101
- 4.3 (a) & (b) Finite-element method simulations of the cross-sections of the MIM antenna of Figs. 4.2 (a) and (b) with $w = 1.65 \mu\text{m}$, for $\theta = 0$ and 60° . (c) & (d) Radiation pattern of the MIM antenna at resonance ($\lambda = 8.88 \mu\text{m}$) for p - and s -polarized light. Further details of the simulation methods used here can be found in Appendix A. Legend: black, absorption cross-section (C_{abs}); red, scattering cross-section (C_{scat}); blue, extinction cross-section (C_{ext}). 102
- 4.4 (a) Topography of a $1.65 \times 1.65 \mu\text{m}^2$ square-patch MIM antenna. (b) Amplitude ($|E|$) and (c) phase (ϕ) images of the near-field optical signal of the patch antenna of panel (a), demodulated at the 3rd harmonic of the tip oscillation frequency. The slight asymmetry in the field distribution arises from the oblique illumination used in the measurements. (d) Sketch illustrating the illumination configuration used in panels (b) and (c). A p -polarized quantum cascade laser source ($\omega = 1126 \text{ cm}^{-1}$) is used with an incidence angle of 60° . The projection of the incident electric field onto the antenna in the xy -plane is indicated by the double arrow marked by E^P . (e) Amplitude and (f) phase from the finite-difference time-domain simulations corresponding to the measurements in panels (b) and (c), computed in the xy -plane 30 nm above the antenna. The color bar in panel (e) is scaled for better agreement with panel (b). The maximal values of the amplitudes of the electric field components in the x , y , and z -directions were found at the vertices of the patch and are given by: $\max(|E_x|) = \max(|E_y|) = 16.44 \text{ V/m}$ and $\max(|E_z|) = 20.23 \text{ V/m}$. (g) Normalized amplitude of the nano-FTIR spectrum measured at the vertex of the patch marked with a star in panel (b). The spectrum is normalized to that of a reference Si sample and the result is shown for the 4th harmonic. The inset shows the simulated electric field enhancement at resonance in the xy -plane 30 nm above the antenna. The far-field absorption spectrum of the same antenna is shown in Fig. A8 of the appendix. 103

4.5	(a) Sketch of a MIM stack consisting of the following layers from top to bottom: Au(50 nm)/SiO ₂ (180 nm)/Au(200 nm), where the layer thickness is indicated between parenthesis. The top Au layer is a sub- λ square patch of side w . (b) Normalized IR-SMS spectra of the single nanoantenna sketched in panel (a) for different widths w . (c) FDTD simulations of the absorption cross-section (normalized by the maximal value) corresponding to the measurements of panel (b). (d) Phase-matching condition for the MIM antenna fundamental resonance mode (λ_1^{res}) and effective extinction coefficient \tilde{k}_{eff} . (e) Calculated intensity maps inside the cavity of a MIM nanoantenna (dashed outline) for the two resonances denoted by the markers in (c). The white scale bars correspond to 1 μm . Reproduced from ref. [17].	105
4.6	(a) Schematic illustration of the BiMIM geometry and IR-SMS technique. The sample consists of a transparent Si substrate on top of which a 200 nm-thick layer of gold is evaporated, then a 300 nm spacer layer of SiO ₂ is deposited, and a final top layer consisting of two 100 nm-thick sub- λ gold square patches, and sides $w_1 = 2 \mu\text{m}$ and $w_2 = 2.5 \mu\text{m}$, separated by a gap g . An SEM image of the investigated sample is shown in the top right corner. The scale bar is 1 μm . (b) Measured IR-SMS far-field thermal emission spectrum of a BiMIM with a 1 μm gap compared to that of its constituent MIM antennas. The antennas resonate near (6.5 μm , 10.5 μm) and (7.2 μm , 11.2 μm), for $w = 2 \mu\text{m}$ and 2.5 μm , respectively.	106
4.7	(a) Measured thermal emission spectra of the BiMIM structure for different gap size g . (b) FDTD calculations of absorption cross-sections for normally incident, unpolarized illumination, corresponding to the measurements. The inset shows a sketch of the dimer geometry showing two of the hybrid modes of the BiMIM, for electric field polarizations parallel (E_{\parallel}) and perpendicular (E_{\perp}) to the dimer axis. The positive and negative signs indicate the surface charge distribution.	107
4.8	(a) Measured thermal emission and (b) calculated emission cross-section of the BiMIM structure with $g = 100 \text{ nm}$ for polarized thermal emission. (c) Plots of the z -component E_z of the electric field in the xy -plane at the top of the square metal patches, at the resonance peaks indicated by the markers (i), (ii), (iii), and (iv) in panel (b). The double arrow indicates the electric field polarization in each case.	109
4.9	(a) Simulated absorption cross-section for unpolarized light for the considered BiMIM structure with $g = 100 \text{ nm}$ compared with that of a symmetric BiMIM whose patches have widths $w_1 = w_2 = 2 \mu\text{m}$. (b) Electric field enhancement plots showing field hot spots in the xy -plane at the top of the metal patches, recorded at the resonance positions in panel (a).	110

- 4.10 (a) Sketch of the s-SNOM configuration used for the mapping of the near-field of a 3×3 -patch MIM antenna. The antenna consists of a stack with the following layers from top to bottom: Au (40 nm)/ZnS (270 nm)/Au (200 nm), where the top layer comprises nine patches of width $w = 1.65 \mu\text{m}$, placed in a 3×3 configuration with a gap of 100 nm (see Appendix G for details on sample fabrication). (b) Scanning electron microscope (SEM) image of the 3×3 -patch MIM antenna. Courtesy of Christophe Dupuis from C2N. See Fig. A6 for more details. (c-g) Near-field images of the measured amplitude of the s-SNOM signal demodulated at the 3rd harmonic and their corresponding FDTD simulations at the resonance frequencies indicated by the markers in panel (i). The simulation results were computed in the xy -plane 30 nm above the Au patches of the antenna, *i.e.*, at the average height of the tip in our experiment ($\Delta z \approx 60$ nm). (e) Atomic force microscope (AFM) image showing the topography of the 3×3 -patch antenna. (h) Projection of the p -polarized incident field onto the antenna in the xy -plane. (i) FEM simulation of the extinction cross-section of the antenna for a p -polarized field incident as sketched in the inset. 111
- 4.11 (a) Amplitude ($|E|$), (b) phase (ϕ), and (c) real part ($\text{Re}\{E\} = |E| \cos \phi$) of the near-field of the antenna, mapped at 940 cm^{-1} . The real part of the electric field shows that charges of opposite sign are present at the patch edges separated by the nanometric gap (100 nm). (d-f) FDTD simulations corresponding to panels (a-c). The antenna is illuminated from the bottom left corner of the panels with p -polarized light incident at 60° from the normal to the surface. The projection of the incident field onto the antenna is indicated by the double arrows in panels (a) and (d). The scale bars correspond to $2 \mu\text{m}$ 113
- 4.12 (a) & (b) Far-field response of the 3×3 -patch MIM antenna versus angle of incidence θ sketched in panel (c). The blue curves correspond to focused microscope reflectivity (*Bruker Hyperion*) spectra of the antenna, each measured with a Cassegrain objective with a different angular collection interval ($\theta \approx 10 - 24^\circ$ for (a) and $\theta \approx 33 - 52^\circ$ for (b)). The red curves are FEM simulations of the extinction cross-section (C_{ext}) of the antenna averaged at three different values of θ within the collection interval of the objective. The two resonance modes of the antenna are marked with the letters "A" and "B" in panel (b). The dips in the reflectivity spectra correspond to the maxima of C_{ext} . (c) Sketch depicting the incident (E_{inc}) and scattered (reflected, E_{scat}) fields in the experiment. A broadband unpolarized global source is used as the illumination. The same objective is used to focus the incident field onto the antenna and collect its scattered field. A diaphragm is also employed to restrict the field of view of the detector to a $50 \times 50 \mu\text{m}^2$ region of the sample. A reference measurement is first performed on a part of the sample with no patterns, giving the intensity of the incident field I_{inc} . This is followed by a measurement with the antenna in the focus of the objective, giving the intensity I_{scat} . The reflectivity is then found from the ratio $R = I_{\text{inc}}/I_{\text{scat}}$. (d-f) FDTD simulations of the electric field enhancement $|E|/|E^P|$, where E^P is the p -polarized incident field sketched in Figs. 4.10 (h) and (i), calculated in xy -plane 30 nm above the patches for the two modes A and B as a function of increasing angle θ 114

4.13	<p>Simulations of the MIM antenna of Fig. 4.10 (a) but with a top layer consisting of only two patches separated by a gap of 100 nm (BiMIM geometry). (a) FEM simulations of the extinction cross-section of the BiMIM structure for two angles of incidence ($\theta = 0^\circ$ and 60°.) as sketched in the inset. The dashed vertical line marks the spectral position of the fundamental resonance mode of a single square patch of the shown BiMIM structure. (b) & (c) FDTD simulations of the electric field enhancement, E / E^P, computed in the xy-plane 30 nm above the BiMIM structure at the resonance frequency $\omega = 1037 \text{ cm}^{-1}$.</p>	116
4.14	<p>(a) Topography of 3×3-patch antennas with a missing element. (b) Measured and (c) computed near-field images of the antennas, mapped at the resonances indicated by arrows in panel (d), and their corresponding FDTD simulations. The antenna is illuminated by p-polarized light from the bottom left corner of the panels with an incidence angle of 60° with respect to the normal to the surface. The double arrow in the top panels of columns (b) and (c) indicates the projection of the incident field polarization onto the antenna. (d) FEM simulations of extinction cross-section spectra of the antennas for p-polarized light incident at 60° with respect to the normal to the surface. The corresponding extinction spectra at smaller angles are shown in Fig. A13.</p>	117
5.1	<p>Depiction of the density of states for various quasi-particles (reproduced from ref. [13]). (a) Charge carriers in condensed matter physics are usually described by the Schrödinger equation with an effective mass m^* that is different from the free electron mass (\hat{H} and \hat{p} are the Hamiltonian and momentum operators, respectively). The effective mass approximates the effect of the particle's potential, which in general may take a very complicated form. (b) Relativistic particles in the limit of zero rest mass follow the Dirac equation, where c is the speed of light and $\vec{\sigma}$ is the Pauli matrix. (c) Charge carriers in graphene are called massless Dirac fermions and are described by a 2D analog of the Dirac equation, with the Fermi velocity $v_F \approx 10^6 \text{ m/s}$ playing the role of the speed of light and a 2D pseudo-spin matrix describing two sub-lattices of the honeycomb lattice. Similar to the real spin that can change its direction between, say, left and right, the pseudo-spin is an index that indicates on which of the two sub-lattices a quasi-particle is located. The pseudo-spin can be indicated by color (<i>e.g.</i> red and green). (d) Bi-layer graphene provides us with yet another type of quasi-particles that have no analog. They are massive Dirac fermions described by a rather bizarre Hamiltonian that combines features of both Dirac and Schrödinger equations. The pseudo-spin changes its color index four times as it moves among four carbon sub-lattices.</p>	122
5.2	<p>Examples of visible light incandescent emission from graphene devices under bias: (a-b) suspended graphene (ref. [26]), (c-e) hBN encapsulated graphene (ref. [27]), and (f-h) hBN-encapsulated graphene with a constriction in the center of the channel (ref. [28]). The images in (b), (d), and (g) are microscope images of the visible light emission of the device under bias. Panels (b), (e), and (h) show the visible light emission spectra of the device under bias (dots), which are fitted by appropriately modeling the Planck blackbody emission of the device (solid curves). The fits provide estimates of the electron gas temperature T_e (legend keys). Notice that a significantly large electric field must be applied across the channel to bring about the visible light emission from these devices. In panel (d), for instance, the applied electric field is as large as $6.6 \text{ V}/\mu\text{m}$ for a channel that is $6 \mu\text{m}$ in length and $3 \mu\text{m}$ in width.</p>	125

- 5.3 (a) Schematic illustration of the geometry of a high-mobility field-effect transistor (HGFET). A mono-layer graphene is encapsulated between two hBN layers, that are placed on a back-gate layer. The top hBN layer is etched, revealing the two ends of the graphene layer. Gold/chromium pads are then evaporated onto the etched regions, creating the source and drain electrodes of the transistor. The region between the two electrodes forms the transistor's channel with an area given by $A = L \times W$, where L and W are the channel length and width, respectively. See Appendix K for more details on the device fabrication process. (b) Three-dimensional sketch of a typical HGFET with a back-gate consisting of an SiO_2/Si substrate. (c) Microscope image of an hBN-encapsulated HGFET with a channel area $A = L \times W \sim 35 \mu\text{m} \times 35 \mu\text{m}$ on an SiO_2/Si back-gate (the transistor's graphene channel is indicated by a black box). The mono-layer graphene is encapsulated between a 65 nm-thick hBN layer from the bottom and an 82-nm-thick hBN layer from the top. The estimated electron mobility of this transistor is $60,000 \text{ cm}^2/\text{V.s}$ at room temperature with a contact resistance of 250Ω . (d) Zoom of the layers forming the encapsulated graphene transistor of panel (b). 126
- 5.4 (a) Low-bias transfer curve of an HGFET measured at 300 K and $V_{ds} = 10 \text{ mV}$. Right inset: Optical image of the transistor. (b) Transfer curves of the transistor as a function of increasing bias voltage V_{ds} . The dashed line is a guide for the eye. The inset shows the evolution of the maximal channel resistance R_{max} as a function of increasing V_{ds} . This indicates the evolution of the gate voltage V_g , at which charge neutrality is reached, as a function of increasing V_{ds} . (c) Non-linear current density to voltage transfer curve ($j = I_{ds}/L$ vs V_{ds}) for the hole-doped regime. The gate voltage (and hence carrier density and Fermi energy) increases linearly in the range $V_g = [0, -14.7] \text{ V}$ (shown in colors, black to red) so that the hole density range is $p = [0, 4.05] \times 10^{12} \text{ cm}^{-2}$, and $E_F = [0, 0.24] \text{ eV}$. (d) Schematic representation of the non-linear interband current (red curve, constant doping) and the intraband current (dashed curve). The intraband current saturates rapidly due to the high electron mobility. However, beyond a threshold bias V_{ZK} , the interband current originating from Zener-Klein tunneling processes (see main text) becomes predominant so that the current saturation is compensated for and an overall non-linear current behavior is observed as in panel (c). 129
- 5.5 Depiction of electronic distribution along a mono-layer graphene channel under large bias. For a tunneling process with a characteristic coherence length, l_{coh} , a threshold electric field $\mathcal{E}_{\text{th}} = |\Delta E_{\text{tun}}|/el_{\text{coh}}$ is required for tunneling to occur, where ΔE_{tun} is the energy difference between the initial and final state. Zener-Klein tunneling processes in graphene (represented by dashed green arrows) occur with a coherence length $l_{\text{coh}} \equiv l_{ZK}$ and $|\Delta E_{\text{tun}}| = 2E_F$ 131
- 5.6 Noise temperature versus Joule heating at various doping concentrations in a bi-layer HGFET. Colors represent doping with respective carrier densities $n = 0$ (red), 0.18 (tangerine), 0.35 (orange), 0.53 (amber), 0.70 (yellow), 0.88 (chartreuse), 1.05 (green), 1.23 (turquoise), 1.40 (cyan), 1.58 (cerulean), 1.75 (blue), $1.93 \times 10^{12} \text{ cm}^{-1}$ (dark blue). Reproduced from ref. [23]. 134
- 5.7 Real part of the optical admittance (Z^{-1}) of hBN (omitting the type I *Reststrahlen* band) on two in-plane wavevector scales to illustrate the far field and HPhP extension of radiation phase space. The impedance matching window in the *Reststrahlen* has an upper bound at $2k_F$. Reproduced from ref. [23]. 135

-
- 5.8 Transport and noise temperature of an hBN-supported bi-layer graphene transistor. (a) Current saturation and Zener–Klein regimes in a high-mobility bi-layer graphene flake of dimensions $L \times W = 3.6 \mu\text{m} \times 3 \mu\text{m}$. The sample (upper inset) is deposited on a 200 nm-thick hBN flake acting both as a bottom gate dielectric (capacitance per unit area $Cg = 0.14 \text{ mF}\cdot\text{m}^{-2}$) and hyperbolic phonon polariton radiator. Carrier density is tuned in the hole doping range – $n = 0$ (red), 0.35 (orange), 0.70 (yellow), 1.05 (green), 1.40 (cyan), 1.75 (blue), $2.10 \times 10^{12} \text{ cm}^{-2}$ (purple). At low bias, intraband current dominates up to a threshold field $\mathcal{E}_{sat} = v_{sat}/\mu$ set by the saturation velocity $v_{sat} \lesssim 3 \times 10^5 \text{ m/s}$ and mobility $\mu \gtrsim 1 \text{ m}^2\cdot\text{V}^{-1}\cdot\text{s}^{-1}$. At large bias, above a Pauli unblocking voltage V_{ZK} (see Eq. (5.3)), the intraband current is fully saturated, and an additional current arising from interband Zener–Klein tunneling with a constant conductance $\sigma_{ZK} \simeq 0.45 \text{ mS}$ sets in. The boundary between intraband and interband transport regimes follows the theoretically expected behavior given by Eq. (5.7) (black dashed line with the circles corresponding to theoretical values of current). (b) Noise temperature $T_N = S_I/4G_{ds}k_B$ deduced from the microwave excess current noise S_I and the differential conductance G_{ds} . Noise thermometry reveals a striking difference between the intraband and interband regimes with a super-linear bias dependence characteristic of "hot" electrons (black dashed line) in the former, dropping toward a linear dependence characteristic of the "cold" electron regime in the latter. The theoretical value for the threshold between cooling and heating due to electroluminescence is indicated by the staggered-dashed line. Reproduced from ref. [23]. 137
- 5.9 (a) Simplified depiction of the phonon-assisted electron-hole recombination process between the source and drain electrodes of a light-emitting diode, which results in the cooling of the diode. (b) Optical power of a GaSb LED as a function of injected bias voltage V_{sd} . Courtesy of the manufacturer. The black cross marks the sub-threshold bias voltage at which cooling due to the recombination process illustrated in panel (a) occurs. 139
- 5.10 Penetration depth of HPhP branches in a 200 nm-thick hBN film for $l \leq 4$ 140

- 5.11 (a) Depiction of the out-of-plane heat transfer in an HGFET with an SiO₂ back-gate. The subsequent mid-IR emission is represented by a red wavy arrow. (b) Schematic illustration of the detection technique used for the characterization of the optical signal (P_{opt} , integrated over the full spectral range of the detector) of an HGFET (inset, $L \times W = 35 \times 35 \mu\text{m}^2$) due to the radiative emission of the SiO₂ back-gate. (c) Spectral radiance of the transistor for an applied electric field $E = V_{ds}/L = 0.77 \text{ V}/\mu\text{m}$ ($V_g = 0 \text{ V}$), measured with the setup of panel (b). The spectrum is subtracted by a reference measurement to remove the contribution of the optical chopper to the detected signal. The spectrum is then normalized by the response function of the setup (see subsection 3.2.1), yielding the spectral radiance of the transistor. The blue-shaded region encloses the *Reststrahlen* band of SiO₂. (d) Spatial scan of the transistor's optical signal. The signal is most intense between the source and drain electrodes, indicating that the emission originates from the transistor's channel. (e) Optical signal as a function of electrical bias. The white-dashed curve marks the threshold for Zener-Klein tunneling. (f) Out-of-plane dissipated power (P_{out}) as a function of electrical bias, computed from $P_{\text{out}} = \Delta T_{\text{SiO}_2}/R_{\text{th}}$, where $\Delta T_{\text{SiO}_2} \simeq 20 - 40 \text{ }^\circ\text{C}$ and $R_{\text{th}} \simeq 357 \text{ K}\cdot\text{W}^{-1}$ (see Appendix M). (g) Joule power (P_{Joule}) as a function of electrical bias. (h) Percentage giving the contribution of the out-of-plane cooling mechanism to the total cooling power obtained from the ratio $\frac{P_{\text{out}}}{P_{\text{Joule}}} = \frac{P_{\text{out}}}{(P_{\text{out}}+P_{\text{in}})}$, where P_{in} is the in-plane cooling power. 142
- 5.12 (a) Comparison between the spectral radiance of a large HGFET ($L \times W = 35 \mu\text{m} \times 35 \mu\text{m}$) under large electrical bias, before (Fig. 5.11 (c)) and after the addition of scatterers, marked with an asterisk and a star, respectively. (b) Spectral radiance of a smaller HGFET ($L \times W = 9.2 \mu\text{m} \times 15.5 \mu\text{m}$, $\mu = 66,000 \text{ cm}^2/\text{V}\cdot\text{s}$, optical image in inset) as a function of increasing electrical bias $E = V_{ds}/L$ ($V_g = 0 \text{ V}$). (c) Evolution of the radiance of the hBN peak, marked by a diamond in panel (b), as a function of the applied electric field E (black circles). The experimental values are fitted to the spectral radiance of a Planck blackbody law (blue triangles), given by $S_P = B(T_e^{\text{NIR}})^4$, where B is a fitting parameter and T_e^{NIR} is the temperature of electrons in graphene under bias. For the two points shown here, we have $(E, T_e^{\text{NIR}}) = (0.47 \text{ V}/\mu\text{m}, 520 \text{ K})$ and $(0.87 \text{ V}/\mu\text{m}, 640 \text{ K})$. B is determined by equating S_P at $E = 0.47 \text{ V}/\mu\text{m}$ to the value of the hBN peak amplitude at the same point. The values for T_e^{NIR} were obtained by characterizing the transistor's thermal radiation in the near-IR spectral range ($\lambda_{\text{NIR}} = 1.4 - 1.6 \mu\text{m}$) as a function of electrical bias using an InGaAs near-IR camera. Courtesy of Marin Tharraul from Laboratoire de Physique de l'Ecole Normale Supérieure (LPENS). 145

5.13	Mid-IR emission of an electroluminescent hBN-encapsulated HGFET with a gold back-gate denoted by <i>Flicker 160</i> (panel (b), inset). (a) Sketch of an hBN-encapsulated HGFET with a gold back-gate. The dimensions (L , channel length; W , channel width; $t_{\text{hBN}}^{\text{b}}$; thickness of bottom hBN layer, thickness of top hBN layer, $t_{\text{hBN}}^{\text{t}}$) and electron mobility (μ) of the transistor considered here are as follows: $L \times W = 6 \mu\text{m} \times 10 \mu\text{m}$, $t_{\text{hBN}}^{\text{b}} = 160 \text{ nm}$, $t_{\text{hBN}}^{\text{t}} = 45 \text{ nm}$, and $\mu \sim 15 \times 10^4 \text{ cm}^2 \cdot \text{V}^{-1} \cdot \text{s}^{-1}$ (see Appendix L for more details). (b) Spectral radiance of the Flicker 160 transistor under electrical bias ($E = V_{\text{ds}}/L = 0.84 \text{ V}\mu\text{m}^{-1}$) and by heating the device with a hot plate, measured via IR-SMS. (c) Optical signal (P_{opt} , integrated over the full spectral range of the detector) of <i>Flicker 160</i> as a function of increasing electrical bias for three values of the doping concentration. The data points show a super-linear dependence of the optical signal on the applied bias, <i>i.e.</i> , $P_{\text{opt}} \propto E^2 = V_{\text{ds}}^2/L^2$. The green triangles correspond to Planck blackbody fits of the experimental data, calculated from near-IR measurements of the electron gas temperature of graphene under electrical bias (courtesy of Marin Tharrault from LPENS).	147
5.14	Mid-IR emission of an electroluminescent hBN-encapsulated HGFET with a gold back-gate denoted by <i>InOut2</i> (panel (c), inset). The dimensions (L , channel length; W , channel width; $t_{\text{hBN}}^{\text{b}}$; thickness of bottom hBN layer, thickness of top hBN layer, $t_{\text{hBN}}^{\text{t}}$) and electron mobility (μ) of this transistor are as follows: $L \times W = 20 \mu\text{m} \times 8.5 \mu\text{m}$, $t_{\text{hBN}}^{\text{b}} = 118 \text{ nm}$, $t_{\text{hBN}}^{\text{t}} = 67 \text{ nm}$, and $\mu \sim 9 \times 10^4 \text{ cm}^2 \cdot \text{V}^{-1} \cdot \text{s}^{-1}$ (see Appendix L for more details). (a) Joule power (P_{Joule}) of the transistor as a function of the applied electrical field $E = V_{\text{ds}}/L$. (c) Scan of the optical signal (P_{opt}) of the transistor as a function of doping concentration n and applied electric field. (c) Line scans at constant doping concentration from panel (b).	149
5.15	Fits of the mid-IR emission of the <i>Flicker 160</i> and <i>InOut2</i> transistors assuming a super-linear dependence on E (panel (a)) and V_{ds} (panel (b)). Symbols: experimental data, solid lines: fits.	150
A1	Geometry used to simulate a single sub- λ antenna using the commercial FEM solver of Maxwell's equations, Comsol Multiphysics. The geometry is bounded by perfectly matched layers (PMLs) of thickness $\lambda/5$ in all directions.	ii
A2	Geometry used to simulate a single sub- λ antenna using the FDTD solver of Maxwell's equations, Lumerical Solutions. The geometry is bounded by perfectly matched layers PMLs in all directions. The distance between the edges of the antenna and the PML boundaries is taken to be $\lambda_{\text{max}}/4$, where λ_{max} is the longest wavelength considered.	iii
A3	FEM calculations of the temperature distribution in a $2.5 \mu\text{m}$ radius SiO_2 sphere (a) on and (b) $1 \mu\text{m}$ above a gold substrate with $T_{\text{substrate}} = 440 \text{ K}$	iv
A4	FEM calculations of absorption cross-section (C_{abs}) of an SiO_2 sphere on gold, with (a) $r_o = 1 \mu\text{m}$ and (b) $r_o = 2.5 \mu\text{m}$, for unpolarized light incident at various angles θ , as sketched in the inset of panel (a). The curves in panel (b) are shifted vertically for clarity and the dashed vertical line shows the surface mode peak position (ω_S).	iv

A5	Simulated absorption cross-section (C_{abs}) of a BiMIM structure for gap size $g = 100$ nm (red curve) presented in the main text (red curve in Fig. 4.7 (b) of the main text), along with the imaginary part of the SiO_2 index of refraction (\tilde{k}_{SiO_2} , blue curve). Optical constants taken from ref. [7]. The comparison of the two shows a high absorption due to SiO_2 in the spectral region between 8 and 13 μm , which prevents the formation of a splitting in the BiMIM emission spectrum in this range.	v
A6	Scanning electron microscope (SEM) images of square-patch metal-insulator-metal (MIM) antennas. (a) A 45° tilted SEM image of a single square-patch MIM antenna of side $w = 1.65 \mu\text{m}$. (b) Tilted SEM image of a 3×3 square-patch MIM antenna with a patch width of $1.65 \mu\text{m}$ and a gap size of 100 nm. (c) Zoom of the gaps is panel (b). (d-f) SEM images of 3×3 square-patch MIM antennas with a missing patch. The scale bars are as follows: (d) $4 \mu\text{m}$, (e) & (f) $3 \mu\text{m}$. Electron beam parameters: High voltage = 10 kV, Current = 0.2 nA, and $30,000 < \text{Magnification} < 350,000$. Courtesy of Christophe Dupuis from C2N (CNRS/University Paris-Sud/Paris-Saclay).	vi
A7	(a) SEM image of 3×3 -patch MIM antenna. (b) Atomic force microscope (AFM) image showing the topography of the antenna. (c) Sketch showing the thicknesses of the various layers of the antenna.	vii
A8	Comparison between the measured IR-SMS and FEM-simulated absorption cross-section spectra of a single square-patch MIM antenna of side $w = 1.65 \mu\text{m}$. The spectra show the fundamental resonance mode of the antenna at 1126 cm^{-1} (cf. Eq. (4.6)).	vii
A9	(a-c) (resp. (d-f)) FDTD simulations of the x , y , and z -components of the electric field of a 3×3 -patch antenna for p -polarized light (resp. s -polarized light), calculated at the resonance marked in panel (i). The plots show that just as in the single square-patch case, the near-field of the antenna is such that $ E_x = E_y < E_z $. (g) & (h) Sketches of the antenna geometry and illumination configuration. (i) FEM simulations of the extinction cross-section of the antenna for p - and s -polarized light.	viii
A10	Approach curves measured at the surface of a large gold pattern with a silicon (Si) tip, showing a comparison between the near-field signal demodulated at the 2nd and 3rd harmonic (blue and red curves, respectively). This comparison demonstrates that demodulation at the 3rd harmonic is required in order to adequately isolate the near-field signal. It is clear that the signal s_3 decays exponentially away from the surface and becomes negligible when the tip is 300 nm away from the sample surface (<i>i.e.</i> , in a fully retracted position), a behavior characteristic of a near-field signal. On the other hand, s_2 includes a large background contribution as it is non-zero when the tip is fully retracted. The background signal mainly originates from laser light back-scattered off the tip shaft as it oscillates away from the sample.	ix
A11	Comparison between near-field images of a 3×3 -patch antenna measured with an Si tip (panel (a)) and a platinum (Pt) coated tip (panel (b)). The image in panel (a) shows a clearly resolved field in the gaps between the patches, while that of panel (b) shows no field in the gaps. This comparison illustrates the fact that a dielectric tip, such as the Si tip used here, minimally perturbs the near-field of a plasmonic nanostructure, whilst a metal-coated tip completely distorts its near-field.	ix

-
- A12 Microscope reflectivity measurements (*Bruker Hyperion*) of a 3×3 -patch MIM antenna as function of gap size g . The measurements were performed using a Cassegrain objective with $\text{NA} = 0.4$ which collects light within an angular interval $\theta \in [10^\circ, 24^\circ]$, where θ is the angle with respect to the normal to the sample surface. x
- A13 Microscope reflectivity measurements of 3×3 -patch MIM antennas with a missing patch ($g = 100$ nm). x
- A14 Transport properties of two electroluminescent hBN-encapsulated HGFETs with a gold back-gate (discussed in chapter 5), denoted as *Flicker 160* and *InOut2* (optical images in the insets of panels (b) and (e)). The dimensions (L , channel length; W , channel width; t_{hBN} , thickness of bottom hBN layer) and electron mobility (μ) for these two transistors are as follows: *Flicker 160* (a-c), $L \times W \times t_{\text{hBN}} = 6 \mu\text{m} \times 10 \mu\text{m} \times 160$ nm and $\mu \sim 15 \times 10^4 \text{ cm}^2 \cdot \text{V}^{-1} \cdot \text{s}^{-1}$; *InOut2* (d-f), $L \times W \times t_{\text{hBN}} = 20 \mu\text{m} \times 8.5 \mu\text{m} \times 118$ nm and $\mu \sim 9 \times 10^4 \text{ cm}^2 \cdot \text{V}^{-1} \cdot \text{s}^{-1}$. The plotted transport properties are as follows: (a) & (d) current-voltage curves at fixed charge carrier density (the carrier density is increased linearly from $n = 0$ to the maximal value in steps of $1 \times 10^{11} \text{ cm}^{-3}$), (b) & (e) differential conductivity σ_{ds} as a function of bias (squares) along with the fits (solid lines) using Eq. (5.4) of the main text, (c) & (f) fits of the IV-curves (blue squares) using Eqs. (5.6)-(5.8), where V_{ZK} and T_e are left as adjustable parameters. The total current fit ($I_{\text{intra}} + I_{\text{inter}}$) is plotted in orange, whereas the intraband current (I_{intra}) appears in green and underlines the quasi-linear increase of interband current at large bias. Courtesy of Aurélien Schmitt who designed, fabricated, and characterized these transistors at Laboratoire de Physique de l'École Normale Supérieure (LPENS). xii
- A15 (a) Comparison between the mid-infrared (mid-IR) spectra of the hBN-encapsulated HGFET of panel (d) with an SiO_2 back-gate under electrical bias and by heating the transistor via a hot plate at various temperatures T . The mid-IR signal is measured using an optical chopper (see Fig. 5.11 (a)). The plotted spectra are corrected by a reference measurement, which removes the contribution of the chopper to the detected signal. (b) Linear fit of the maxima of the spectra obtained with the hot plate (S_{max}) as a function of temperature. From the comparison of panel (a) we find that the temperature of SiO_2 back-gate varies between $T_{\text{SiO}_2} \simeq 50 - 60$ °C when the transistor is electrically biased. (c) Increase in the temperature of the SiO_2 back-gate (ΔT_{SiO_2}) as a function of electrical bias. (d) Left: an optical image of the transistor under study, right: equivalent sketch, in which the heat conduction in the back-gate under the graphene channel ($L \times W = 35 \times 35 \mu\text{m}^2$) of the transistor is modeled via an effective thermal resistance $R_{\text{th}} = R_{\text{ox}} + R_{\text{Si}} = 356.66$ K/W, where R_{ox} and R_{Si} correspond to the thermal resistance in the SiO_2 and Si layers, respectively (see ref. [9] for more details). Here, $t_{\text{ox}} = 285$ nm is the thickness of the SiO_2 layer and $k_{\text{ox}} = 1.4$ W/m.K and $k_{\text{Si}} = 150$ W/m.K are the thermal conductivities of SiO_2 and Si, respectively. Using this model and the result of panel (c), we can compute the power dissipated, P_{out} to the SiO_2 layer via out-of-plane radiative cooling due to the electroluminescence of the transistor. Formally, this is written as $P_{\text{out}} = \Delta T_{\text{SiO}_2} / R_{\text{th}}$. The result of this calculation is plotted in Fig. 5.11 (f) of the main text. xiii

A16 Absorptivity (A) of the *Flicker 160* HGFET (optical image in inset) as a function of electrical bias, determined from microscope reflectivity measurements (*Bruker Hyperion*). Since the transistor is built on a gold back-gate the absorptivity is given by $A = 1 - R$, where R is the measured reflectivity. Measurements for minimal ($V_{ds} = 0$ and $n = 0$) and maximal ($V_{ds} = V_{ds}^{\max} = 5$ V and $n = n_{\max} = 6 \times 10^{11}$ cm $^{-2}$) electrical bias are presented. It is clear that the measured absorptivity spectra are overlapping with a maximal variation of the hBN peak at 1350 cm $^{-1}$ of only $\sim +0.2\%$ between $V_{ds} = 0$ V and $V_{ds} = V_{ds}^{\max}$. We conclude that the transistor's absorptivity varies negligibly as a function of applied electrical bias. . xiv

A17 Temperature of optical phonons, deduced from Stokes-anti-Stokes Raman thermometry, as a function of electrical bias (V_{ds}) for the *Flicker 160* HMGFET (see Figs. A14 (a-c)). xv

List of Tables

3.1	Scattering and absorption cross-sections of a spherical particle of radius $a = 30$ nm in air at $\lambda = 10.6$ μm for different materials.	62
3.2	Fitting parameters used in the Drude-Lorentz model for the dielectric functions of the SiO_2 and hBN layers.	68
3.3	Spectrally integrated power reaching the detector at $T^* = 440$ K, for two different Cassegrain objectives. The power is integrated over the spectral range $\lambda \in [6, 14]$ μm . It is assumed that $C_{\text{em}} = 20$ μm^2 for the antenna and $\epsilon_\lambda = 1$ for the background.	75
5.1	Room temperature thermal properties of suspended graphene compared to those of silicon (Si) and typical metals. The listed thermal properties correspond to the thermal conductivity (κ), specific heat capacity at constant pressure (C_p), and thermal diffusivity (α_D). More comprehensive lists of thermal properties of materials can be found in the literature (<i>e.g.</i> , ref. [22]). *This includes both the lattice and electron gas contributions to the specific heat.	123
5.2	Electron mobility (μ) of graphene on various substrates compared to that of state-of-the-art materials. Graphene mobility strongly depends on its substrate, the best yet being hBN. At room temperature, the electron mobility of graphene is superior to that of state-of-the-art transport materials, however, at low temperatures, the mobility of the two-dimensional electron gas (2DEG) in AlGaAs/GaAs quantum wells is still 10 times better.	128

Chapter 1

Introduction

The study of light-matter interaction at the subwavelength (sub- λ) scale has been at the core of recent advancements in nanoscience and nanotechnology. Originally, this has been chiefly motivated by the apparent benefits of miniaturization and integration of electronic circuits for the computer industry. In more recent years, however, research in this field has been rather driven by the fact that, as we move to smaller and smaller scales, new physical effects that may be exploited in future technological applications may be uncovered. For instance, if the size of an object was to be perpetually diminished, at some stage, one would reach the molecular level and even the atomic level, below which physical and chemical properties are dramatically different from those of the original material. In essence, the properties of materials at very small scales may be quite different from those of the corresponding bulk materials.

In the wake of the increasing trend toward nanoscience and nanotechnology, the study of electromagnetic phenomena at the sub- λ scale has become an absolute necessity. Since the diffraction limit precludes the focusing of light to dimensions smaller than roughly one-half of the wavelength, traditionally, deeply sub- λ features were largely inaccessible. Nevertheless, in recent years, several new approaches to "shrink" the diffraction limit (or even overcome it) have been theorized and subsequently implemented experimentally. A central goal of sub- λ physics (and nano-optics in particular) is to extend the use of optical techniques to length scales beyond the diffraction limit. The most obvious potential technological applications that arise from breaking the diffraction barrier are super-resolution microscopy and ultra-high-density data storage. Further, one may envision the design and engineering of nanostructures for light manipulation.

Some of the most beautiful examples of how sub- λ structures can bring about unique optical phenomena can be found in nature. Chameleons, for instance, possess the extraordinary ability to exhibit complex and rapid color changes during social interactions such as male contests or courtship. This shift in color is brought upon through the active tuning of a lattice of guanine nanocrystals within their skin, which changes how light is reflected off their bodies [1]. Another example can be found in the depths of the deep sea, where ultra-black fish lurk inconspicuously. A layer of densely packed melanosomes (characteristic size $\sim 400 - 800$ nm) endows these fish

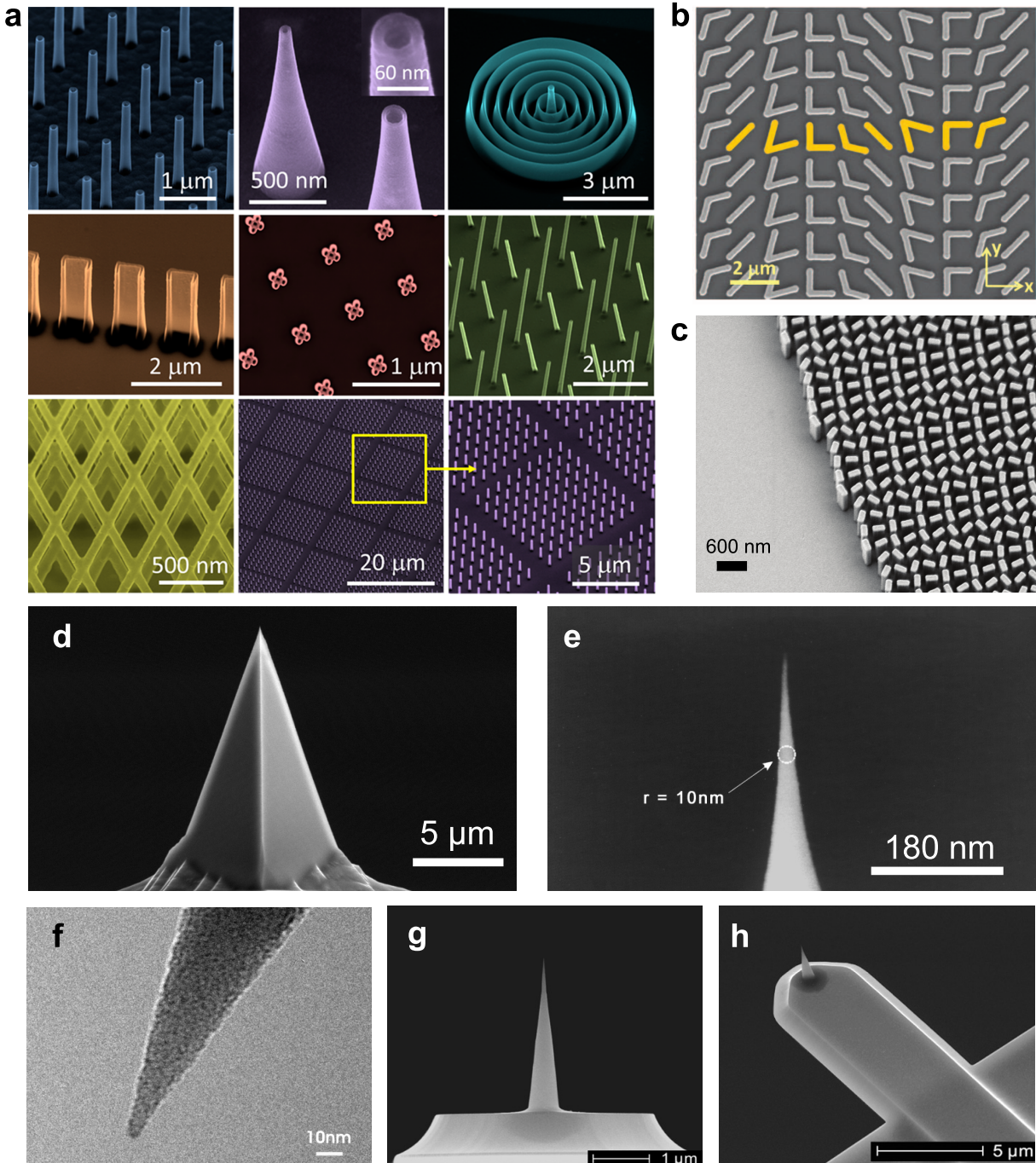


Figure 1.1: Scanning electron microscope (SEM) images of various examples of nanostructures, fabricated via lithography techniques. (a) Hollow out-of-plane nanostructures (ref. [2]). (b) & (c) Planar nanostructures (panel (b), ref. [3]; panel (c), ref. [4]). (d-h) Commercially available tips used in scanning-probe techniques. Courtesy of *Nanosensors*TM (panels (d-f)) and *NanoWorld AG* (panels (g) and (h)).

with extremely low reflectance ($< 0.5\%$), making them virtually undetectable against the pitch-black background [5].

The recent advancements in nanoscience and nanotechnologies have made it possible to routinely design artificial nanostructures and study their interactions with light (some exam-

ples are provided in Fig. 1.1). In particular, with the advent of scanning probe techniques (see Figs. 1.1 (d-h)), high-resolution electron microscopes, lithography tools, focused ion-beam milling systems, and so on, it has become possible to measure, fabricate, and manipulate individual structures down to the nanometer scale. The study of these individual sub- λ structures is an essential step toward extending the breadth of light applications. The aim of the current manuscript is to push the limits of various highly sensitive techniques, such as the tools mentioned above, to probe the mid-infrared¹ (mid-IR) electromagnetic radiation of single- or few-element sub- λ resonators.

To illustrate the fundamental limits of conventional microscopy, we recount here the previously mentioned diffraction limit. A simple way to arrive at this limit is by making an analogy with quantum mechanics through the application of the Heisenberg uncertainty principle to photons as follows [6]. Since the propagation of light in free space is determined by the dispersion relation $\hbar\omega = \hbar ck_0$, which connects the wavevector $k_0 = \sqrt{k_x^2 + k_y^2 + k_z^2}$ of a photon with its angular frequency ω via the speed of propagation c , the Heisenberg uncertainty principle for photons yields

$$\hbar\Delta k_x \Delta x \geq \frac{\hbar}{2}, \quad (1.1)$$

or

$$\Delta x \geq \frac{1}{2\Delta k_x}. \quad (1.2)$$

This result can be interpreted as follows. The spatial confinement that can be achieved for photons is inversely proportional to the spread in the magnitude of wavevector components in the respective spatial direction (x in this case). Such a spread in wavevector components occurs for instance in a light field that converges toward a focus, *e.g.*, behind a lens. Such a field may be represented by a superposition of plane waves traveling at different angles. The maximum possible spread in the wavevector component k_x is the total length of the free-space wavevector $k_0 = 2\pi/\lambda$.² This leads to

$$\Delta x \geq \frac{\lambda}{4\pi}, \quad (1.3)$$

which closely resembles the well-known expression for the diffraction limit, which was determined independently by Ernest Abbe in 1873 [7] and Lord Rayleigh in 1879 [8]. Note that the spatial confinement that can be achieved is limited only by the spread of wavevector components in a given direction.

In order to increase the spread of wavevector components we can simply choose two arbitrary perpendicular directions in space, *e.g.*, x and z , and increase one wavevector component to values beyond the total wavevector while at the same time requiring the wavevector in the perpendicular direction to become purely imaginary. If this is the case, then we can still fulfill the requirement $k_0 = \sqrt{k_x^2 + k_y^2 + k_z^2} = 2\pi/\lambda$. If we choose to increase the wavevector in the x -direction then the

¹We particularly focus on the *long-wave infrared* spectral region ($\lambda = 7 - 14 \mu\text{m}$).

²The correction due to the numerical aperture of the lens is omitted here for simplicity.

possible range of wavevectors in this direction is also increased and the confinement of light is no longer limited by Eq. (1.3). However, increasing the confinement in the x -direction comes at the cost of confinement in the z -direction as well, resulting from the purely imaginary wavevector component in this direction ($k_z = i|k_z|$) that is necessary to compensate for the large wavevector component in the x -direction. Indeed, introducing the purely imaginary wavevector component into the expression for a plane wave we obtain $\exp(ik_z z) = \exp(-|k_z|z)$. If the infinite free space were to be divided into two half-spaces sharing a boundary at $z = 0$, it is clear that our formalism leads to an exponentially decaying field, an evanescent wave, on either side of the boundary.

These simple arguments show, that in the presence of an inhomogeneity in space (such as the boundary between two different media), the diffraction limit for the confinement of light is no longer strictly valid, but in principle, infinite confinement of light becomes, at least theoretically, possible. This insight forms the basis of the field of nano-optics. A key question arises here, however, that is, how should material structures be shaped to actually realize the theoretically possible field confinement? Another key issue is the nature of the physical consequences of the presence of exponentially decaying and strongly confined fields.

A fertile ground for probing such inquiries is presented through the study and manipulation of surface optical excitations known as *surface polaritons* [9–11]. In the near-infrared (near-IR) to the visible spectral range, *surface plasmon-polaritons* are ubiquitous. These are mixed surface excitations characteristic of noble metals such as gold and silver. In the mid-IR, on the other hand, surface optical excitations known as *surface phonon-polaritons* arising in polar dielectrics, such as diatomic crystals, are more commonplace. This is due to the fact that most polar dielectric materials have optical phonons at mid-IR frequencies³, which can couple to p -polarized light, resulting in the aforementioned surface excitations. As the name implies, surface polaritons have surface wave character so that they decay exponentially away from the surface and possess large in-plane wavevector, satisfying the conditions outlined in the previous paragraphs. We underline here the fact that surface polaritons are associated with a substantial number of localized surface modes, which results in significant enhancement of the local electromagnetic density of states near the surface [9, 12, 13]. The properties of these surface waves will be discussed in greater detail in chapters 2 and 3.

When dealing with surface optical excitations, one is inevitably met with the issue of the large momentum mismatch between surface polaritons of large in-plane wavevector and propagating light in free space. This all but prevents one from harnessing the benefits associated with surface polaritons unless sub- λ structures are utilized to decouple the electromagnetic field from the surface. For example, one may rule a sub- λ grating on the surface of a polar dielectric substrate so that diffractive scattering of surface phonon-polaritons occurs. Using this approach, it has been shown that highly directional thermal emission can be achieved [14]. Another approach would entail the use of sub- λ antennas – devices that convert freely propagating electromagnetic radiation into localized energy and vice versa. The tip of a scattering-scanning near-field optical microscope, for instance, acts as an antenna that efficiently couples the near-fields of a surface

³In contrast, the plasma frequency in metals is typically in the ultraviolet spectral range.

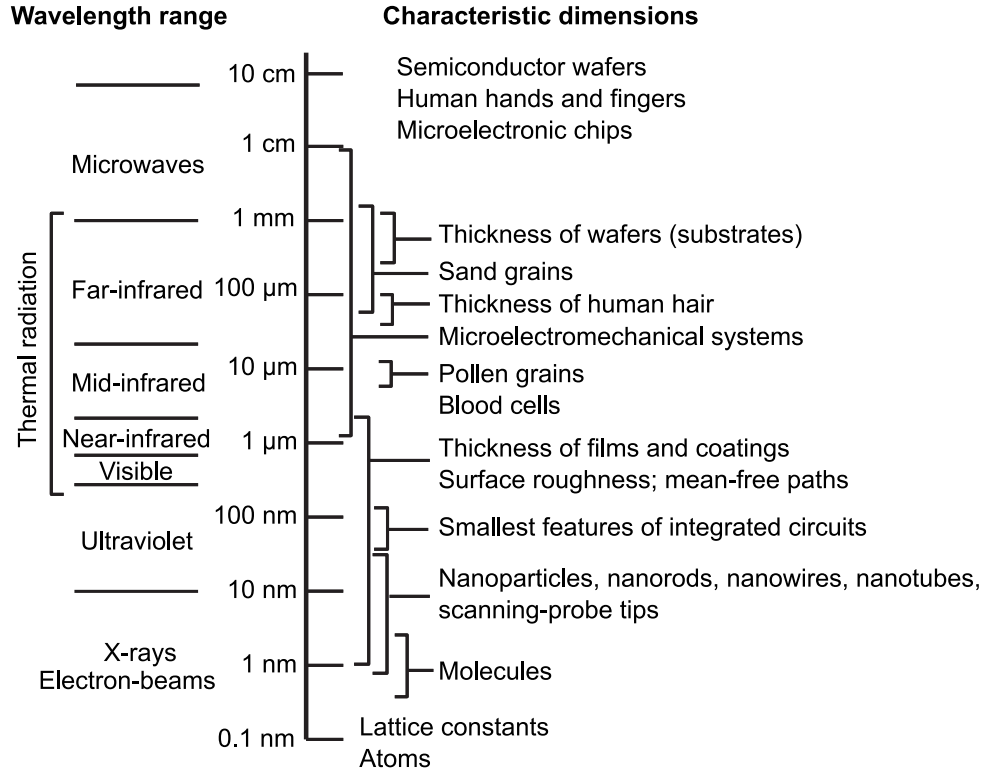


Figure 1.2: Diagram illustrating characteristic length scales as compared with the wavelength of the electromagnetic spectrum. Reproduced from ref. [28].

to the far-field where they can be detected. Although sub- λ antennas have their origins in the radio wave to microwave spectral range⁴, sub- λ antennas have become increasingly prevalent in the mid-IR [15–17] and even down to the optical range [18, 19]. Infrared metasurfaces assembled from sub- λ antennas have been used in a wide variety of applications, such as radiative cooling [20, 21], photo-detection [22–26], and solar cell design [27].

Since the sub- λ scale is defined with respect to the wavelength of electromagnetic radiation, it is instructive at this point to compare characteristic length scales with various wavelengths across the electromagnetic spectrum (Fig. 1.2). This comparison provides an idea of what can be classified as sub- λ for each wavelength. Figure 1.2 shows that currently available microelectromechanical systems generally produce micro-machining capabilities from several millimeters down to a few micrometers. The smallest features of integrated circuits, on the other hand, have reached sizes on the order of a few nanometers, as have thin films, whose layer thickness ranges from a few nanometers up to several micrometers. A spectral region that is of great fundamental and practical interest is that of thermal radiation, which covers a part of the ultraviolet, the entire visible ($\lambda \simeq 380 - 760$ nm) and infrared spectra, and a portion of the microwave region. Thermal radiation follows the *Planck blackbody law* which describes the spectral radiance of blackbody radiation as a function of wavelength at any given temperature. The peak of blackbody spectral radiance occurs at the so-called *thermal wavelength*, which scales inversely with

⁴In this spectral range, the typical size of a sub- λ antenna is on the order of $\lambda/100$ ($\lambda \sim 30$ cm for a cell phone).

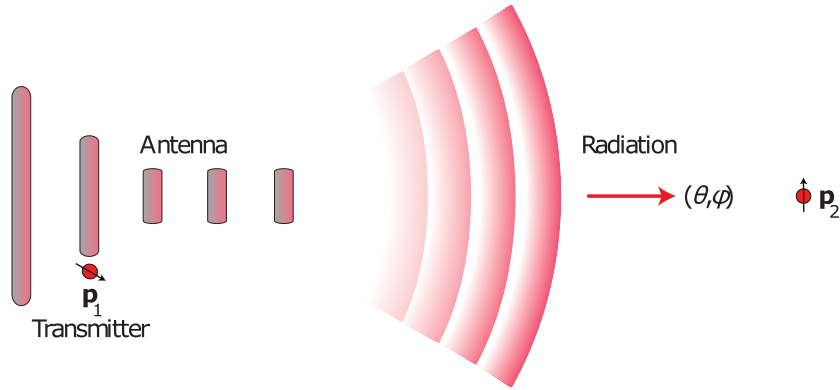


Figure 1.3: Schematic illustration of the enhancement in the transmission efficiency from a transmitter (dipole \mathbf{p}_1) to a receiver (dipole \mathbf{p}_2) via an antenna. Reproduced from ref. [19].

temperature according to *Wien's law*. For instance, the temperature of the surface of the Sun is $\sim 5800 - 6000$ K so that the solar spectrum is most intense at a wavelength of about 500 nm and spans a broad range from 100 nm to 1 mm, *i.e.*, from the ultraviolet to the far-infrared. On the other hand, materials at room temperature emit blackbody radiation centered at a wavelength of $10 \mu\text{m}$.

As far as diffraction-limited instruments are concerned, an optical microscope can provide a magnification of up to 100 times with a resolution of 200 to 300 nm. Going further down the ladder of length scales, atoms, and molecules are on the order of $0.1 - 1$ nm, falling in the X-ray and electron-beam wavelength region. Thus, X-ray and electron microscopes are typically used for determining crystal structures and defects and imaging nanostructures. In the 1980s, scanning probe microscopes and scanning near-field optical microscopes were developed as a means of overcoming the resolution limit set by diffraction. These techniques enabled unprecedented capabilities for the visualization and manipulation of nanostructures, such as nanowires, nanotubes, nanocrystals, single molecules, individual atoms, and the like.

In this manuscript, we will focus solely on the study of sub- λ nanostructures centered around a wavelength of $10 \mu\text{m}$ (or in the mid-IR spectral range between 6 and $14 \mu\text{m}$), a spectral region of great interest for thermography, radiative cooling⁵, and photo-detection. Figure 1.3 depicts a typical situation in which a sub- λ antenna is introduced to increase the transmission efficiency between a transmitter and a receiver (represented by dipoles here). This enhancement can be achieved by increasing the total amount of radiation released by the transmitter. The efficiency of this process, or the antenna efficiency, is given by [19]

$$\epsilon_{\text{rad}} = \frac{P_{\text{rad}}}{P} = \frac{P_{\text{rad}}}{P_{\text{rad}} + P_{\text{abs}}}, \quad (1.4)$$

where P is the total power dissipated by the antenna, P_{rad} is the radiated power and P_{abs} is the power dissipated through other means, such as by absorption in the antenna.

Other important antenna parameters include the antenna's electromagnetic cross-sections,

⁵The atmospheric transparency window, in which the Earth's atmosphere is transparent to electromagnetic radiation, is in the mid-IR spectral range between 8 and $14 \mu\text{m}$.

which can be much larger than the antenna’s geometrical cross-section. This feature can be utilized to enhance electromagnetic fields within the vicinity of sub- λ particles, such as molecules for instance. This enhancement can be formally outlined in relation to the antenna’s absorption cross-section C_{abs} as follows. Suppose we consider a dipole-like receiver whose absorption cross-section is $C_{\text{abs},0}$ when decoupled from an antenna. The unit vector in the direction of the absorption dipole axis is denoted as \mathbf{n} and the incident field at the location of the receiver is \mathbf{E}_0 . Once we couple the receiver to an antenna, the field at the receiver increases to \mathbf{E} and the antenna cross-section is related to the receiver cross-section by [19]

$$\frac{C_{\text{abs}}}{C_{\text{abs},0}} = \frac{|\mathbf{n} \cdot \mathbf{E}|^2}{|\mathbf{n} \cdot \mathbf{E}_0|^2}. \quad (1.5)$$

The term on the right-hand side of Eq. (1.5) is the local field intensity enhancement factor, which in the near-field of sub- λ antennas can readily reach values on the order of $10^4 - 10^6$ [29–31]. In the mid-IR, this property can be exploited for applications such as surface-enhanced infrared absorption spectroscopy [32, 33].

An interesting property of radio wave antennas is that they have design rules related to the wavelength of incident radiation, λ . For example, a half-wave antenna has a length $L = \lambda/2$, and a Yagi–Uda antenna (Fig. 1.4 (a)) has separations between its elements that correspond to certain fractions of λ (see Fig. 1.4 (b)). Since all elements are proportional to λ , it is straightforward to scale the antenna design from one wavelength to another. This scaling fails at optical frequencies because the penetration of radiation into metals can no longer be neglected but optical analogs of radio frequency antennas can still be implemented by applying scaling rules that depend on the antenna effective wavelength λ_{eff} [34] (see for instance Figs. 1.4 (c) and (d)). In the mid-IR, sub- λ plasmonic antennas, such as metal-insulator-metal (MIM) cavity antennas, which are analogs of radio frequency patch antennas, have an effective wavelength $\lambda_{\text{eff}} = \lambda/n_{\text{eff}}$, where n_{eff} is the effective index of refraction of the cavity [35]. The sub- λ cavity of a MIM antenna exhibits Fabry-Perot resonances that conveniently scale with the width of the cavity w , following $m\lambda_{\text{eff}}/2 \approx w$, where m is the mode order [36]. In addition to their spectral tunability, MIM cavities have also been shown to be angularly-independent [37–39]. As such, sub- λ MIM antennas are characterized by a high degree of versatility and have been assembled in a wide array of configurations [17, 21, 23, 24, 26, 37, 38, 40–46].

In a similar fashion, dielectric resonators have recently emerged as an alternative to various plasmonic antennas [49, 50]. This is mainly due to the fact that dielectric antennas feature, generally in the near-IR, both electric and magnetic resonances, and exhibit less losses than their plasmonic counterparts, particularly in the visible spectral range [51–60]. The geometrical electrical and magnetic Mie modes supported by high-refractive-index dielectric sub- λ particles, such as Si nanospheres, have been studied extensively at visible and near-IR wavelengths [61–63]. In the mid-IR, absorbing dielectric resonators, such as polar dielectric SiO₂ microspheres, have been widely used for radiative cooling applications [64–69]. Their emissivity is indeed high in the mid-IR atmospheric transparency window, while they scatter light with very little absorption at visible and near-IR wavelengths, where the solar spectrum is prominent.

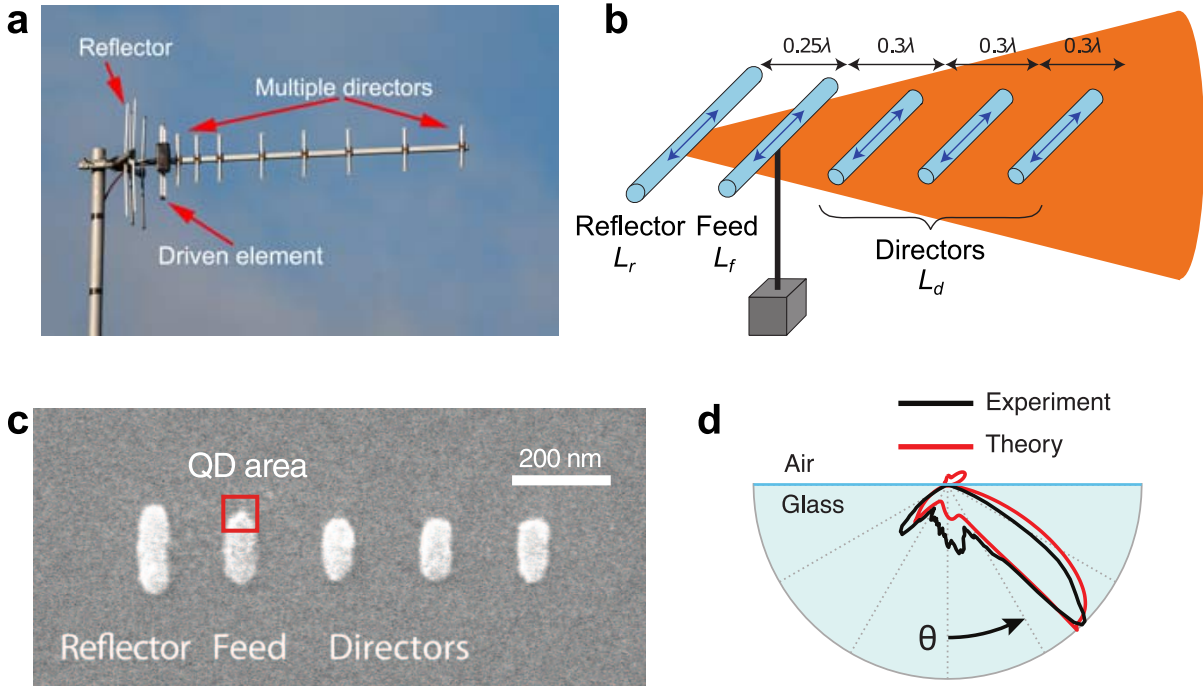


Figure 1.4: (a) Image of a radio-frequency Yagi-Uda antenna. (b) Schematic illustration of the dimensions of the various elements of a Yagi-Uda antenna with respect to the operating wavelength of the antenna λ (reproduced from ref. [47]). In general, a Yagi-Uda antenna consists of 5 or more half-wave antennas, which are detuned with respect to each other. A feed element of length $L_f = \lambda/2$ is driven so that it emits electromagnetic radiation, while smaller director elements (length $L_d < L_f$) passively direct (scatter) the radiation in the forward direction (to the right of panel (b)). A larger reflector element (length $L_r > L_f$) suppresses any back-scattered radiation. The resulting emission of this antenna configuration is, thus, highly directional. (c) SEM image of an optical Yagi-Uda antenna, whose feed element is coupled to a quantum dot, enabling uni-directional emission at $\lambda \sim 800$ nm [48]. (d) Angular radiation pattern in the polar angle (θ) for the Yagi-Uda antenna of panel (c), showing a narrow emission lobe.

For such applications, tailoring the infrared radiative properties of individual dielectric resonating microspheres is of crucial importance for enhancing radiative cooling efficiency. Microspheres are typically self-assembled on a substrate or within a matrix. Most studies aiming at modeling the optical response of such randomized metamaterials are restricted to low particle densities and make use of effective medium theory calculations [64, 70, 71]. Both the inter-particle interactions and the presence of a large and extended thermal radiation background in the mid-IR, generally preclude the measurement of the intrinsic mid-IR thermal radiation properties of single dielectric microspheres. In the current manuscript, we will routinely employ techniques such as infrared spatial modulation spectroscopy (IR-SMS) [46] and scattering-scanning near-field optical microscopy (s-SNOM) to study the mid-IR response of individual sub- λ structures.

Finally, with the emergence of atomically thin van der Waals materials such as graphene and hexagonal boron nitride (see Fig. 1.5), it has become possible to investigate a slew of exotic optical and transport phenomena [72]. In particular, doped graphene is host to surface plasmon-

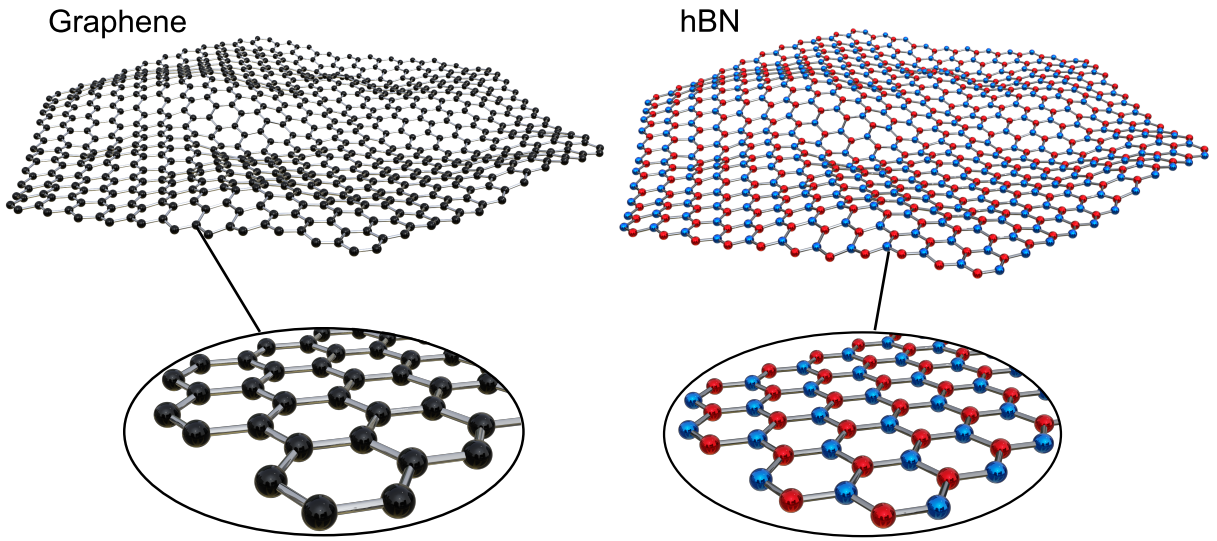


Figure 1.5: Depiction of the atomically thin van der Waals materials graphene and hexagonal boron nitride (hBN). Graphene consists of a single sheet of carbon atoms (represented as black spheres) in a honeycomb lattice and is characterized as a semi-metal with no band-gap. hBN is a polar dielectric made up of boron and nitride atoms (red and blue spheres) also in a honeycomb lattice. Typically, graphene is assembled as mono-, bi-, or tri-layer graphene, while hBN is exfoliated on a substrate, forming a flake that is a few hundred atomic layers thick.

polaritons of exceptionally low-loss character at infrared frequencies [73], while hexagonal boron nitride (hBN) is characterized by its hyperbolic phonon-polaritons in the mid-IR [74]. The presence of such surface optical excitations, in concert with the extraordinary thermal and electrical properties of graphene, has enabled the fabrication of high-mobility devices based on the combination of graphene and hexagonal boron nitride. When subjected to large electrical bias, these graphene devices may be of special interest for light applications, as suggested by electrical noise measurements [75]. In the current manuscript, we will directly investigate this property by performing optical measurements of the infrared light produced by hBN-encapsulated high-mobility graphene field-effect transistors.

This manuscript is organized as follows. In chapter 2 we outline the essential theoretical concepts required for a thorough understanding of surface optical excitations. Surface polaritons both in isotropic and anisotropic materials are discussed in a variety of geometries, such as in a half-space, a sphere, and thin film heterostructures. Dispersion relations, penetrations depths, and propagation lengths of surface polaritons are all computed for these geometries, and their properties are discussed in detail.

In chapter 3 we experimentally probe the spectral signatures of surface polaritons in dielectric media. We start by giving an overview of near-field microscopy techniques and give a comprehensive illustration of s-SNOM, which we employ to perform near-field spectroscopy of polar dielectric substrates. We also detail the far-field IR-SMS technique and present two sets of measurements of polar dielectric media with this technique. The first set of measurements consists of detecting the far-field thermal radiation from single sub- λ antennas patterned

via optical lithography on polar dielectric substrates. These measurements constitute a novel demonstration of how sub- λ antennas can be used to scatter the near-fields of a sample to the far-field where they are detected. In the second set of measurements, we present the first experimental investigation of the far-field thermal radiation of single sub- λ spheres [76]. We study polar dielectric spheres made of SiO_2 , in which either a phonon-mode-dominated or a Mie-mode-dominated spectral response can occur due to the peculiar dielectric response of the material in the mid-infrared. For the sake of comparison, we also show results on non-polar spheres made up of PTFE.

In chapter 4 we shift our attention to the study of sub- λ MIM cavity antennas. We begin by presenting the fundamental properties of MIM cavities and then outline the response of square patch-MIM antennas in the near- and far-field. From there we illustrate through IR-SMS measurements and finite-difference-time-domain (FDTD) simulations the coupling behavior through mode hybridization in a single pair of square-patch MIM antennas separated by a nanometric gap [17]. We then move on to the study of a 3×3 -patch MIM antenna consisting of 9 sub- λ square patches in near-field interaction. Using s-SNOM measurements, complemented by FDTD and finite-element method simulations, we reveal field features of the 3×3 antenna confined to length scales on the order of $\lambda/100$. Using focused microscope reflectivity measurements, we also show that the 3×3 antenna exhibits an angularly-dependent response, in contrast to the single square-patch MIM antenna case.

Chapter 5 of this thesis is dedicated to the study of the mid-IR emission of high-mobility hBN-encapsulated graphene field-effect transistors (HGFETs). In the first part of this chapter, we provide an overview of electron transport in graphene under electrical bias. In the second part, we present experimental signatures of radiative cooling and emission due to the mid-IR electroluminescence of HGFETs under large bias.

We end with some concluding remarks and perspectives for future investigation.

References

- [1] J Teyssier, SV Saenko, D Van Der Marel, and MC Milinkovitch. “Photonic crystals cause active colour change in chameleons”. *Nat. Commun.* 6.1 (2015), pp. 1–7.
- [2] F De Angelis, M Malerba, M Patrini, E Miele, G Das, A Toma, RP Zaccaria, and E Di Fabrizio. “3D hollow nanostructures as building blocks for multifunctional plasmonics”. *Nano Lett.* 13.8 (2013), pp. 3553–3558.
- [3] N Yu, P Genevet, MA Kats, F Aieta, JP Tetienne, F Capasso, and Z Gaburro. “Light propagation with phase discontinuities: generalized laws of reflection and refraction”. *Science* 334.6054 (2011), pp. 333–337.
- [4] M Khorasaninejad, WT Chen, RC Devlin, J Oh, AY Zhu, and F Capasso. “Metalenses at visible wavelengths: Diffraction-limited focusing and subwavelength resolution imaging”. *Science* 352.6290 (2016), pp. 1190–1194.
- [5] AL Davis, KN Thomas, FE Goetz, BH Robison, S Johnsen, and KJ Osborn. “Ultra-black camouflage in deep-sea fishes”. *Curr. Biol.* 30.17 (2020), pp. 3470–3476.
- [6] L Novotny and B Hecht. *Principles of nano-optics*. Cambridge University Press, 2012.
- [7] E Abbe. “Beiträge zur Theorie des Mikroskops und der mikroskopischen Wahrnehmung”. *Arch. Mikroskop. Anat.* 9.1 (1873), pp. 413–468.
- [8] L Rayleigh. “Investigations in optics, with special reference to the spectroscope”. *Lond. Edinb. Dublin philos. mag.* 8.49 (1879), pp. 261–274.
- [9] K Joulain, JP Mulet, F Marquier, R Carminati, and J-J Greffet. “Surface electromagnetic waves thermally excited: Radiative heat transfer, coherence properties and Casimir forces revisited in the near field”. *Surf. Sci. Rep.* 57.3-4 (2005), pp. 59–112.
- [10] VM Agranovich. *Surface polaritons*. Elsevier, 2012.
- [11] DN Basov, MM Fogler, and FJ Garcia de Abajo. “Polaritons in van der Waals materials”. *Science* 354.6309 (2016), aag1992.
- [12] Y De Wilde, F Formanek, R Carminati, B Gralak, PA Lemoine, K Joulain, JP Mulet, Y Chen, and JJ Greffet. “Thermal radiation scanning tunnelling microscopy”. *Nature* 444.7120 (2006), pp. 740–743.
- [13] A Babuty, K Joulain, PO Chapuis, JJ Greffet, and Y De Wilde. “Blackbody spectrum revisited in the near field”. *Phys. Rev. Lett.* 110.14 (2013), p. 146103.
- [14] JJ Greffet, R Carminati, K Joulain, JP Mulet, S Mainguy, and Y Chen. “Coherent emission of light by thermal sources”. *Nature* 416.6876 (2002), pp. 61–64.
- [15] R Adato, S Aksu, and Ha Altug. “Engineering mid-infrared nanoantennas for surface enhanced infrared absorption spectroscopy”. *Mater. Today* 18.8 (2015), pp. 436–446.
- [16] J Kim, A Dutta, GV Naik, AJ Giles, FJ Bezares, CT Ellis, JG Tischler, AM Mahmoud, H Caglayan, OJ Glembocki, et al. “Role of epsilon-near-zero substrates in the optical response of plasmonic antennas”. *Optica* 3.3 (2016), pp. 339–346.

- [17] L Abou-Hamdan, C Li, R Haidar, V Krachmalnicoff, P Bouchon, and Y De Wilde. “Hybrid modes in a single thermally excited asymmetric dimer antenna”. *Opt. Lett.* 46.5 (2021), pp. 981–984.
- [18] P Bharadwaj, B Deutsch, and L Novotny. “Optical antennas”. *Adv. Opt. Photon.* 1.3 (2009), pp. 438–483.
- [19] L Novotny and N Van Hulst. “Antennas for light”. *Nat. Photon.* 5.2 (2011), pp. 83–90.
- [20] AP Raman, MA Anoma, L Zhu, E Rephaeli, and S Fan. “Passive radiative cooling below ambient air temperature under direct sunlight”. *Nature* 515.7528 (2014), pp. 540–544.
- [21] W Yu, Y Lu, X Chen, H Xu, J Shao, X Chen, Y Sun, J Hao, and N Dai. “Large-Area, Broadband, Wide-Angle Plasmonic Metasurface Absorber for Midwavelength Infrared Atmospheric Transparency Window”. *Adv. Opt. Mater.* 7.20 (2019), p. 1900841.
- [22] NI Landy, S Sajuyigbe, JJ Mock, DR Smith, and WJ Padilla. “Perfect metamaterial absorber”. *Phys. Rev. Lett.* 100.20 (2008), p. 207402.
- [23] D Palaferri, Y Todorov, A Bigioli, A Mottaghizadeh, D Gacemi, A Calabrese, A Vasanelli, L Li, AG Davies, EH Linfield, et al. “Room-temperature nine- μm -wavelength photodetectors and GHz-frequency heterodyne receivers”. *Nature* 556.7699 (2018), pp. 85–88.
- [24] P Bouchon, C Koechlin, F Pardo, R Haidar, and JL Pelouard. “Wideband omnidirectional infrared absorber with a patchwork of plasmonic nanoantennas”. *Opt. Lett.* 37.6 (2012), pp. 1038–1040.
- [25] B Fix, J Jaeck, B Vest, M Verdun, G Beaudoin, I Sagnes, JL Pelouard, and R Haidar. “Nanostructured diode for infrared photodetection through nondegenerate two-photon absorption”. *Appl. Phys. Lett.* 111.4 (2017), p. 041102.
- [26] Y Nga Chen, Y Todorov, B Askenazi, A Vasanelli, G Biasiol, R Colombelli, and C Sirtori. “Antenna-coupled microcavities for enhanced infrared photo-detection”. *Appl. Phys. Lett.* 104.3 (2014), p. 031113.
- [27] MD Kelzenberg, SW Boettcher, JA Petykiewicz, DB Turner-Evans, MC Putnam, EL Warren, JM Spurgeon, RM Briggs, NS Lewis, and HA Atwater. “Enhanced absorption and carrier collection in Si wire arrays for photovoltaic applications”. *Nat. Mater.* 9.3 (2010), pp. 239–244.
- [28] ZM Zhang, ZM Zhang, and Luby. *Nano/microscale heat transfer*. Vol. 410. Springer, 2007.
- [29] L Novotny, RX Bian, and XS Xie. “Theory of nanometric optical tweezers”. *Phys. Rev. Lett.* 79.4 (1997), p. 645.
- [30] KB Crozier, A Sundaramurthy, GS Kino, and CF Quate. “Optical antennas: Resonators for local field enhancement”. *J. Appl. Phys.* 94.7 (2003), pp. 4632–4642.
- [31] A Kinkhabwala, Z Yu, S Fan, Y Avlasevich, K Müllen, and WE Moerner. “Large single-molecule fluorescence enhancements produced by a bowtie nanoantenna”. *Nat. Photon.* 3.11 (2009), pp. 654–657.
- [32] L Dong, X Yang, C Zhang, B Cerjan, L Zhou, ML Tseng, Y Zhang, A Alabastri, P Nordlander, and NJ Halas. “Nanogapped Au antennas for ultrasensitive surface-enhanced infrared absorption spectroscopy”. *Nano Lett.* 17.9 (2017), pp. 5768–5774.
- [33] A Fabas, H El Ouazzani, JP Hugonin, C Dupuis, R Haidar, JJ Greffet, and P Bouchon. “Dispersion-based intertwined SEIRA and SPR effect detection of 2, 4-dinitrotoluene using a plasmonic metasurface”. *Opt. Express* 28.26 (2020), pp. 39595–39605.
- [34] L Novotny. “Effective wavelength scaling for optical antennas”. *Phys. Rev. Lett.* 98.26 (2007), p. 266802.
- [35] S Collin, F Pardo, and JL Pelouard. “Waveguiding in nanoscale metallic apertures”. *Opt. Express* 15.7 (2007), pp. 4310–4320.
- [36] J Yang, C Sauvan, A Jouanin, S Collin, JL Pelouard, and P Lalanne. “Ultrasmall metal-insulator-metal nanoresonators: impact of slow-wave effects on the quality factor”. *Opt. Express* 20.15 (2012), pp. 16880–16891.

-
- [37] Y Todorov, L Tosetto, J Teissier, AM Andrews, P Klang, R Colombelli, I Sagnes, G Strasser, and C Sirtori. “Optical properties of metal-dielectric-metal microcavities in the THz frequency range”. *Opt. Express* 18.13 (2010), pp. 13886–13907.
- [38] C Koechlin, P Bouchon, F Pardo, J Jaeck, X Lafosse, JL Pelouard, and R Haidar. “Total routing and absorption of photons in dual color plasmonic antennas”. *Appl. Phys. Lett.* 99.24 (2011), p. 241104.
- [39] J Hao, J Wang, X Liu, WJ Padilla, L Zhou, and M Qiu. “High performance optical absorber based on a plasmonic metamaterial”. *Appl. Phys. Lett.* 96.25 (2010), p. 251104.
- [40] E El Shamy, J Jaeck, R Haidar, and P Bouchon. “Light scattering by correlated disordered assemblies of nanoantennas”. *Appl. Phys. Lett.* 115.4 (2019), p. 041103.
- [41] R Gillibert, M Malerba, D Spirito, V Giliberti, L Li, AG Davies, EH Linfield, L Baldassarre, R Colombelli, and M Ortolani. “Nanospectroscopy of a single patch antenna strongly coupled to a mid-infrared intersub-band transition in a quantum well”. *Appl. Phys. Lett.* 117.10 (2020), p. 101104.
- [42] M Malerba, M Jeannin, S Pirodda, L Li, AG Davies, E Linfield, A Bousseksou, JM Manceau, and R Colombelli. “A “Janus” double sided mid-IR photodetector based on a MIM architecture”. *Appl. Phys. Lett.* 119.18 (2021), p. 181102.
- [43] Q Lévesque, M Makhsiyani, P Bouchon, F Pardo, J Jaeck, N Bardou, C Dupuis, R Haidar, and JL Pelouard. “Plasmonic planar antenna for wideband and efficient linear polarization conversion”. *Appl. Phys. Lett.* 104.11 (2014), p. 111105.
- [44] P Chevalier, P Bouchon, J Jaeck, D Lauwick, N Bardou, A Kattnig, F Pardo, and R Haidar. “Absorbing metasurface created by diffractionless disordered arrays of nanoantennas”. *Appl. Phys. Lett.* 107.25 (2015), p. 251108.
- [45] M Makhsiyani, P Bouchon, J Jaeck, JL Pelouard, and R Haidar. “Shaping the spatial and spectral emissivity at the diffraction limit”. *Appl. Phys. Lett.* 107.25 (2015), p. 251103.
- [46] C Li, V Krachmalnicoff, P Bouchon, J Jaeck, N Bardou, R Haidar, and Y De Wilde. “Near-field and far-field thermal emission of an individual patch nanoantenna”. *Phys. Rev. Lett.* 121.24 (2018), p. 243901.
- [47] T Kosako, Y Kadoya, and HF Hofmann. “Directional control of light by a nano-optical Yagi–Uda antenna”. *Nat. Photon.* 4.5 (2010), pp. 312–315.
- [48] AG Curto, G Volpe, TH Taminiau, MP Kreuzer, R Quidant, and NF van Hulst. “Unidirectional emission of a quantum dot coupled to a nanoantenna”. *Science* 329.5994 (2010), pp. 930–933.
- [49] AI Kuznetsov, AE Miroshnichenko, ML Brongersma, YS Kivshar, and B Luk’yanchuk. “Optically resonant dielectric nanostructures”. *Science* 354.6314 (2016).
- [50] S Bidault, M Mivelle, and N Bonod. “Dielectric nanoantennas to manipulate solid-state light emission”. *J. Appl. Phys.* 126.9 (2019), p. 094104.
- [51] A Devilez, N Bonod, J Wenger, D Gérard, B Stout, H Rigneault, and E Popov. “Three-dimensional sub-wavelength confinement of light with dielectric microspheres”. *Opt. Express* 17.4 (2009), pp. 2089–2094.
- [52] A Krasnok, M Caldarola, N Bonod, and A Alú. “Spectroscopy and biosensing with optically resonant dielectric nanostructures”. *Adv. Opt. Mater.* 6.5 (2018), p. 1701094.
- [53] MK Schmidt, R Esteban, JJ Sáenz, I Suárez-Lacalle, S Mackowski, and J Aizpurua. “Dielectric antennas—a suitable platform for controlling magnetic dipolar emission”. *Opt. Express* 20.13 (2012), pp. 13636–13650.
- [54] AE Krasnok, AE Miroshnichenko, PA Belov, and YS Kivshar. “All-dielectric optical nanoantennas”. *Opt. Express* 20.18 (2012), pp. 20599–20604.
- [55] B Rolly, B Stout, and N Bonod. “Boosting the directivity of optical antennas with magnetic and electric dipolar resonant particles”. *Opt. Express* 20.18 (2012), pp. 20376–20386.
- [56] J Van de Groep and A Polman. “Designing dielectric resonators on substrates: Combining magnetic and electric resonances”. *Opt. Express* 21.22 (2013), pp. 26285–26302.

- [57] I Staude, AE Miroshnichenko, M Decker, NT Fofang, S Liu, E Gonzales, J Dominguez, TS Luk, DN Neshev, I Brener, et al. “Tailoring directional scattering through magnetic and electric resonances in subwavelength silicon nanodisks”. *ACS Nano* 7.9 (2013), pp. 7824–7832.
- [58] NA Butakov and JA Schuller. “Designing multipolar resonances in dielectric metamaterials”. *Sci. Rep.* 6.1 (2016), pp. 1–8.
- [59] J Proust, F Bedu, B Gallas, I Ozerov, and N Bonod. “All-dielectric colored metasurfaces with silicon Mie resonators”. *ACS Nano* 10.8 (2016), pp. 7761–7767.
- [60] R Regmi, J Berthelot, PM Winkler, M Mivelle, J Proust, F Bedu, I Ozerov, T Begou, J Lumeau, H Rigneault, et al. “All-dielectric silicon nanogap antennas to enhance the fluorescence of single molecules”. *Nano Lett.* 16.8 (2016), pp. 5143–5151.
- [61] A Garcia-Etxarri, R Gómez-Medina, LS Froufe-Pérez, C López, L Chantada, Fr Scheffold, J Aizpurua, M Nieto-Vesperinas, and JJ Sáenz. “Strong magnetic response of submicron silicon particles in the infrared”. *Opt. Express* 19.6 (2011), pp. 4815–4826.
- [62] AE Miroshnichenko, AB Evlyukhin, YS Kivshar, and BN Chichkov. “Substrate-induced resonant magneto-electric effects for dielectric nanoparticles”. *ACS Photonics* 2.10 (2015), pp. 1423–1428.
- [63] H Sugimoto and M Fujii. “Broadband dielectric–metal hybrid nanoantenna: Silicon nanoparticle on a mirror”. *ACS Photonics* 5.5 (2018), pp. 1986–1993.
- [64] Y Zhai, Y Ma, SN David, D Zhao, R Lou, G Tan, R Yang, and X Yin. “Scalable-manufactured randomized glass-polymer hybrid metamaterial for daytime radiative cooling”. *Science* 355.6329 (2017), pp. 1062–1066.
- [65] CM Liu, NZ Hu, Q Li, and M Qiu. “Metal-dielectric hybrid structure for radiative cooling”. *J. Phys. Conf. Ser.* Vol. 1077. 1. IOP Publishing. 2018, p. 012003.
- [66] J Jaramillo-Fernandez, GL Whitworth, JA Pariente, A Blanco, PD Garcia, C Lopez, and CM Sotomayor-Torres. “A Self-Assembled 2D Thermofunctional Material for Radiative Cooling”. *Small* 15.52 (2019), p. 1905290.
- [67] J Feng, M Santamouris, and K Gao. “The radiative cooling efficiency of silica sphere embedded polymethylpentene (TPX) systems”. *Sol. Energy Mater.* 215 (2020), p. 110671.
- [68] M Chen, D Pang, X Chen, and H Yan. “Investigating the effective radiative cooling performance of random dielectric microsphere coatings”. *Int. J. Heat Mass Transf.* 173 (2021), p. 121263.
- [69] B Xiang, R Zhang, Y Luo, S Zhang, L Xu, H Min, S Tang, and X Meng. “3D porous polymer film with designed pore architecture and auto-deposited SiO₂ for highly efficient passive radiative cooling”. *Nano Energy* 81 (2021), p. 105600.
- [70] MS Wheeler, JS Aitchison, and M Mojahedi. “Coated nonmagnetic spheres with a negative index of refraction at infrared frequencies”. *Phys. Rev. B* 73.4 (2006), p. 045105.
- [71] MS Wheeler, JS Aitchison, J Chen, GA Ozin, and M Mojahedi. “Infrared magnetic response in a random silicon carbide micropowder”. *Phys. Rev. B* 79.7 (2009), p. 073103.
- [72] AK Geim and IV Grigorieva. “Van der Waals heterostructures”. *Nature* 499.7459 (2013), pp. 419–425.
- [73] M Jablan, H Buljan, and M Soljačić. “Plasmonics in graphene at infrared frequencies”. *Phys. Rev. B* 80.24 (2009), p. 245435.
- [74] S Dai, Z Fei, Q Ma, AS Rodin, M Wagner, AS McLeod, MK Liu, W Gannett, W Regan, K Watanabe, et al. “Tunable phonon polaritons in atomically thin van der Waals crystals of boron nitride”. *Science* 343.6175 (2014), pp. 1125–1129.
- [75] E Baudin, C Voisin, and B Plaçais. “Hyperbolic phonon polariton electroluminescence as an electronic cooling pathway”. *Adv. Funct. Mater.* 30.8 (2020), p. 1904783.

- [76] L Abou-Hamdan, L Coudrat, S Bidault, V Krachmalnicoff, R Hadar, P Bouchon, and Y De Wilde. “Transition from Phononic to Geometrical Mie Modes Measured in Single Subwavelength Polar Dielectric Spheres”. *ACS Photonics* 9.7 (2022), pp. 2295–2303.

Chapter 2

Fundamentals of surface polaritons in bulk materials and subwavelength heterostructures

In this chapter, we will introduce the fundamentals of surface optical excitations (or *surface polaritons*), which make up the near-field of various materials¹ and are at the heart of many interesting coherence phenomena [1–3]. The properties of surface polaritons will be described for a host of important geometries, starting from a half-space and then working our way through the thin film and sphere geometries. Subsequently, we will present the theory of surface polaritons in anisotropic materials. The theoretical concepts that will be presented here form the basis of the experimental studies of the superseding chapters.

Suppose we consider a medium in which a surface vibrational excitation occurs with which we can associate an effective dimension² λ and an angular frequency ω . For

$$\lambda \gg d, \tag{2.1}$$

where d is a mean interatomic spacing, the response of the medium to the excitation is essentially that of a continuum, since, within the length λ , there exists a large number of atoms.

At this point, several continuum characterizations are possible. If one considers the medium to be an elastic continuum describable in terms of an appropriate set of elastic constants, there occur excitations which are the surface analog of acoustic phonons, the *Rayleigh waves* [4]. Here we will instead be interested in lattice vibrations associated with significant long-range electromagnetic fields. In the long-wavelength or continuum limit, Eq. (2.1), the system's response to these electromagnetic fields is described by the macroscopic dielectric function $\varepsilon(\omega)$. The classic examples of such lattice vibrations are the optical vibrational modes in a polar³ diatomic crystal, known as *surface phonon-polaritons* (SPhPs), which are mixed surface excitations arising due to the coupling of incoming photons with the optical phonons of the crystal.

¹Particularly diatomic crystals and metals.

²This may be a wavelength or some other length that appropriately characterizes the scale of spatial variation.

³The term "polar" here refers to a dielectric material with a permanent electric dipole moment.

2.1 Local dielectric continuum theory of polar dielectrics and metals

We begin our treatment of surface optical excitations with a discussion of the local dielectric continuum theory [5].

Consider, for simplicity, a bulk, homogeneous, isotropic system. We can then write the relation between the electric displacement field $\mathbf{D}(\mathbf{r}, t)$ at position \mathbf{r} and time t , and the suitably averaged electric field $\mathbf{E}(\mathbf{r}, t)$ as

$$\mathbf{D}(\mathbf{r}, t) = \int_0^t dt' \int \varepsilon_R(\mathbf{r} - \mathbf{r}', t - t') \mathbf{E}(\mathbf{r}', t') d^3 r', \quad (2.2)$$

where $\varepsilon_R(\mathbf{r} - \mathbf{r}', t - t')$ is the real-space, real-time response function.

Defining the Fourier transforms for the wavevector \mathbf{k} , with $|\mathbf{k}| = 2\pi/\lambda$, where λ is the wavelength, and the angular frequency ω :

$$\tilde{\mathbf{D}}(\mathbf{k}, \omega) = \int d^3 r \int \mathbf{D}(\mathbf{r}, t) e^{i\omega t} e^{-i\mathbf{k}\cdot\mathbf{r}} dt \quad (2.3)$$

$$\tilde{\mathbf{E}}(\mathbf{k}, \omega) = \int d^3 r \int \mathbf{E}(\mathbf{r}, t) e^{i\omega t} e^{-i\mathbf{k}\cdot\mathbf{r}} dt \quad (2.4)$$

$$\varepsilon(\mathbf{k}, \omega) = \int d^3 r \int \varepsilon_R(\mathbf{r}, t) e^{i\omega t} e^{-i\mathbf{k}\cdot\mathbf{r}} dt \quad (2.5)$$

we get from Eq. (2.2)

$$\tilde{\mathbf{D}}(\mathbf{k}, \omega) = \varepsilon(\mathbf{k}, \omega) \tilde{\mathbf{E}}(\mathbf{k}, \omega). \quad (2.6)$$

The presence of \mathbf{k} in the dielectric function indicates that the displacement at point \mathbf{r} depends on the electric field over a region of space about \mathbf{r} , that is, the response of the medium is non-local or, in other words, spatial dispersion has been included. We can, nevertheless, impose a local response requirement on the system as follows

$$\varepsilon_R(\mathbf{r} - \mathbf{r}', t - t') = \delta(\mathbf{r} - \mathbf{r}') \varepsilon'_R(t - t'), \quad (2.7)$$

where δ is the Dirac delta function. This leads to

$$\tilde{\mathbf{D}}(\mathbf{k}, \omega) = \varepsilon(\omega) \tilde{\mathbf{E}}(\mathbf{k}, \omega). \quad (2.8)$$

It should be noted, however, that this local theory can only be valid in the long-wavelength regime since $\varepsilon(\omega) = \lim_{\mathbf{k} \rightarrow 0} \varepsilon(\mathbf{k}, \omega)$.

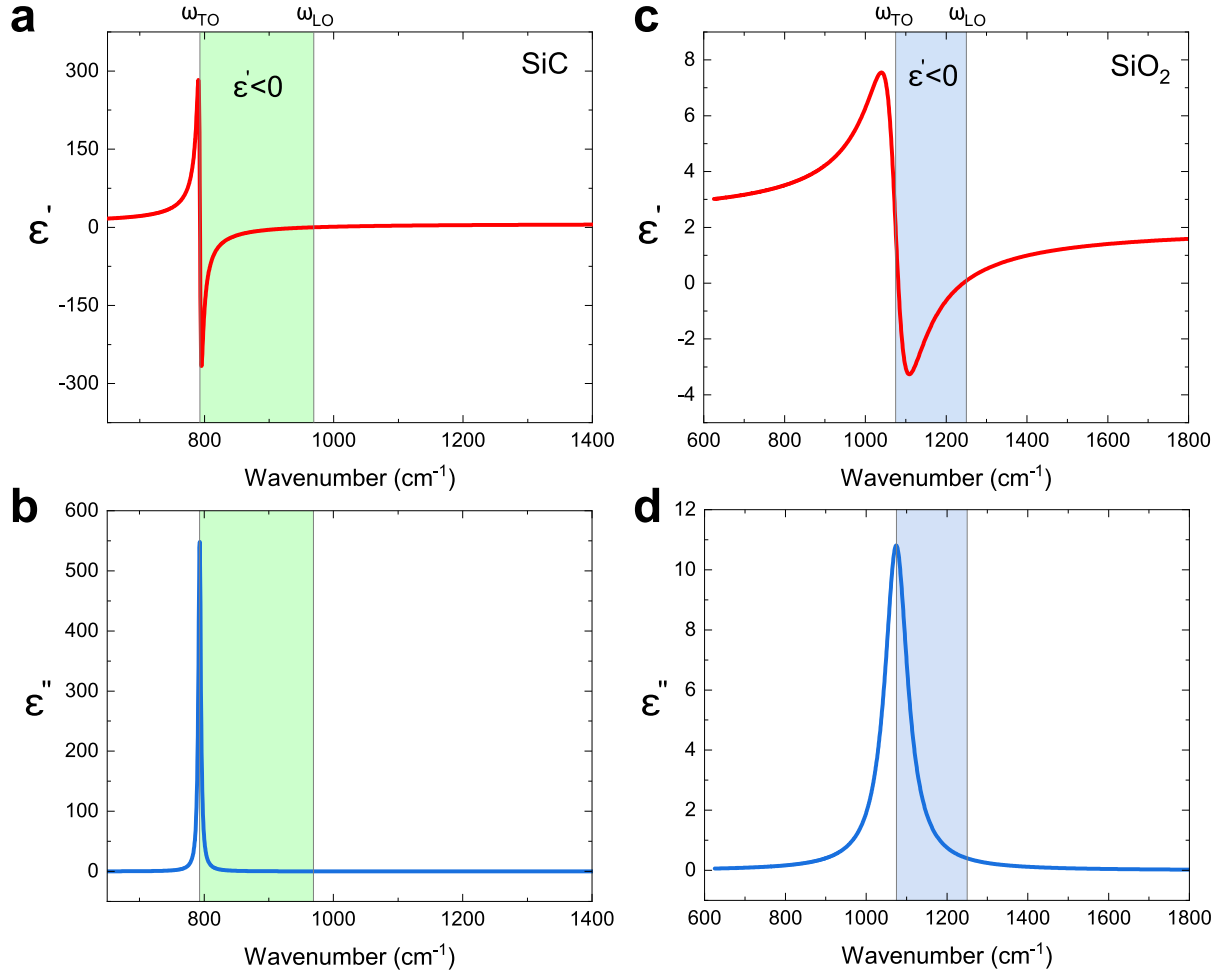


Figure 2.1: Real (ϵ') and imaginary (ϵ'') parts of the dielectric function vs wavenumber ($1/\lambda$) for SiC (panels (a) and (b)), and SiO₂ (panels (c) and (d)), calculated from the Drude-Lorentz model Eq. (2.9). For SiC: $\omega_{\text{TO}} = 793 \text{ cm}^{-1}$, $\omega_{\text{LO}} = 969 \text{ cm}^{-1}$, $\epsilon_{\infty} = 6.7$, and $\gamma = 4.76 \text{ cm}^{-1}$. For SiO₂: $\omega_{\text{TO}} = 1075 \text{ cm}^{-1}$, $\omega_{\text{LO}} = 1250 \text{ cm}^{-1}$, $\epsilon_{\infty} = 1.97$, and $\gamma = 69 \text{ cm}^{-1}$. Optical constants taken from ref. [6]. The shaded regions indicate the material's *Reststrahlen* band between ω_{TO} and ω_{LO} , in which the real part of the dielectric function is negative.

2.1.1 The dielectric function of polar semi-conductors: the Drude-Lorentz model

The dielectric function of polar diatomic crystals can be readily described using the *Drude-Lorentz* model with a single oscillator

$$\epsilon(\omega) = \epsilon_{\infty} + \frac{\epsilon_0 - \epsilon_{\infty}}{\omega_{\text{TO}}^2 - \omega^2 - i\gamma\omega} \omega_{\text{TO}}^2. \quad (2.9)$$

Here, ω_{TO} is the long-wavelength transverse optical phonon frequency, γ is a damping constant, and ϵ_{∞} and ϵ_0 are the values of $\epsilon(\omega)$ for $\omega \gg \omega_{\text{TO}}$, and $\omega \ll \omega_{\text{TO}}$, respectively. The real and imaginary parts of the dielectric function given by Eq. (2.9) are shown in Fig. 2.1 for two typical polar dielectric materials, namely SiC and SiO₂.

The longitudinal optical frequency ω_{LO} is the frequency for which $\epsilon(\omega) = 0$ and is given in

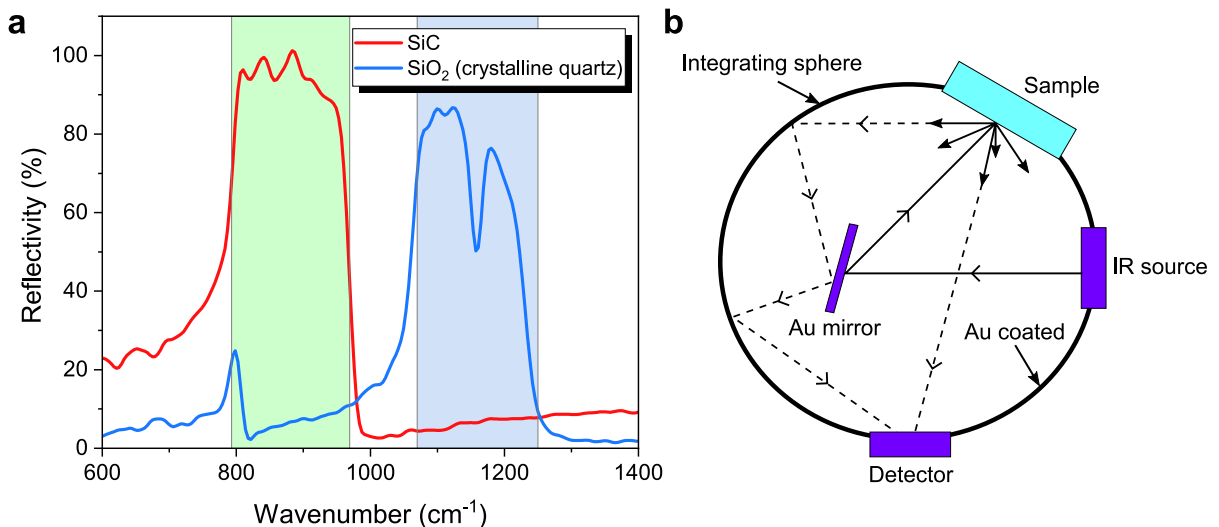


Figure 2.2: (a) Infrared reflectivity of SiC and crystalline quartz measured using Fourier transform infrared (FTIR) spectroscopy with an integrating sphere. The integrating sphere is sketched in panel (b). The integrating sphere consists of a gold-coated sphere, which collects both diffuse and specularly reflected light off the sample surface. Both SiC and crystalline SiO₂ have substantial reflectivity in their *Reststrahlen* bands (shaded regions), with the reflectivity of SiC reaching values close to 100%.

terms of ω_{TO} by the Lyddane-Sachs-Teller relation [7]

$$\omega_{\text{LO}} = \sqrt{\frac{\epsilon_0}{\epsilon_\infty}} \omega_{\text{TO}}. \quad (2.10)$$

Using this relation, the dielectric function of Eq. (2.9) can be rewritten as

$$\epsilon(\omega) = \epsilon_\infty \left(1 + \frac{\omega_{\text{LO}}^2 - \omega_{\text{TO}}^2}{\omega_{\text{TO}}^2 - \omega^2 - i\gamma\omega} \right). \quad (2.11)$$

As shown in Figs. 2.1 (a) and (c), the real part of the dielectric function becomes negative in the frequency region $\omega_{\text{TO}} < \omega < \omega_{\text{LO}}$ (shaded regions). This frequency range is known as the *Reststrahlen* band, in which the dielectric material behaves as a metal, exhibiting significant reflectivity (see Fig. 2.2 (a)). The *Reststrahlen* band is also the spectral region in which surface optical excitations, such as SPhPs, arise, as will be seen later.

The imaginary part of the dielectric function, ϵ'' , which arises from the inclusion of a non-zero damping constant, γ , in the dielectric model, accounts for the retardation effects in the medium. This is readily illustrated by the *Beer-Lambert law*, which describes the exponential attenuation of the intensity of a beam propagating through a medium as

$$I(z) = I_0 e^{-\beta z}, \quad (2.12)$$

where, z is the penetration depth in the medium, I_0 is the intensity of the beam at position $z = 0$, and β is the absorption coefficient.

The absorption coefficient is related to the imaginary part of the index of refraction⁴ of the medium, $\tilde{n} = \sqrt{\epsilon} = n + i\kappa$, through

$$\beta = \frac{4\pi\kappa}{\lambda}. \quad (2.13)$$

Since $\kappa = \epsilon''/2n$, it is clear from Eqs. (2.12) and (2.13) that absorption can only occur if the medium has a complex dielectric function with a non-zero imaginary part. In the case of polar dielectric media, such as SiC and SiO₂, the imaginary part of the dielectric function has a large maximum at ω_{TO} (see Figs. 2.1 (b) and (d)), indicating that the material is resonantly absorbing at this frequency.

2.1.2 The dielectric function of metals: the free electron gas

Like the diatomic crystals, discussed in subsection 2.1.1, metals are host to surface optical excitations called *surface plasmon-polaritons* (SPPs), particularly in the visible spectral range. The optical properties of metals can be explained by a *plasma model*, where a gas of free electrons of number density n_e moves against a fixed background of positive ion cores. In this model, details of the lattice potential and electron-electron interactions are not taken into account. Instead, one simply assumes that some aspects of the band structure are incorporated into the effective optical mass m^* of each electron. The electrons oscillate in response to the applied electromagnetic field, and their motion is damped via collisions occurring with a characteristic collision frequency given by the damping constant $\gamma = 1/\tau$. τ is known as the relaxation time of the free electron gas, which is typically on the order of 10^{-14} s at room temperature, corresponding to $\gamma = 100$ THz.

The equation of motion for an electron from the plasma gas, of effective mass m^* , subjected to an external electric field \mathbf{E} is

$$m^*\ddot{\mathbf{x}} + m^*\gamma\dot{\mathbf{x}} = -e\mathbf{E}. \quad (2.14)$$

If a harmonic time dependence, $\mathbf{E}(t) = \mathbf{E}_0 e^{-i\omega t}$, of the driving field is assumed, a particular solution of this equation describing the oscillation of the electron is $\mathbf{x}(t) = \mathbf{x}_0 e^{-i\omega t}$. The complex amplitude \mathbf{x}_0 incorporates any phase shifts between driving field and response via

$$\mathbf{x}_0(t) = \frac{e}{m^*(\omega^2 + i\gamma\omega)} \mathbf{E}. \quad (2.15)$$

The displaced electrons contribute to the macroscopic polarization $\mathbf{P} = -n_e e \mathbf{x}$, which is explicitly given by

$$\mathbf{P} = -\frac{n_e e^2}{m^*(\omega^2 + i\gamma\omega)} \mathbf{E}. \quad (2.16)$$

Using the relation $\mathbf{D} = \mathbf{E} + \mathbf{P}/\epsilon_0$ (where ϵ_0 is the permittivity of free space), yields

⁴Also known as the extinction coefficient.

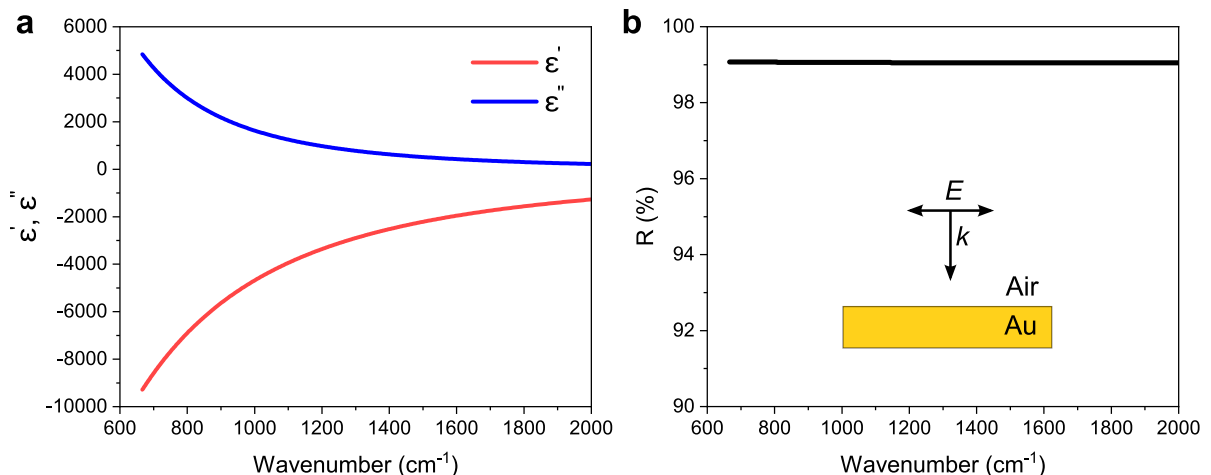


Figure 2.3: (a) Real (ϵ') and imaginary (ϵ'') parts of the dielectric function of gold based on Eq. (2.19). $\lambda_p = 159$ nm and $\Gamma = 0.0048$. (b) Reflectivity of a gold surface (black curve), calculated from the Fresnel reflection coefficient at normal incidence: $R = |(\tilde{n} - 1)/(\tilde{n} + 1)|^2$, where $\tilde{n} = \sqrt{\epsilon' + i\epsilon''}$. The Au interface maintains a high reflectivity of ~ 99 % over the entire plotted infrared spectral range.

$$\mathbf{D} = \mathbf{E} \left(1 - \frac{n_e e^2}{m^* \epsilon_o (\omega^2 + i\gamma\omega)} \right). \quad (2.17)$$

Using Eq. (2.8), one readily arrives at the dielectric function of a free electron gas

$$\epsilon(\omega) = 1 - \frac{\omega_p^2}{(\omega^2 + i\gamma\omega)}, \quad (2.18)$$

where $\omega_p^2 = e^2 n_e / m^* \epsilon_o$ gives the *plasma frequency*. For most metals $n_e \approx 10^{22}$ cm $^{-3}$ so that $\omega_p \approx 10^{16}$ s $^{-1}$, *i.e.*, the plasma frequency for metals is in the ultraviolet spectral range. For gold and silver, the plasma frequency corresponds to a photon wavelength of $\lambda_p = 159$ and 135 nm, respectively.

By comparing Eqs. (2.9) and (2.18), we can make the following formal correspondences: ω_{LO} for the polar dielectric corresponds to ω_p for the electron gas; ω_{TO} for the polar dielectric corresponds to $\omega = 0$ for the electron gas.

It is usually convenient to write the dielectric function of Eq. (2.18) in terms of the wavelength and the dimensionless damping constant $\Gamma = \gamma/\omega_p$, as follows

$$\epsilon(\lambda) = 1 - \frac{1}{\frac{\lambda_p}{\lambda} \left(\frac{\lambda_p}{\lambda} + i\Gamma \right)}. \quad (2.19)$$

The dielectric function resulting from Eq. (2.19) for gold is plotted in Fig. 2.3 for infrared frequencies. It can be seen that over the entire infrared spectral range considered, the real part of the dielectric function of gold remains large and negative. As a consequence, gold maintains high reflectance at infrared frequencies, acting as an almost perfect mirror (see Fig. 2.3 (b)).

It is instructive to note that in the plasma model the skin depth can be approximated by $\delta = c/\omega_p$ [8], where c is the speed of light in vacuum. In gold, the skin depth of infrared photons is $\delta \approx 25$ nm and, for most metals at room temperature, $\delta \approx 100$ nm [9]. The short penetration depths characteristic of metals are at the origin of the large field enhancements exhibited by various plasmonic structures.

2.2 Surface polaritons within the local dielectric continuum theory

In this section, we will detail the local theory of surface polaritons at the boundaries of semi-infinite media and thin films, as well as for the sphere geometry.

2.2.1 Surface polaritons in a semi-infinite medium

We consider a half-space ($z > 0$) of a boundary-active medium in contact with a half-space ($z < 0$) of a boundary-inactive medium (Fig. 2.4). The dielectric function of the former we write as $\varepsilon(\omega)$ and for the inactive medium, we write the dielectric function as ε_I , which we take to be constant for the moment. Both media are considered to be non-magnetic so their magnetic susceptibility μ is unity. We would like to solve for the type of electromagnetic field arrangement such a system supports. More precisely, we are interested in the field arrangement which is dependent on the fact that there is a surface present.

Consider an electric field with components both perpendicular and parallel to the $z = 0$ boundary of Fig. 2.4. We take these components as $E_z(x, z, t)$ and $E_x(x, z, t)$. Then, from Maxwell's equations with no external sources,

$$\nabla \cdot \mathbf{B} = 0, \quad (2.20)$$

$$\nabla \cdot \mathbf{D} = 0, \quad (2.21)$$

$$\nabla \times \mathbf{E} = -\frac{1}{c} \frac{\partial \mathbf{B}}{\partial t}, \quad (2.22)$$

$$\text{and, } \nabla \times \mathbf{H} = \frac{1}{c} \frac{\partial \mathbf{D}}{\partial t}, \quad (2.23)$$

there must be a magnetic induction component $B_y(x, z, t)$. This general field arrangement is referred to as p -polarized⁵. We note that, in contrast to, say, a calculation of the reflectance for the system of Fig. 2.4, here we are dealing with a situation in which a source for these fields is explicitly absent. Instead, our procedure is to assume that such a p -polarized field arrangement can exist and assess the consequences. Therefore, the modes that arise from such a calculation are true normal modes of the system.

Since we have translational invariance in the x -direction, we can make a Fourier transform in this direction (with Fourier transform variable k) as well as in time (with Fourier transform

⁵Also known as TM-polarization. The orthogonal polarization is referred to as s -polarization or TE-polarization.

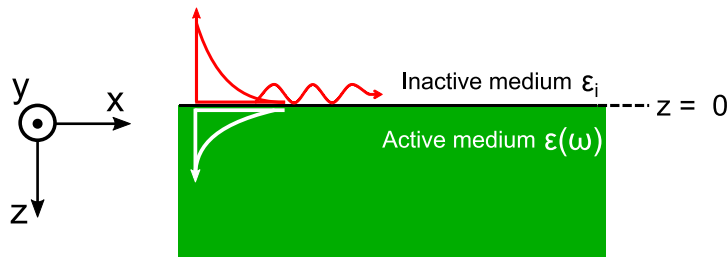


Figure 2.4: Sketch of the half-space geometry. Surface polaritons can propagate along the interface between the active and inactive media.

variable ω) and, thus, write all field components in the form

$$E_x(x, z, t) = \tilde{E}_x(z) e^{ikx} e^{-i\omega t}. \quad (2.24)$$

From Eqs. (2.22) and (2.23), we then have

$$\frac{d\tilde{B}_y}{dz} = \frac{i\omega\varepsilon}{c} \tilde{E}_x, \quad (2.25)$$

$$k\tilde{B}_y = -\frac{\omega\varepsilon}{c} \tilde{E}_z, \quad (2.26)$$

$$\text{and, } \frac{d\tilde{E}_x}{dz} - ik\tilde{E}_z = i\frac{\omega}{c} \tilde{B}_y, \quad (2.27)$$

where we have used the relations $\tilde{D} = \varepsilon\tilde{E}$ and $\tilde{B} = \mu\tilde{H}$.

Differentiating Eq. (2.25) with respect to z and using Eqs. (2.25) and (2.26), we find

$$\frac{d^2\tilde{E}_x}{dz^2} - \alpha^2\tilde{E}_x = 0 \quad (2.28)$$

$$\text{where } \alpha^2 = k^2 - \varepsilon\frac{\omega^2}{c^2}. \quad (2.29)$$

Eqs. (2.28) and (2.29) make up the scalar Helmholtz equation defining the field \tilde{E}_x . The Helmholtz equation (2.28) is valid for both half-spaces ($z > 0$ and $z < 0$) with the appropriate choice of ε .

We consider first the boundary active medium ($z > 0$) and we assume that $\alpha^2 > 0$ and $\alpha > 0$. Then, from Eqs. (2.28) and (2.25)-(2.27), the physically valid solution for the field components is

$$\tilde{E}_x(z) = K e^{-\alpha z}, \quad (2.30)$$

$$\tilde{E}_z(z) = \frac{ik}{\alpha} K e^{-\alpha z}, \quad (2.31)$$

$$\text{and, } \tilde{B}_y(z) = -\frac{i\omega}{c} \frac{\varepsilon}{\alpha} K e^{-\alpha z}, \quad (2.32)$$

with K an integration constant. Thus, we see that the fields decay exponentially from the surface into the medium, indicating that this solution arises as a consequence of the presence of the boundary. The total field present at the interface, then, propagates along the x -direction and decays exponentially away from the surface, as sketched in Fig. 2.4.

For the inactive medium ($z < 0$), we replace ε with ε_I in Eq. (2.29). Defining α_I by

$$\alpha_I^2 = k^2 - \varepsilon_I \frac{\omega^2}{c^2}, \quad (2.33)$$

and assuming $\alpha_I^2 > 0$ and $\alpha_I > 0$, the field components in the boundary-inactive medium are given by

$$\tilde{E}_x(z) = K' e^{\alpha_I z}, \quad (2.34)$$

$$\tilde{E}_z(z) = -\frac{ik}{\alpha_I} K' e^{\alpha_I z}, \quad (2.35)$$

$$\text{and, } \tilde{B}_y(z) = \frac{i\omega}{c} \frac{\varepsilon_I}{\alpha_I} K' e^{\alpha_I z} \quad (2.36)$$

with K' another integration constant. Thus the fields in the boundary-inactive medium also decay exponentially from the surface.

From the continuity of the fields \tilde{E}_x , \tilde{D}_z , and \tilde{H}_y at the boundary $z = 0$, or equivalently from the continuity of the surface impedance at $z = 0$ (defined here as⁶ $Z = E_x/H_y$), we find that $K = K'$ and

$$\varepsilon = -\frac{\alpha}{\alpha_I} \varepsilon_I. \quad (2.37)$$

After squaring, Eq. (2.37) can be rewritten as

$$\frac{\varepsilon \varepsilon_I}{\varepsilon + \varepsilon_I} = \frac{k^2}{(\omega/c)^2}. \quad (2.38)$$

Eqs. (2.37) and (2.38) specify the dispersion relation $\omega(k)$ of a normal mode of the system sketched in Fig. 2.4. In particular, if the boundary-active medium ($z > 0$) is a polar dielectric or a metal, then the normal modes that arise from Eq. (2.38) correspond to the SPhP and SPP modes, respectively. It is then possible to say a number of things about the character of these normal modes without specifying the functional form of the dielectric functions.

In most cases of interest, the boundary-inactive medium will be chosen so that $\varepsilon_I > 0$. Then, from Eq. (2.37) and our assumptions concerning α and α_I , the normal modes occur for frequencies such that $\varepsilon(\omega) < 0$. It follows directly, then, that $\varepsilon(\omega) < -\varepsilon_I$. Thus, one may note here that the domain of validity of SPhPs in polar dielectrics is restricted to the frequency range $\omega_{\text{TO}} < \omega < \omega_{\text{LO}}$ or the *Reststrahlen* band. Rewriting Eq. (2.38) as

$$\frac{1}{\varepsilon} + \frac{1}{\varepsilon_I} = \frac{\omega^2}{c^2 k^2}, \quad (2.39)$$

⁶In vacuum, impedance is usually defined as $Z_0 = |\mathbf{E}|/|\mathbf{H}| = \sqrt{\mu_0/\varepsilon_0} \approx 377 \Omega$.

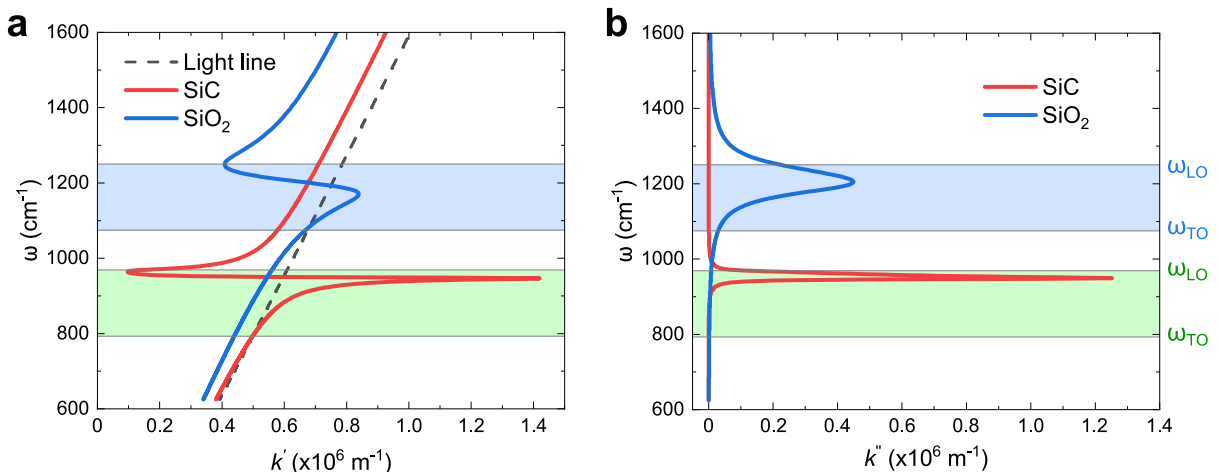


Figure 2.5: (a) Real (ω vs k') and (b) imaginary (ω vs k'') parts of the dispersion curves of the normal modes for a vacuum/SiC half-space (red curves) and a vacuum/SiO $_2$ half-space (blue curves). The modes corresponding to the SPhPs are given by the portion of the curves in the material's *Reststrahlen* band (shaded regions) between ω_{TO} and ω_{LO} , where the real part of the dielectric function is negative (see Figs. 2.1 (a) and (c)).

one can also see that for $k^2 \gg \omega^2/c^2$, that is, k much larger than the wave vector of a photon of frequency ω , the normal mode frequency is that for which $\epsilon \rightarrow -\epsilon_I$. If the inactive medium is a vacuum, the normal mode occurs for frequencies such that $\epsilon < -1$ and, for large k the normal mode frequency is that for which $\epsilon(\omega) = -1$.

To solve explicitly for the normal modes, we first note that since $\epsilon(\omega)$ is complex, it is clear from Eq. (2.38) that either ω or k must be complex or both. The approach that we will take is to assume that ω is real and solve for a complex wavevector $k = k' + ik''$. Alternatively, one can take k to be real and solve for $\omega = \omega' + i\omega''$. The two approaches are equivalent in terms of the information contained in their resulting real dispersion relation (*i.e.* ω vs k' or ω' vs k). However, the imaginary part provides different information in each case; k'' is related to the mode's propagation length (as will be illustrated later), while ω'' is related to its lifetime.

The resulting real dispersion curves of the normal modes at a vacuum/SiC interface and a vacuum/SiO $_2$ interface are plotted in Fig. 2.5 (a). The dispersion curves consist of two branches: a radiative branch with $\omega > ck$ and a non-radiative branch with $\omega < ck$. We will focus our discussion on the latter branch as it is the one consisting of the propagating SPhP modes. It is important to note here that although we specialize our discussion to SPhPs, the main properties and behavior of such surface modes will be equivalent to that of SPPs in metals, and can be deduced analogously, in a fashion similar to that illustrated at the end of subsection 2.1.2. As evident from Fig. 2.5, the SPhP modes correspond to normal modes with large wavevectors. Therefore, these modes cannot couple to propagating waves due to the large momentum mismatch and are thus restricted to propagating along the surface.

The behavior of the dispersion curve of SPhPs, shown in Fig. 2.5 (a), can be more easily illustrated in the absence of damping ($\gamma = 0$), since in this case, there exists an analytical solution to Eq. (2.38). Taking $\gamma = 0$ in Eq. (2.11), combining it with Eq. (2.39), and defining

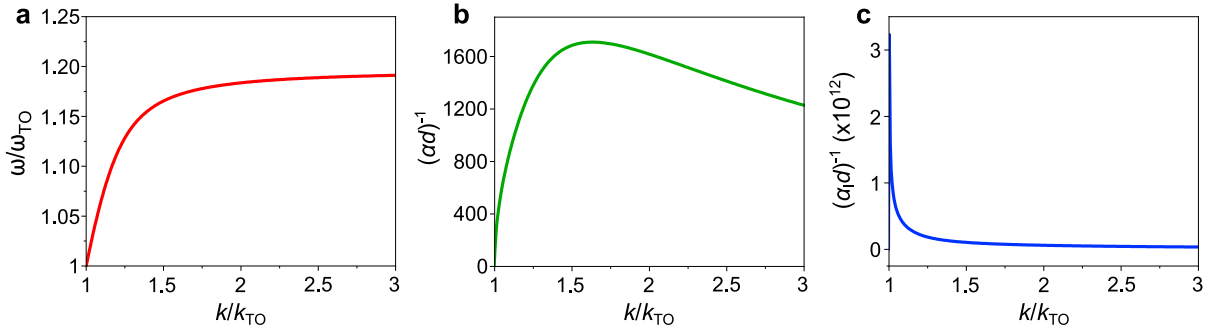


Figure 2.6: (a) Dispersion relation of SPhPs in a vacuum/SiC half-space in the absence of damping ($\gamma = 0$ in Eq. (2.11)) obtained from solving Eq. (2.42) and plotted as a function of dimensionless frequency $\omega/\omega_{\text{TO}}$ and dimensionless wavevector k/k_{TO} . For SiC $\omega_{\text{LO}}/\omega_{\text{TO}} = 1.22$. (b) & (c) Dimensionless penetration depths of SPhPs $(\alpha d)^{-1}$ in SiC (panel (b)) and $(\alpha_I d)^{-1}$ in vacuum (panel (c)), where $d = 5 \text{ \AA}$ is the mean interionic spacing.

$$\omega_k^2 = c^2 k^2 \left(\frac{1}{\varepsilon_\infty} + \frac{1}{\varepsilon_I} \right), \quad (2.40)$$

and

$$\omega_\infty^2 = \frac{\varepsilon_\infty \omega_{\text{LO}}^2 + \varepsilon_I \omega_{\text{TO}}^2}{\varepsilon_\infty + \varepsilon_I} = \omega_{\text{TO}}^2 \frac{\varepsilon_0 + \varepsilon_I}{\varepsilon_\infty + \varepsilon_I}, \quad (2.41)$$

where ω_∞ is the frequency for which $\varepsilon(\omega) + \varepsilon_I = 0$ or the frequency of the SPhP mode in the limit of large k ,⁷ the result is

$$\omega^2 = \frac{(\omega_k^2 + \omega_{\text{LO}}^2)}{2} + \left[(\omega_k^2 + \omega_{\text{LO}}^2)^2 - 4\omega_k^2 \omega_\infty^2 \right]^{1/2}. \quad (2.42)$$

This dispersion curve starts at $\omega = 0$ for $k = 0$ and increases monotonically to the asymptotic limit ω_∞ as $k \rightarrow \infty$. However, we saw above that the SPhP mode occurs only when $\alpha_I > 0$ and $\varepsilon < -\varepsilon_I$. For positive ε_I , this means that Eq. (2.42) is a legitimate solution only for $k^2 \geq \varepsilon_I (\omega_{\text{TO}}/c)^2$. When $k^2 = \varepsilon_I (\omega_{\text{TO}}/c)^2$, $\omega = \omega_{\text{TO}}$.

In Fig. 2.6 (a) the dispersion relation given in Eq. (2.42) is shown for $\varepsilon_I = 1$, corresponding to vacuum, and $\varepsilon_0 = 10.004$, $\varepsilon_\infty = 6.7$, and $\omega_{\text{TO}} = 793 \text{ cm}^{-1}$ corresponding to SiC [6]. For large k , the asymptotic frequency is $\omega/\omega_{\text{TO}} = 1.195$, for which $\varepsilon(\omega) = -1$. From Fig. 2.5 (a), it can be seen that the dispersion curve reaches its asymptote at a frequency $\omega_\infty \sim 948 \text{ cm}^{-1}$ (resp. $\sim 1170 \text{ cm}^{-1}$) for SiC (resp. SiO₂). We underscore here the fact that at this asymptotic frequency, there exists a significant number of modes with large wavevector k . The influence of this asymptotic behavior on the local near-field spectral response will be discussed in greater detail in chapter 3. We also note that the dispersion curve for the case of SiO₂ terminates at much smaller wavevectors than the case of SiC (see Fig. 2.5 (a), blue curve), indicating that SPhPs are more damped in SiO₂, due to its amorphous nature. At small k , as follows from the comments given in the previous paragraph, the dispersion curve terminates on the light line

⁷For metals, we have $\omega_\infty = \omega_p/\sqrt{2}$ for $\varepsilon_I = 1$, if losses are neglected. This frequency lies in the near ultraviolet.

($\omega = ck$) at the frequency $\omega = \omega_{\text{TO}}$.

For large k , $k \gg \omega_{\text{TO}}/c$, we see from Eqs. (2.29) and (2.33) that $\alpha \approx \alpha_I \approx k$. Thus, the electromagnetic fields and the ionic motion associated with the surface polariton penetrate the crystal only to a depth of order $\delta_z = |\alpha|^{-1} \approx |k|^{-1}$. Here it must be kept in mind that the present theory is valid only if $d \ll |\alpha|^{-1}$, where d is the interionic spacing. The surface polariton frequency has essentially reached its asymptotic value for $k \sim 2.5 k_{\text{TO}}$ (see Fig. 2.6), where k_{TO} is defined by

$$k_{\text{TO}} = \frac{\omega_{\text{TO}}}{c}. \quad (2.43)$$

For SiC, the value for $2.5 k_{\text{TO}}$ is about $1.246 \times 10^{-4} \text{ \AA}^{-1}$, while the average interionic spacing is $\sim 5 \text{ \AA}$, so the conditions for the validity of the local theory are well satisfied here. As k decreases from the asymptotic region, the depth of penetration of the fields, and hence of the ionic motion, increases roughly until the dispersion curve turns rather sharply downward where $k \sim 1.632 k_{\text{TO}}$ (see Fig. 2.6 (a)). The maximum penetration depth $(\alpha^{-1})_{\text{max}}$, thus, satisfies

$$(\alpha^{-1})_{\text{max}} \sim (1.632 k_{\text{TO}})^{-1}. \quad (2.44)$$

As k decreases from $1.632 k_{\text{TO}}$, the penetration decreases rapidly and, as the termination point is approached, $\alpha^{-1} \rightarrow 0$. Thus the polariton is strongly localized at the surface for large k and near the low- k termination point but less so for intermediate values of k . This fact is illustrated in Fig. 2.6 (b) which shows α^{-1} as a function of k for SiC. Note, however, that α_I^{-1} increases monotonically with decreasing k and becomes infinite at the low- k termination point (see Fig. 2.6 (c)).

As mentioned previously, the propagation length, L_p , of SPhPs on the surface can be evaluated from the imaginary part of the polariton wavevector k , as follows

$$L_p = \frac{1}{2|k''|}. \quad (2.45)$$

It can be seen immediately from Eq. (2.45) that, if losses are neglected, the propagation length of SPhPs is infinite. In real materials, however, the polariton propagation length is finite and scales inversely with damping. In Fig. 2.7, we plot both surface penetration depths, $\delta_z = |\alpha|^{-1}$ and $\delta_z^I = |\alpha_I|^{-1}$, as well as the polariton propagation length L_p for vacuum/SiC and vacuum/SiO₂ interfaces, with material damping included. We note that, just like in the non-retarded case ($\gamma = 0$), the electromagnetic fields penetrate deeper into the boundary-inactive medium (vacuum in this case) than the boundary-active medium (cf. blue and red curves in Fig. 2.7).

The influence of damping on the surface polariton propagation length is clearly illustrated by comparing Figs. 2.7 (c) and (d). Interestingly, SPhPs propagate over distances that are several tens of wavelengths, on the surface of SiC, a crystal with a high degree of purity, and reaches as high as 100λ at ω_{TO} , where λ is the free-space wavelength (see Fig. 2.7 (c)). It has been shown that a delocalized electromagnetic surface mode, either coupled to a plasmon or a phonon in the material, correlates the near-field on distances on the order of its propagation length. We

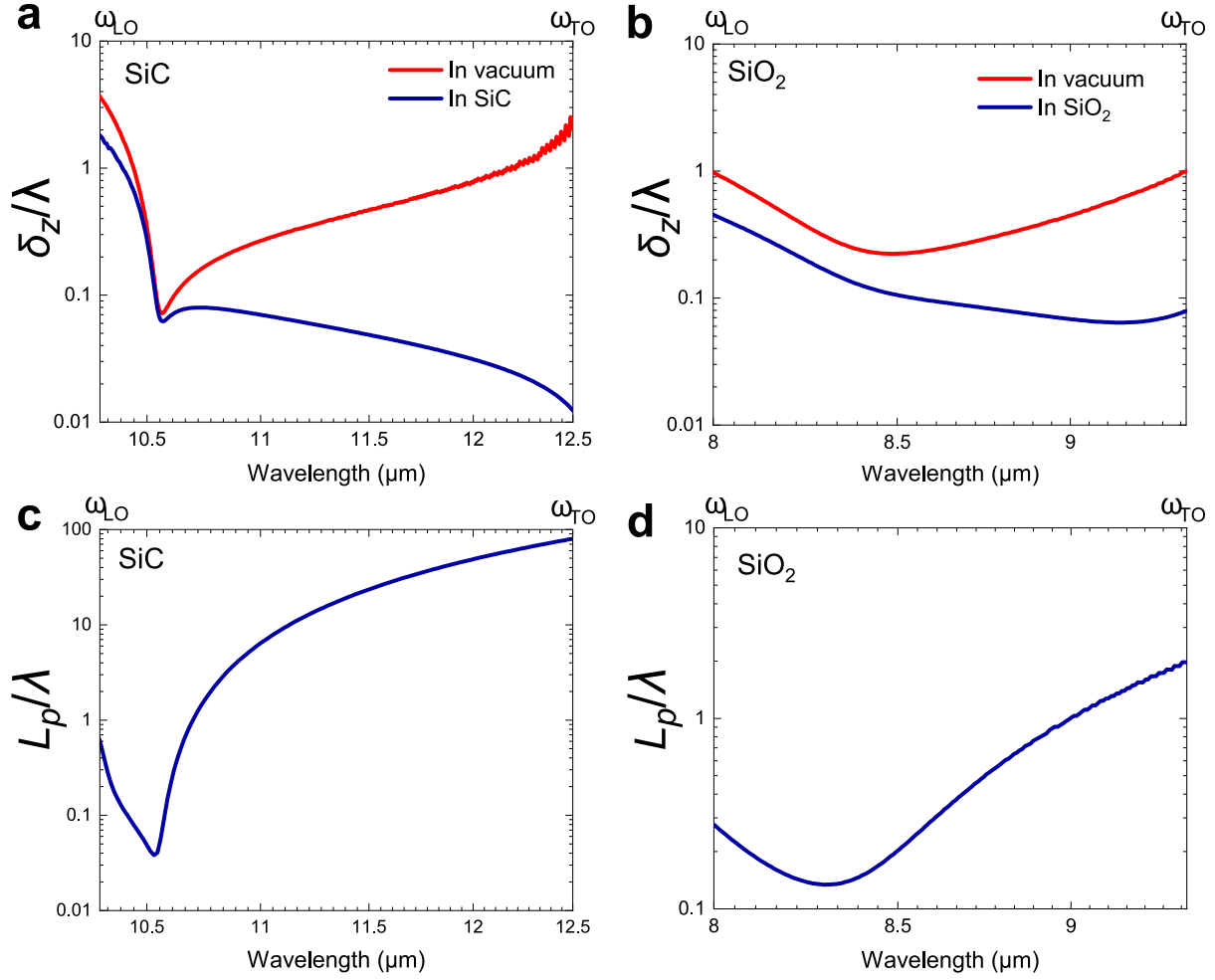


Figure 2.7: Dimensionless penetration depth $\delta_z/\lambda = |\alpha|^{-1}/\lambda$, in the boundary-active medium, and $\delta_z^I/\lambda = |\alpha_I|^{-1}/\lambda$, in the boundary-inactive medium (for $\varepsilon_I = 1$), where $\lambda = 2\pi c/\omega$ is the wavelength in vacuum, for SPhPs at (a) a vacuum/SiC interface and (b) a vacuum/SiO₂ interface. (c) and (d) Dimensionless propagation length L_p/λ of SPhPs, at the surface of SiC and SiO₂, respectively.

have seen that the propagation length at a vacuum/SiC interface easily reaches several tenths of λ , thus resulting in substantial spatial coherence [1]. On the other hand, the propagation length on the surface of amorphous SiO₂ is much shorter, on the order of $\sim \lambda$ (see Fig. 2.7 (d)). In general, the polariton propagation length is maximal at ω_{TO} and decreases monotonically with increasing frequency, reaching a minimum value at the asymptotic frequency ω_∞ , for which $\varepsilon(\omega) = -1$, and finally increases again for $\omega > \omega_\infty$, up to ω_{LO} . The minimal value of L_p at ω_∞ indicates that, at this frequency, the polaritons are highly localized at the center from which they are launched. This behavior follows directly from the trend of k'' , which attains large values as $\omega \rightarrow \omega_\infty$ (so that L_p is minimal), and falls off rather sharply on either side of this frequency (see Fig. 2.5 (b)).

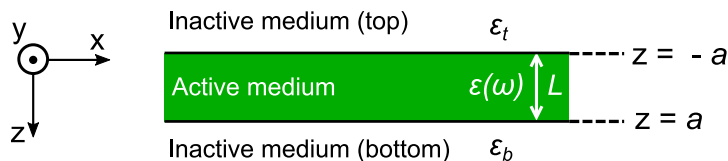


Figure 2.8: Geometry and notation of a thin film of thickness $L = 2a$ and dielectric function $\varepsilon(\omega)$. The film is sandwiched between two inactive media of dielectric constants ε_t and ε_b , from the top and bottom, respectively. All media are considered to be non-magnetic, *i.e.*, $\mu = 1$.

2.2.2 Surface polaritons in thin films

The effect of a finite active medium thickness on the SPhPs discussed in the previous subsection can easily be obtained as follows. Consider a film of thickness L as sketched in Fig. 2.8. From Eq. (2.44), it is clear that if L satisfies

$$L > 1.632 (\alpha^{-1})_{\max} \sim \frac{1}{k_{\text{TO}}}, \quad (2.46)$$

both surfaces can support SPhPs, and the presence of the second surface has no effect on a polariton propagating along the original surface. Thus, a film of thickness $k_{\text{TO}}L > 1$ is effectively of infinite thickness insofar as the surface polariton is concerned.

On the other hand, for a film such that $k_{\text{TO}}L < 1$, there will in general be two surface polaritons as a result of the interaction of the fields from the two surfaces. For a half-space, the real part of the fields in the boundary-active medium are given by: $\text{Re}(E_x) = e^{-\alpha z} \cos(kx - \omega t)$ and $\text{Re}(E_z) = -\frac{k}{\alpha} e^{-\alpha z} \sin(kx - \omega t)$. Part of these fields is represented in Fig. 2.9 (a). The direction of the arrows indicates a particular choice for the sign of the amplitude factor K in Eqs. (2.30)-(2.32). A corresponding sketch for a second half-space appears in Fig. 2.9 (b) with the same sign of the associated amplitude factor (*i.e.*, the electric field components parallel to the surfaces are in the same direction). A rough representation of the field corresponding to a film of thickness L can then be obtained by superposing Figs. 2.9 (a) and (b). The resultant of this superposition is shown in Fig. 2.9 (c). When the amplitude factors have the opposite sign the corresponding figures are Figs. 2.9 (d-f).

On the basis of Fig. 2.9 and the considerations of the preceding subsection, we can draw several conclusions concerning the surface polaritons for a thin film. The polariton of Fig. 2.9 (c), for which the electric field and, thus, the polarization is predominantly parallel to the surface, will have a frequency lower than that of the half-space polariton for the same k . We will call the frequency of this mode ω_- . This follows from the fact that the fields in the film superpose in such a way that the surface charge⁸, which provides the driving force for the oscillation, is reduced from the corresponding half-space case. In contrast, the polariton of Fig. 2.9 (f), with polarization essentially perpendicular to the surface, has a surface charge that is larger in magnitude than the corresponding half-space case and thus a higher frequency. We will call the frequency of this mode ω_+ . As k increases to values such that $kL \gg 1$, the surface polaritons become highly localized at the surfaces, the fields from the two surfaces no longer overlap, and

⁸In a half-space, the surface charge σ is proportional to $-(\frac{k}{\alpha} + \frac{k}{\alpha_t}) \sin(kx - \omega t)$ (see ref. [5], page 367)

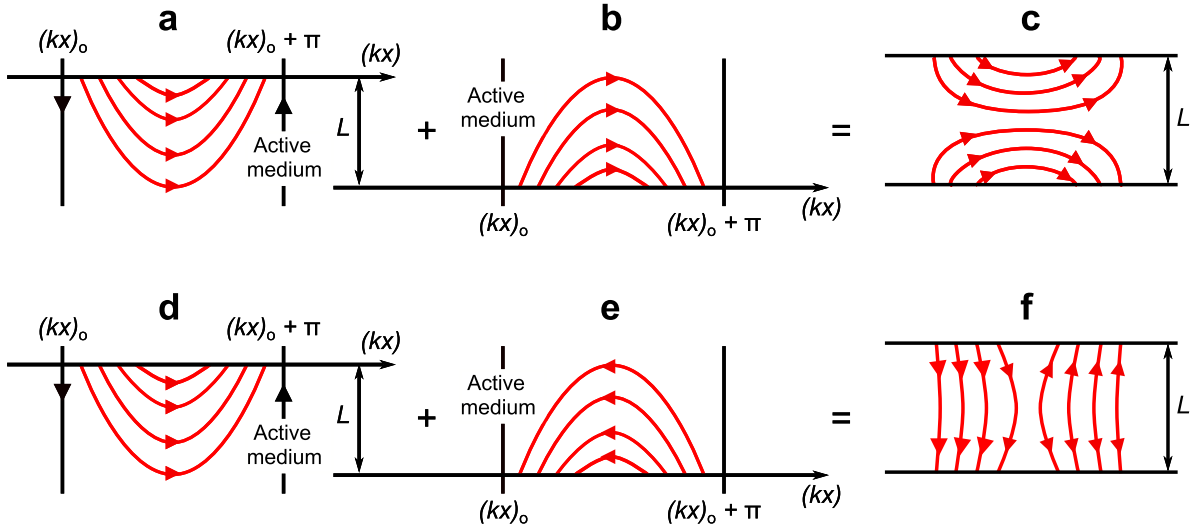


Figure 2.9: A physical representation of the real part of the surface polariton electric fields within a thin film (thickness L such that $k_{\text{TO}}L \ll 1$) as obtained from the fields for the surface polariton in a half-space. (a) and (b) Electric fields of the two half-spaces having the same sign of the amplitude factor. (d) and (e) Electric fields of the two half-spaces having the opposite sign of the amplitude factor. The sign of the amplitude factor is specified by the arrows in each case. (c) (resp. (f)) Resultant field from the superposition of panels (a) and (b) (resp. panels (d) and (e)).

the polariton frequencies will become those of the associated half-space problems. There will now be, however, two distinct surface mode frequencies in the large- k limit if the inactive media on the two sides of the active film have different dielectric functions. Since the low- k termination point of the polariton corresponds to strong localization at the surface, the polariton frequencies for these values of k must approach the corresponding half-space frequencies. For different inactive media on the two sides of the film, there will, of course, be two distinct termination points, both with $\omega = \omega_{\text{TO}}$. The conclusions of the previous paragraph are then sketched in Fig. 2.10.

Analytically, the behavior of the dispersion curves of SPhPs in a thin film of thickness $L = 2a$, as shown in Fig. 2.8, are described by the following equation⁹ (see ref. [5], page 375)

$$(S)_{\pm} = \frac{(S_b + S_t)(e^{-2\alpha a} + e^{2\alpha a}) \mp [(S_b - S_t)^2(e^{-2\alpha a} + e^{2\alpha a})^2 + 16S_b S_t]^{1/2}}{2(e^{-2\alpha a} - e^{2\alpha a})}, \quad (2.47)$$

where the (+) and (-) signs on the left-hand side are associated with the ω_+ and ω_- polariton branches, respectively, and the following definitions were used

⁹This equation can readily be obtained by following the procedure outlined in subsection 2.2.1, except that one must add a term $\propto e^{\alpha z}$ in the field components for $|z| < a$, to account for the finite thickness of the film, and apply the boundary conditions at the two surfaces $z = +a$ and $z = -a$.

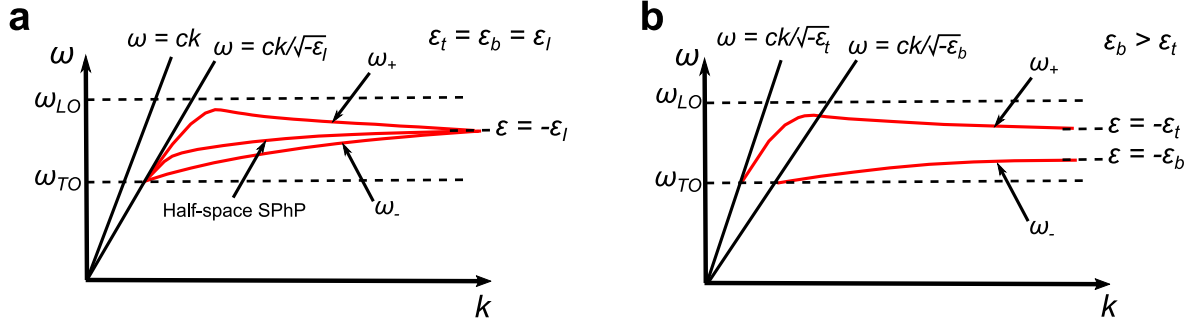


Figure 2.10: Sketch of the dispersion curves of SPhPs corresponding to the thin film geometry of Fig 2.8 for (a) $\varepsilon_t = \varepsilon_b = \varepsilon_I \geq 1$ and (b) $\varepsilon_b > \varepsilon_t \geq 1$.

$$S = \frac{\varepsilon(\omega)}{\alpha}, \quad S_t = \frac{\varepsilon_t}{\alpha_t}, \quad \text{and} \quad S_b = \frac{\varepsilon_b}{\alpha_b}. \quad (2.48)$$

$$\alpha^2 = k^2 - \varepsilon\omega^2/c^2, \quad \alpha_t^2 = k^2 - \varepsilon_t\omega^2/c^2, \quad \text{and} \quad \alpha_b^2 = k^2 - \varepsilon_b\omega^2/c^2. \quad (2.49)$$

Although Eq. (2.47) is complicated, we can nonetheless demonstrate the validity of the principal features of Fig. 2.10. Suppose $\alpha a \rightarrow \infty$ and $\varepsilon_b > \varepsilon_t \geq 1$. Then

$$(S)_- = \left(\frac{\varepsilon}{\alpha}\right)_- = -S_b = -\frac{\varepsilon_b}{\alpha_b}, \quad (2.50)$$

while

$$(S)_+ = \left(\frac{\varepsilon}{\alpha}\right)_+ = -S_t = -\frac{\varepsilon_t}{\alpha_t}. \quad (2.51)$$

For large k , where $\alpha \approx \alpha_t \approx k$, Eq. (2.50) is just $\varepsilon = -\varepsilon_b$ and we obtain the asymptotic frequency for ω_- of Fig. 2.10 (b). Similarly, for large k , the equation resulting from the solution $(S)_+$, is $\varepsilon = -\varepsilon_t$ and we obtain the asymptotic frequency of the ω_+ mode.

The limit $\alpha a \rightarrow \infty$, with a fixed, occurs not only for large k , but also near the low- k termination points where $\omega \rightarrow \omega_{\text{TO}}$ and $\text{Re}(\varepsilon) \rightarrow -\infty$. From Eq. (2.50) we see that the termination point for the ω_- mode is

$$\alpha_b|_{\omega=\omega_{\text{TO}}} = 0 \quad \text{or} \quad k = \frac{\omega_{\text{TO}}\sqrt{\varepsilon_b}}{c}, \quad (2.52)$$

while from Eq. (2.51) the termination point for the ω_+ mode is

$$\alpha_t|_{\omega=\omega_{\text{TO}}} = 0 \quad \text{or} \quad k = \frac{\omega_{\text{TO}}\sqrt{\varepsilon_t}}{c}, \quad (2.53)$$

corresponding to the limits shown in Fig.2.10 (b).

Finally, we must demonstrate that the frequency ω_+ rises above that of the asymptotic limit while that of ω_- stays below. This is most easily accomplished by considering a very thin film and intermediate values of k so that α is well behaved and we can examine the $\alpha a \rightarrow 0$ limit of

Eq. (2.47). We find

$$\lim_{\alpha a \rightarrow 0} (S)_- = -\frac{S_b + S_t + [(S_b - S_t)^2 + 4S_b S_t]^{1/2}}{2\alpha a}, \quad (2.54)$$

and

$$\lim_{\alpha a \rightarrow 0} (S)_+ = -\frac{\alpha a}{4} \left[\frac{2(S_b + S_t)^2 - (S_b - S_t)^2}{(S_b + S_t)} \right]. \quad (2.55)$$

Since S_b and S_t are positive here, we see from Eq. (2.54) that $(S)_-$ is a large negative number which means that

$$\omega_- \geq \omega_{\text{TO}}, \quad (2.56)$$

a frequency below the asymptotic frequency for the ω_- mode. From Eq. (2.55) we see that S_+ , is a small negative number so

$$\omega_+ \leq \omega_{\text{LO}}, \quad (2.57)$$

a frequency above the asymptotic limit for the ω_+ mode. Thus the validity of the general features shown in Fig. 2.10 (b) is established.

It is interesting to note that for a thin film and k values such that $\alpha a \ll 1$, the ω_+ mode occurs essentially at ω_{LO} while the ω_- mode occurs at the ω_{TO} .

Generally, in the discussion above, we have considered inactive media for which $\varepsilon_b, \varepsilon_t \geq 1$. One particularly important exception to this restriction occurs if the active film is placed on a good conductor, whose dielectric function can be written in the form given in Eq. (2.18), and bound from the top by a dielectric medium with $\varepsilon_I \geq 1$. The frequency ω_p in Eq. (2.18), the plasma frequency, is for most metals very high, $5 \times 10^{15} \leq \omega_p \leq 30 \times 10^{15} \text{ s}^{-1}$. Since the polaritons we are considering here have frequencies in the range of 10^{14} s^{-1} , the dielectric function of the conductor in this frequency range will be a very large negative number, $\varepsilon_c \sim -10^5$, if we take for the moment $\gamma \rightarrow 0$ in Eq. (2.18). This suggests immediately that we can consider a good conductor in the present context as a perfect conductor, *i.e.*, $\varepsilon_c \rightarrow -\infty$, and thus incapable of supporting an electric field parallel to its surface. The continuity of the electric field components tangential to the surface, then, dictates that E_x must vanish at the active medium-metal boundary.

For a particular choice of the integration constants, the electric fields parallel to the surface can be cast as follows

$$\tilde{E}_x = \begin{cases} e^{\alpha_I z}, & z < -a \\ e^{-\alpha z} \mp e^{\alpha z}, & |z| < a \\ e^{-\alpha_c z}, & z > a \end{cases}, \quad (2.58)$$

where α_c for the conducting backplate is given by $\alpha_c^2 = k^2 - \varepsilon_c \omega^2 / c^2$.

In Eq. (2.58) for $|z| < a$, the upper sign is associated with the ω_+ mode and the lower sign with

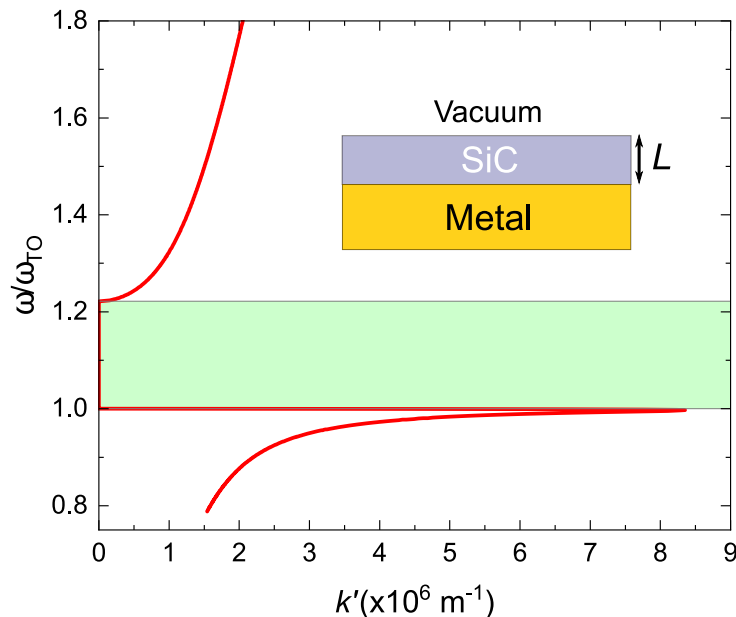


Figure 2.11: Dispersion curves for normal modes for which $k^2 = \epsilon\omega^2/c^2$, for a SiC film of thickness L on a metallic backplate.

the ω_- mode. It is clear from Eq. (2.58) that the condition $E_x = 0$ at the film/metal boundary ($z = a$), is only satisfied in this case for the ω_+ polariton in the limit $\alpha a \rightarrow 0$. This limit is attained for very thin films, such that $\alpha a \ll 1$, in which we have seen that the ω_+ polariton occurs at the longitudinal optical phonon frequency. For thicker films, on the other hand, the condition $E_x = 0$ is met in the limit $\alpha \rightarrow 0$, that is, for $k^2 \rightarrow \epsilon\omega^2/c^2$. The modes for which $\omega^2 = c^2k/\epsilon$ are plotted in Fig. 2.11 for a SiC film of thickness L on a metallic backplate. The plot shows that the only modes that can occur in this case have frequencies such that $\omega \leq \omega_{\text{TO}}$ or $\omega \geq \omega_{\text{LO}}$ so that no modes are found within the *Reststrahlen* band. Interestingly, the dispersion curve in this limit reaches an asymptotic value, at which many large wavevector modes exist, at a frequency slightly lower than the transverse optical phonon frequency ω_{TO} (see Fig. 2.11).

2.2.3 Virtual modes in a polar dielectric sphere

We turn now to the case where the active medium is a non-magnetic subwavelength (sub- λ) sphere of radius r_o and dielectric function $\epsilon(\omega)$, surrounded by a dielectric medium with $\epsilon_I \geq 1$ (Fig. 2.12). We have seen that for planar surfaces the surface modes are genuine normal modes of the system when the dielectric function is real (so that ω and k are real). For the current case, on the other hand, only transverse modes (for which $\nabla \cdot E = 0$) with complex frequencies may occur, corresponding to *pseudo-normal modes* or *quasi-normal modes*. Since the fields considered here are harmonic in time (cf. Eq. (2.24)), these excitations of the system decay in time through radiative losses. In other words, the electromagnetic fields of the active medium couple to electromagnetic fields in the inactive medium which have outgoing radiative wave character at infinity rather than being evanescent as they are for the surface modes. These modes will hereafter be referred to as *virtual modes* [5, 10], as they correspond to temporally

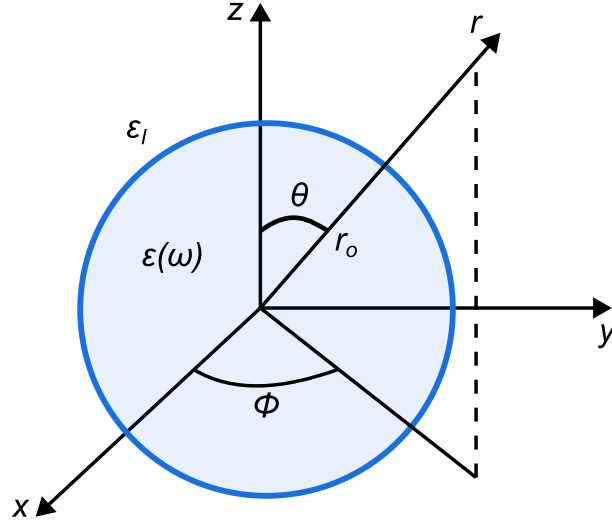


Figure 2.12: Geometry and notation of the sphere problem, in which a sphere of dielectric function $\varepsilon(\omega)$, occupying the region $r \leq r_o$, is surrounded by an inactive medium of dielectric constant ε_I ($r > r_o$). Both media are considered to be non-magnetic.

decaying fields. In contrast to the non-radiative modes of planar geometries, the virtual modes of a sphere couple strongly to optical radiation incident upon the system. This will be reciprocally demonstrated in chapter 3 by directly measuring the far-field thermal emission of a single sub- λ sphere (section 3.3).

The transverse modes of the sphere of Fig. 2.12 are given by the following equations [10]

$$\varepsilon_I h_l^{(1)}(\rho_2)[\rho_1 j_l(\rho_1)]' - \varepsilon j_l(\rho_1)[\rho_2 h_l^{(1)}(\rho_2)]' = 0, \quad (2.59)$$

(electric modes)

$$h_l^{(1)}(\rho_2)[\rho_1 j_l(\rho_1)]' - j_l(\rho_1)[\rho_2 h_l^{(1)}(\rho_2)]' = 0, \quad (2.60)$$

(magnetic modes)

where j_l and $h_l^{(1)}$ are the spherical Bessel and Hankel functions of the first kind, respectively, $\rho_1 = \frac{2\pi r_o}{\lambda} \sqrt{\varepsilon}$, $\rho_2 = \frac{2\pi r_o}{\lambda} \sqrt{\varepsilon_I}$, $l = 1, 2, \dots$ is the mode number, and $'$ denotes differentiation with respect to the argument of the Bessel functions. The terms *electric* and *magnetic* refer to p and s field polarizations, respectively. Due to the azimuthal symmetry of the problem, each solution to the equations above is $(2l + 1)$ -fold degenerate.

In general, a polar dielectric sphere exhibits transverse modes of three types: (i) low-frequency modes having frequency $\omega \leq \omega_{\text{TO}}$, where the real part of the sphere's dielectric function is positive ($\varepsilon' > 0$) (ii) high-frequency modes for which $\omega \geq \omega_{\text{LO}}$, and (iii) surface modes with frequencies that are intermediate between ω_{TO} and ω_{LO} , where $\varepsilon' < 0$.

It is convenient for the discussion that follows to introduce the dimensionless frequency

$$\Omega = \frac{\omega}{\omega_{\text{TO}}} = \Omega' + i\Omega'', \quad (2.61)$$

and the dimensionless radius

$$W = r_o k_{\text{TO}} \sqrt{\varepsilon_I}, \quad (2.62)$$

where k_{TO} is given by Eq. (2.43). As $W \rightarrow 0$, all the low-frequency modes have $\Omega' \rightarrow 1$ and the high-frequency modes have $\Omega' \rightarrow \infty$. For $W \rightarrow \infty$, the low-frequency modes have $\Omega' \rightarrow 0$ and the high frequency modes have $\Omega' \rightarrow \omega_{\text{LO}}/\omega_{\text{TO}}$.

It is instructive to examine the properties of the surface modes in the limit $W \rightarrow 0$ where both ρ_1 and ρ_2 in Eq. (2.59) approach zero. We have then $j_l(\rho_1) \approx \rho^l$ and $h_l^{(1)}(\rho_2) \approx \rho_2^{-(l+1)}$ so that Eq. (2.59) becomes

$$\varepsilon(\omega) = -\frac{(l+1)}{l} \varepsilon_I. \quad (2.63)$$

For $l = 1$, Eq. (2.63) gives the well-known *Fröhlich* condition ruling the intrinsic resonance of an oscillating dipole in the electrostatic limit [11], as we will see in chapter 3. Using Eqs. (2.10) and (2.11) with $\gamma = 0$, the frequencies, now real, resulting from Eq. (2.63) are

$$\Omega_l^2 = \frac{\omega_l^2}{\omega_{\text{TO}}^2} = \frac{\varepsilon_0 l + \varepsilon_I(l+1)}{\varepsilon_\infty l + \varepsilon_I(l+1)}, \quad (2.64)$$

According to Eq. (2.64), for an SiO₂ sphere in vacuum, the first order surface mode occurs at 1165 cm⁻¹. In reality, since SiO₂ is a highly lossy material, the real surface mode frequency will be slightly red-shifted compared to that given by Eq. (2.64), which neglects material damping. As W increases, the real parts of the surface mode frequencies decrease and, if losses are neglected, can be approximated by

$$\Omega_l^2 \approx \frac{\varepsilon_0 l + \varepsilon_I(1+l)(1+\Delta)}{\varepsilon_\infty l + \varepsilon_I(1+l)(1+\Delta)}, \quad (2.65)$$

with

$$\Delta = \frac{W^2(l+1/2)}{l(l-1/2)(l+3/2)} \left\{ \frac{\varepsilon_0 l + \varepsilon_I(1+l)}{\varepsilon_\infty l + \varepsilon_I(1+l)} \right\}. \quad (2.66)$$

Finally, we comment on the evanescent nature of the surface modes of a sphere. In the radial direction r , the electric field components are given by

$$(E_r)_l \propto \begin{cases} (\rho_1 R)^{-1} j_l(\rho_1 R), & r < r_o \\ (\rho_2 R)^{-1} h_l^{(1)}(\rho_2 R), & r > r_o \end{cases}, \quad (2.67)$$

where $R = r/r_o$. When $W \ll 1$, the radial dependence of $(E_r)_l$, is $(E_r)_l \propto R^{l-1}$ inside the sphere and $(E_r)_l \propto R^{-(l+2)}$ outside, so that the fields decay away from the surface $r = r_o$ and become increasingly localized at the surface with increasing l . The surface nature of the modes is, thus, evident from the preceding remarks.

2.3 Surface polaritons in anisotropic media

In this section, we outline the theory of surface polaritons in anisotropic media, *i.e.*, media for which the dielectric function ε is different along one or more directions. Special focus is given to the anisotropic materials hexagonal boron nitride (hBN) and graphene. Both hBN and graphene belong to a class of materials known as *van der Waals* materials [12]. These are two-dimensional (2D) atomic crystals that can be readily stacked in a heterostructure with a precisely chosen sequence. This stacking is facilitated by the fact that these materials naturally "stick" together due to van der Waals interactions between the layers.

This section will also serve as a primer to chapter 5, in which an experimental study of the electromagnetic and transport properties of transistor devices based on the materials mentioned above, will be thoroughly presented.

2.3.1 Hyperbolic phonon-polaritons in an anisotropic semi-infinite medium

Let us consider the half-space geometry of Fig. 2.4 where the active medium consists of an anisotropic dielectric material of dielectric tensor ε_{ij} , where $i, j = 1, 2, 3$. In this case, there exist principal axes whose orientations are in general frequency dependent. If the coordinate axes coincide with these principal axes, the dielectric tensor becomes

$$\varepsilon = \begin{pmatrix} \varepsilon_x & 0 & 0 \\ 0 & \varepsilon_y & 0 \\ 0 & 0 & \varepsilon_z \end{pmatrix}. \quad (2.68)$$

We consider that the surface waves at the interface propagate in the x -direction and that the principal axes of the anisotropic medium are aligned with the Cartesian axes of Fig. 2.4 so that the dielectric tensor is given by Eq. (2.68). The wavevector in the direction of decay of the surface waves within the active medium (*i.e.*, in the z -direction), is given by

$$\alpha^2 = \frac{\varepsilon_x}{\varepsilon_z} \left(k^2 - \frac{\omega^2}{c^2} \varepsilon_z \right). \quad (2.69)$$

The z -component of the wavevector in the inactive medium can be found from Eq. (2.33).

By applying the condition $\nabla \cdot \mathbf{D} = 0$ at the boundary $z = 0$, we obtain the dispersion relation

$$\frac{\varepsilon_x}{\alpha} = -\frac{\varepsilon_I}{\alpha_I}. \quad (2.70)$$

An alternative expression for the dispersion relation can be obtained by squaring Eq. (2.70) and using Eqs. (2.69) and (2.33). This yields

$$k^2 = \frac{\omega^2}{c^2} \varepsilon_I \varepsilon_z \frac{\varepsilon_x - \varepsilon_I}{\varepsilon_x \varepsilon_z - \varepsilon_I^2}. \quad (2.71)$$

We consider now a uniaxial crystal, in which $\varepsilon_x = \varepsilon_y$, with the optic axis perpendicular to the surface, such that $\varepsilon_z = \varepsilon_{\parallel}$, and $\varepsilon_x = \varepsilon_y = \varepsilon_{\perp}$. One such crystal is hexagonal boron nitride (hBN). hBN also has the unique property that its dielectric function can be negative

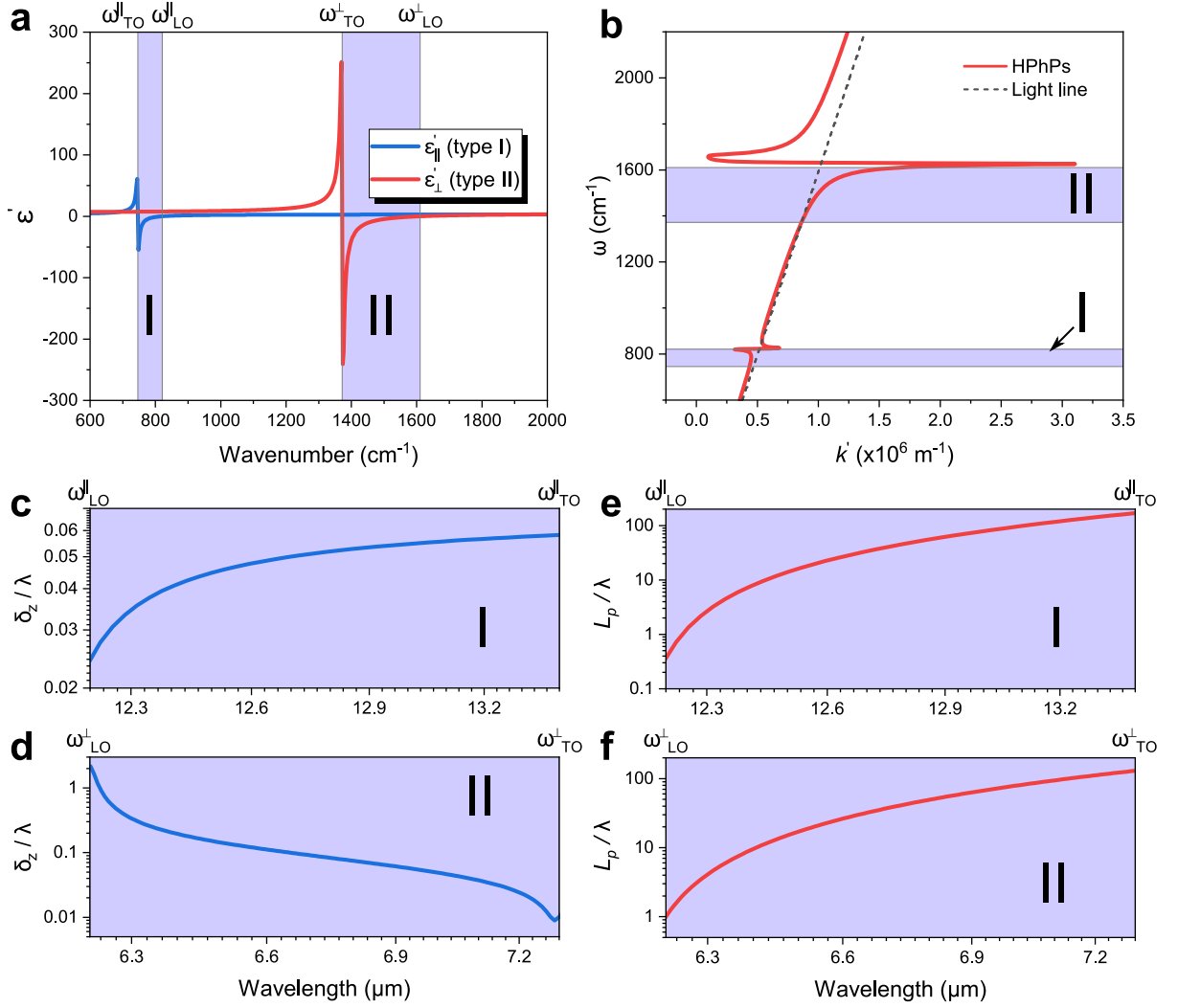


Figure 2.13: (a) Real part (ϵ') of the dielectric function of hBN, obtained by applying Eq. (2.11) for the parallel and perpendicular directions. The purple-shaded regions indicate the two *Reststrahlen* bands of hBN. The optical constants appropriate for hBN are: $\epsilon_\infty^\parallel = 2.95$, $\epsilon_0^\parallel = 3.57$, $\omega_{TO}^\parallel = 746$ cm⁻¹, $\omega_{LO}^\parallel = 820.65$ cm⁻¹, and $\gamma^\parallel = 4$ cm⁻¹, for the perpendicular direction, and $\epsilon_\infty^\perp = 4.87$, $\epsilon_0^\perp = 6.71$, $\omega_{TO}^\perp = 1372$ cm⁻¹, $\omega_{LO}^\perp = 1610.5$ cm⁻¹, and $\gamma^\perp = 5$ cm⁻¹ for the parallel direction [13] (b) Real dispersion curve (ω vs k') of an hBN half-space bound by vacuum. (c) & (d) Dimensionless penetration depth δ_z/λ , where λ is the wavelength in free space, of type I and II HPhPs in hBN. (e) & (f) Dimensionless propagation length L_p/λ of type I and II HPhPs on the hBN surface.

either in the x - or z -direction¹⁰, *i.e.*, $\epsilon_x\epsilon_z < 0$, in its two *Reststrahlen* bands at mid-infrared frequencies (see Fig. 2.13 (a)). In the material's *Reststrahlen* bands, the isofrequency surface: $(k_x^2 + k_y^2)/\epsilon_z + k_z^2/\epsilon_x = (\omega/c)^2$ [14], is an open hyperboloid, which is an open surface, in stark contrast to the closed spherical dispersion in an isotropic medium. Thus, hBN belongs to a class of materials known as *hyperbolic materials*.

¹⁰More generally stated, the dielectric function can be negative either in the in-plane direction (\perp to z -axis) or the out-of-plane direction (\parallel to z -axis) since the x and y -directions are equivalent here.

The dispersion relation (2.71) can then be rewritten in the following form for a uniaxial crystal

$$k^2 = \frac{\omega^2}{c^2} \varepsilon_I \varepsilon_{\parallel} \frac{\varepsilon_{\perp} - \varepsilon_I}{\varepsilon_{\perp} \varepsilon_{\parallel} - \varepsilon_I^2}. \quad (2.72)$$

Note that in this case, all directions of propagation in the xy -plane are equivalent.

The normal modes resulting from Eq. (2.72) for an hBN half-space bound by vacuum are plotted in Fig. 2.13 (b). The surface modes that exist within the two *Reststrahlen* bands are termed here *hyperbolic surface phonon-polaritons* (HPhPs), due to the hyperbolic nature of hBN. The HPhP modes within the low-frequency *Reststrahlen* band ($\omega_{\text{TO}}^{\parallel} < \omega < \omega_{\text{LO}}^{\parallel}$), where only one component of the tensor ε' is negative, are referred to as *type I* HPhPs while that of the high-frequency *Reststrahlen* band ($\omega_{\text{TO}}^{\perp} < \omega < \omega_{\text{LO}}^{\perp}$), where the x and y components of the tensor ε' are negative, are called *type II* HPhPs. The penetration depth and propagation length of the HPhP modes are subsequently calculated from Eqs. (2.69) and (2.45) and shown in Figs. 2.13 (c-f).

For the most part, the properties of the surface modes in an hBN half-space have already been thoroughly discussed in subsection 2.2.1. We will only make note here of a few subtle differences between the type I and II HPhPs. Strikingly, type I HPhPs have negative dispersion, that is, the dispersion branch tends to lower frequencies with increasing wavevector, while type II HPhPs have positive dispersion (see Fig. 2.13 (b)). Similar contrasting behavior is observed when comparing the penetration depths of type I and II HPhPs (Figs. 2.13 (c) and (d)). While the penetration depth of type I HPhPs decreases monotonically from $\omega_{\text{TO}}^{\parallel}$ to $\omega_{\text{LO}}^{\parallel}$, that of type II HPhPs increases monotonically from $\omega_{\text{TO}}^{\perp}$ to $\omega_{\text{LO}}^{\perp}$. Since type I HPhPs exist in the low-frequency *Reststrahlen* band, they are associated with smaller wavevectors as compared to type II HPhPs¹¹ (see Fig. 2.13 (b)). However, the propagation length of both types of HPhPs follows the same trend and, on average, is on the same order compared to the wavelength (see Figs. 2.13 (e) and (f)).

2.3.2 Surface plasmon-polaritons in free-standing graphene

Graphene is an anisotropic material consisting of a 2D sheet of carbon atoms. It is usually fabricated as a mono- or multi-layer sheet that is either suspended or placed on a substrate. Doped graphene has been shown to support surface plasmon-polaritons (SPPs) [15] which are characterized by a low-loss nature at infrared frequencies [16].

Analogously to the polar dielectrics and metals discussed heretofore, whose response to electromagnetic fields is described by their dielectric function, graphene's influence can be entailed through the inclusion of its sheet conductivity σ . For low energies ($\hbar\omega \ll E_F$, where E_F is the *Fermi energy*), the sheet conductivity of graphene is given by the *Drude conductivity*, σ_D as follows [17]

$$\sigma(\omega) = \sigma_D(\omega) = \frac{E_F e^2}{\pi \hbar} \frac{i}{\hbar(\omega + i\Gamma)}. \quad (2.73)$$

¹¹About one order of magnitude smaller.

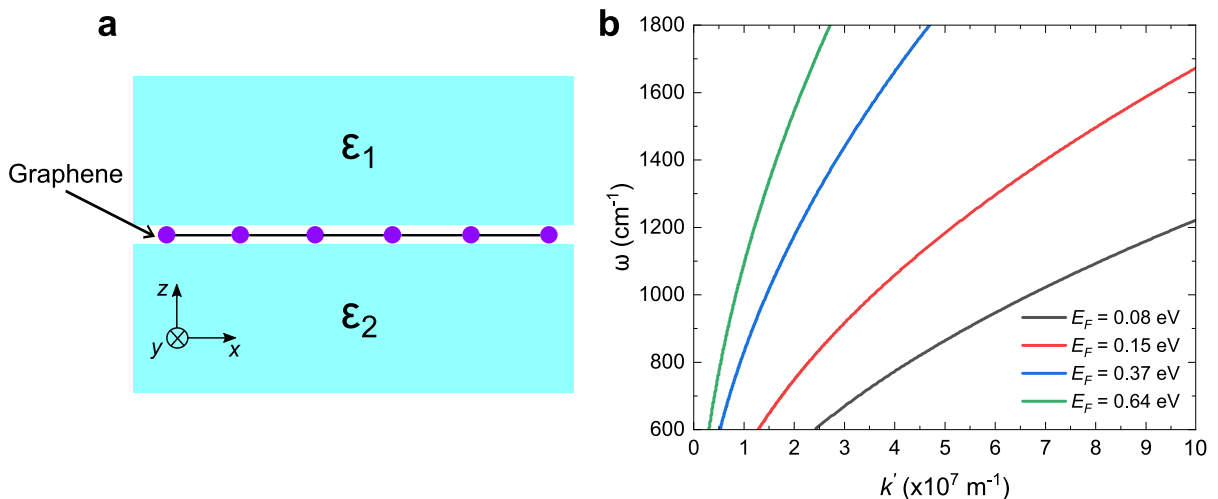


Figure 2.14: (a) sketch of a monolayer graphene encapsulated between two semi-infinite media of dielectric constants ϵ_1 and ϵ_2 . (b) Dispersion curves of free-standing graphene in vacuum for various Fermi energies (E_F) for electron mobility $\mu_e = 10^4 \text{ cm}^2/\text{V.s}$.

In the above relation, $\Gamma = ev_F^2/\mu_e E_F$, represents the phenomenological scattering rate or damping constant of electrons due to impurity scattering, in which μ_e is the electron mobility, and v_F is the Fermi velocity.

In general, the sheet conductivity of graphene can be cast in the following form [18, 19]

$$\sigma(k, \omega) = -\frac{ie^2}{4\hbar} \frac{\xi}{\sqrt{v_F^2 k^2 - \xi^2}} \left[1 + G\left(\frac{\hbar\xi + 2E_F}{\hbar v_F k}\right) - G\left(\frac{\hbar\xi - 2E_F}{\hbar v_F k}\right) \right] - \frac{2i}{\pi} \frac{e^2 \omega E_F}{(\hbar v_F k)^2}, \quad (2.74)$$

where, $G(\eta) = -\frac{1}{\pi}(\eta\sqrt{1-\eta^2} - \cos^{-1}(\eta))$, and $\xi = \omega + i\frac{\Gamma}{\hbar}$.

The dependence on the wavevector k is explicit in Eq. (2.74), while in (2.73) the k -dependence is included through the dispersion relation $\omega(k)$. The dispersion relation of SPPs in graphene sandwiched between two semi-infinite media of dielectric functions ϵ_1 and ϵ_2 (Fig. 2.13 (a)), is given by [17]

$$\frac{\epsilon_1}{\alpha_1} + \frac{\epsilon_2}{\alpha_2} + \frac{i\sigma(k, \omega)}{\omega\epsilon_0} = 0, \quad (2.75)$$

where, $\alpha_j = \sqrt{k^2 - \epsilon_j \frac{\omega^2}{c^2}}$, ($j = 1, 2$), gives the wavevector component in the z -direction for medium j , $k = k' + ik''$ is the wavevector in the direction of propagation of the surface plasmons, $\epsilon_0 = 8.854 \times 10^{-12} \text{ F/m}$ is the permittivity of free space, and $\sigma(k, \omega)$ is found from Eq. (2.73) or (2.74).

The dispersion curve, obtained by solving Eq. (2.75) for a free-standing mono-layer graphene in vacuum, is shown in Fig. 2.14 (b) for various Fermi energies, E_F , at a typical electron mobility value of $10^4 \text{ cm}^2/\text{V.s}$. The key feature to note from the dispersion curves of Fig. 2.14 (b), is the fact that surface polariton modes in graphene are associated with extremely large wavevectors¹².

¹²Reaching as high as two orders of magnitude larger than that of semi-infinite polar dielectric crystals.

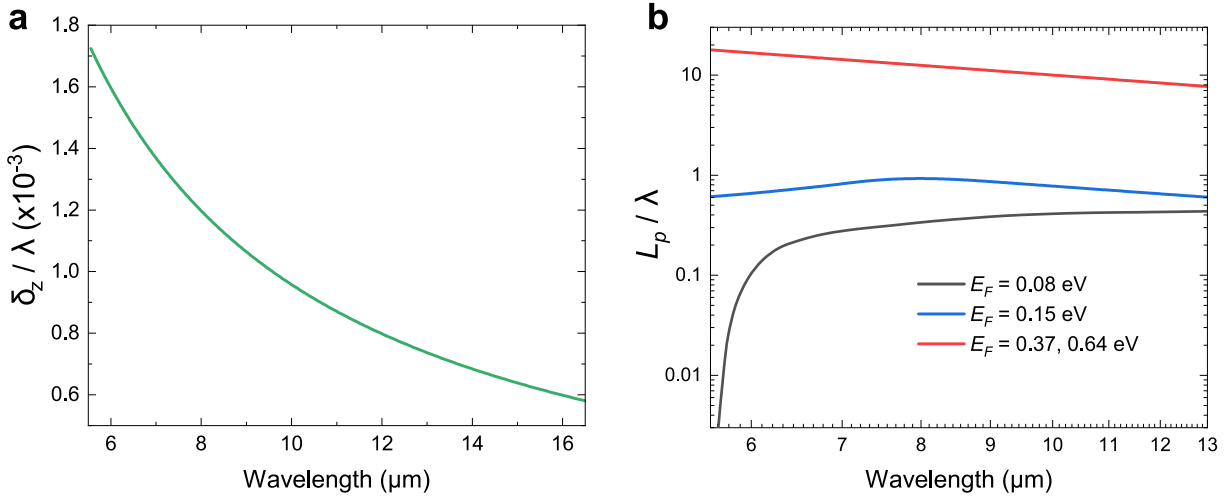


Figure 2.15: (a) Dimensionless penetration depth δ_z/λ of surface plasmons of a free-standing graphene in vacuum for $0.08 \leq E_F \leq 0.64$ eV. The curves for different Fermi energies are overlapping so that a single curve appears in panel (a). (b) Dimensionless propagation length L_p/λ of SPPs in free-standing graphene in vacuum for various Fermi energies. The value for the electron mobility is taken to be $\mu_e = 10^4$ cm²/V.s.

This is a direct consequence of the 2D nature of graphene and the absence of defects. Like SPhPs in polar dielectric crystals, the dispersion curve of surface plasmons in graphene increases monotonically from lower frequencies towards an asymptotic value at which several large wavevector modes exist. It is clear from Fig. 2.14 (b), however, that the asymptotic value for SPPs in free-standing graphene is reached at frequencies much higher than the mid-IR frequencies considered here.

Figure 2.15 illustrates the behavior of the surface plasmon penetration depth (panel (a)) and propagation length (panel (b)) in free-standing graphene in vacuum as a function of Fermi energy. The surface plasmons of graphene in vacuum are extremely localized at the surface, penetrating the surrounding vacuum to a depth of only ~ 9.58 nm that is constant with respect to the Fermi energy (see Fig. 2.15 (a)). The plasmon propagation length, on the other hand, varies between 9.56 nm $< L_p < 768$ nm for low Fermi energies ($E_F \leq 0.15$ eV) and increases, at higher Fermi energies ($E_F \geq 0.37$ eV), to about 100 μ m on average (Fig. 2.15 (b)).

2.4 Hexagonal boron nitride (hBN)/graphene heterostructures

As mentioned in the beginning of section 2.3, van der Waals materials can be stacked together in a heterostructure. We will examine in this section some common examples of these heterostructures. Particularly, we will concern ourselves here with the polariton modes that can arise in such systems.

2.4.1 hBN thin film on a substrate

We begin by considering a thin hBN film of thickness d on a substrate as sketched in Fig. 2.16. A widely used substrate for preparing thin hBN flakes is SiO₂, due to its compatibility with most

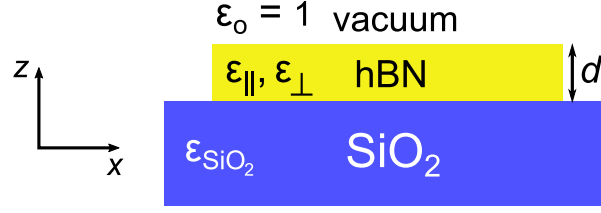


Figure 2.16: Sketch of an hBN thin film of thickness d placed on an SiO_2 substrate.

hBN exfoliation techniques. In practice, the SiO_2 substrates that are used in this manuscript, are composed of an amorphous SiO_2 layer with a thickness of ~ 285 nm on top of a bulk silicon (Si) layer. If we consider, for the moment, the SiO_2 thin film on the Si substrate only, then, as we have seen in subsection 2.2.2, the SPhPs supported by this layered system should exhibit two polariton branches ω_+ and ω_- with large k asymptotic values reached when $\text{Re}(\varepsilon_{\text{SiO}_2}) = -1$ for the upper polariton ω_+ , and $\text{Re}(\varepsilon_{\text{SiO}_2}) = -\varepsilon_{\text{Si}} = -11.7$ for the lower polariton branch ω_- (see Fig. 2.10 (b)).

Nevertheless, the large damping inherent to amorphous SiO_2 precludes the excitation of the lower polariton branch, as the lowest value of the real part of $\varepsilon_{\text{SiO}_2}$ is $\min\{\text{Re}(\varepsilon_{\text{SiO}_2})\} \approx -4$ (see Fig. 2.1 (c)). The polariton response, in this case, is independent of the SiO_2 layer thickness, *i.e.*, the response is the same as that of bulk SiO_2 . Thus, in order to fully describe the polaritonic response of such samples, it is sufficient to consider a three-layered vacuum/hBN/ SiO_2 structure.

An alternative approach to that presented in subsection 2.2.2 to obtain the dispersion curves of surface polaritons, is to evaluate the poles of the reflection coefficient r_p of the multi-layer system for p -polarized light. The reflection coefficient r_p for the multi-layer structure of Fig. 2.16 is given by [20]

$$r_p = \frac{r_0 + r_1 e^{2i\alpha_1 d}}{1 + r_0 r_1 e^{2i\alpha_1 d}}, \quad (2.76)$$

where,

$$r_0 = \frac{\varepsilon_{\perp} \alpha_0 - \varepsilon_0 \alpha_1}{\varepsilon_{\perp} \alpha_0 + \varepsilon_0 \alpha_1} \quad (2.77)$$

$$r_1 = \frac{\varepsilon_{\text{SiO}_2} \alpha_1 - \varepsilon_{\perp} \alpha_2}{\varepsilon_{\text{SiO}_2} \alpha_1 + \varepsilon_{\perp} \alpha_2}. \quad (2.78)$$

In the above formulae, r_0 and r_1 are the reflection coefficients at the vacuum/hBN and hBN/ SiO_2 interfaces, respectively. $\alpha_0 = \sqrt{\varepsilon_0 \frac{\omega^2}{c^2} - k^2}$, $\alpha_1 = \sqrt{\varepsilon_{\perp} \frac{\omega^2}{c^2} - \frac{\varepsilon_{\perp}}{\varepsilon_{\parallel}} k^2}$, and $\alpha_2 = \sqrt{\varepsilon_{\text{SiO}_2} \frac{\omega^2}{c^2} - k^2}$ give the z -components of the wavevector in vacuum, hBN, and SiO_2 , respectively, and k is the wavevector along the direction of propagation of HPhPs.

The dispersion curves of HPhPs can be visualized from the maxima of $\text{Im}(r_p)$ for real k , as shown in Fig. 2.17 (a) for a 135 nm hBN film on SiO_2 . One can see from the plot, that several dispersion branches appear within the two *Reststrahlen* bands of hBN. The hBN thickness considered here is on the order of a few hundred atomic layers (~ 375 layers), so that, the multiple HPhP branches observed result from Fabry-Perot resonances confined between the two

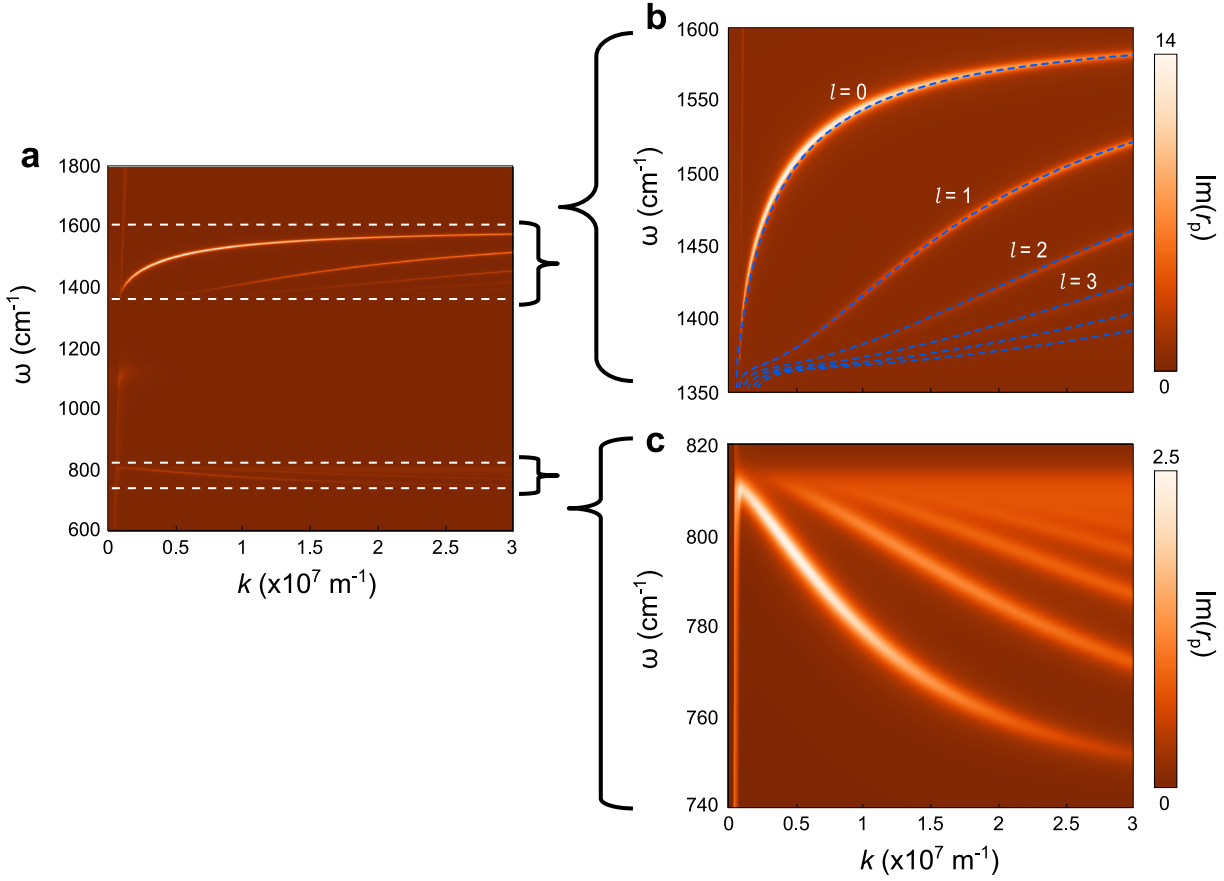


Figure 2.17: (a) Color map of the imaginary part of the reflection coefficient ($\text{Im}(r_p)$) given by Eq. (2.76) for $d = 135$ nm. The branches resulting from the maxima of $\text{Im}(r_p)$ correspond to the various dispersion curves of the HPhP modes of the hBN thin film. (b) and (c) Zooms of the two *Reststrahlen* bands of hBN, marked by the white dashed lines in panel (a). The blue dashed lines in panel (b) were obtained by solving Eq. (2.79) for multiple values of l .

interfaces of the hBN thin film. By comparing Fig. 2.17 (b) and (c), it can be seen that the branches of type I (Fig. 2.17 (c)) and II (Fig. 2.17 (b)) HPhPs have contrasting dispersion as discussed in subsection 2.3.1. One can also observe in Fig. 2.17 (a) a weak resonance around 1130 cm^{-1} , attributed to the polariton resonance of the SiO_2 substrate (see subsection 2.2.1).

Analytically, one can account for the multiple HPhP branches observed in Fig. 2.17 (a) as quantized modes of order $l = 0, 1, 2, 3, \dots$, described by the following formula [20]

$$k_l = -\frac{\psi}{d} \left[l\pi + \tan^{-1} \left(\frac{\varepsilon_0}{\varepsilon_{\perp} \psi} \right) + \left(\frac{\varepsilon_{\text{SiO}_2}}{\varepsilon_{\perp} \psi} \right) \right], \quad (2.79)$$

in which

$$\psi = -i \frac{\sqrt{\varepsilon_{\parallel}}}{\sqrt{\varepsilon_{\perp}}}. \quad (2.80)$$

The dispersion curves of HPhPs of the air/hBN/ SiO_2 heterostructure can thus be obtained by solving Eq. (2.79) for $k = k' + ik''$. One can verify the equivalence of the two methods of obtaining the dispersion curves illustrated above, by comparing, for instance, the resulting

type II HPhP branches in each case (cf. Fig. 2.17 (b), blue dashed curves and bright color plot curves).

From Fig. 2.17 (b), we can see that the lowest order HPhP mode ($l = 0$) has an asymptotic frequency of $\omega_\infty \sim 1580 \text{ cm}^{-1}$. Higher order modes ($l \geq 1$) have a lower asymptotic frequency that decreases with increasing l , down to the edge of the *Reststrahlen* band, near ω_{TO} . It is clear, nonetheless, that the higher-order HPhP modes reach their asymptotic frequency at larger wavevectors k .

2.4.2 Graphene on hBN

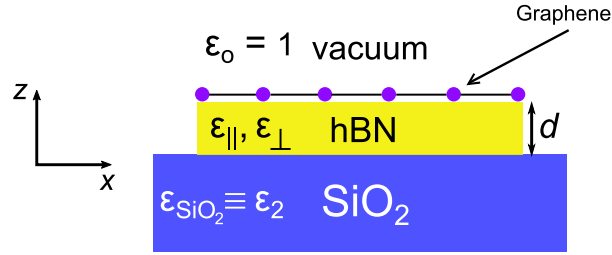


Figure 2.18: Sketch of the geometry and notation of the vacuum/graphene/hBN/SiO₂ heterostructure.

We will now study the effect of adding a graphene layer on top of the hBN thin film structure of the previous subsection (Fig. 2.18). The stack of layers in this heterostructure can be divided into three regions: $z > 0$ ($j = 0$, vacuum), $-d < z < 0$ ($j = 1$, hBN), and $z < -d$ ($j = 2$, SiO₂), where d is the thickness of the hBN layer.

In this case, the total reflection coefficient for p -polarized waves can be written as follows [19]

$$r_p = \frac{r_{01} + r_{12}(1 - r_{01} - r_{10})e^{2i\alpha_1 d}}{1 - r_{10}r_{12}e^{2i\alpha_1 d}}, \quad (2.81)$$

where,

$$r_{01} = \frac{Q_1 - Q_0 + S}{Q_1 + Q_0 + S}, \quad r_{10} = \frac{Q_0 - Q_1 + S}{Q_1 + Q_0 + S}, \quad r_{12} = \frac{Q_2 - Q_1}{Q_1 + Q_2}, \quad r_{21} = \frac{Q_1 - Q_2}{Q_1 + Q_2}, \quad (2.82)$$

$$\alpha_j = \sqrt{\varepsilon_j^\perp \left(\frac{\omega^2}{c^2} - \frac{k^2}{\varepsilon_j^\parallel} \right)}, \quad \text{Im}(\alpha_j) > 0, \quad Q_j = \frac{\varepsilon_j^\perp}{\alpha_j}, \quad \text{and}, \quad S = \frac{1}{\varepsilon_0} \frac{\sigma(k, \omega)}{\omega}.$$

The influence of graphene on the response of the heterostructure in Fig. 2.18 is added through the parameter $S \propto \sigma(k, \omega)$ in (2.82), in which $\sigma(k, \omega)$ is the sheet conductivity of graphene (see subsection 2.3.2).

The dispersion curves, based on Eq. (2.81), for a 60 nm-thick hBN film are visualized in Fig. 2.19, with and without graphene. Fig. 2.19 (a) represents the typical multi-branch HPhP response of an hBN thin film observed in subsection 2.4.1. Fig. 2.19 (b), on the other hand, presents the dispersion of the new hyperbolic plasmon–phonon polariton (HPPP) modes of the graphene/hBN heterostructure, that arise from the mixing of the surface plasmons of graphene

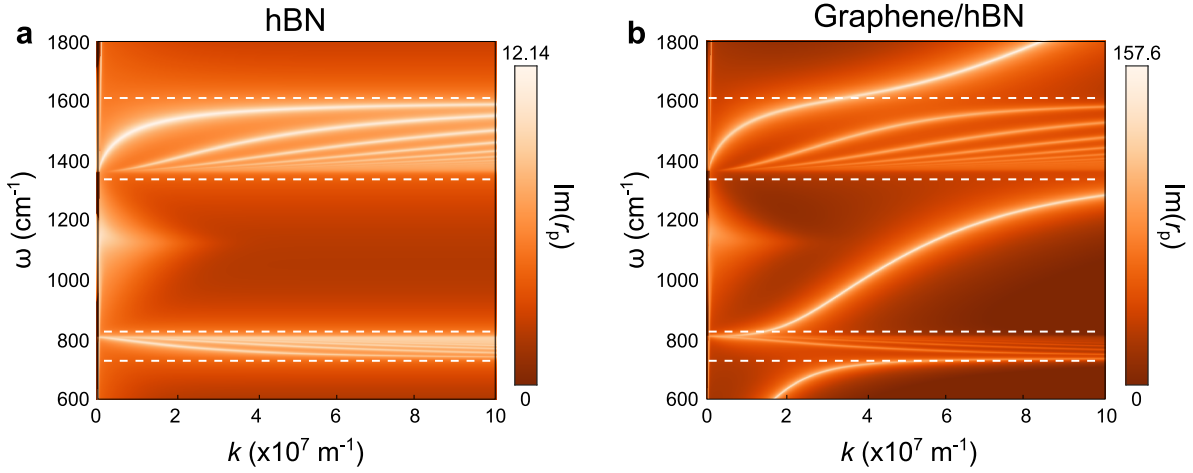


Figure 2.19: (a) Dispersion branches of a 60 nm hBN thin film on SiO₂ (b) Dispersion branches of the graphene/hBN heterostructure of Fig. 2.18 for $d = 60$ nm, $E_F = 0.37$ eV and $\mu_e = 10^4$ cm²/V.s. The dashed white lines enclose the two *Reststrahlen* bands of hBN.

and the HPhPs of hBN. The modification of the hyperbolic response by graphene is clearly manifested in the blue-shift of the HPPP frequencies with respect to those of the HPhPs (cf. Figs. 2.19 (a) and (b)). This is particularly obvious for the lowest-order hyperbolic branch ($l = 0$). The shift of momenta (at a fixed frequency) is opposite in the two hyperbolic bands: negative in the type II band and positive in the type I band [19]. This contrasting behavior stems from the polariton dispersion being negative and positive in the type I and II regions, respectively. The change in the polariton wavelength induced by graphene can be described by the following equation

$$\Delta\lambda = \frac{\lambda_{\text{HPPP}} - \lambda_{\text{HPhP}}}{\lambda_{\text{HPhP}}} \approx \frac{\lambda_p}{\pi d} \frac{\varepsilon_{\parallel}}{1 - \varepsilon_{\parallel}\varepsilon_{\perp}}, \quad (2.83)$$

where λ_{HPPP} and λ_{HPhP} are the wavelengths of HPPPs and HPhPs, respectively, and $\lambda_p = 2\pi/k_p$ is the plasmon wavelength of graphene. Using this formula, it has been shown that the influence of graphene remains substantial in hBN as thick as $d = 300$ nm [19].

2.4.3 Encapsulated graphene

We can take the discussion of subsection 2.4.2 a step further by adding a thin hBN capping layer on top of the graphene layer so that it is encapsulated between two hBN thin films of thicknesses d_1 and d_2 (Fig. 2.20). The formalism of subsection 2.4.2 can easily be generalized to accommodate the additional top hBN layer. Following the same notation as before, the vacuum/hBN/graphene/hBN/SiO₂ heterostructure of Fig. 2.20 can be divided into four regions: $z > 0$ ($j = 0$, vacuum), $-d_1 < z < 0$ ($j = 1$, hBN), $-d_1 - d_2 < z < -d_1$ ($j = 2$, hBN), and $z < -d_1 - d_2$ ($j = 3$, SiO₂). The total reflection coefficient of the structure can then be obtained by adding the two hBN thin films successively, using Eq. (2.81). The reflection coefficient for the first film is written as

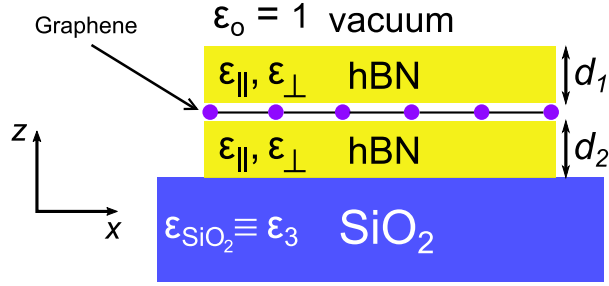


Figure 2.20: Sketch of a graphene layer encapsulated between two hBN thin films of thicknesses d_1 and d_2 .

$$r_p^1 = \frac{r_{12} + r_{23}(1 - r_{12} - r_{21})e^{2i\alpha_2 d_2}}{1 - r_{21}r_{23}e^{2i\alpha_2 d_2}}. \quad (2.84)$$

The addition of the second film yields the total reflection coefficient of the stack:

$$r_p^{\text{total}} = \frac{r_{01} + r_p^1(1 - r_{01} - r_{10})e^{2i\alpha_1 d_1}}{1 - r_{10}r_p^1 e^{2i\alpha_1 d_1}}. \quad (2.85)$$

In the above two equations, $r_{12} = (Q_2 - Q_1 + S)/(Q_2 - Q_1 + S)$, $r_{21} = (Q_1 - Q_2 + S)/(Q_2 - Q_1 + S)$, S , r_{ij} ($ij \neq 12, 21$), and α_j , can all be obtained as in (2.82).

As presented in Fig. 2.21, the dispersion branches of the HPPP modes of this heterostructure, exhibit the same behavior as in subsection 2.4.2. However, the influence of graphene, in this case, becomes important only for high Fermi energies ($E_F \geq 0.37$ eV) and is almost completely negligible when the graphene is close to neutrality (see Fig. 2.21, $E_F = 0.03$ eV).

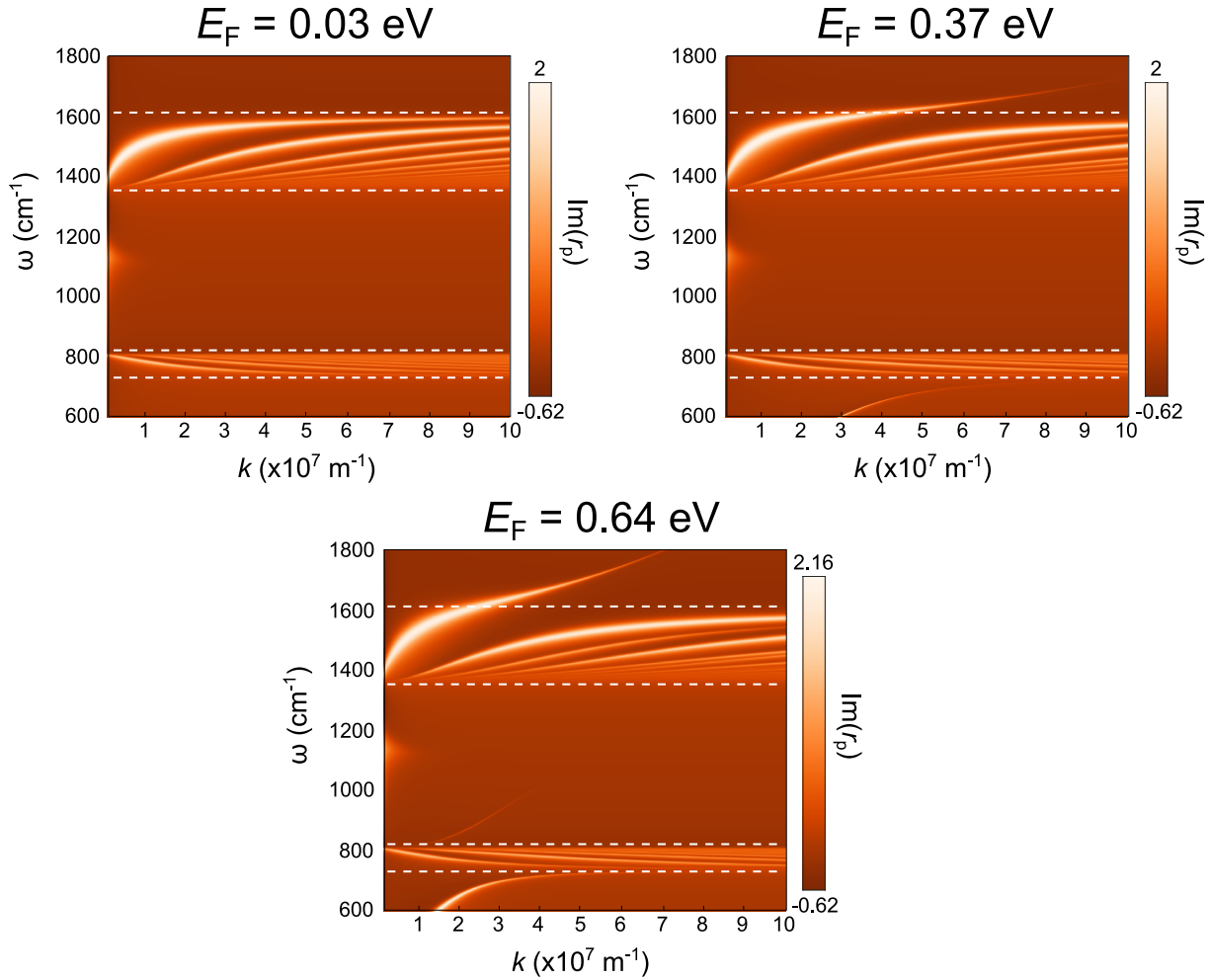


Figure 2.21: Dispersion curves of the hBN/graphene/hBN heterostructure, with hBN thickness $d_1 = 50$ nm and $d_2 = 30$ nm, for $\mu_e = 60,000$ cm²/V.s at three different values of the Fermi energy E_F . The dashed white lines enclose the two *Reststrahlen* bands of hBN.

2.5 Conclusion

We have presented in this chapter the local dielectric continuum theory of surface optical excitations in polar dielectric crystals. A cornucopia of polaritonic structures was introduced and discussed. We began by illustrating the surface modes of a polar semi-infinite medium, which was followed by a treatment of surface polaritons in the thin film and sphere geometries. The second part of this chapter was dedicated to the theory of surface polaritons in anisotropic materials, namely, in graphene and hBN. We have seen that surface polaritons consist of large wavevector modes whose dispersion has an asymptotic frequency at which many large- k modes exist. The abundance of surface modes at this frequency, along with their long propagation lengths, which can be several times the wavelength, are at the basis of many spectral and spatial coherence phenomena that can be observed in the near-field. The theory outlined in this chapter and the discussion therein, form the groundwork upon which the experimental studies of the following chapters are based. In the next chapter, we will experimentally probe the spectral signatures of the polaritonic structures discussed here, using techniques, such as scattering-scanning near-field

optical microscopy and infrared spatial modulation spectroscopy.

References

- [1] R Carminati and JJ Greffet. “Near-field effects in spatial coherence of thermal sources”. *Phys. Rev. Lett.* 82.8 (1999), p. 1660.
- [2] JJ Greffet, R Carminati, K Joulain, JP Mulet, S Mainguy, and Y Chen. “Coherent emission of light by thermal sources”. *Nature* 416.6876 (2002), pp. 61–64.
- [3] K Joulain, JP Mulet, F Marquier, R Carminati, and J-J Greffet. “Surface electromagnetic waves thermally excited: Radiative heat transfer, coherence properties and Casimir forces revisited in the near field”. *Surf. Sci. Rep.* 57.3-4 (2005), pp. 59–112.
- [4] Lord Rayleigh. “On waves propagated along the plane surface of an elastic solid”. *Proc. London Math. Soc.* 1.1 (1885), pp. 4–11.
- [5] KL Kliever and R Fuchs. *Theory of dynamical properties of dielectric surfaces*. Vol. 27. Wiley, UK, 1974.
- [6] ED Palik. *Handbook of optical constants of solids*. Vol. 3. Academic press, 1998.
- [7] RH Lyddane, RG Sachs, and E Teller. “On the polar vibrations of alkali halides”. *Phys. Rev.* 59.8 (1941), p. 673.
- [8] S Collin, F Pardo, and JL Pelouard. “Waveguiding in nanoscale metallic apertures”. *Opt. Express* 15.7 (2007), pp. 4310–4320.
- [9] SA Maier. *Plasmonics: fundamentals and applications*. Vol. 1. Springer, 2007.
- [10] R Fuchs and KL Kliever. “Optical modes of vibration in an ionic crystal sphere”. *J. Opt. Soc. Am.* 58.3 (1968), pp. 319–330.
- [11] H Fröhlich. “Theory of Dielectrics: Oxford Univ”. 1949, pp. 149–155.
- [12] AK Geim and IV Grigorieva. “Van der Waals heterostructures”. *Nature* 499.7459 (2013), pp. 419–425.
- [13] Y Cai, L Zhang, Q Zeng, L Cheng, and Y Xu. “Infrared reflectance spectrum of BN calculated from first principles”. *Solid State Commun.* 141.5 (2007), pp. 262–266.
- [14] Y Guo, W Newman, CL Cortes, and Z Jacob. “Applications of hyperbolic metamaterial substrates”. *Adv. OptoElectron.* 2012 (2012).
- [15] M Bordag and IG Pirozhenko. “Surface plasmons for doped graphene”. *Phys. Rev. D* 91.8 (2015), p. 085038.
- [16] M Jablan, H Buljan, and M Soljačić. “Plasmonics in graphene at infrared frequencies”. *Phys. Rev. B* 80.24 (2009), p. 245435.
- [17] MS Ukhtary and R Saito. “Surface plasmons in graphene and carbon nanotubes”. *Carbon* 167 (2020), pp. 455–474.
- [18] B Wunsch, T Stauber, F Sols, and F Guinea. “Dynamical polarization of graphene at finite doping”. *New J. Phys.* 8.12 (2006), p. 318.
- [19] S Dai, Q Ma, MK Liu, T Andersen, Z Fei, MD Goldflam, M Wagner, K Watanabe, T Taniguchi, M Thiemens, et al. “Graphene on hexagonal boron nitride as a tunable hyperbolic metamaterial”. *Nat. Nanotechnol.* 10.8 (2015), pp. 682–686.

- [20] S Dai, Z Fei, Q Ma, AS Rodin, M Wagner, AS McLeod, MK Liu, W Gannett, W Regan, K Watanabe, et al. “Tunable phonon polaritons in atomically thin van der Waals crystals of boron nitride”. *Science* 343.6175 (2014), pp. 1125–1129.

Chapter 3

Experimental study of surface polaritons in dielectric media

As we have seen in the previous chapter, surface optical excitations making up the near-field of polar dielectric crystals, are confined to a distance $\sim \lambda$ near the surface. Their experimental detection, therefore, requires the utilization of a near-field probe capable of coupling the near-field evanescent modes of the surface to outgoing propagating waves. The resulting outgoing waves can then be detected with a detector placed in the far-field of the sample. In this chapter, we will discuss near-field detection techniques at length and present experimental measurements of the near-field spectral response of various polar and hyperbolic dielectric crystals. We will also present a novel near-field spectroscopy technique based on the combination of local scatterers with a far-field detection method. The last part of this chapter is devoted to the experimental study of the far-field thermal radiation of subwavelength (sub- λ) polar dielectric spheres.

3.1 Near-field microscopy techniques

Ernst Abbe in 1873 [1] and Lord Rayleigh in 1879 [2] studied the required angular separation between two objects for their images to be resolved by an optical imaging system. They concluded that the resolution of a conventional microscope is diffraction limited such that the smallest resolvable distance is approximately $\lambda/2n$, where λ is the wavelength in vacuum and n is the refractive index of the medium. From an experimentalist's point of view, this limit can be rather disheartening as even with the use of an oil immersion lens ($n \approx 1.5$), the imaging sharpness would still be limited to the order of a wavelength.

The concept of near-field imaging was first introduced in 1928 by Synge, in which he proposed the use of a sub- λ aperture, as small as 10 nm in diameter, to introduce light to a section of the sample, placed within a 10 nm distance, which could move in its plane with a step size less than 10 nm [3]. By measuring the transmitted light with a photoelectric cell and a microscope, an *ultra-microscopic image* could be constructed. Following up on his original work, Synge subsequently illustrated the idea of using piezoelectricity in microscopy in a 1932 paper [4]. It

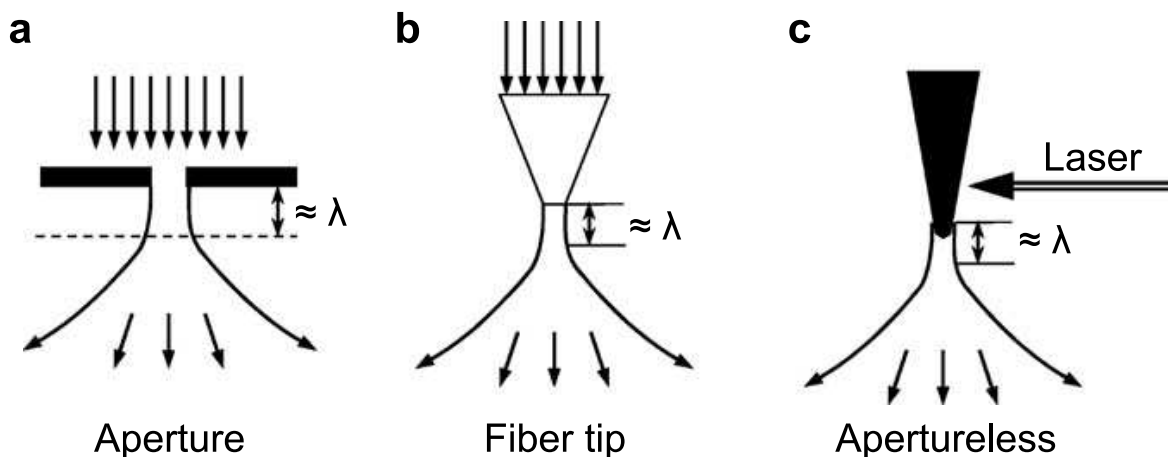


Figure 3.1: Schematic illustration of different scanning near-field optical microscopy (SNOM) techniques reproduced from ref. [6]. (a) Aperture on an opaque plate. (b) Aperture at the end of a coated optical fiber. (c) Apertureless- or scattering-SNOM with a laser-illuminated metallic tip. The opening or the tip is much smaller than the wavelength λ . The electric field is highly collimated in the near-field within a distance of λ and diverges as the distance increases.

was many years later, however, that near-field imaging was experimentally demonstrated in a seminal work entitled "Super-resolution aperture scanning microscope" [5]. The authors of this experimental study demonstrated near-field imaging with a resolution of $\lambda/60$ using 10 GHz microwave radiation ($\lambda = 3$ cm). With the advent and development of various piezoelectric elements, light sources, and optical fibers, near-field microscopy techniques, such as scanning near-field optical microscopy (SNOM), have become common-place in our present time. SNOM has become a powerful tool in the study of fundamental space- and time-dependent processes with a spatial resolution less than 50 nm. Many SNOM setups use an aperture to focus light onto a sub- λ region of the sample and are combined with an atomic force microscope (AFM) for highly controllable movement and position sensing. An alternative approach is to use a metallic AFM tip to couple the far-field radiation with the near-field electromagnetic waves in a sub- λ region underneath the tip. This is the so-called *apertureless* SNOM, which does not require an optical fiber or an aperture. This technique will hereafter be referred to as *scattering-scanning near-field optical microscopy* or s-SNOM.

Figure 3.1 illustrates the three most common SNOM designs. The first is an aperture-based setup, where a very small opening is formed on an opaque plate and collimated light is incident from above. The second is based on a tapered optical fiber whose tip serves as an aperture. The third is the s-SNOM setup that uses a sharp metallic (or dielectric) tip, which reflects (scatters) the incident laser light. All three designs have one thing in common. The light is confined to a narrow region whose width may be much less than a wavelength. Furthermore, the electromagnetic field within one wavelength distance is very intense and highly collimated. In the near-field region, evanescent waves dominate. Because the amplitude of an evanescent wave decays exponentially away from the aperture or tip, the far-field, or the radiation field diverges and becomes very weak. In the following, we will focus solely on the s-SNOM technique.

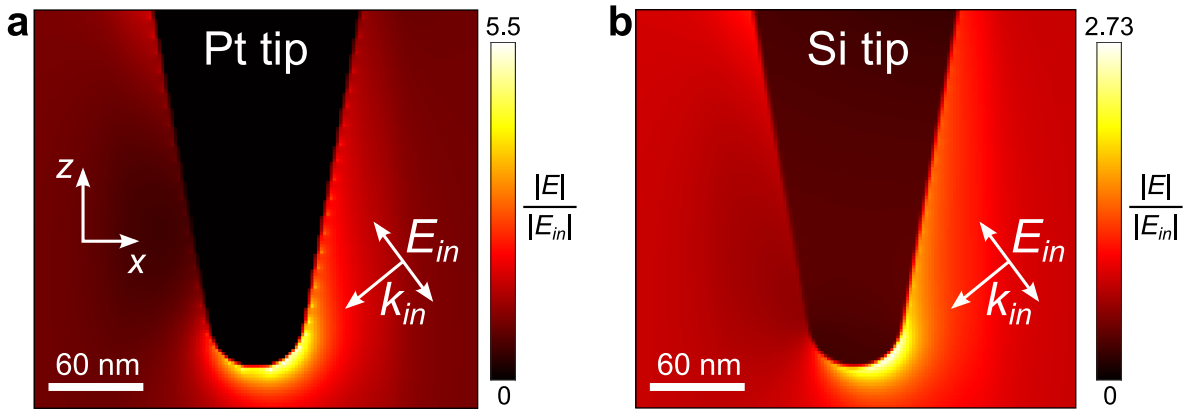


Figure 3.2: Finite-difference time-domain (FDTD) simulations of the electric field enhancement, $|\mathbf{E}|/|\mathbf{E}_{in}|$, in the near-field of a scattering tip illuminated by a laser beam with an incident field amplitude $|\mathbf{E}_{in}|$. The laser beam is considered to be a monochromatic Gaussian beam with $\lambda_{\text{Laser}} = 10.6 \mu\text{m}$ that is focused onto the tip with a focusing objective of numerical aperture, $\text{NA} = 0.46$. The incident field \mathbf{E}_{in} is polarized along the z -axis and the wavevector k_{in} giving the direction of propagation of the field is angled at 60° from the z -axis. The tip apex is assumed to have a radius of curvature $a = 30 \text{ nm}$. Panel (a) shows the simulation result for a platinum (Pt) tip with $\epsilon_{\text{Pt}} = -1450.7 + 1051i$ and panel (b) shows the result for a silicon (Si) tip with $\epsilon_{\text{Si}} = 11.7$. Further details on the FDTD simulations presented in this figure can be found in Appendix B.

The tip of an s-SNOM allows high-intensity laser energy to be focused to nanoscale dimensions. This is more clearly demonstrated in Fig 3.2, which simulates the electric field enhancement in the near-field of an illuminated tip. As seen from the figure, a large field enhancement over the intensity of the irradiating light is found at the tip apex. This *lightning-rod effect*¹ results in the focusing of the irradiated light at nanometric length scales, determined by the size of the tip apex. When brought into close proximity with a sample surface, the tip then can excite the evanescent fields of the sample while simultaneously acting as a sub- λ scatterer, scattering the sample's near-fields to the far-field. One can think of the tip in this context as a sub- λ grating coupling large wavevector modes with $k \sim 1/a$ to propagating modes, where a is the radius of the tip apex.

Finally, the comparison between Figs. 3.2 (a) and (b) reveals that a metallic tip with its characteristic short penetration depth (see subsection 2.1.2), leads to a larger field enhancement at the tip apex as compared to a dielectric tip. It is evident from Fig. 3.2 (b) that the fields penetrate deeper into the dielectric tip as the field inside the tip is non-zero (we calculate a field amplitude of $0.23|\mathbf{E}_{in}|$ inside the Si tip and zero inside the Pt tip). Metallic tips also scatter light more efficiently, as we will see later. Nevertheless, the use of dielectric tips, such as Si tips, might be favorable in certain types of near-field microscopy measurements. We will see a more concrete example of this in chapter 4.

Describing the scattering of light from a tip placed in the near-field of a sample can be effected by deriving an interaction series that accounts for multiple scattering events within the

¹Also referred to as *field-line crowding*.

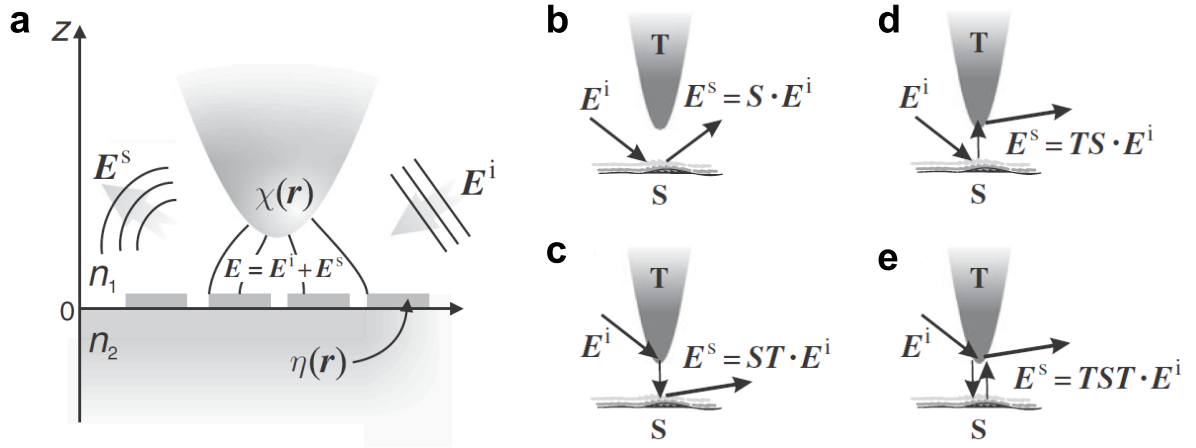


Figure 3.3: (a) Geometry and definitions for the discussion of light scattering from the tip-sample region. The tip and sample are illuminated by an incident field \mathbf{E}^i and a scattered wave \mathbf{E}^s is produced so that the total field after scattering is given by $\mathbf{E} = \mathbf{E}^i + \mathbf{E}^s$. The tip and sample are described by the dielectric susceptibilities $\chi(\mathbf{r})$ and $\eta(\mathbf{r})$, respectively. (b-e) Different types of nanoscale microscopy techniques categorized according to the leading term in the Born series. Reproduced from ref. [7].

tip/sample region. We consider the geometry sketched in Fig. 3.3 (a), in which a tip/sample region is illuminated by an incident field \mathbf{E}^i . The incoming field induces a scattered wave \mathbf{E}^s , which is what one detects in the far-field. The total field is then given by $\mathbf{E} = \mathbf{E}^i + \mathbf{E}^s$, where \mathbf{E} satisfies the vector Helmholtz equations $(\nabla^2 + k^2)\mathbf{E} = 0$. In this picture, several processes may arise in which an incoming photon is converted into a scattered photon. For instance, the incoming photon may be scattered only at the tip or only at the sample before traveling into the far-field. More complicated multiple-scattering processes may of course also occur, *e.g.*, tip-sample-tip scattering. One may assume that the overall scattering is well described by a sum of the contributions of different scattering processes and that the sum converges after a few orders since multiple scattering is expected to become negligible with increasing order. This is the so-called *Born approximation* in which \mathbf{E}^s is written as a series² of the following form [8]

$$\mathbf{E}^s(\mathbf{r}, \omega) = \sum_{n=1}^{\infty} (\mathbf{S} + \mathbf{T}_0)^n \cdot \mathbf{E}^i, \quad (3.1)$$

where we have defined $\mathbf{S} \cdot \mathbf{E} = \int dV' \mathbf{S}(\mathbf{r}, \mathbf{r}') \mathbf{E}$, and $\mathbf{T}_0 \cdot \mathbf{E} = \int dV' \mathbf{T}_0(\mathbf{r}, \mathbf{r}') \mathbf{E}$ with $\mathbf{S}(\mathbf{r}, \mathbf{r}') = k_0^2 \mathbf{G}(\mathbf{r}, \mathbf{r}') \eta(\mathbf{r}')$ and $\mathbf{T}_0(\mathbf{r}, \mathbf{r}') = k_0^2 \mathbf{G}(\mathbf{r}, \mathbf{r}') \chi(\mathbf{r}')$ ($k_0 = 2\pi/\lambda$), in which $\eta(\mathbf{r})$ and $\chi(\mathbf{r})$ are the dielectric susceptibilities of the sample and tip, respectively (see Fig. 3.3 (a)). Here $\mathbf{G}(\mathbf{r}, \mathbf{r}')$ is the dyadic Green function of the system consisting of two semi-infinite half-spaces of background dielectric constants, which we assume to be $n_1 = 1$ and n_2 . The terms \mathbf{S} and \mathbf{T}_0 account for scattering processes by the sample and tip, respectively.

Assuming that the field scattered by the tip, $\mathbf{E}_{\text{tip}}^s(\mathbf{r}, \omega)$, is known and that the sample is only

²This series is usually referred to as the *Born series*.

weakly scattering, the overall scattered field can be written in the following closed form³

$$\mathbf{E}^s(\mathbf{r}, \omega) = [\mathbf{T} + \mathbf{S} + \mathbf{TS} + \mathbf{TST} + \dots] \cdot \mathbf{E}^i \quad (3.2)$$

where $\mathbf{T} = \sum_{j=1}^{\infty} (\mathbf{T}_0)^j$ and $\mathbf{E}_{\text{tip}}^s = \mathbf{T} \cdot \mathbf{E}$.

SNOM techniques can, therefore, be classified according to which term of Eq. (3.2) is the leading term in the interaction series. Such a classification is represented graphically in Figs. 3.3 (b-e). For example, conventional far-field microscopy is characterized by the \mathbf{S} term only (Fig. 3.3 (b)), whereas illumination-mode near-field optical microscopy relies on the \mathbf{ST} term of Eq. (3.2) and is sketched in Fig. 3.3 (c). Figure 3.3 (d) depicts collection-mode near-field optical microscopy, represented by the \mathbf{TS} term. Finally, Fig. 3.3 (e) illustrates the s-SNOM technique in which the tip acts as an antenna probe and is described by the \mathbf{TST} term.

3.1.1 Scattering-scanning near-field optical microscopy (s-SNOM) setup

The optical near-field measurements that will be presented in this chapter and chapter 4 were performed using a commercial *NeaSpec* s-SNOM setup (see Fig. 3.4 (a)). As sketched in Fig. 3.4 (b), an AFM-cantilever, with a sharp tip at its end, is brought into contact with the sample surface. The cantilever can be thought of as a beam of length L and diameter $2R$, as sketched in Fig. 3.5 (a). Such a beam has a fundamental resonance frequency of oscillation given by [9]

$$\omega_0 = 1.76 \sqrt{\frac{\mathcal{Y}}{\rho}} \frac{R}{L^2}, \quad (3.3)$$

where \mathcal{Y} is Young's modulus and ρ the specific mass density of the beam. Commercially available AFM cantilevers typically have a fundamental resonance frequency $\omega_0 \sim 250$ kHz. During a measurement, the cantilever is driven at a fixed frequency Ω close to the resonance frequency given by Eq. (3.3) so that the tip oscillates at the same frequency and intermittently hits the surface of the sample. In this configuration, the AFM is said to be operated in *tapping mode*. The tapping amplitude typically ranges between 20 and 100 nm.

The back-face of the cantilever (opposite to tip side) is usually coated with aluminum or some other reflecting metal. A visible laser spot is focused on the tip-end of the cantilever and the back-reflected light is collected by a four-quadrant detector that enables the measurement of the amplitude and phase of the mechanical oscillations of the cantilever. When the tip starts to interact with a surface, the resonance frequency will shift and the oscillation amplitude will drop. This situation is depicted in Figs. 3.5 (c) and (d) for a cantilever that is externally driven at a variable frequency ω . The amplitude and phase of the cantilever oscillation are shown for two different distances d between the tip apex and the sample surface. Figures 3.5 (e) and (f) show the amplitude shift and the phase shift, respectively, as functions of the distance d for the case in which the cantilever is driven at its resonance frequency $\omega = \omega_0$. The distance range over which the amplitude and phase vary depends on the tip diameter. Because of the monotonic behavior of the curves in Figs. 3.5 (e) and (f), amplitude and phase are well-suited feedback signals to

³See ref. [7], subsection 5.1, for full derivation.

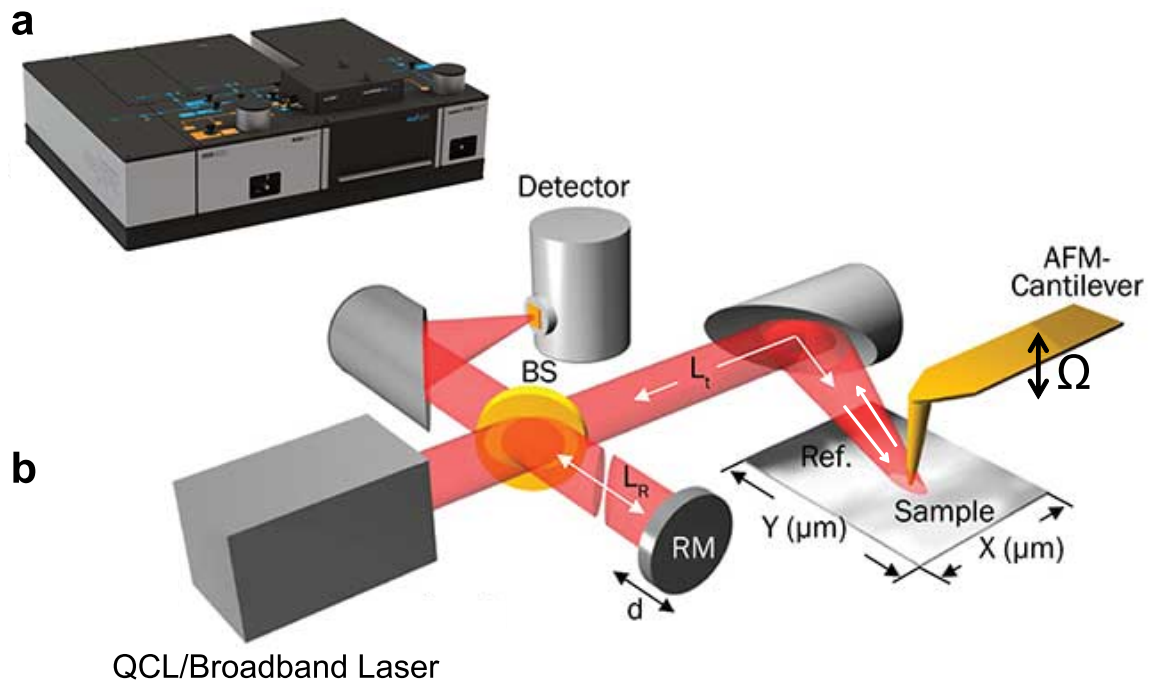


Figure 3.4: (a) Image of the commercial *NeaSpec* s-SNOM setup. All the optics are enclosed within a compact box setup in order to minimize perturbations that can be introduced to the tip from the environmental conditions of the experimental room. The particular configuration that is shown here has two modules: a near-field imaging module (left side) and a near-field spectroscopy module (right side), also known as nano-FTIR. (b) Sketch of the optical setup of the s-SNOM in the back-scattering configuration. Depending on which module is used, either a single wavelength tunable quantum cascade laser (QCL) or a broadband laser is used as the light source. The abbreviations used in panel (b) are: beam splitter (BS) and reference mirror (RM). Courtesy of *Neaspec GmbH*.

establish and maintain contact between the tip and the sample. As illustrated in Figs. 3.5 (c) and (d), the resonance frequency increases as the oscillating tip is advanced towards the sample surface and thus the frequency shift $\Delta\omega$ can be used as an alternative feedback signal. A diagram representing a feedback loop by which tip/sample contact can be established is shown in Fig. 3.5 (b). A piezoelectric element plunges or retracts the tip to maintain a predefined setpoint value (determining the point of contact with the sample surface) in response to the feedback mechanism as the sample surface is scanned. In practice, the atomic force microscopy part of a scanning near-field microscope utilizes the amplitude and phase of oscillation, frequency shift, and quality factor of the cantilever resonance as feedback signals to map the topography of the sample.

The optical near-field signal of the sample is contemporaneously detected as the topography is being mapped. As shown in Fig. 3.4 (b), a parabolic mirror with numerical aperture, $NA = 0.46$, is used to focus a laser light source on the tip/sample region with an incidence angle of 60° (measured with respect to the normal to the sample surface). The light is focused at a sub- λ region underneath the tip (as a result of the lightning-rod effect previously mentioned), exciting

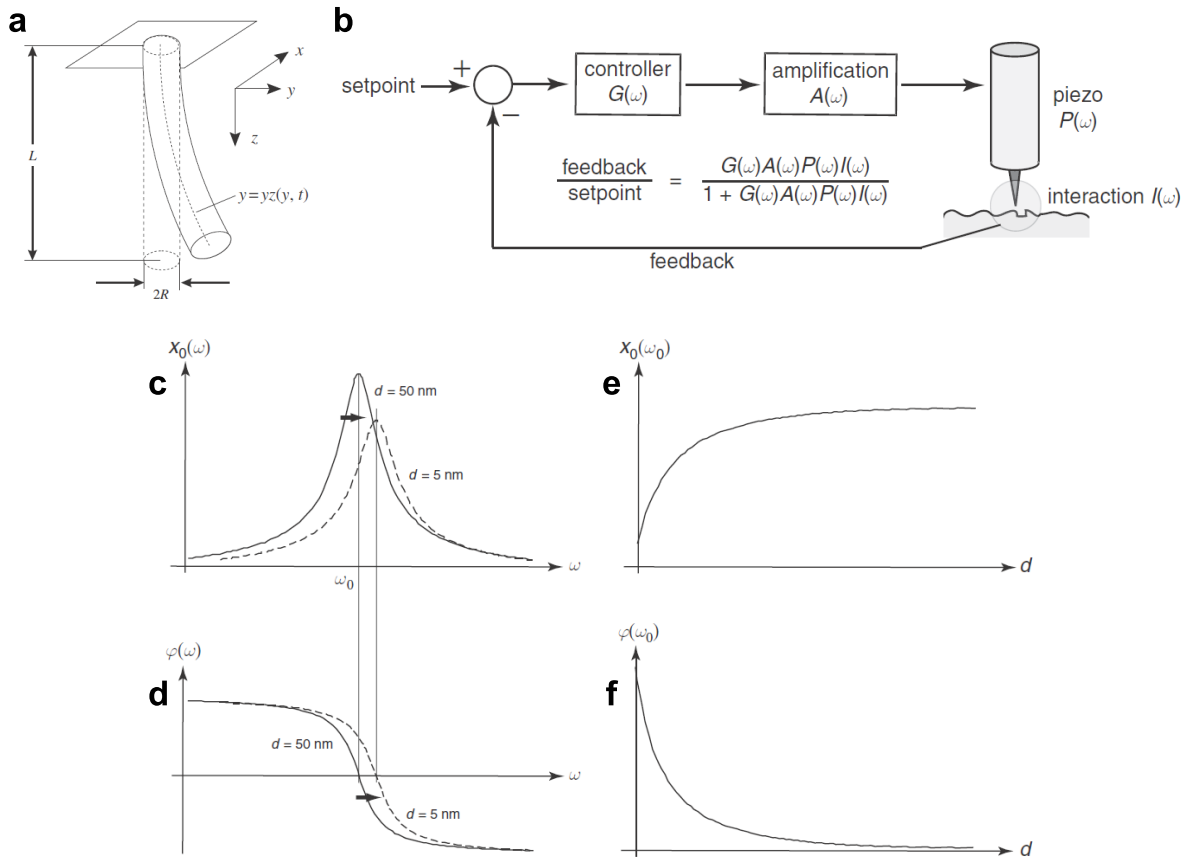


Figure 3.5: (a) Sketch of a beam of length L and diameter $2R$ fixed at one end and allowed to oscillate freely on the other. (b) A diagram representing the feedback loop employed in scanning probe microscopy such as s-SNOM to establish and maintain contact with the sample surface. This is done by measuring an *interaction signal* that is compared to an externally defined setpoint. Ideally, the measured interaction signal should correspond to the externally defined setpoint when the tip is in contact. The speed and stability of the feedback loop depend on the parameters of the controller $G(\omega)$. (c-f) Resonance of a vibrating beam. The amplitude $x_0(\omega)$ (panel (c)) and phase $\varphi(\omega)$ (panel (d)) of a beam driven at a frequency ω . As the beam-end starts to interact with a sample surface, the resonance shifts and the amplitude drops. (e) and (f) show the amplitude and phase at frequency $\omega = \omega_0$ as functions of the distance d between the beam-end (tip) and the surface. The distance range over which the amplitude and phase vary depends on the interaction area (tip sharpness). Reproduced from ref. [7].

the sample's near-fields, which are then scattered by the tip as depicted in Fig. 3.3 (e). The tip-scattered light is collected with the same parabolic mirror used to focus the light onto the sample. This particular collection configuration is usually referred to as *back-scattering mode* SNOM⁴. The collected light then passes through a *pseudo-heterodyne* interferometer, whose reference beam is shifted by a frequency Δ using a vibrating piezoelectric element, before being refocused via a parabolic mirror onto a liquid nitrogen-cooled mercury-cadmium-telluride (MCT) detector. It should be underlined here, that in contrast to a classical Michelson interferometer,

⁴s-SNOM can also be operated in *transmission mode*, in which a different parabolic mirror is used to collect the light transmitted from the sample region underneath the tip.

in which two reference mirrors form the two arms of the interferometer, the tip/sample region in the current setup forms one arm of the interferometer, while the other is formed by a reference mirror (see Fig. 3.4 (b)). This results in an asymmetric interferogram. The power measured at the detector is, then, given by

$$S = S_{\text{ref}} + S_{\text{scat}} + 2\sqrt{S_{\text{ref}}S_{\text{scat}}} \cos(\Delta t + \phi) \quad (3.4)$$

generated by the interference of the strong reference beam of signal S_{ref} , and the weak scattered light of the tip of signal S_{scat} .

Both the amplitude and phase of the detected signal are measured using a high-frequency lock-in amplifier operating at the frequency $\Delta + n\Omega$ (where n designates the order of harmonic signal demodulation). This demodulation scheme is required in order to suppress any background signal. It is usually necessary to demodulate the detected signal at the second or third harmonic to improve the signal-to-noise ratio and to better isolate the near-field signal [10–13].

At this point, we can distinguish between two different types of measurements that can be performed with this setup, depending on the light source used. Using a tunable *quantum-cascade laser* (QCL), one can perform near-field imaging of the sample at a selected wavelength λ_{QCL} . These types of measurements will be presented in chapter 4, in which s-SNOM is employed to map the near-field of a sub- λ antenna. The second type of measurements, which are the focus of the current chapter, are near-field spectroscopy measurements that are performed with a broadband infrared laser source. Such measurements are usually referred to as *nano-Fourier transform infrared* (nano-FTIR) spectroscopy⁵. The nano-FTIR setup shown in Fig. 3.4 (a) is equipped with an *optical parametric amplifier* (OPA) broadband infrared light source, whose bandwidth can be tuned to the spectral region of interest⁶. The nano-FTIR setup can be used to identify the polaritonic resonances of the polar dielectric materials introduced in the preceding chapter, or for general absorption spectroscopy of molecular fingerprints with a 20 nm spatial resolution [14].

For nano-FTIR measurements, interferometric detection demodulated at the n th-harmonic of the tip tapping frequency Ω alone is sufficient to suppress the background signal [10–12]. Since the distance z_{tip} between the sample and the nearest point of the tip (z_0) undergoes harmonic oscillations, that is

$$z_{\text{tip}}(t) = z_0 + \Delta z(1 - \cos \Omega t), \quad (3.5)$$

where $\Delta z \sim 60$ nm, typically, the amplitude $s_n(\omega)$ and phase $\phi_n(\omega)$ of the signal demodulated at the tapping harmonics are given by

$$S_n = s_n e^{i\phi_n} = \frac{1}{T} \int_0^T e^{in\Omega t} S(\omega, t) dt, \quad T = \frac{2\pi}{\Omega}, \quad (3.6)$$

in which $S(\omega, t)$ is the interferometric signal measured at the detector before demodulation, and

⁵Which is the near-field analog of far-field FTIR spectroscopy.

⁶In this manuscript we will be primarily interested in the mid-infrared spectral range centered around a wavelength of 10 μm .

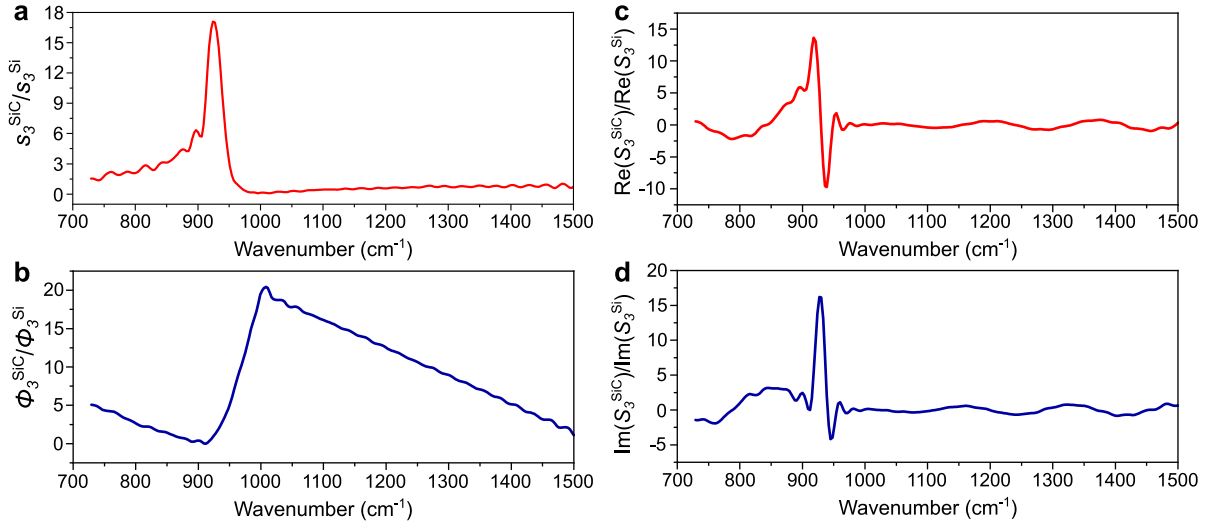


Figure 3.6: Nano-FTIR spectroscopy of SiC. (a) amplitude, (b) phase, (c) real part, and (d) imaginary part of the near-field signal on SiC, $S_3^{\text{SiC}} = s_3^{\text{SiC}} e^{i\phi_3^{\text{SiC}}}$, normalized to the signal of a reference Si substrate, $S_3^{\text{Si}} = s_3^{\text{Si}} e^{i\phi_3^{\text{Si}}}$. The detected signal is demodulated at the 3rd harmonic. Tapping parameters: tip oscillation frequency, $\Omega = 241$ kHz, and tapping amplitude, $\Delta z = 55$ nm.

ω is the frequency of the laser source.

The nano-FTIR spectrum of a 6H-SiC sample is presented in Fig. 3.6. The near-field signal of the SiC substrate, $S_n^{\text{SiC}} = s_n^{\text{SiC}} e^{i\phi_n^{\text{SiC}}}$, is normalized to that of a reference Si sample, $S_n^{\text{Si}} = s_n^{\text{Si}} e^{i\phi_n^{\text{Si}}}$, with $\varepsilon_{\text{Si}} = 11.7$. This normalization procedure ensures that artifacts that may arise due to the spectral dependence of the MCT detector response or laser intensity, are removed from the nano-FTIR spectrum. The amplitude and phase of the normalized signal are shown in Figs. 3.6 (a) and (b), respectively, for $n = 3$. The reference sample acts as a specular reflector of the incident field light that is focused onto the sample via the tip so that the amplitude, s_n^{Si} , gives the incident field amplitude. The normalized signal amplitude is, thus, proportional to the local electric field enhancement between the tip apex and the sample. As seen in Fig. 3.6 (a), the incident electric field amplitude is greatly enhanced at the surface of SiC, reaching as high as 17 times the incident field amplitude. This substantial enhancement is a direct consequence of the resonance of the surface phonon-polariton modes of a SiC half-space [15], near 930 cm^{-1} , which was introduced in the preceding chapter.

On the other hand, the real and imaginary parts of the normalized signal (Figs. 3.6 (c) and (d)) mirror the real and imaginary parts of the local dielectric function of the sample [16]. For a polar crystal such as SiC, the real and imaginary parts of the signal are modified by the polaritonic response of the material. The imaginary part in particular, which corresponds to the near-field absorption by the sample, has a peak at 930 cm^{-1} (see Fig. 3.6 (d)), that is, near the asymptotic frequency of a SiC half-space (see subsection 2.2.1). The existence of many surface phonon-polariton modes at this frequency means that light focused on the sample by the tip can couple to many in-plane modes, resulting in the large near-field absorption observed.

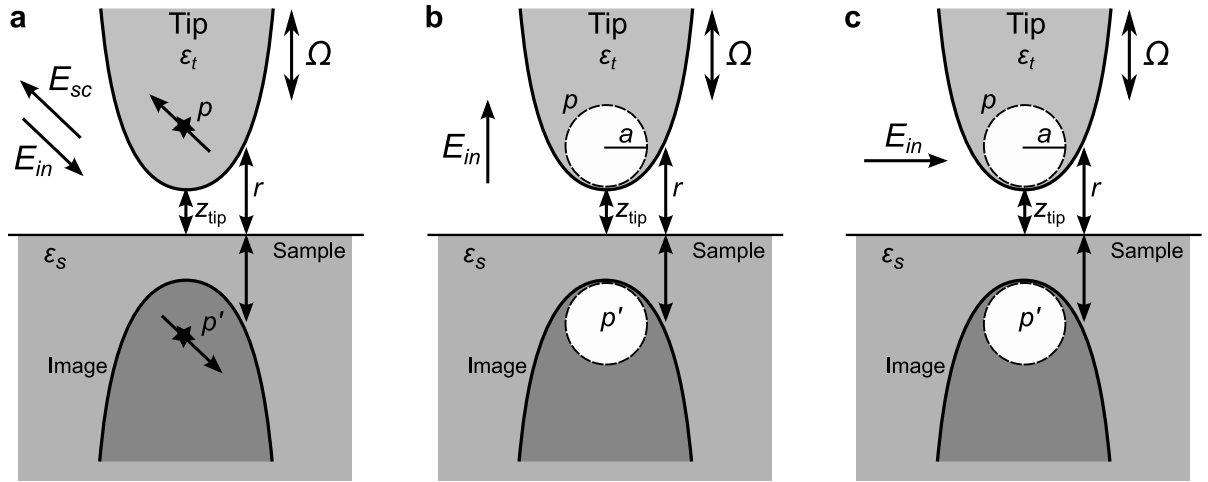


Figure 3.7: (a) Schematic representation of the tip above a sample surface and its image in the sample. (b) and (c) Representation of the point dipole approximation [12], in which the tip and its image are replaced by two spherical particles of dipole moments p and p' , respectively, and radius a . The applied electric field, E_{in} , is assumed to be perpendicular to the sample surface in panel (b) and parallel to it in panel (c).

3.1.2 Modeling s-SNOM

Consider the s-SNOM geometry shown in Fig. 3.7 (a), in which an oscillating tip is in the vicinity of a sample of dielectric function ϵ_s , with an electric field E_{in} , incident at the tip/sample region. The applied electric field induces a dipole in the tip, which itself induces an image dipole in the sample. The signal that one observes, in this case, is the light scattered by the effective dipole emerging from the combination of tip and sample dipoles [17, 18], given by

$$E_{sc} \propto (1 + r_p)^2 \alpha_{\text{eff}} E_{in}, \quad (3.7)$$

where r_p is the Fresnel reflection coefficient for p -polarized light and α_{eff} is the effective polarizability of the combined tip and sample dipoles. The $(1 + r_p)^2$ term is a far-field factor that takes into account the fact that the total external field illuminating the tip consists of the sum of the incident wave and the wave reflected off the sample [19].

The plots of Fig. 3.2 reveal that the field in the vicinity of an illuminated tip is mostly confined to the tip apex due to the lightning-rod effect (see section 3.1). It is, therefore, reasonable to assume that the tip and image dipoles can be replaced by spherical particles of radius a and dipole moments p and p' , as illustrated in Figs. 3.7 (b) and (c). If the electric field E_{in} is assumed to be perpendicular to the sample surface (Fig. 3.7 (b)), then $p' = \beta p$, while if E_{in} is parallel to the surface (Fig. 3.7 (c)), we have $p' = -\beta p$, where $\beta = (\epsilon_s - 1)/(\epsilon_s + 1)$ is the electrostatic reflection coefficient. The preceding remarks form the basis of the *point-dipole model* that is commonly used to model s-SNOM measurements [12]. Under these assumptions, we have⁷

⁷See ref. [12] for full derivation.

$$\alpha_{\text{eff}}^{\perp} = \frac{\alpha_{\text{tip}}(1 + \beta)}{1 - \alpha_{\text{tip}}\beta/16\pi r^3} \quad (3.8)$$

for E_{in} perpendicular to the sample surface, and

$$\alpha_{\text{eff}}^{\parallel} = \frac{\alpha_{\text{tip}}(1 - \beta)}{1 - \alpha_{\text{tip}}\beta/32\pi r^3} \quad (3.9)$$

for E_{in} parallel to the sample surface. In the above, $r = z_{\text{tip}}(t) + a$, where $z_{\text{tip}}(t)$ is given by Eq. (3.5), and α_{tip} is the tip polarizability, which, in the current context, is given by the electrostatic polarizability of a spherical dipole of radius $a \ll \lambda$ (*Rayleigh limit*) and dielectric permittivity ε_t , that is⁸

$$\alpha_{\text{tip}} = 4\pi a^3 \frac{\varepsilon_t - 1}{\varepsilon_t + 2}. \quad (3.10)$$

s-SNOM data are usually normalized by a reference. Since the normalization procedure eliminates all other factors in Eq. (3.7), it suffices to evaluate α_{eff} only, when modeling experimental data. The amplitude, s_n^{norm} , and phase, ϕ_n^{norm} , of the normalized s-SNOM signal are, therefore, given by

$$s_n^{\text{norm}} = \frac{s_n^{\text{sample}}}{s_n^{\text{ref}}} = \frac{|\alpha_{\text{eff},n}^{\text{sample}}|}{|\alpha_{\text{eff},n}^{\text{ref}}|}, \quad (3.11)$$

and

$$\phi_n^{\text{norm}} = \phi_n^{\text{sample}} - \phi_n^{\text{ref}} = \arg(\alpha_{\text{eff},n}^{\text{sample}}) - \arg(\alpha_{\text{eff},n}^{\text{ref}}), \quad (3.12)$$

$\alpha_{\text{eff},n}^{\text{sample}}$ and $\alpha_{\text{eff},n}^{\text{ref}}$ being the effective polarizabilities of the sample and reference after demodulation at the n th harmonic, which are obtained by integrating over the period of modulation as in Eq. (3.6), *i.e.*,

$$\alpha_{\text{eff},n}^{\text{sample (ref)}} = \frac{1}{T} \int_0^T e^{in\Omega t} \alpha_{\text{eff}}^{\text{sample (ref)}}(\omega, t) dt, \quad (3.13)$$

where, $\alpha_{\text{eff}}^{\text{sample (ref)}}(\omega, t)$ are given by Eq. (3.8) or (3.9).

The point-dipole model reproduces the enhancement in material contrasts observed in the near-field (see Fig. 3.8) but ultimately only provides a qualitative agreement with experimental results. A quantitative agreement, on the other hand, is beyond the scope of this model. This is because the point-dipole model fails to take into account the elongated shape of the tip. In reality, due to its elongated shape, the tip preferentially scatters light that is polarized along the normal to the sample surface, in other words, it has a polarizability tensor

$$\alpha_{\text{tip}} = \begin{pmatrix} \alpha_{\text{tip}}^{\parallel} & 0 & 0 \\ 0 & \alpha_{\text{tip}}^{\parallel} & 0 \\ 0 & 0 & \alpha_{\text{tip}}^{\perp} \end{pmatrix}, \quad (3.14)$$

⁸See for example ref. [20], page 139.

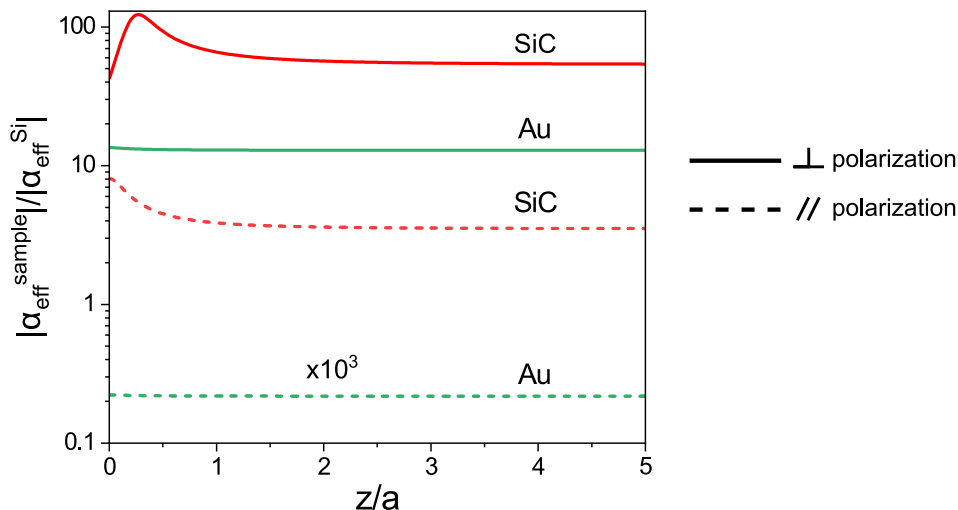


Figure 3.8: Effective polarizability amplitude at $\lambda = 10.6 \mu\text{m}$ for a platinum (Pt) tip of radius $a = 30 \text{ nm}$, at a distance $z_{\text{tip}} = z$ above SiC and Au, normalized by that of a Si reference sample. Due to the polariton resonance of SiC, the near-field is highly enhanced (about ten times more) above SiC as compared to that of Au, which acts as a mirror in the mid-infrared (see Fig. 2.3 (b)). Solid lines correspond to field polarization perpendicular to the sample surface, while dashed curves correspond to parallel field polarization. For both SiC and Au, the amplitude ratio is larger for the perpendicular field polarization.

with $\alpha_{\text{tip}}^{\perp}$ slightly larger than $\alpha_{\text{tip}}^{\parallel}$. The point-dipole model, nonetheless, provides a simple method to gain valuable insights regarding the influence of tip size and material on its scattering efficiency. For a particle whose size is small compared to the wavelength, the scattering (C_{scat}) and absorption (C_{abs}) cross-sections can be found from its polarizability α as follows⁹

$$C_{\text{scat}} = \frac{k_0^4}{6\pi} |\alpha|^2, \quad (3.15)$$

and

$$C_{\text{abs}} = k_0 \text{Im}(\alpha). \quad (3.16)$$

For a spherical particle of radius a , α is given by Eq. (3.10). The above expressions, thus, show that C_{scat} scales like a^6 , while C_{abs} scales like a^3 so that $C_{\text{abs}} \gg C_{\text{scat}}$. Additionally, Eqs. (3.15) and (3.16) show that for non-metallic particles for which $(\varepsilon_t - 1)/(\varepsilon_t + 2)$ only varies slightly with respect to the wavelength, we have

$$Q_{\text{scat}} = \frac{C_{\text{scat}}}{\pi a^2} \propto \frac{1}{\lambda^4}, \quad \text{and} \quad Q_{\text{abs}} = \frac{C_{\text{abs}}}{\pi a^2} \propto \frac{1}{\lambda}, \quad (3.17)$$

where Q_{scat} and Q_{abs} are the scattering and absorption efficiencies of the particle. The above limit is the *Rayleigh scattering limit*, which indicates that non-metallic particles that are small with respect to the wavelength scatter light of shorter wavelength more efficiently. This scattering phenomenon is the reason behind the blue color of the sky and oceans. Since extinction

⁹See ref. [20], page 140.

Material	C_{scat} ($\times 10^{-2}$ nm ²)	C_{abs} (nm ²)
Pt	0.0756	0.198
Au	0.0755	0.041
Si	0.046	0.0027

Table 3.1: Scattering and absorption cross-sections of a spherical particle of radius $a = 30$ nm in air at $\lambda = 10.6$ μm for different materials.

is the sum of scattered and absorbed light, the scaling relations given in (3.17) also show that there is a reddening of the spectrum of incident light upon transmission through a collection of sufficiently small spheres whose optical constants vary little with wavelength. We can conclude from the above remarks that dielectric tips scatter light of shorter wavelength more efficiently.

One may also note from Eq. (3.10) that a metallic tip can scatter or absorb resonantly when $\text{Re}(\varepsilon_t) = -2$ and $\text{Im}(\varepsilon_t) \ll 1$. This is the Fröhlich resonance condition introduced in subsection 2.2.3 (cf. Eq. (2.63) for $l = 1$). In this limit, the tip acts as a resonant antenna that efficiently couples the near-fields to the far-field. In practice, however, one would be ill-advised to use a resonant tip as a near-field probe, as this can significantly alter the sample's local fields, particularly when probing nanostructures in which large field enhancements are confined to tiny gaps (see chapter 4).

The scattering and absorption cross-sections at a wavelength of 10.6 μm are listed for a tip approximated by a sphere of radius $a = 30$ nm for three typical materials, namely: platinum (Pt), gold (Au), and silicon (Si). It is clear that the Pt and Au tips scatter more than the Si tip but the Si tip is less lossy, and thus minimally perturbs the sample's near-field. In general, metallic tips are well-suited to probe polaritonic and hyperbolic materials, while dielectric tips are preferred when studying the local field of a nanostructure such as a plasmonic antenna.

When a tip interacts with a surface, α_{eff} is enhanced, which translates into enhanced scattering and absorption cross-sections of the effective tip/sample region. Figs. 3.9 (a) and (b) present the resulting cross-sections of a Pt and a Si tip above an Au or Si surface, for perpendicular and parallel field polarizations. We can draw the following conclusions from the plots. (i) For both Pt and Si tips scattering and absorption along the perpendicular direction are predominant. (ii) Both absorption and scattering cross-sections of the Pt tip are larger than that of the Si tip, with the scattering cross-section being only slightly larger, however. (iii) Absorption is more effective than scattering, even for weakly absorbing samples such as Au and Si. With smaller tip diameters this is even more so due to the scaling behavior discussed above. (iv) Cross-sections for both tips are larger above Au than Si for the perpendicular polarization, while the opposite is true for the parallel polarization. The reason behind point (i) can be illustrated as follows. For the parallel polarization, the tip and image dipoles are anti-parallel so that they nearly cancel in the total scattering on Au. This cancellation is less perfect with Si, however, which is a less effective mirror than Au. This explanation is further corroborated by the contrasting behavior reported in (iv).

As mentioned previously, a quantitative agreement with experimental data necessitates a model in which the elongated shape of the tip is included. One such model is the *finite-dipole*

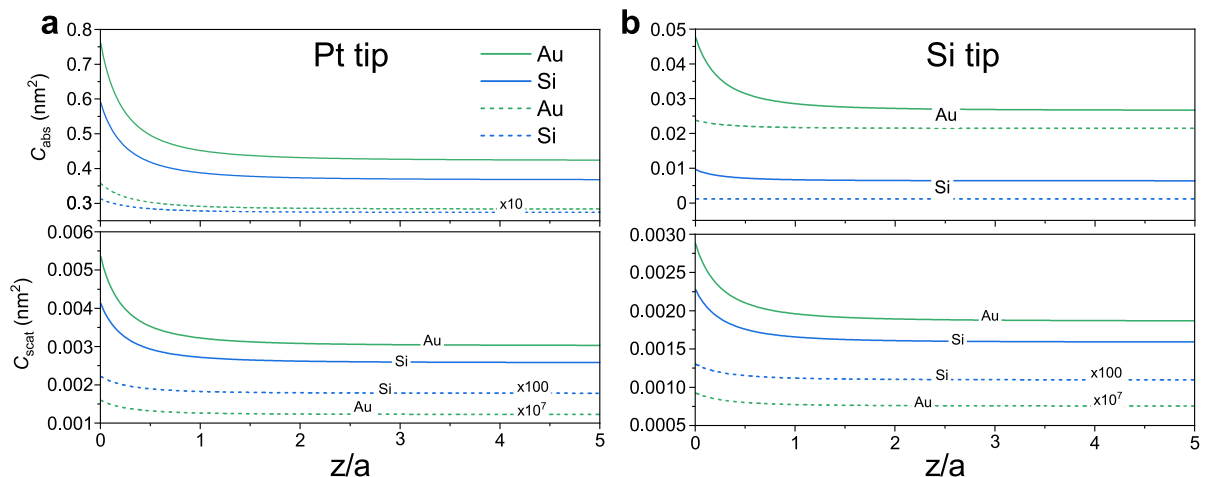


Figure 3.9: Absorption (C_{abs}) and scattering (C_{scat}) cross-sections at $\lambda = 10.6 \mu\text{m}$ of (a) a Pt tip and (b) a Si tip ($a = 30 \text{ nm}$), above Au (green curves) and Si (blue curves). Solid lines correspond to electric field polarization perpendicular to the surface, while dashed lines correspond to the parallel polarization. Optical constants: $\varepsilon_{\text{Pt}} = -1450.7 + 1051i$, $\varepsilon_{\text{Au}} = -4680 + 1674.5i$, and $\varepsilon_{\text{Si}} = 11.7 + 0.00084i$.

model [17, 21], in which the tip is considered as an elongated dipole (see Fig. 3.10 (a)). Briefly, the finite-dipole model can be described as follows¹⁰. The tip is represented by a perfectly conducting spheroid which is polarized by an external field E_{in} . The fields at the ends of the spheroid are approximated by opposite point charges $\pm Q_0$, which together form the dipole $p_0 \approx 2LQ_0$, where $2L$ is the length of the spheroid. Only the lower monopole Q_0 is assumed to be relevant for the near-field interaction with the sample. It induces a charge distribution close to the sample surface, the field of which can be described by an image charge $-\beta Q_0$ in the sample, where $\beta = (\varepsilon_2 - \varepsilon_1)/(\varepsilon_2 + \varepsilon_1)$ as before, with ε_1 and ε_2 the dielectric functions of the surrounding medium and the sample, respectively ($\varepsilon_1 = 1$ for air). The near-field interaction with the sample induces additional charges in the tip. This interaction is treated electrostatically through the addition of an opposite point charge $-Q_1$ at the center of the tip and a positive charge Q_1 at the lower end of the spheroid (see Fig. 3.10 (a)), forming the dipole $p_1 \approx Q_1 L$. The image of Q_1 in the sample, can again be written as $-\beta Q_1$.

The response of the spheroid to external monopole charges (*i.e.*, to the image charges $-\beta Q_0$ and $-\beta Q_1$) is then approximated by the near-field induced by the point monopole Q_1 at the lower end of the spheroid, which is considered to be at a position $W_1 \approx a/2$, different from the position $W_0 \approx 1.31a$ of Q_0 (a is the tip radius). With this assumption, which is an approximation of the actual image charge distribution within the spheroid¹¹, the curvature of the tip is considered. A self-consistent treatment of the problem leads to the amount of the induced charge Q_1 that has two contributions stemming from the polarization of the sample by Q_0 and by Q_1 itself, *i.e.*,

$$Q_1 = \beta(f_0 Q_0 + f_1 Q_1), \quad (3.18)$$

¹⁰We will follow the derivation of the finite-dipole model outlined in ref. [21].

¹¹For this approximation it is assumed that the tip is perfectly conducting.

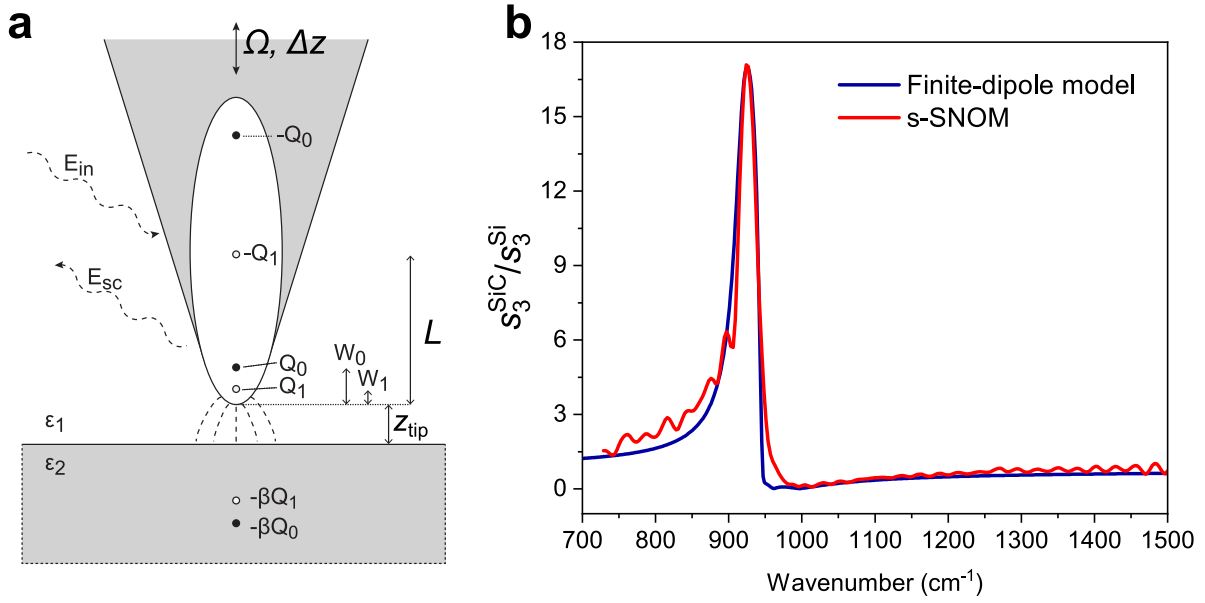


Figure 3.10: (a) Geometry of the finite-dipole model. Reproduced from ref. [21]. (b) Comparison between the normalized s-SNOM amplitude, $s_3^{\text{SiC}}/s_3^{\text{Si}}$, presented in Fig. 3.6 (a) above SiC and the corresponding fit result from the finite-dipole model (Eq. (3.20)). Fit parameters: $a = 20$ nm, $L = 300$ nm, and $g = 0.7e^{0.18i}$. The optical constants used for SiC are given in Fig. 2.1.

where the functions f_0 and f_1 include the geometric properties of the system and are given by

$$f_i = \left(g - \frac{a + 2z_{\text{tip}} + W_i}{2L} \right) \frac{\ln \frac{4L}{a + 4z_{\text{tip}} + 2W_i}}{\ln \frac{4L}{a}}, \quad (3.19)$$

in which $i = 0$ or 1 , z_{tip} the vertical tip-sample separation found from Eq. (3.5), and g an empirical geometry factor, which describes the portion of the near-field induced charge in the tip, relevant to the interaction. For typical s-SNOM tip geometries, $|g| = 0.7 \pm 0.1$.

The field of the back-scattered light, E_{sc} , is proportional to the effective polarizability α_{eff} of the tip as in (3.7), and can be calculated from the ratio between p_1 and p_0 :

$$\alpha_{\text{eff}} \propto \frac{p_1}{p_0} + 1 = \frac{1}{2} \frac{\beta f_0}{1 - \beta f_1} + 1. \quad (3.20)$$

Here, the Fourier component $\alpha_{\text{eff},n}$ of $\alpha_{\text{eff}}(\omega, t)$, is computed as in Eq. (3.13) and the constant offset $+1$ in Eq. (3.20) is neglected. The normalized amplitude and phase can then be subsequently calculated in the usual way from Eqs. (3.11) and (3.12).

Figure 3.10 (b) shows the resulting finite-dipole model fit corresponding to the nano-FTIR data reported in Fig. 3.6 for SiC. The following fit parameters were used: $a = 20$ nm, $L = 300$ nm, and $g = 0.7e^{0.18i}$. It is evident from the figure that the finite-dipole model reproduces the experimental spectrum with excellent quantitative agreement. Since the properties of the nano-FTIR spectrum of SiC have already been discussed in the previous subsection, we will only mention the influence of the fitting parameters on the resulting spectrum here. The major influence on the resulting fit arises from the tip radius a and the geometrical parameter g .

In particular, a affects the spectral position of the observed polaritonic resonance, whereas, g influences its amplitude.

3.1.3 Determining the local thickness and dielectric properties of hBN flakes with s-SNOM

The excellent quantitative agreement with experimental data given by the finite-dipole model, suggests that the model can be used reversibly to determine properties of the sample, such as layer thicknesses and dielectric constants, from nano-FTIR measurements. A common problem in nano-optics, and optics in general, is the precise determination of the optical constants of the sample under study. The most reliable method of experimentally determining the complex infrared dielectric function of a sample is *infrared ellipsometry* [22]. Typically, determining the optical constants of a sample with ellipsometry involves fitting a dielectric model (such as the Drude-Lorentz model presented in subsection 2.1.1) to the ratio r_p/r_s , where r_j ($j = p$ or s) is the complex reflection coefficient obtained from the sample's reflectivity $R_j = |r_j|^2$, measured for p - and s -polarized light at various angles of incidence. In the infrared, this measurement procedure requires the fabrication of bulk samples in order to get an appreciable signal, especially since a global source is used with a spot size of several millimeters. However, this is not feasible when dealing with atomically thin crystals or low-dimensional materials. Additionally, ellipsometry requires knowledge of the various thicknesses of the individual layers of a multi-layer sample. The high spatial resolution of s-SNOM makes it an ideal alternative to probe both layer thicknesses, as well as, local dielectric properties of the materials mentioned above.

In this subsection, we will outline a method of determining the thickness of hBN flakes using nano-FTIR and the finite-dipole model. To this end, hBN was exfoliated on an SiO₂ substrate resulting in hBN flakes about $\sim 30 \times 30 \mu\text{m}^2$ in size, with thicknesses ranging from a few nanometers to a couple of microns¹²(see Fig. 3.11 (a)). A nano-FTIR spectrum was measured on one of the hBN flakes and on the SiO₂ substrate next to it. The corresponding normalized amplitudes are shown in Fig. 3.11 (b).

The nano-FTIR spectrum of the hBN flake yields three peaks at 807 cm^{-1} , 1125 cm^{-1} , and 1370 cm^{-1} . The middle peak (at 1125 cm^{-1}) corresponds to the polariton resonance of the SiO₂ substrate (cf. Fig. 3.11 (b), blue curve). The appearance of this peak in the nano-FTIR spectrum of the hBN flake indicates that the measured flake is thinner than the penetration depth of the SPhPs of the SiO₂ substrate (see subsection 2.2.1). The amplitude of this peak is, thus, directly related to the thickness of the hBN layer. Therefore, our procedure will be to fit the amplitude of this peak using the finite-dipole model with the thickness of the hBN layer as a fitting parameter. We note that the spectra shown in Fig. 3.11 (b) are similar to those reported in ref. [23].

The finite-dipole model presented in subsection 3.1.2 can readily be extended to a three-layer system such as the one sketched in Fig. 3.12 (a). We will only give the result of this extension here and refer the reader to ref. [21] for further details. The potential response Φ of the sample to the potential of a charge Q placed at a distance z_0 above layer 2 in Fig. 3.12 (a) is given by

¹²These samples were prepared by Aurélien Schmitt at Laboratoire de Physique de l'École Normale Supérieure.

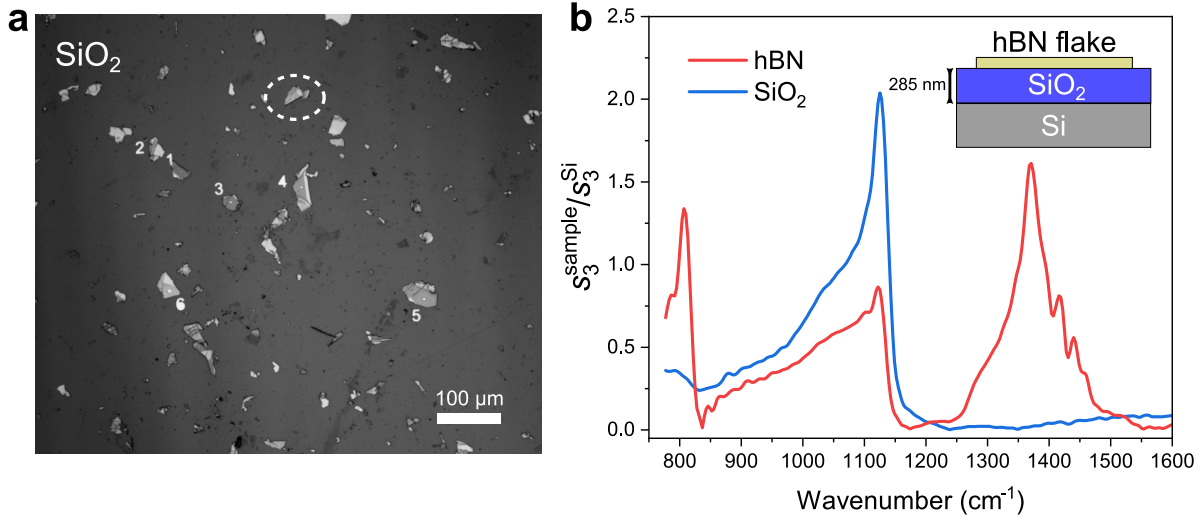


Figure 3.11: (a) Microscope image ($\times 10$ magnification) showing the exfoliated hBN flakes on the SiO₂ substrate. The substrate consists of a 285 nm SiO₂ layer on top of a bulk Si layer. (b) Normalized amplitudes of the nano-FTIR spectra measured on an hBN flake (such as the one encircled in panel (a)) and on the SiO₂ substrate next to the flake, demodulated at the 3rd harmonic of the tip oscillation frequency. The amplitudes are normalized by the nano-FTIR amplitude of a reference Si sample.

$$\Phi = \int_0^\infty A(k) e^{kz} J_0(kr) dk, \quad (3.21)$$

with

$$A(k) = e^{-2kz_0} \frac{\beta_{12} + \beta_{23} e^{-2kd}}{1 - \beta_{12}\beta_{23} e^{-2kd}}. \quad (3.22)$$

In the above, J_0 is the zeroth order Bessel function of the first kind, d is the thickness of layer 2, and β_{ij} ($i, j = 1, 2, 3$) is the electrostatic reflection coefficient at the interface ij , defined by

$$\beta_{ij} = \frac{\varepsilon_i - \varepsilon_j}{\varepsilon_i + \varepsilon_j}. \quad (3.23)$$

As in the previous subsection, the potential response Φ is approximated by the potential of an image monopole $Q' = -\beta_X Q$ at a distance X underneath the sample surface, with $\beta_X = -\Phi^2/\Phi'|_{z=0}$ and $X = \Phi/\Phi'|_{z=0} - z_0$, where $'$ denotes differentiation with respect to z .

We can now compute (β_X^0, X_0) and (β_X^1, X_1) for the heights of the charges Q_0 and Q_1 , respectively, that were introduced in the previous subsection. Subsequently, the finite-dipole model can be extended to the layered sample of Fig. 3.12 (a) by replacing W_0 (resp. W_1) in Eq. (3.19) with X_0 (resp. X_1), then inserting it along with its corresponding β_X^0 (resp. β_X^1) in Eq. (3.20).

Since the thickness of the SiO₂ layer is known (285 nm), the measurement on the SiO₂ substrate can be used to fix the parameters of the model pertaining to the tip geometry, *i.e.*, the tip radius a and length L (see Fig. 3.10 (a)). The resulting fit of the three-layer finite-dipole

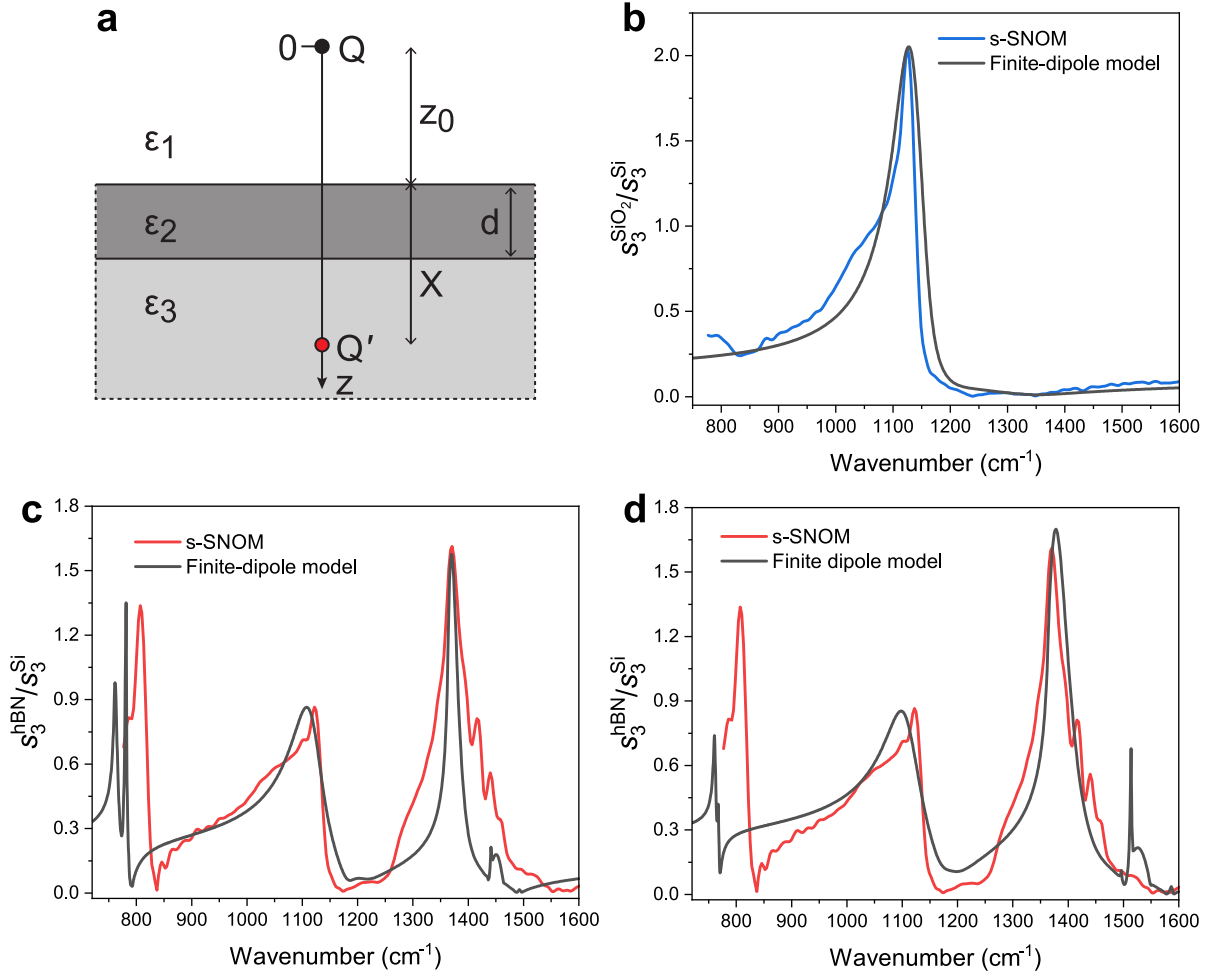


Figure 3.12: (a) Sketch of the three-layer geometry used in the extension of the finite-dipole model to a multi-layer sample. Reproduced from ref. [21]. (b) Comparison between the normalized amplitude of the nano-FTIR spectrum measured on the SiO_2 substrate and the corresponding amplitude obtained from the three-layer finite-dipole model (panel (a)) with $\varepsilon_1 = 1$, $\varepsilon_2 = \varepsilon_{\text{SiO}_2}$, $\varepsilon_3 = \varepsilon_{\text{Si}} = 11.7$, and $d = 285$ nm. (c) and (d) Same as panel (b) but for hBN. Here the finite-dipole model result is obtained by taking $\varepsilon_1 = 1$, $\varepsilon_2 = \varepsilon_{\text{hBN}}$, $\varepsilon_3 = \varepsilon_{\text{SiO}_2}$, and $d = 10$ nm. Panel (c) shows the fit result for $w_1 = 1$ and $w_1 = 5$ in Eq. (3.24), while panel (d) shows the result of the fit with $w_1 = w_2 = 1$.

model is shown in Fig. 3.12 (b) (black curve). The fit yields the geometrical parameters: $a = 10$ nm, $L = 600$ nm, and $g = 0.7e^{0.032i}$. These values are then used in the fit of the measurement on the hBN flake. As stated previously, the polariton resonance of the SiO_2 substrate can be used as a gauge of the hBN flake thickness. In particular, the strength of this peak decreases with increasing thickness of the hBN layer¹³. By varying the thickness d of the hBN layer in the finite-dipole model until the polariton resonance of the SiO_2 substrate (at 1125 cm^{-1}) arising in the air/hBN/ SiO_2 structure matches that of the nano-FTIR measurement on hBN, we get that $d = 10$ nm. The hBN hyperbolic phonon-polariton resonances (at 807 cm^{-1} and 1370 cm^{-1}),

¹³We have verified this experimentally by performing nano-FTIR measurements on thicker hBN flakes, which showed only the polariton resonance of hBN.

on the other hand, are related to the dielectric properties of the hBN layer. To describe the dielectric functions of the hBN and SiO₂ layers, we use a Drude-Lorentz model with a single oscillator (see subsection 2.1.1). As the dielectric properties of hBN and SiO₂ may vary slightly from sample to sample, we consider the parameters of the Drude-Lorentz model (Eq. (2.11)) as fitting parameters here. The first guess for these parameters is taken from the literature¹⁴. We note here that the dielectric function of hBN can be determined experimentally by fitting a dielectric model to microscope reflectivity measurements of an hBN flake (see methods section of ref. [26]). However, this method requires the preparation of large hBN flakes, on the order of $50 \times 50 \mu\text{m}^2$, as well as the use of several objectives of varying numerical aperture in order to vary the angle of incidence and collection of the microscope reflectivity measurement. For simplicity we use the optical constants of hBN reported in ref. [25], which were calculated from first principles. We also underline here that, contrary to the experimental method listed above, the current method only requires two quick measurements and can be applied to hBN flakes of any size.

To account for the anisotropy of hBN, we introduce a weighted average dielectric function

$$\varepsilon_{\text{hBN}} = \frac{2w_1\varepsilon_{\perp}^{\text{hBN}} + w_2\varepsilon_{\parallel}^{\text{hBN}}}{2w_1 + w_2}, \quad (3.24)$$

where $\varepsilon_{\perp}^{\text{hBN}}$ and $\varepsilon_{\parallel}^{\text{hBN}}$ are the dielectric functions of hBN in the direction perpendicular and parallel to the optical axis¹⁵, and $w_1 \geq 1$ and $w_2 \geq 1$ are their respective weights. We have already seen that the field probed by the tip of an s-SNOM is mostly dominated by the out-of-plane field. Thus, the tip is expected to be more sensitive to the dielectric properties of the sample in the out-of-plane direction, *i.e.*, to $\varepsilon_{\parallel}^{\text{hBN}}$ in this case. We then take $1 \leq w_1 \leq w_2$, with $w_{1,2}$ as positive integers to be fitted.

Within the framework of the Drude-Lorentz model, the amplitudes of the hBN peaks observed in Fig. 3.11 (b) scale inversely with the damping constants $\gamma_{\perp}^{\text{hBN}}$ and $\gamma_{\parallel}^{\text{hBN}}$ of the hBN layer. After fixing the thickness of the hBN layer as outlined above, we fit the values of $\gamma_{\perp}^{\text{hBN}}$ and $\gamma_{\parallel}^{\text{hBN}}$ so that the finite-dipole model yields hBN peak amplitudes matching that of Fig. 3.11 (b) (red curve). The resulting fit with $w_1 = 1$ and $w_2 = 5$ is plotted in Fig. 3.12 (c) and the fit parameters are listed in table 3.2.

Layer material	ε_{∞}	ε_0	ω_{TO} (cm ⁻¹)	ω_{TO} (cm ⁻¹)	γ (cm ⁻¹)
SiO ₂ ($\varepsilon_{\text{SiO}_2}$)	2.1	2.77	1065	1230	64
hBN ($\varepsilon_{\parallel}^{\text{hBN}}$)	3	3.45	760	815	5.65
hBN ($\varepsilon_{\perp}^{\text{hBN}}$)	4.87	6.71	1360	1596.4	2.1

Table 3.2: Fitting parameters used in the Drude-Lorentz model for the dielectric functions of the SiO₂ and hBN layers.

The quantitative agreement of the finite-dipole model used here is evident from the comparison with the experimental result shown in Fig. 3.12 (c). However, the fitting procedure fails

¹⁴Ref. [24] for SiO₂ and ref. [25] for hBN.

¹⁵The optical axis is considered to be perpendicular to the sample surface.

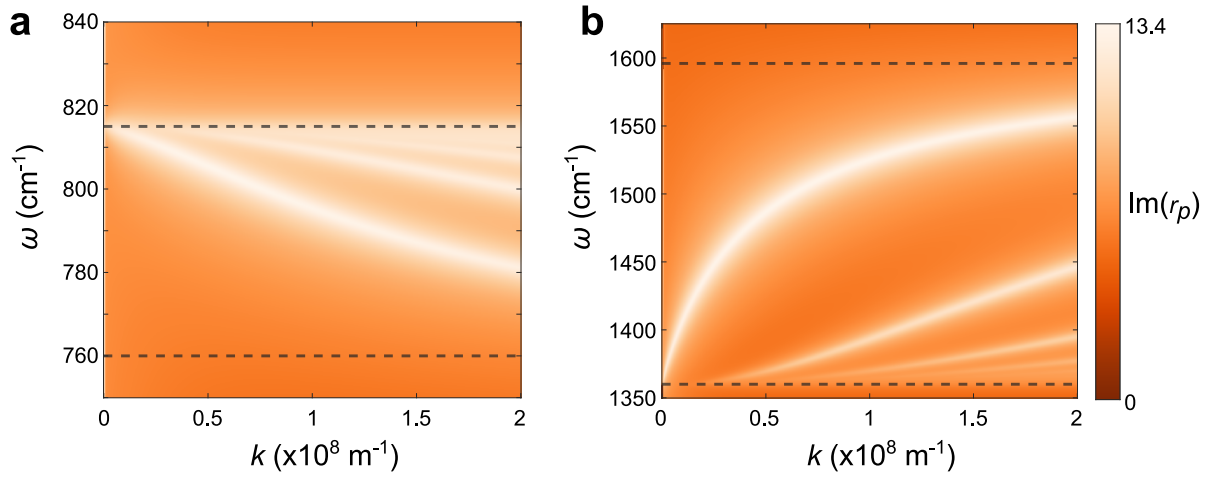


Figure 3.13: Dispersion curves of the HPhP modes of the air/hBN/SiO₂ multi-layer structure of Fig. 3.12 (c) visualized from the maxima of the imaginary part of the reflection coefficient of the structure for *p*-polarized waves, given by Eq. (2.76). Panel (a) shows type I HPhP branches and panel (b) shows the type II branches. The black dashed lines show the limits of the two *Reststrahlen* bands of hBN.

to yield the correct frequency of the hBN resonance at 807 cm⁻¹, which is red-shifted in the fitted spectrum. The fit also overestimates the quality factor of the second hBN resonance at 1370 cm⁻¹ (cf. Fig. 3.12 (c) red and black curves). Taking $w_1 = w_2 = 1$ (Fig. 3.12 (d)) more closely reproduces the experimentally observed quality factor of the second hBN resonance but the disagreement with the first resonance increases. Since the second hBN resonance arises due to the negative real part of $\varepsilon_{\perp}^{\text{hBN}}$, we can conclude that this fitting technique is more suitable for the study of the in-plane dielectric properties of the sample.

Finally, we comment on the origin of the two resonance peaks that are observed in the near-field spectrum of hBN. We have already alluded to the fact these are resonances of the hyperbolic phonon-polaritons of hBN that exist within its two *Reststrahlen* bands (see subsection 2.3.1). Interestingly, the resonance corresponding to the type I HPhPs is near the upper bound of the first *Reststrahlen* band (807 cm⁻¹), *i.e.*, close to the longitudinal optical phonon frequency, while that corresponding to the type II HPhPs is at the lower end of the second *Reststrahlen* band (1370 cm⁻¹), which is close to the frequency of the type II transverse optical phonon frequency (see Fig. 3.12 (c)). Fig. 3.13 shows the dispersion curves of HPhPs for a 10 nm hBN thin film on SiO₂, calculated from Eq. (2.76). Similarly to what we have seen in subsection 2.4.1, type II HPhP branches originate near $\omega_{\text{TO}}^{\perp} = 1360$ cm⁻¹ and increase monotonically towards an asymptotic value at large k . The key aspect to note here, however, is that infinitely many HPhP branches exist at frequencies slightly above $\omega_{\text{TO}}^{\perp}$ (see Fig. 3.13 (b)). The large number of HPhP modes in this frequency region translates into the observed resonance at 1370 cm⁻¹ in the nano-FTIR spectrum of hBN (Fig. 3.11 (b), red curve). The same can be said of the resonance of the type I HPhPs at 807 cm⁻¹, except that we have to keep in mind that type I HPhPs have negative dispersion (see subsection 2.4.1), so that the resonance appears slightly below $\omega_{\text{LO}}^{\parallel}$, where infinitely many HPhP branches appear (Fig. 3.13 (a)).

3.2 Near-field spectroscopy of surface polaritons with scattering disks

In this section, we will present near-field thermal radiation spectroscopy measurements of polar dielectric crystals using a far-field detection technique known as *infrared spatial modulation spectroscopy*¹⁶ (IR-SMS), which is a far-field infrared detection method capable of measuring the thermal emission of a single sub- λ object [28]. In order to scatter the near-field signal of the sample to the far-field, we rely on local scatterers, which are fabricated using optical lithography on the surface of the sample. The high sensitivity of the IR-SMS technique allows one to measure the signal scattered by a single sub- λ object, making this method comparable to the near-field microscopy techniques discussed heretofore. We mention here that thermal analogs of s-SNOM have already been implemented for near-field thermal radiation microscopy [29] and spectroscopy [18, 30]. Nevertheless, since the method we propose utilizes lithography-based scatterers of well-known shape and size, it presents an advantage over tip-based techniques in terms of modeling experimental data. We will, however, only present experimental data obtained with this technique. We leave the modeling of such experimental data for future work, which may be performed using a rigorous coupled wave analysis (RCWA) solver for instance.

3.2.1 Infrared spatial modulation spectroscopy: a far-field technique

We begin by illustrating the IR-SMS technique, which is a far-field infrared detection method that will regularly be employed in this manuscript for the measurement of the far-field emission of sub- λ resonators. This technique has been inspired by a similar far-field detection scheme relying on the spatial modulation of a sub- λ particle, which was implemented in the visible spectral range using a laser source ($\lambda = 532$ nm) [27]. In the current case, thermal emission from a sub- λ particle placed on a homogeneous substrate is brought upon by heating the sample to a uniform temperature T^* above the thermal bath, via a hot plate (Fig. 3.14 (a)). The emitted thermal radiation is then collected from the sample using a Cassegrain objective¹⁷ (numerical aperture, NA), which has a conic collection – except for a blind solid angle around the optical axis due to the presence of a secondary mirror (see Fig. 3.14 (a)). The collected radiation then passes through a *step-scan* operated Fourier transform infrared (FTIR) spectrometer before

¹⁶Spatial modulation has also been implemented in the visible spectral range using a laser source (see ref. [27]).

¹⁷The IR-SMS measurements that will be presented in this manuscript were performed with a Cassegrain objective with NA = 0.5 or 0.78. We will specify later which Cassegrain objective was used depending on the measurements under discussion.

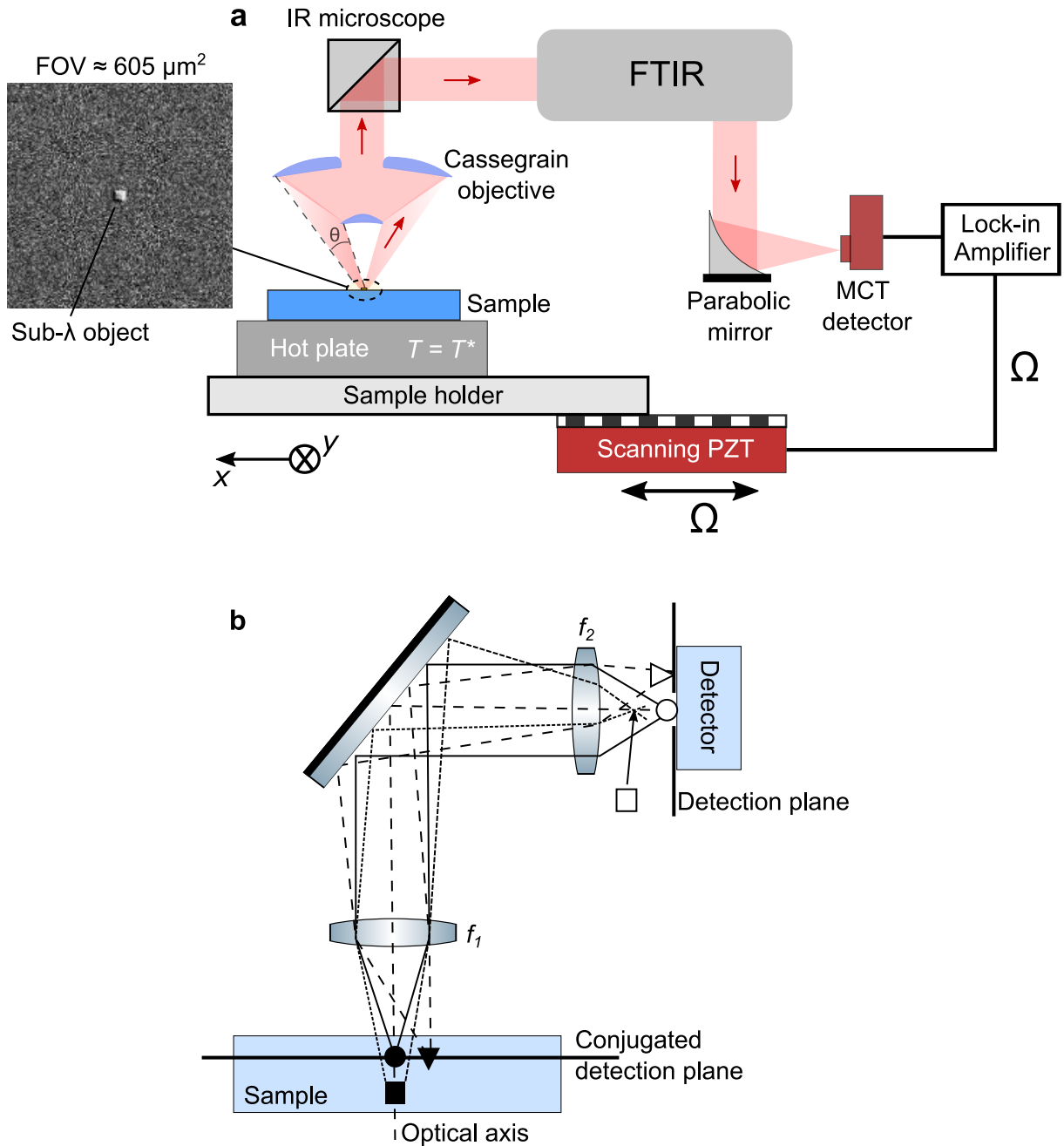


Figure 3.14: (a) Schematic illustration of the IR-SMS technique. The inset on the left shows a microscope image of a sub- λ square patch antenna over a uniform background substrate. The antenna is optically conjugated with the active area of the detector and a piezoelectric translation stage is used to modulate its position in the detector's field of view (FOV). The field of view size is determined by the size of the active area of the detector ($250 \times 250 \mu\text{m}^2$ here) and the magnification, M , of the collection optics. (b) Confocal configuration equivalent to the optical setup of panel (a), consisting of a collection lens of focal length f_1 and a focusing lens of focal length f_2 . Three objects in the sample are depicted. Only the object (circle) on the optical axis lying in the conjugated detection plane in the object space reaches the center of the active area of the detector, producing a maximal detected signal. The other objects (triangle and square) are either focused to the sides of the active area (triangle) or arrive at the detector unfocused such that their signals are either minimal or suppressed. The magnification of the two-lens system shown here is given by $M = f_2/f_1$.

being refocused via an Au-coated parabolic mirror onto a liquid-nitrogen-cooled mercury cadmium telluride (MCT) detector, enabling the measurement of a thermal radiation spectrum.

In this configuration, the setup can be equated to a confocal detection scheme consisting of two lenses of focal lengths f_1 and f_2 , corresponding to that of the Cassegrain objective and parabolic mirror, respectively (Fig. 3.14 (b)). Confocal microscopy is typically implemented with a pinhole placed in front of the detector. The principle of this detection technique is based on the fact that light not originating from the focal area will not be able to pass through the detection pinhole and hence cannot reach the detector. Laterally displaced beams will be blocked by the detector aperture and beams originating from points displaced along the optical axis will not be focused in the detection plane and therefore will be strongly attenuated by the detection pinhole. This effect is illustrated qualitatively in Fig. 3.14 (b).

For the particular setup of Fig. 3.14 (a), the equivalent confocal magnification is given by $M = \frac{f_2}{f_1} = \frac{50.8}{5} \frac{\text{mm}}{\text{mm}} = 10.16$. The detector that we use here has an active area of $250 \times 250 \mu\text{m}^2$ so that the field of view of the detector is $\sim (250/M)^2 = (24.6)^2 \mu\text{m}^2$. The small active area of the detector, and the fact that its detectivity falls off away from its center¹⁸, can be used to induce a spatial filtering of the detected signal analogous to that of the pinhole in confocal microscopy. Consider a sub- λ object placed on the heated sample surface that is optically conjugated with the detector's active area. As the sample surface is isothermal, the thermal radiation signal at the detector will be dominated by an overwhelming background signal produced by the regions surrounding the sub- λ object. To filter out this background, the sample is laterally modulated with an amplitude $A \sim 25 \mu\text{m}$, at a frequency Ω , by means of a piezoelectric translation stage. This induces a spatial dependence on the signal contribution coming from the single sub- λ object, as its position oscillates within the detector's field of view. We extract this contribution through lock-in detection, by demodulating the detected signal at the frequency Ω , or at a higher harmonic, eliminating the large background.

Since the sub- λ particle is modulated sinusoidally along the x -direction, its position can be written as

$$x(t) = x_0 + \frac{A}{2} \sin \Omega t, \quad (3.25)$$

where x_0 is the position of the particle with respect to the optical axis. Thus, for a small amplitude of modulation one can perform a Taylor series expansion of the detected signal, $S(x, y; \lambda, t)$, around x_0 as follows

$$S(x, y; \lambda, t) \sim S(x_0) + \frac{A}{2} \sin \Omega t \left(\frac{\partial S}{\partial x} \right)_{x=x_0} + \frac{A^2}{4} \sin^2 \Omega t \left(\frac{\partial^2 S}{\partial x^2} \right)_{x=x_0} + \dots \quad (3.26)$$

The first term in Eq. (3.26) is a DC offset corresponding to the uniform background signal of the substrate while the remaining terms correspond to the higher harmonics of the signal arising from the spatial modulation of the sub- λ particle under study¹⁹. The signal demodulated at the

¹⁸More precisely, the detected signal falls off away from the center of the detector active area following a Gaussian-like behavior with a full width at half maximum of $\sim 17 \mu\text{m}$ (see ref. [28]).

¹⁹The substrate on which the sub- λ particle lies upon, is assumed to be homogeneous and thus translationally invariant.

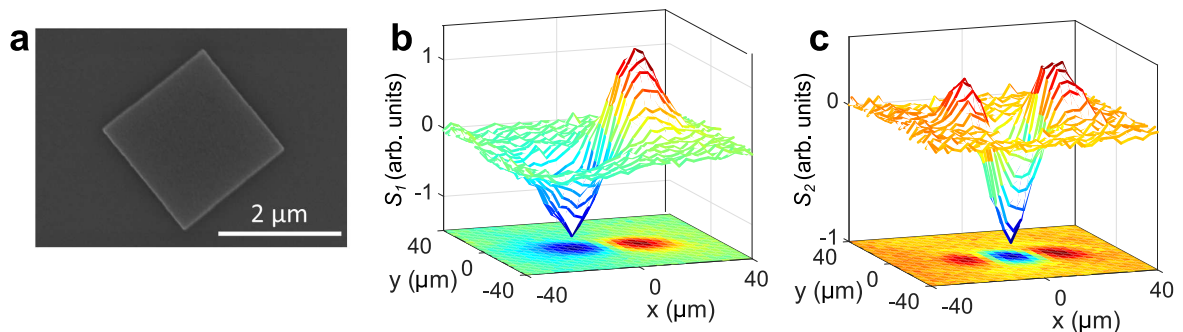


Figure 3.15: (a) Scanning electron microscope (SEM) image of a square patch metal-insulator-metal (MIM) antenna of side $w = 2 \mu\text{m}$. MIM antennas will be discussed in greater detail in chapter 4. (b) and (c) Spatial scans of the signal of the single antenna of panel (a), demodulated at the 1st and 2nd harmonic, respectively.

n th harmonic, $S_n(x, y; \lambda)$, can be found by integrating over the modulation period $T = 2\pi/\Omega$:

$$S_n(x, y; \lambda) = \frac{1}{T} \int_0^T S(x, y; \lambda, t) \sin(n\Omega t) dt. \quad (3.27)$$

By replacing Eq. (3.26) in (3.27) we can see that the constant DC term $S(x_0)$ cancels out so that the background signal of the substrate is effectively eliminated by the demodulation procedure. In practice, the lock-in amplifier integrates the signal over a time constant $\tau = mT$, with $m \geq 1$, so that the detected signal may undergo multiple modulations during the time τ . This has the effect of increasing the signal-to-noise ratio and better isolating the signal coming from the modulated particle.

Since the ultimate goal is to perform FTIR spectroscopy of the demodulated signal, one must keep in mind that the stabilization time of the moving mirror of the FTIR's Michelson interferometer, which is operated in step-scan mode, is proportional to the lock-in time constant²⁰. Increasing the lock-in time constant, therefore, will result in an increase in the total time required to record a full interferogram (signal intensity I vs interferometer mirror delay δ). Longer interferograms are more sensitive to drifts, which may result in an asymmetrical interferogram²¹ that ultimately produces an erroneous Fourier transform. Hence, a compromise must be made when selecting the appropriate time constant. In our case, $\Omega = 21$ Hz and we typically select a time constant $\tau = 500$ ms so that $m = 1.67$. For the interferogram, we choose a stabilization time of 6τ and the intensity I is recorded at 315 points of the mirror delay. This yields a total time of 15.75 minutes for a full interferogram. Increasing the time constant further will result in the aforementioned drifts. Instead, the measurement is repeated multiple times and the resulting Fourier-transformed spectra are averaged.

Figures 3.15 (b) and (c) show the (x, y) -plane spatial scans of the spectrally-integrated

²⁰Ideally, the stabilization time should be set to 5 or 6τ .

²¹The signal I of the interferogram is a result of the interference of the signal coming from the two arms (mirrors) of the Michelson interferometer, at the beam-splitter. At the center of the interferogram ($\delta = 0$) the two signals interfere constructively, giving maximal intensity. Away from $\delta = 0$ the intensity drops due to destructive interference. The drop in I on both sides of $\delta = 0$ is symmetric.

IR-SMS signals, $S_1(x, y)$ and $S_2(x, y)$ ²², of a single 2 μm -square-patch metal-insulator-metal antenna (see Fig. 3.15 (a)) that is modulated along the x -direction ($A = 25 \mu\text{m}$). Demodulation at the 1st harmonic yields two lobes with opposite signs and a minimum ($S_1 \approx 0$) at $x = 0$. On the other hand, S_2 has three lobes of alternating sign with one extremum at the position $(x, y) = (0, 0)$. Interestingly, the lobes extend over a spatial region that is several tens of microns and are well separated. We underscore here the importance of the fact that at the position $(x, y) = (0, 0)$ (*i.e.*, at the optical axis) S_1 vanishes while S_2 has an extremum. This means that the single antenna can be positioned at the optical axis with sub- λ precision by displacing the piezoelectric element so that the conditions $S_1 \approx 0$ and $|S_2| \approx \max(S_2)$ are simultaneously satisfied. In practice, the antenna is placed at the position where the maximal signal is detected, that is, at one of the extrema of the lobes, so that the thermal emission spectrum is recorded with the highest possible signal-to-noise ratio.

We turn now to the physical meaning of the detected signal. For a surface of area B at temperature T^* , the power emitted within a solid angle $d\xi = \sin\theta d\theta d\phi$ is given by²³

$$\frac{dP_\lambda^{\text{em}}}{d\xi} = B\epsilon_\lambda L_0(\lambda, T^*) \cos\theta, \quad (3.28)$$

where ϵ_λ is the spectral emissivity of the surface²⁴ and L_0 is the *Planck blackbody spectral radiance* in $\text{W}\cdot\text{sr}^{-1}\cdot\text{m}^{-3}$ written as

$$L_0(\lambda, T^*) = \frac{2hc^2}{\lambda^5} \frac{1}{\exp\left(\frac{hc}{\lambda k_B T^*}\right) - 1}. \quad (3.29)$$

By definition, a blackbody absorbs (equivalently, emits) all light incident upon it so that its emissivity is unity. A sub- λ object, such as a resonant nano-antenna, can be thought of as a blackbody surface whose surface area is equivalent to the antenna's *emission cross-section*, C_{em} , and thus from Eq. (3.28), the power emitted by the antenna within the solid angle $d\xi$ reads

$$\frac{dP_\lambda^{\text{ant}}}{d\xi} = C_{\text{em}} L_0(\lambda, T^*) \cos\theta. \quad (3.30)$$

For a finite-sized object, one can equate the emission cross-section to the absorption cross-section, C_{abs} . This is the local form of Kirchhoff's law of blackbody radiation [33].

We may now formally write the power measured at the detector as follows

$$P_\lambda^{\text{det}} = P_\lambda^{\text{ant, det}} + P_\lambda^{\text{bg, det}}, \quad (3.31)$$

where

²²The λ dependence is dropped from the argument of S_n here since the demodulated signals presented in Figs. 3.15 (b) and (c) are integrated over the entire spectral range of the detector.

²³The $\cos\theta$ factor appears due to the fact that a blackbody is a *Lambertian* source (*i.e.* obeying Lambert's cosine law [31]).

²⁴The emissivity ϵ_λ of a surface is equivalent to its absorptivity α_λ by Kirchhoff's law [32].

	NA	θ_{\min}	θ_{\max}	$P^{\text{ant, det}}$ (nW)	$P^{\text{bg, det}}$ (nW)
Obj. 1	0.5	10°	30°	5.2	157.7
Obj. 2	0.78	33°	52°	7.7	232.6

Table 3.3: Spectrally integrated power reaching the detector at $T^* = 440$ K, for two different Cassegrain objectives. The power is integrated over the spectral range $\lambda \in [6, 14]$ μm . It is assumed that $C_{\text{em}} = 20 \mu\text{m}^2$ for the antenna and $\epsilon_\lambda = 1$ for the background.

$$P_\lambda^{\text{ant, det}} = \int_0^{2\pi} d\phi \int_{\theta_{\min}}^{\theta_{\max}} d\theta \sin \theta \cos \theta C_{\text{em}}(\lambda) L_0(\lambda, T^*), \quad (3.32)$$

is the power emitted by the antenna that reaches the detector, and

$$P_\lambda^{\text{bg, det}} = \int_0^{A_{\text{det}}} \int_0^{A_{\text{det}}} dx dy \int_0^{2\pi} d\phi \int_{\theta_{\min}}^{\theta_{\max}} d\theta \sin \theta \cos \theta \epsilon_\lambda L_0(\lambda, T^*), \quad (3.33)$$

is the power emitted by the background.

In the above, $A_{\text{det}} = (250/M) \mu\text{m}$, θ_{\min} and θ_{\max} are the minimum and maximum collection angles of the Cassegrain objective, and $C_{\text{em}}(\lambda)$ is the emission cross-section of the sub- λ antenna. Table 3.3 lists the spectrally integrated powers, $P^{\text{ant, det}}$ and $P^{\text{bg, det}}$, for two different objectives of varying numerical aperture and collection angles. These values are obtained by integrating Eqs. (3.32) and (3.33) over the spectral range $\lambda \in [6, 14]$ μm . The antenna is considered to have an emission cross-section of $20 \mu\text{m}^2$ and the background is considered as an ideal blackbody with an emissivity of 1.

This calculation shows that the power emitted by a sub- λ antenna that is captured by our detection system is on the order of a few nanoWatts and is only a few percent of the background power reaching the detector. In reality, the detected power is expected to be even lower since we have neglected the fact that the detector is less sensitive away from the center of its active area and neglected the losses from the various optical components used to guide the beam to the detector. Nonetheless, this provides an order-of-magnitude of the signals that we are dealing with here and clearly illustrates the high sensitivity of the IR-SMS technique.

We can gain more precise insight into the power of the detected signal by examining the lock-in signal, which is given in milliVolts. The photons that are incident on the active area of the detector are converted into a photo-current²⁵. The photo-current then passes through a trans-impedance circuit in order to amplify the signal before reaching the lock-in amplifier. The trans-impedance circuit converts the incident power measured at the detector into a voltage that is displayed on the lock-in amplifier. One can therefore compute the incident optical power, P_{opt} , for a given voltage V_{LI} read on the lock-in amplifier as follows

²⁵Not all photons are converted into a photo-current since the quantum efficiency of the detector is usually less than 1.

$$P_{\text{opt}} = \frac{V_{\text{LI}}}{G\mathcal{R}_{\text{det}}}, \quad (3.34)$$

where G is the gain of the trans-impedance circuit and \mathcal{R}_{det} is the detector's *responsivity* in V/W.

In our case, we use an MCT detector (*Infrared Associates Inc.*) with $\mathcal{R}_{\text{det}} = 36287$ V/W and a trans-impedance gain $G = 3570$. Typically, we find that for a $2 \times 2 \mu\text{m}^2$ antenna $V_{\text{LI}} \sim 1$ mV. Thus, Eq. (3.34) gives an optical power $P_{\text{opt}} \approx 7.7$ pW. This shows that the actual detected signal of a single sub- λ antenna is three orders of magnitude lower than the one calculated in the previous paragraph. This is mainly due to the detector's detectivity (see below) and losses from the various optical components used to guide the beam.

We have established so far that the raw (*i.e.*, untreated) spectral signal, S_n^{ant} , of a sub- λ antenna, measured using the IR-SMS technique, is proportional to the product of the antenna absorption (emission) cross-section and the blackbody spectral radiance, that is, $S_n^{\text{ant}}(\lambda, T^*) \propto C_{\text{abs}}(\lambda)M_0(\lambda, T^*)$, in which M_0 is the Planck blackbody spectral radiance in $\text{W}\cdot\text{m}^{-3}$. The constant of proportionality is the *spectral response function*, r_ν , which is determined by the instrumental response²⁶ of the setup. The response function of the setup can be readily obtained by measuring the response of a reference blackbody sample and following the calibration procedure outlined in ref. [34].

Consider a setup in which the thermal emission of a sample is measured after passing through an FTIR spectrometer. In this case, the signal reaching the detector can be cast as follows

$$C_\nu = r_\nu(L_\nu + L_\nu^0), \quad (3.35)$$

where L_ν is the spectral radiance of the sample and L_ν^0 is the spectral radiance due to instrumental emission²⁷, both in $\text{W}\cdot\text{m}^{-1}$.

If the sample is a blackbody source whose thermal emission is measured at two different temperatures, T_c and T_h ($T_c < T_h$), then Eq. (3.35) can be solved to yield the following

$$r_\nu = \frac{C_{h\nu} - C_{c\nu}}{B_\nu(T_h) - B_\nu(T_c)}, \quad (3.36)$$

and

$$L_\nu^0 = \frac{C_{h\nu}}{r_\nu} - B_\nu(T_h) = \frac{C_{c\nu}}{r_\nu} - B_\nu(T_c), \quad (3.37)$$

where B_ν is the Planck blackbody spectral radiance in $\text{W}\cdot\text{m}^{-1}$ and, $C_{h\nu}$ and $C_{c\nu}$, are the uncalibrated spectra of the blackbody sample measured at the temperatures T_h and T_c , respectively.

To evaluate the response function of our setup, we measure the thermal emission of a reference blackbody sample through the same optical path with the FTIR operated in *rapid-scan*²⁸ mode.

²⁶This includes the spectral dependence of the detector, transmission of the FTIR beam-splitter, and the spectral dependence (if any) of all other optical components of the setup.

²⁷The subscript $\nu = 1/\lambda$ here denotes the wavenumber, which is conventionally used in FTIR spectroscopy in units of cm^{-1} .

²⁸Also known as *continuous scan* due to the fact that the moving mirror of the interferometer is translated continuously.

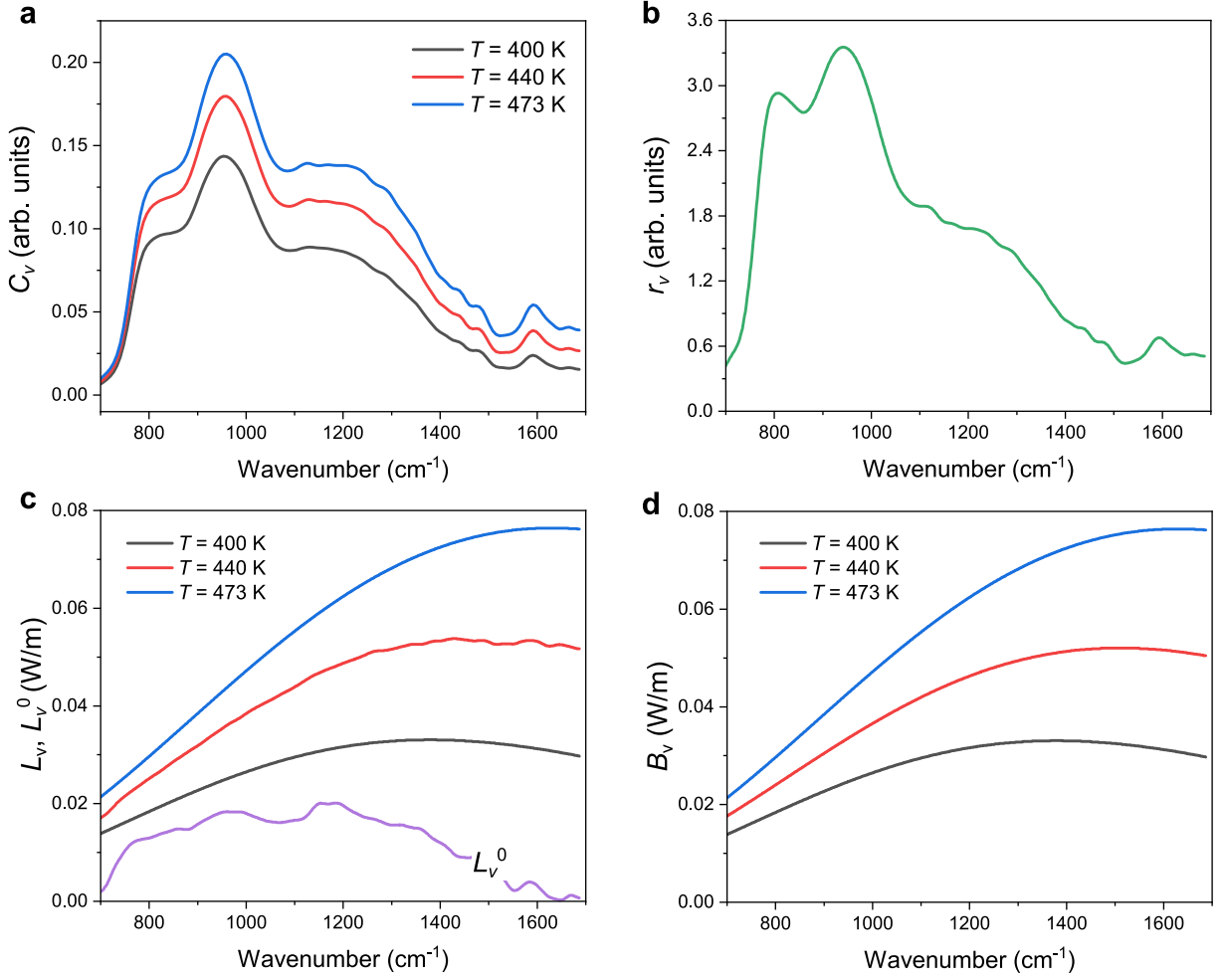


Figure 3.16: (a) Uncalibrated spectra of the thermal emission of a reference blackbody sample at variable temperature T . (b) Spectral response function (r_ν) of the optical setup computed from Eq. (3.36). (c) Measured blackbody spectra of panel (a) after calibration ($L_\nu = \frac{C_\nu}{r_\nu} - L_\nu^0$) and (d) their corresponding Planck blackbody spectral radiance.

The measured blackbody response is shown in Fig. 3.16 (a) for various temperatures. The sample temperature is set by an electrically-controlled hot plate and is measured using a thermo-couple tip at the surface of the sample.

Although the spectra of Fig. 3.16 (a) are broadband, they lack the main characteristic that is to be expected for an ideal blackbody source. Contrary to a blackbody source, the spectral position at which the measured intensity is maximal is invariant with respect to temperature. According to Wien's law, the peak wavelength, λ_{\max} , of the intensity spectrum of a blackbody source is expected to scale inversely with respect to its temperature following the relation: $\lambda_{\max} = b/T$ with $b = 2898 \mu\text{m.K}$. This behavior is absent in Fig. 3.16 (a) since, as we have already mentioned, the raw signal is a product of the response function and the sum of the emission from the sample and the various instruments used in the setup (see Eq. (3.35)).

By using the measured spectra of Fig. 3.16 (a) in Eqs. (3.36) and (3.37) we can compute the experimental spectral response function and instrumental offset of our setup. The resulting

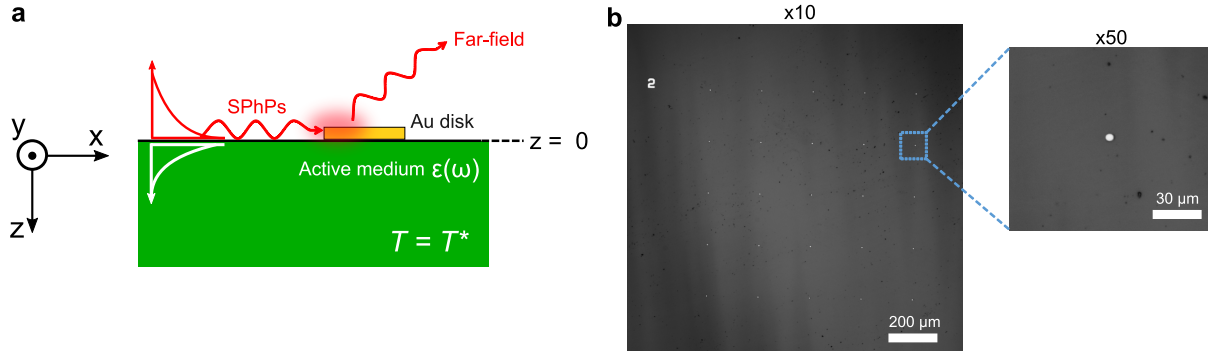


Figure 3.17: (a) Sketch representing the scattering of thermally excited surface polaritons by an Au disk at the surface. (b) Microscope images of Au disks that were patterned via optical lithography on the surface of a SiC substrate. The disks are 110 nm thick and are of varying diameters.

response function is presented in Fig. 3.16 (b). It is clear that the spectral response is maximal at a wavenumber close to 1000 cm^{-1} and falls off away from this frequency. This is due to the fact that the *detectivity*²⁹, D^* , of the MCT detector is maximal at a wavelength of $10 \mu\text{m}$, which is the main reason behind why the spectra in Fig. 3.16 (a) all have a peak at this wavelength. Typically, the detectivity of an infrared detector is optimized at a certain wavelength by tuning the alloy concentration in the semi-conductor material³⁰ making up its active area, so that the band-gap energy matches that of the photon energy. Away from the optimal wavelength, the detectivity falls off following a bell-shaped distribution.

The spectral radiance curves of the blackbody sample resulting from the above calibration procedure are plotted in Fig. 3.16 (c). Indeed, we find that the calibrated spectra follow the Planck blackbody distribution (cf. Fig. 3.16 (d)).

3.2.2 Near-field spectroscopy of a SiC substrate with a gold disk

As we have already mentioned at the beginning of this section, the goal is to perform near-field spectroscopy using a far-field technique. To couple the near-field signal to the far-field, a sub- λ scatter, such as an Au disk, must be patterned at the surface of the sample. This situation is depicted in Fig. 3.17 (a). A sample consisting of a surface polariton-active material is heated uniformly to a temperature, T^* , above the thermal bath, so that all the modes of the sample are excited through thermal fluctuations (including propagating surface modes). The disk acts as a local scatterer, scattering the propagating surface modes of the sample to the far-field where they can be detected using the IR-SMS technique.

Gold disks of diameters ranging from 2 to $8 \mu\text{m}$ were patterned using optical lithography on a SiC substrate³¹(see Fig 3.17 (b)). Since we are interested in the signal scattered by a single disk, and owing to the long propagation lengths of SPhPs on SiC (see subsection 2.2.1),

²⁹The detectivity or specific detectivity is usually measured in *Jones* units. $1 \text{ Jones} = 1 \text{ cm} \cdot \text{Hz}^{1/2} \cdot \text{W}^{-1}$.

³⁰Mercury-cadmium-telluride ($\text{Hg}_{1-x}\text{Cd}_x\text{Te}$) in our case.

³¹The samples that will be discussed in this section were fabricated via optical lithography by Aurélien Schmitt at Laboratoire de Physique de l'Ecole Normale Supérieure.

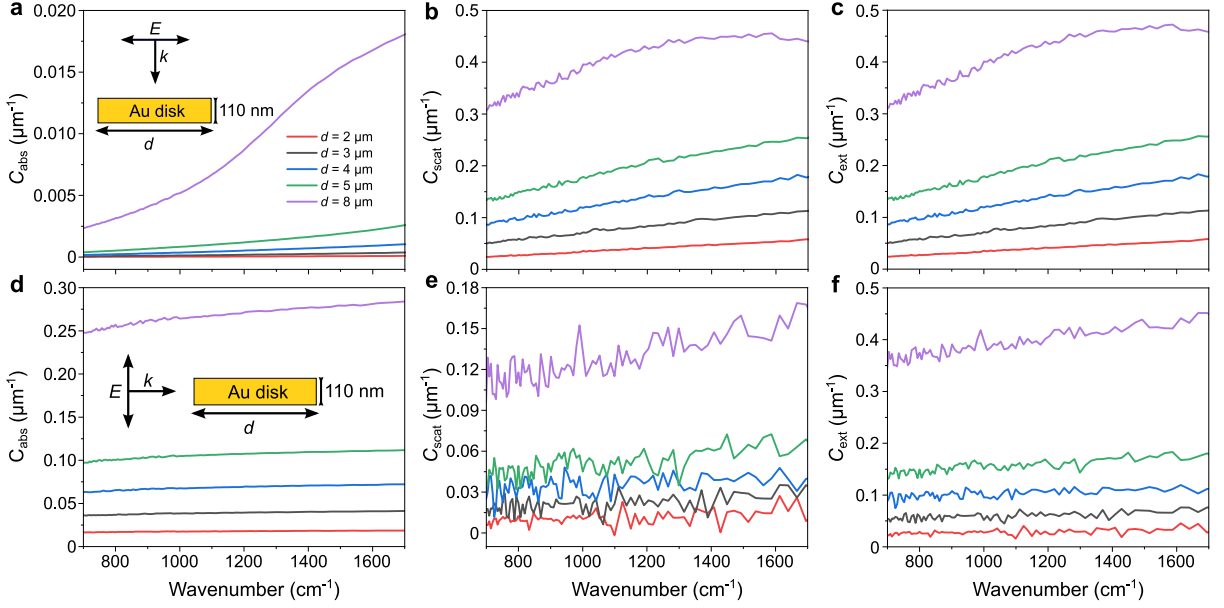


Figure 3.18: Finite-element method (FEM) calculations of the cross-sections of a gold disk in air. (a) & (d) Absorption cross-section (C_{abs}). (b) & (e) Scattering cross-section (C_{scat}). (c) & (f) Extinction cross-section ($C_{\text{ext}} = C_{\text{abs}} + C_{\text{scat}}$). The top panels correspond to the electric field incident upon the disk from the top and the bottom panels are for electric field incident upon the disk from the side (see insets of panels (a) and (d)). Details on FEM simulations can be found in Appendix A.

the disks were fabricated $200 \mu\text{m}$ apart so that they are well isolated. It is important to note here that the disk must only act as a passive scatterer of the sample's near-fields and not as a resonant structure itself. This ensures that the sample's near-fields are minimally perturbed by the presence of the disk. To quantify the scattering behavior of the disk we performed finite-element method simulations of the cross-sections of an Au disk, of diameter $2 \mu\text{m} \leq d \leq 8 \mu\text{m}$, in air (Fig. 3.18). The results show that even for the largest disk considered ($d = 8 \mu\text{m}$, magenta curves) the cross-sections of the disk are almost completely spectrally-flat within the frequency range that we consider here. It is interesting to note that, contrary to the spherical probes discussed in subsection 3.1.2, absorption is either less than scattering (cf. Figs. 3.18 (a) and (b)) or comparable to it (cf. Figs. 3.18 (d) and (e)). This can be attributed to the larger size of the disk as compared to that of the aforementioned spherical probes.

The sample temperature was raised to $T^* = 440 \text{ K}$ so that propagating surface phonon-polaritons in SiC are excited and a spectrum of the near-field signal scattered by a single disk is measured via IR-SMS as outlined in the previous section. To remove any temperature or instrumental dependence, the detected signal, $S_{\text{disk}}(\omega, T^*)$, was normalized by the response of a reference blackbody sample, $S_{\text{BB}}(\omega, T^*)$, which was measured with the same optical path. The normalized signal $S_{\text{norm}}(\omega) = S_{\text{disk}}(\omega, T^*)/S_{\text{BB}}(\omega, T^*)$ for an Au disk with $d = 2 \mu\text{m}$ is shown in Fig. 3.19 (a). One can clearly see that the spectrum is dominated by the near-field polariton resonance of SiC at 930 cm^{-1} , which has already been discussed in subsection 3.1.1. In addition to the polariton resonance, there exists a dip in the spectrum at the longitudinal

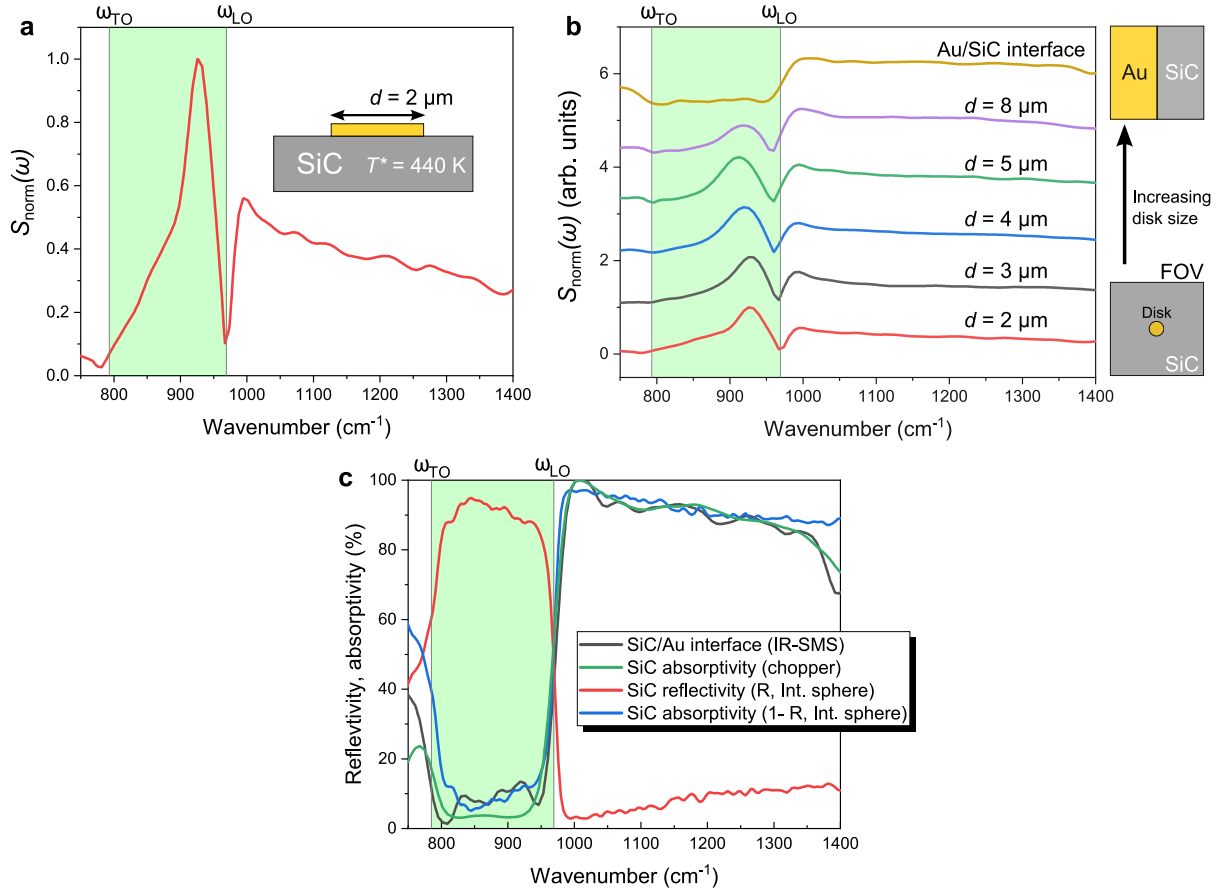


Figure 3.19: Far-field characterization of the near-field thermal radiation scattered by a single sub- λ Au disk (diameter, $d = 2 \mu\text{m}$) on a SiC substrate. The far-field signal is detected using the IR-SMS technique and normalized to the response of a reference blackbody sample. (b) IR-SMS spectra of the scattered near-field signal as a function of increasing disk diameter d . (c) Far-field absorption of a SiC substrate measured using three different techniques: IR-SMS at an Au/SiC substrate (black curve), optical chopping (green curve), and using an integrating sphere (blue curve). For the latter method, the absorptivity A was obtained from $A = 1 - R$, where R (red curve) is the sample's reflectivity (the sample was thick enough that the transmission was effectively zero). The optical chopper measurement was performed with the same optical setup as that of the IR-SMS technique except that the spatial modulation of the sample was replaced by the optical chopping of the signal by the blades of the chopper. The detected signal was demodulated at the frequency of chopping to improve the signal-to-noise ratio. To remove the signal coming from the blades of the chopper we performed a measurement on the bare SiC substrate and a reference measurement on a large Au pattern and took the difference of the two. The green-shaded regions mark the *Reststrahlen* band of SiC between ω_{TO} and ω_{LO} .

optical phonon frequency ω_{LO} which is followed by an increase again and a semi-flat behavior at higher frequencies.

We have already elaborated in the previous subsection on the fact that the signal observed in the IR-SMS experiment corresponds to the absorption from the sample by Kirchhoff's law. And since this is a far-field detection technique coupled with a near-field probe (the sub- λ disk), then the detected signal, in this case, is a sum of both the near- and far-field absorption of the

sample. One may argue, however, that since the substrate is uniform, the far-field response of the substrate should cancel out, as illustrated in subsection 3.2.1, and only the near-field response would be measured. This is only partially true in the current problem as we clearly observe far-field signatures of the SiC substrate in the spectrum shown in Fig. 3.19 (a). In particular, the dip at ω_{LO} corresponds to the low absorption of SiC at the upper edge of the *Reststrahlen* band (cf. Fig. 3.19 (c)).

This behavior can be understood by examining the detected signal in more detail. Since the Au disk is modulated in and out of the field of view of the detector, and the detected signal is demodulated at the frequency of this modulation (see subsection 3.2.1), then the detected signal is roughly given by the difference

$$\Delta S_{\text{det}} = |S_{\text{disk}}^{\text{in}} - S_{\text{disk}}^{\text{out}}|, \quad (3.38)$$

where $S_{\text{disk}}^{\text{in}}$ and $S_{\text{disk}}^{\text{out}}$ are the signals with the disk in and out of the detector's field of view, respectively. The latter signal simply corresponds to the bulk far-field absorption of the area of the SiC substrate filling the detector's field of view, which we denote as S_{bulk} . On the other hand, $S_{\text{disk}}^{\text{in}}$, can be further divided into two parts as follows

$$S_{\text{disk}}^{\text{in}} = S_{\text{scat}} + S'_{\text{bulk}}, \quad (3.39)$$

in which S_{scat} is the near-field signal scattered by the disk and S'_{bulk} is the bulk signal as before only this time the area of the substrate within the field of view is slightly reduced due to the presence of the disk. We can therefore rewrite Eq. (3.38) as a sum of two terms, a near-field term, and a far-field term:

$$\Delta S_{\text{det}} = |S_{\text{scat}} - \Delta S_{\text{bulk}}|, \quad (3.40)$$

where the far-field term, $\Delta S_{\text{bulk}} = S_{\text{bulk}} - S'_{\text{bulk}}$, is expected to scale with the size of the disk. We mention that since the scattering cross-section of the disk also scales with disk size (see Fig. 3.18), S_{scat} is expected to scale in the same manner.

To determine which term dominates in Eq. (3.40) as the disk size increases, we measured the IR-SMS spectra of a single disk as a function of increasing diameter d (Fig. 3.19 (b)). In addition to measuring spectra up to a disk diameter $d = 8 \mu\text{m}$, we also performed a measurement on a part of the sample that includes a gold pattern that is large enough to fill the detector's field of view, in which the modulation was performed at the interface between the Au pattern and the bare SiC substrate (Fig. 3.19 (b), gold colored curve). The latter measurement should correspond solely to the bulk absorption of SiC, S_{bulk} , since by virtue of Eq. (3.38), it is the difference between the thermal emission signal of SiC and Au, in which the thermal emission of Au can be neglected due to its high reflectance at infrared wavelengths (see Fig. 2.3 (b)). This is corroborated by the absence of the polariton resonance for this measurement, as well as by the comparison in Fig. 3.19 (c).

Due to the step-like behavior of the far-field absorption of SiC in the mid-infrared, in which the absorption switches from almost zero in the *Reststrahlen* band to almost 100 % for frequencies

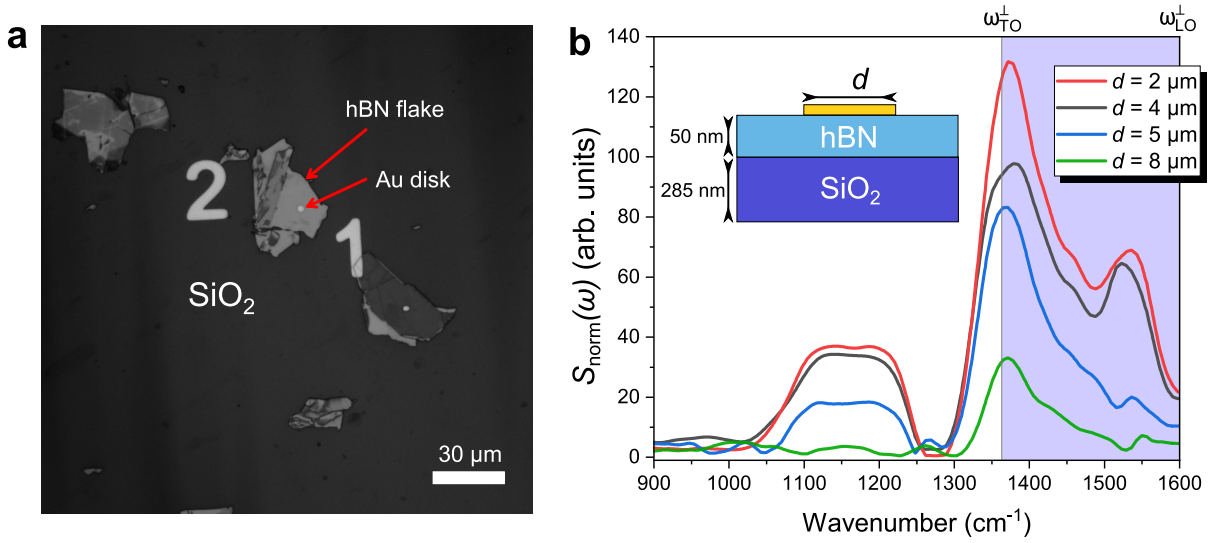


Figure 3.20: (a) Microscope image ($\times 50$ magnification) showing two 50-nm-thick hBN flakes, each with a single sub- λ Au disk on top. The disks were fabricated via optical lithography. Each flake has a disk with a different diameter d . The disks shown here correspond to (1) $d = 2 \mu\text{m}$ and (2) $d = 3 \mu\text{m}$. The disks all have a thickness of 110 nm. (b) Normalized IR-SMS spectra of a single Au disk of diameter d placed on an hBN flake as in panel (a). The purple-shaded region marks the type II *Reststrahlen* band of hBN.

$\omega > \omega_{\text{LO}}$ (see Fig. 3.19 (c)), one can ascertain the dominance of either term in Eq. (3.40) by examining the relative ratio between the amplitude of the polariton peak and that of the semi-flat part of the spectrum for $\omega > \omega_{\text{LO}}$ in Fig. 3.19 (b). By comparing these two amplitudes we find that the near-field contribution to the signal is predominant up to a disk diameter of 4 μm . For $d = 5 \mu\text{m}$ (Fig. 3.19 (b), green curve), the two contributions are comparable. Increasing the disk size further results in an enhancement of the far-field signal over that of the scattered near-field (see Fig. 3.19 (b), magenta curve). Additionally, increasing the disk size leads to a clear broadening of the SiC polariton resonance. We can conclude, therefore, that smaller disk sizes lead to better isolation of the near-field signal. One must keep in mind, however, that reducing the disk size too much decreases the disk's scattering cross-section which will result in a significant reduction in the possible near-field signal that may be detected.

3.2.3 Near-field spectroscopy of hBN thin films with local scatterers

We will now apply the near-field spectroscopy scheme of the previous subsection on an anisotropic hyperbolic material, namely on thin hBN flakes. Optical lithography was carried out on the sample used in subsection 3.1.3 to pattern a single sub- λ disk on some of the hBN flakes (see Fig. 3.20 (a)). Several hBN flakes were measured, each with a single disk of different diameter d , using IR-SMS. The resulting normalized spectra are plotted in Fig. 3.20 (b). For small disks ($d \leq 4 \mu\text{m}$) the spectra exhibit three resonance peaks: a broad peak centered at 1165 cm^{-1} and two other peaks at 1371 cm^{-1} and 1537 cm^{-1} . The first two peaks correspond to the polariton resonances of the SiO₂ substrate and the hBN thin film, respectively, as discussed in subsec-

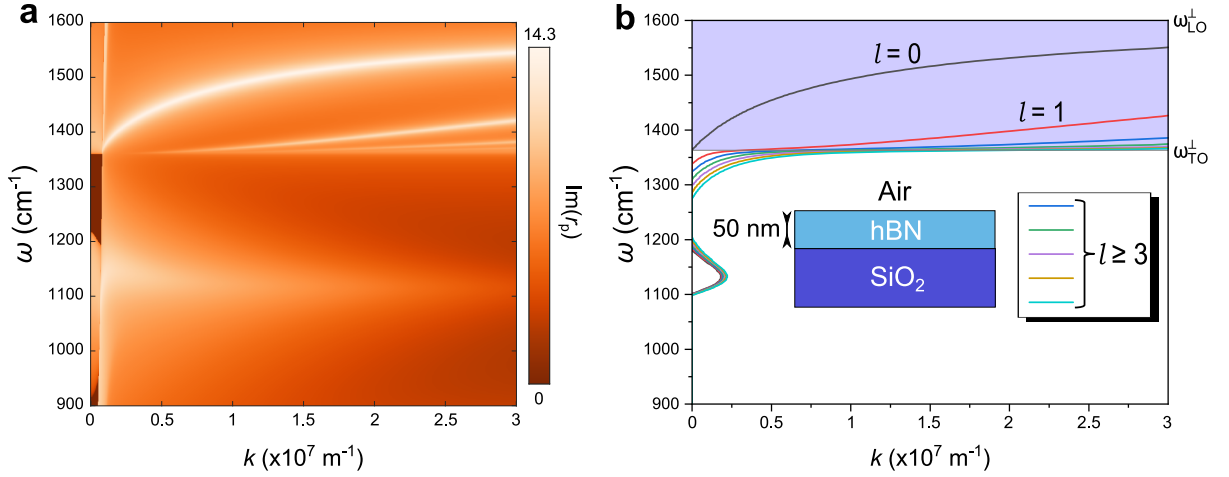


Figure 3.21: HPhP branches of the three-layer system sketched in the inset of panel (b), obtained from (a) the maxima of the imaginary part of Eq. (2.76) and (b) by solving Eq. (2.79) for mode number $0 \leq l \leq 6$. The purple-shaded region in panel (b) marks the *Reststrahlen* band corresponding to the type II HPhPs in hBN between $\omega_{\text{TO}}^{\perp}$ and $\omega_{\text{LO}}^{\perp}$.

tion 3.1.3. The third peak at 1537 cm^{-1} , which was previously unobserved in subsection 3.1.3, is another hyperbolic phonon-polariton resonance that arises within the *Reststrahlen* band of hBN.

To identify the origin of the resonance peaks observed in Fig. 3.20 (b), we calculated the dispersion curves of the HPhP modes of the air/hBN/SiO₂ multi-layer system corresponding to our sample (Fig. 3.21). One can clearly see from Fig. 3.21 that the lowest order HPhP branch ($l = 0$) of the multi-layer system has a large- k asymptotic value at $\omega = 1550 \text{ cm}^{-1}$, while all the higher order modes with $l > 1$ are overlapping near the transverse optical phonon frequency $\omega_{\text{TO}}^{\perp}$. Thus, the resonance observed at 1537 cm^{-1} in Fig. 3.20 (b) corresponds to the lowest order HPhP branch in hBN, whilst the resonance at 1371 cm^{-1} of higher amplitude, results from the lumped higher order HPhP branches.

As the disk size is increased, the amplitude of the observed resonances decreases, and in particular for $d \geq 4 \mu\text{m}$ the polariton resonance at 1537 cm^{-1} almost completely vanishes. This is due to the fact that the near-field contribution to the detected signal decreases with increasing disk size (see subsection 3.2.2). The amplitudes of the two polariton resonances of hBN decay disproportionately, however, since one is a resonance that corresponds to a single HPhP branch ($\omega = 1537 \text{ cm}^{-1}$), while the other comprises a resonance due to an infinite set of HPhP branches ($\omega = 1371 \text{ cm}^{-1}$), as discussed above.

In order to test the robustness of this near-field spectroscopy method, we also performed far-field detection of the scattered near-field signal of hBN flakes using an optical chopper, as described in Fig. 3.22 (a). Since the sensitivity of this detection scheme is significantly lower than that of the IR-SMS technique, we patterned a large number of scatterers filling the entire area of the hBN flake. The scatterers have a characteristic size of $2 \mu\text{m}$ and were distributed at random with a separation distance of $2 \mu\text{m}$. In Fig. 3.22 (b) we show the resulting spectra of two hBN flakes, each with a different type of scatterer, one with Au disks on top of the hBN

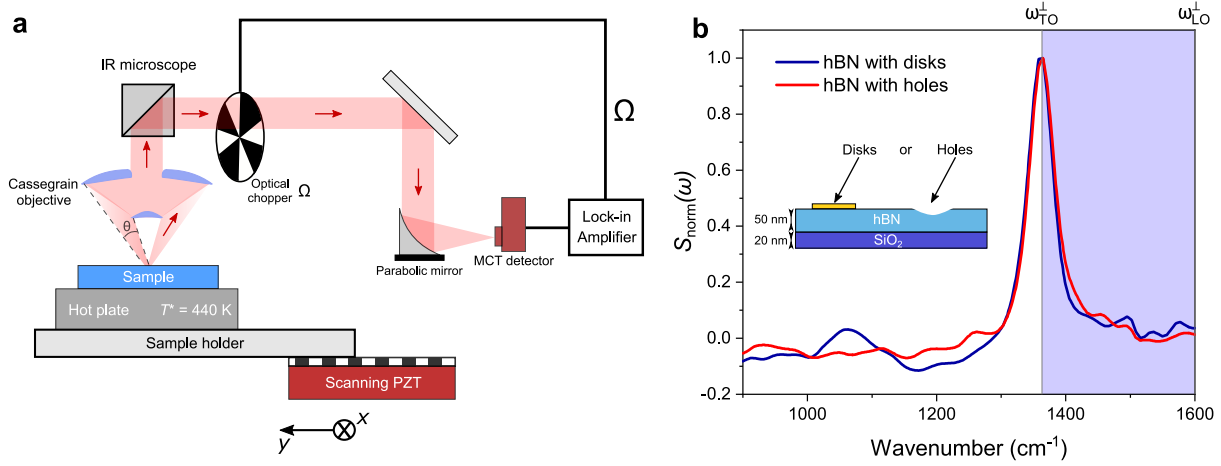


Figure 3.22: (a) Schematic illustration of the optical setup used to perform far-field optical characterization with a chopper. The setup is equivalent to that shown in Fig. 3.14 (a), except that the lateral modulation of the sample is replaced by the optical chopping of the light that is collected from the sample by the blades of the chopper. (b) Normalized far-field spectra, measured with the setup of panel (a), of an hBN flake with multiple Au disks (blue curve) and an hBN flake in which multiple holes were etched (red curve). Each spectrum is the result of the difference of two measurements, one with the hBN flake in the detection plane, and the other with the bare SiO₂ in the detection plane. The second measurement serves as a reference to remove the signal coming from the blades of the chopper.

layer (blue curve), and another with holes etched into the hBN (red curve). The disks have a diameter of 2 μm and a thickness of 110 nm. The holes have similar shape and size, except that their depth is equivalent to the thickness of the hBN layer (50 nm) at the center and decays radially outward (see Fig. 3.22 (b), inset).

It is clear from Fig. 3.22 (b) that both scatterers produce almost identical spectra, in which only the hBN resonance at $\omega_{\text{TO}}^{\perp}$ is resolved. The absence of the second hBN resonance that was previously observed, can be attributed to the much lower experimental sensitivity here. We note that the SiO₂ polariton resonance is also absent since the SiO₂ layer is much thinner (20 nm) here.

3.3 Far-field thermal radiation of a subwavelength polar dielectric sphere on a gold substrate

Heretofore, we have dealt with surface polaritons that are confined to the near-field of planar surfaces, requiring a near-field probe (such as an AFM tip or a local scatterer) to be measured in the far-field. We turn our attention now to the study of sub- λ polar-dielectric resonators. In particular, we report in this section the first investigation of the mid-IR thermal radiation of single sub- λ SiO₂ microspheres supporting surface phonon-polariton modes, using IR-SMS [35]. As we have seen in subsection 2.2.3, the surface modes of a sphere are coupled to outgoing propagating waves and thus can be directly measured in the far-field.

The study of the mid-IR thermal radiation of single sub- λ SiO₂ spheres presented here, could

be of particular interest to radiative cooling applications. This is due to their high emissivity in the mid-IR atmospheric transparency window, which is contrasted by a high scattering efficiency with minimal absorption at visible and near-infrared wavelengths, where the solar spectrum is prominent.

3.3.1 Infrared spatial modulation spectroscopy of single SiO₂ spheres on an Au substrate

To be able to measure the thermal radiation spectra of single microspheres, we place them on a gold substrate, which has the advantage of having a low emissivity at infrared wavelengths while acting as a mirror, directing the emitted radiation in the half-space where the collection optics are located (see Fig. 3.23 (a)). We note here that this situation is of interest for radiative cooling applications where a metallic mirror is often used as a substrate for reflectivity enhancement [36–38].

A solution of commercially available SiO₂ microspheres (Sigma Aldrich), of known size, is diluted and deposited on a 100 nm-thick gold substrate (see Appendix C for sample preparation). The sample is first examined with a visible microscope to determine the positions of single spheres (see Figs. 3.23 (b-e), insets). The far-field thermal radiation of the selected single spheres is then measured using IR-SMS as outlined in subsection 3.2.1.

The normalized IR-SMS spectra, $S_{\text{norm}}(\omega) = S_{\text{sphere}}(\omega, T^*)/S_{\text{BB}}(\omega, T^*)$ ³², of spheres of radii ranging from $r_o = 1$ to $2.5 \mu\text{m}$ are shown in Figs. 3.23 (b-e). The measurements show a prominent peak near 1130 cm^{-1} for the smallest sphere measured (Fig. 3.23 (b)), which vanishes as the sphere radius increases above $1 \mu\text{m}$ (Figs. 3.23 (c-e)) and is supplemented by a new predominant peak, near 1040 cm^{-1} , below the transverse optical phonon frequency (ω_{TO}) of SiO₂.

Previous studies have considered the problem of scattering by a sphere on a substrate analytically. Nevertheless, simple analytical solutions exist only for limited cases, such as a sphere replaced by electric and magnetic dipoles at its center [40–42] or for a perfectly electrically conducting substrate [43, 44]. We also note that calculating the thermal emission of a macroscopic sphere close to a substrate requires the framework of fluctuational electrodynamics and the discrete dipole approximation [45]. As mentioned in subsection 3.2.1, however, thermal emission from a sub- λ particle can be evaluated reciprocally by determining its absorption cross-section.

In an effort to quantitatively model our results, including the effect of the gold substrate, we performed finite-element method (FEM) simulations (Comsol Multiphysics) of the absorption cross-section of the solitary SiO₂ sphere on a gold surface (Figs. 3.23 (b-e), dotted curves). The advantage of this approach is two-fold; it allows one to solve for the full electromagnetic field within the considered geometry while precisely taking into account all the geometrical and material properties of our samples – most notably the dielectric function of the gold substrate

³²This normalization procedure is based on the assumption that the sphere and substrate are thermalized to the hot plate temperature (440 K). Due to the inherently small contact area between the sphere and substrate [39], we have assessed the possibility of a thermal gradient arising within the sphere as a consequence of conductive cooling through air and the sphere (see Appendix D). We find that the sphere temperature deviates by less than 1 K from the substrate temperature, thus validating our assumption.

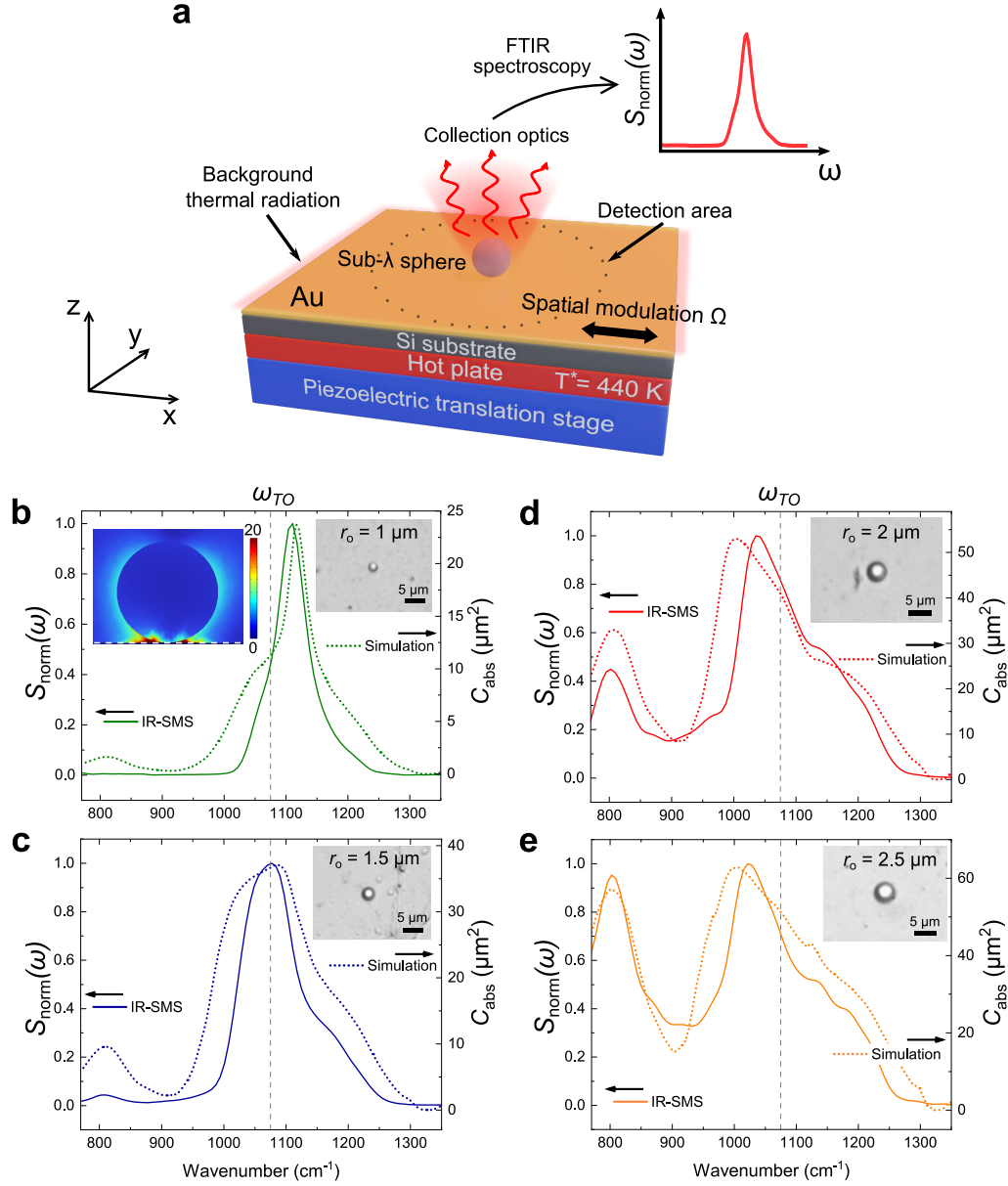


Figure 3.23: (a) Schematic illustration of an IR-SMS measurement of a single sub- λ sphere. (b-e) Measured IR-SMS thermal radiation spectra of single sub- λ SiO_2 spheres on a gold substrate (solid curves, left axis, normalized to 1), along with FEM simulations of their absorption cross-section (C_{abs} , dotted curves, right axis), for $r_o = 1, 1.5, 2,$ and $2.5 \mu\text{m}$. The dashed vertical line marks the spectral position of the transverse optical phonon resonance frequency (ω_{TO}) in SiO_2 . The plotted FEM spectra correspond to the absorption cross-section (C_{abs}) of the sphere on gold, simulated with unpolarized light, averaged for incident angles from 10 to 30° (see Appendix A for more details). The insets show visible microscope images of the measured spheres, taken using a $\times 50$, $\text{NA}=0.55$ visible objective. The left inset of panel (b) shows the simulated electric field enhancement $|E|/|E_0|$, where $|E_0|$ is the amplitude of the incident electric field (incident at 20° from the normal), calculated at the peak of the absorption cross-section, in the xz -plane for a sphere with $r_o = 1 \mu\text{m}$ on a gold surface. The white dashed line indicates the intersection of the gold substrate with the sphere.

3.3. Far-field thermal radiation of a subwavelength polar dielectric sphere on a gold substrate

– without any approximations. For an accurate representation of the angular interval in which emission from our sample is collected by the Cassegrain objective used in the measurements³³, we simulated the absorption cross-section of the sphere on gold for unpolarized light impinging at various angles from 10 to 30° (measured from the normal to the Au substrate) and averaged the resulting spectra (see Appendix E, Fig. A4, for the corresponding angle-resolved spectra), which provides a good fit with the measurements (cf. Figs. 3.23 (b-e), solid and dotted curves).

Interestingly, the simulations show that very high absorption cross-sections can be reached when the dielectric sphere is placed on the metallic substrate. For comparison, the measured sphere with $r_o = 1 \mu\text{m}$ on a gold substrate, has an absorption cross-section of $24 \mu\text{m}^2$ (Fig. 3.23 (b), dotted curve), at a wavelength of $8.85 \mu\text{m}$ ($\sim 1130 \text{ cm}^{-1}$), while a typical mid-IR plasmonic antenna of the same characteristic size has an absorption cross-section of $18 \mu\text{m}^2$, at a resonance wavelength of $7 \mu\text{m}$ [28].

To gain further qualitative insight regarding the origin of the resonances observed in Figs. 3.23 (b-e) and to highlight any similarities or differences between the case of a sphere on a metallic substrate and a sphere in free space, we have also performed Mie theory calculations of the absorption cross-section of the measured spheres in vacuum (Figs. 3.24 (c-f)), which we illustrate below.

As we have already seen in subsection 2.2.3, the virtual modes of a polar dielectric sphere all have complex frequencies and can be classified into three types: (i) low-frequency modes having frequency $\omega \leq \omega_{\text{TO}}$, where the real part of the sphere’s dielectric function is positive ($\epsilon' > 0$) (ii) high-frequency modes for which $\omega \geq \omega_{\text{LO}}$, and (iii) surface modes with frequencies that are intermediate between ω_{TO} and ω_{LO} , where $\epsilon' < 0$ (see Fig. 3.24 (b)). However, in an optical experiment, the measured observables, such as the sphere’s cross-sections, correspond to real frequencies.

The cross-sections of a sphere in free space, illuminated by a plane wave, can be calculated from Mie theory as follows [20, 46].

$$C_{\text{ext}} = \frac{\lambda^2}{2\pi} \sum_{l=1}^{\infty} (2l+1) \text{Re}(a_l + b_l), \quad (3.41)$$

$$C_{\text{scat}} = \frac{\lambda^2}{2\pi} \sum_{l=1}^{\infty} (2l+1) (|a_l|^2 + |b_l|^2), \quad (3.42)$$

and

$$C_{\text{abs}} = C_{\text{ext}} - C_{\text{scat}}, \quad (3.43)$$

where a_l and b_l , are *scattering coefficients*, and l is the mode number.

In this context, the fields are expanded in terms of multipoles, alternatively of the electric and magnetic type, given by the scattering coefficients a_l and b_l , respectively. Hence, a_1 and b_1 correspond to the electric and magnetic dipolar modes, a_2 and b_2 correspond to the electric and

³³The measurements presented here were performed with a $\times 36$, $\text{NA} = 0.5$ Cassegrain objective that collects light between 10 and 30° (measured from the normal to the sample surface).

magnetic quadrupolar modes, and so on.

The scattering coefficients can be cast in the following form

$$a_l = \frac{\varepsilon j_l(\rho_1)[\rho_2 j_l(\rho_2)]' - j_l(\rho_2)[\rho_1 j_l(\rho_1)]'}{\varepsilon j_l(\rho_1)[\rho_2 h_l^{(1)}(\rho_2)]' - h_l^{(1)}(\rho_2)[\rho_1 j_l(\rho_1)]'}, \quad (3.44)$$

$$b_l = \frac{j_l(\rho_1)[\rho_2 j_l(\rho_2)]' - j_l(\rho_2)[\rho_1 j_l(\rho_1)]'}{j_l(\rho_1)[\rho_2 h_l^{(1)}(\rho_2)]' - h_l^{(1)}(\rho_2)[\rho_1 j_l(\rho_1)]'}. \quad (3.45)$$

In the above, j_l and $h_l^{(1)}$ are the spherical Bessel and Hankel functions of the first kind, respectively, $\rho_1 = \frac{2\pi r_o}{\lambda} \sqrt{\varepsilon}$, $\rho_2 = \frac{2\pi r_o}{\lambda}$, and $'$ denotes differentiation with respect to the argument of the Bessel functions.

The frequencies of the sphere's transverse virtual modes correspond to that of vanishing denominators of the real parts of the scattering coefficients a_l and b_l (cf. Eqs. (3.44)-(3.45) and Eqs. (2.59)-(2.60) with $\varepsilon_I = 1$), thus, each virtual mode coincides with a peak in the sphere's cross-section spectrum.

Figures 3.24 (c-f) show Mie theory calculations of the absorption cross-section, calculated from Eq. (3.43), corresponding to the measured spheres in vacuum (black curves), along with the individual contributions of the first few electric and magnetic modes (given by the coefficients a_l and b_l) to the absorption cross-section in each case (colored curves). Data reported in ref. [24] were used for the dielectric constant of SiO₂ (Fig. 3.24 (b)). For $r_o = 1 \mu\text{m}$, a sharp resonance peak is observed in the total absorption cross-section between ω_{TO} and ω_{LO} (blue shaded region), near 1130 cm^{-1} . This peak corresponds to the spheres' surface mode, which represents the mid-IR phononic counterpart of plasmonic resonances characteristic of noble metals in the visible spectral range. We have shown in subsection 2.2.3 that in the quasi-electrostatic approximation, this mode's frequency coincides with the condition: $\varepsilon' = -(l+1)/l$ (cf. Eq. (2.63) with $\varepsilon_I = 1$), for which $l=1$ gives the frequency of the Fröhlich mode. In addition to becoming predominant as the sphere size decreases [47], the surface mode has been shown to be exclusively of electric nature [48]. As evidenced by Fig. 3.24 (c), the dominant contribution to the surface mode peak in the smallest considered sphere comes from the electric dipolar mode (cf. Fig. 3.24 (a)), hence, corresponding to the Fröhlich mode, while as the sphere radius increases, contributions from higher order modes, such as the quadrupolar electric mode (a_2 , blue curves), and the octupolar mode (a_3 , turquoise curve), become more pronounced (see Fig. 3.24 (f)).

By comparing the calculated absorption cross-sections of the spheres with and without the gold substrate (Figs. 3.23 (b-e), and Figs. 3.24 (c-f), respectively), it is clear that the metallic substrate induces a large enhancement of the spheres' absorption cross-section. In particular, for the smallest considered sphere, which mainly exhibits dipolar emission, the FEM simulation with the gold substrate shows an enhancement of the sphere's absorption cross-section above the unitary limit of $3\lambda^2/8\pi$ (where λ is the resonance wavelength) for a resonant dipole in vacuum [49]. This limit corresponds to $9.35 \mu\text{m}^2$ at 1130 cm^{-1} . As shown in the left inset of Fig. 3.23 (b), the presence of the gold substrate leads to a large electric field enhancement between the sphere and substrate, giving rise to increased local field absorption by the sphere. This increase is ultimately expressed in the large values of C_{abs} obtained in Figs. 3.23 (b-e) for the sphere on

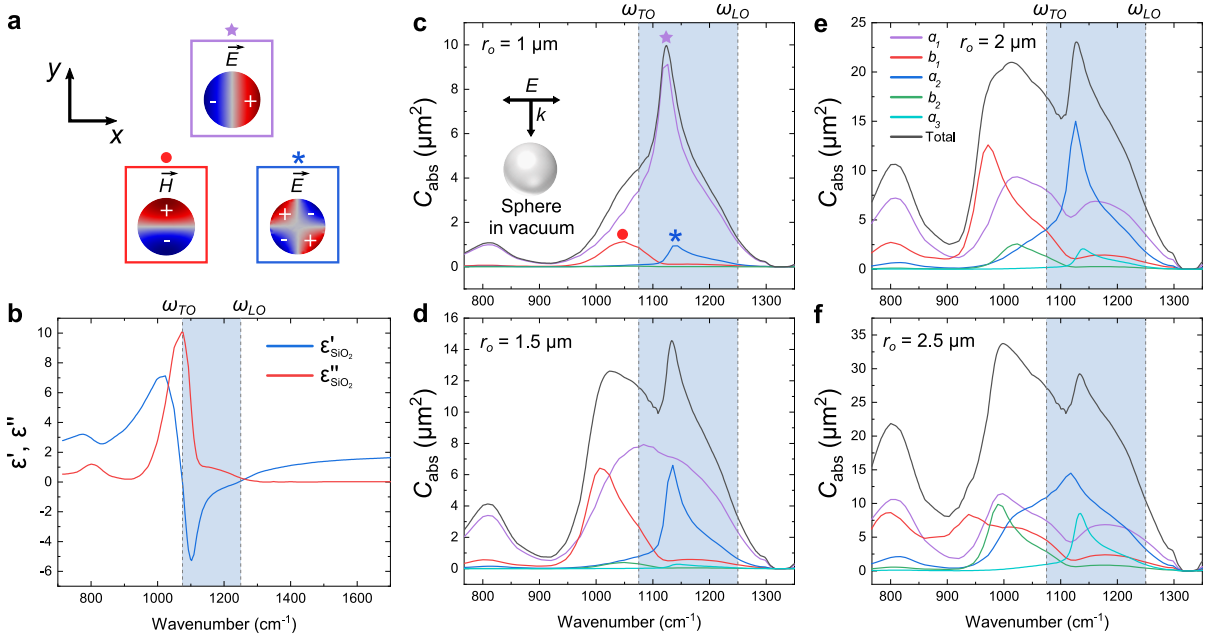


Figure 3.24: (a) Simulated distribution of the electric (\vec{E}) and magnetic (\vec{H}) fields inside an SiO₂ sphere of radius $r_o = 1 \mu\text{m}$, in vacuum (for electric field incident into the page and polarized along x) at the maxima of the peaks indicated by the markers in panel (c). They correspond to the electric dipole (star), magnetic dipole (circle), and electric quadrupole (asterisk) modes of the sphere. (b) Real (ϵ'_{SiO_2}), and imaginary ($\epsilon''_{\text{SiO}_2}$) parts of the dielectric function of SiO₂, taken from ref. [24]. The blue shaded region indicates the *Reststrahlen* band between the transverse (ω_{TO}) and the longitudinal (ω_{LO}) optical phonon frequencies in which the real part of the dielectric function is negative. (c-f) Mie theory calculation of the absorption cross-section of SiO₂ spheres in vacuum, of radii (c) $r_o = 1 \mu\text{m}$, (d) $r_o = 1.5 \mu\text{m}$, (e) $r_o = 2 \mu\text{m}$, and (f) $r_o = 2.5 \mu\text{m}$, along with the individual contributions of the first few electric and magnetic modes to the absorption cross-section.

gold.

In contrast to a sphere in vacuum, the pronounced surface mode peak (between ω_{TO} and ω_{LO}) is markedly absent in the thermal radiation spectra of a sphere on a gold substrate for $r_o > 1 \mu\text{m}$ (Figs. 3.24 (c-e)). As r_o increases above $1 \mu\text{m}$, the electric dipolar mode red-shifts towards ω_{TO} , where the material absorbs resonantly (see Figs. 3.24 (d-f), a_1 , magenta). The electric dipolar mode, thus, broadens due to material losses and increased radiative damping with increasing sphere size and eventually splits into two peaks, one with frequency $\omega < \omega_{\text{TO}}$, and another with $\omega_{\text{TO}} < \omega < \omega_{\text{LO}}$ (Figs. 3.24 (e) and (f), magenta curve). For spheres with diameters above $2 \mu\text{m}$, we also observe a major contribution to the radiation spectrum from the magnetic dipolar mode below ω_{TO} (Figs. 3.24 (d-f), red curve). The electric and magnetic dipolar Mie modes correspond to the spheres' low-frequency transverse mode, which is predominant in the total absorption (equivalently, emission) spectrum of the sphere on gold. The emergence of these modes can be explained by the large real part of the dielectric constant of SiO₂, ϵ'_{SiO_2} , just below ω_{TO} (see Fig. 3.24 (b)). The magnetic modes in particular arise from the coupling of circular displacement currents of the electric field, with incoming radiation, when $2r_o \sim \lambda/n$

[50], where n is the real part of the index of refraction of the sphere, and λ is the wavelength of incident light. It is also interesting to note that $\varepsilon'_{\text{SiO}_2}$ is positive in this spectral region, while it is negative in the *Reststrahlen* band, which changes the nature of the observed resonances.

In Figs. 3.23 (b-e) we can, thus, observe a transition from an absorption cross-section dominated by a phononic mode ($r_o = 1 \mu\text{m}$, $\varepsilon'_{\text{SiO}_2} < 0$, Fig. 3.23 (b)) to that dominated by electric and magnetic dipolar geometrical Mie modes ($r_o > 1 \mu\text{m}$, $\varepsilon'_{\text{SiO}_2} > 0$, Figs. 3.23 (c-e)). These results also show that a sphere radius of $1.5 \mu\text{m}$ can be considered as a cross-over value between the two observed absorption regimes.

Figures 3.24 (c-f) also show a peak in the absorption spectrum around 800 cm^{-1} , which is invariant with respect to sphere size. This peak results from the bulk absorption of SiO_2 , due to the presence of a local maximum in the imaginary part of the dielectric function at this frequency (see Fig. 3.24 (b)). Note that the high-frequency transverse modes ($\omega \geq \omega_{\text{LO}}$) will not be discussed here as they arise at very large frequencies (several times ω_{TO}) for the sphere sizes considered here [51], which lie outside of the spectral range accessible by our experiment.

Overall, the gold substrate leads to an enhancement of the spheres' low-frequency mode – which is dominated by electric and magnetic dipolar Mie modes – over the spheres' surface mode (cf. Figs. 3.23 (c-e) with Figs. 3.24 (d-f)). A slight red-shift in the spheres' resonance peaks is also observed in the presence of the substrate. This is a signature of the interaction with the gold substrate [52–54]. In the mid-IR, the Au substrate acts as a mirror. When a sphere is placed on top of it, it might look, at first glance, as a dimer of two stacked spheres. Yet, when considering near-field interactions, the situation is dramatically different due to the π phase-shift of the in-plane electric field component, induced by the metallic surface, as sketched in Fig. 3.25 (a). For spheres that act as dipoles very close to the surface in the quasi-electrostatic limit [12], the effect of the substrate is described by the sphere's interaction with the induced image charges of opposite sign. The observed red-shift is a direct consequence of the attraction between the sphere and its image.

As presented in Figs. 3.24 (d) and (e), a large contribution to the surface mode for the 1.5 and $2 \mu\text{m}$ radius spheres, in the absence of the substrate, comes from the electric quadrupolar mode (a_2 , blue curve), while the sphere's low-frequency mode arises mainly due to the electric dipolar Mie mode (a_1 , magenta curve). Figure 3.25 (b) (top panel) shows the simulated electric field enhancement map calculated at the surface mode frequency (1130 cm^{-1}), which indeed reveals a distribution expected for a quadrupolar mode. When the gold substrate is introduced, the presence of charges near the bottom of the sphere, that are in close proximity to the induced image charges for this mode (Fig. 3.25 (a)), leads to a strong field enhancement and confinement between the sphere and substrate (Fig. 3.25 (b), bottom panel). This leads to an increased cross-section with respect to the isolated sphere case, as well as a distortion of the mode's field distribution, resulting in a quasi-total suppression of the sphere's surface mode, in good agreement with the absence of the peak near 1130 cm^{-1} in Figs. 3.23 (c) and (d).

For a radius of $2.5 \mu\text{m}$, the measurements and simulations show that the surface mode is again observable in the presence of the substrate (Fig. 3.23 (e)). When the sphere is that large, the sphere/image pair, which was heretofore of sub- λ dimensions, becomes comparable to the

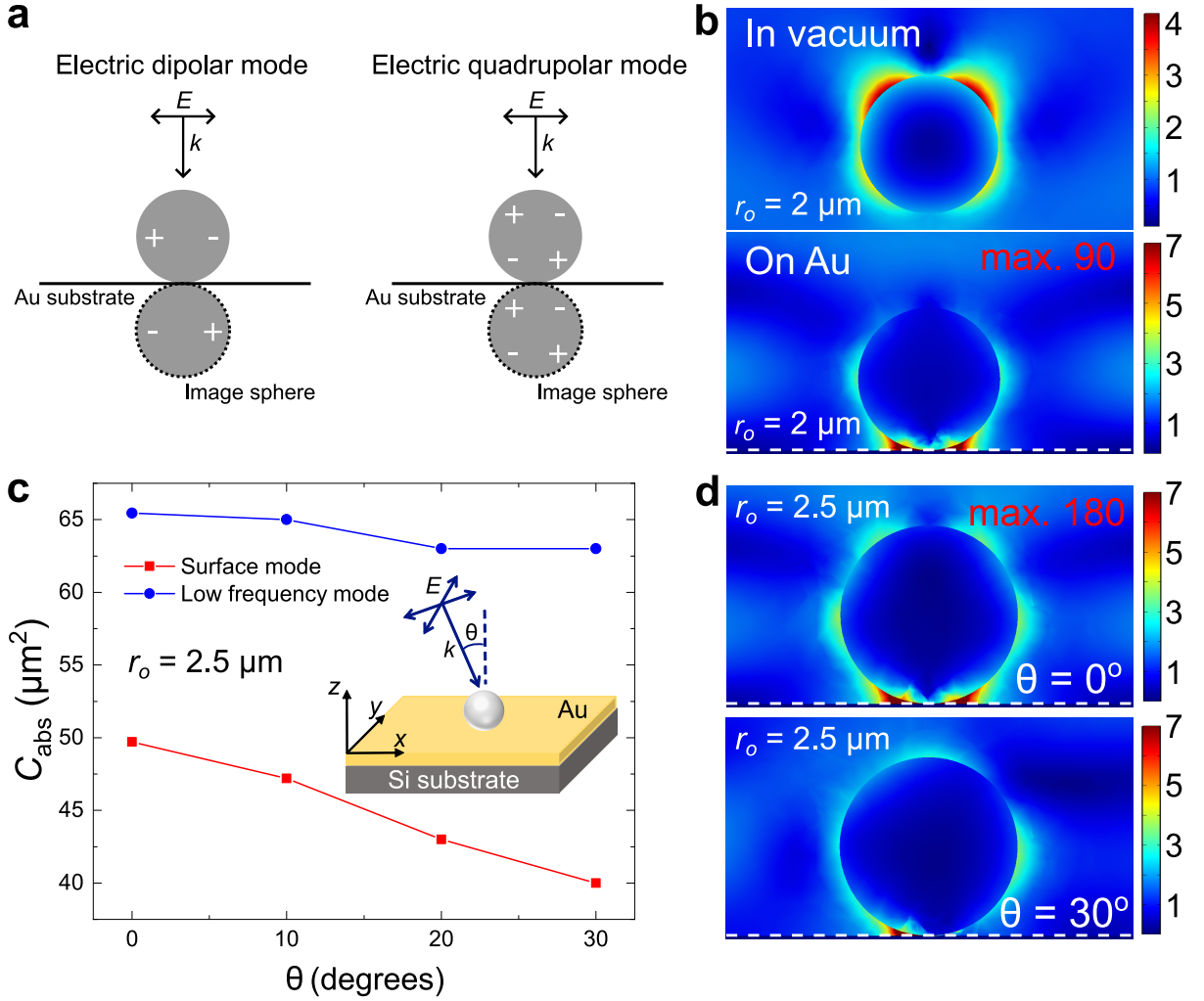


Figure 3.25: (a) Sketch of the sphere and image sphere charges, induced by the gold substrate, for the electric dipolar and quadrupolar modes. (b) Simulated electric field enhancement ($|E|/|E_0|$), calculated at the electric quadrupolar mode frequency in the xz -plane for a sphere with $r_o = 2 \mu\text{m}$ in vacuum (top panel), and on an Au substrate (bottom panel), for normal incidence, $\theta = 0^\circ$. Due to the large field enhancement between the sphere and substrate, the color bar in the bottom panel is scaled to reveal the field features. The value in the top right inset in red indicates the maximal calculated field enhancement near the point of intersection between the sphere and the gold substrate. The white dashed line indicates the intersection of the gold substrate with the sphere. (c) Calculated absorption cross-section at the surface and low-frequency virtual modes of an SiO_2 sphere with $r_o = 2.5 \mu\text{m}$ on Au, for unpolarized light incident at various angles θ , as sketched in the inset. (d) Electric field enhancement plots of an SiO_2 sphere with $r_o = 2.5 \mu\text{m}$ on gold, for $\theta = 0$ and $\theta = 30^\circ$.

wavelength of excited thermal radiation (equivalently to the wavelength of incident radiation in the calculations, since emissivity is equal to absorptivity). The behavior, in this case, is no longer dominated by quasi-electrostatic interactions, and the quadrupolar mode is found to be less degraded on the gold substrate, for normal incidence, compared to the case of spheres with smaller diameters (see Fig. 3.25 (d), top panel). Higher order modes, such as the octupolar mode (see Fig. 3.24 (f), turquoise curve), are also excited and contribute to the sphere's surface

mode for this large size. Consequently, the surface mode is still observable near 1130 cm^{-1} in the measured thermal radiation spectrum in this case (Fig. 3.23 (e)), in spite of the perturbation induced by the metallic substrate.

In addition to inducing image charges of the sphere, the gold substrate breaks the spherical symmetry so that the resonances of the sphere become dependent on the properties of the incident electric field, *i.e.*, on the field's polarization and angle of incidence [55]. By the principle of reciprocity, this means that the far-field thermal radiation spectrum of a sphere on a substrate will depend on the angle at which it is probed – determined by the reflective objective in our measurements, which is not the case for a sphere in vacuum or surrounded by a homogeneous dielectric medium.

To elucidate this point, and to study the influence of the angle of incidence on the sphere's virtual modes, we show in Fig. 3.25 (c) the values of the absorption cross-section, obtained from FEM simulations of a sphere with $r_o = 2.5\ \mu\text{m}$, on a gold substrate, for various angles of incidence θ (from 0 to 30°), at the frequencies of the surface mode (1130 cm^{-1}) and low-frequency mode (1000 cm^{-1}) (see Fig. A4 (b), Appendix E, for full spectra). It is found that the surface mode in this case is greatly influenced by the angle of incidence, whereas the low-frequency virtual mode, with its characteristic dipolar emission, is unaffected (see Fig. 3.25 (c), blue circles). The surface mode peak exhibits a significant contribution to the total absorption cross-section, at normal incidence, for a sphere with $r_o = 2.5\ \mu\text{m}$, on gold (see Fig. A4 (b)). Nevertheless, its contribution decreases with increasing angle and disappears completely at 30° (Fig. A4 (b), green curve). At large angles, the asymmetry of the induced charges around the sphere results in a reduction of the sphere's surface mode peak. This is corroborated by the field plot in Fig. 3.25 (d) (bottom panel), which shows a distorted field distribution around the sphere at 30° incidence, near the surface mode frequency.

3.3.2 Thermal radiation of sub- λ PTFE spheres

In order to show that the unique spectral features exhibited by the studied sub- λ SiO_2 spheres originate from the excitation of virtual SPhP modes in combination with geometrical Mie modes, we measured the thermal radiation of a sub- λ polytetrafluoroethylene (PTFE) sphere, with $r_o = 1.5\ \mu\text{m}$, placed on a gold substrate (Fig. 3.26 (a)). PTFE is a polymer with high absorption in the mid-IR and no *Reststrahlen* band (see Fig. 3.26 (b), inset). The measurement and corresponding simulation reveal two peaks near 1159 and 1220 cm^{-1} , akin to the bulk absorption peaks of PTFE (cf. Fig. 3.26 (b), inset). Further, Mie theory calculations of a PTFE sphere in vacuum with variable radius r_o (Fig. 3.26 (b)) show that the absorption spectrum is invariant with respect to sphere size.

The absorption length of mid-IR photons in PTFE, at its absorption peaks, is around $1\ \mu\text{m}$ (calculated as $\lambda/4\pi\kappa$, where κ is the imaginary part of the index of refraction). For a sub- λ PTFE sphere to be resonant at mid-IR frequencies, its characteristic size should thus be smaller than $1\ \mu\text{m}$. This is too small to produce size-dependent absorption resonances at mid-IR wavelengths. Bulk features, therefore, dominate the absorption spectrum of such lossy spheres. By contrast, the investigated SiO_2 spheres display phononic and size-dependent resonances, in spite of an

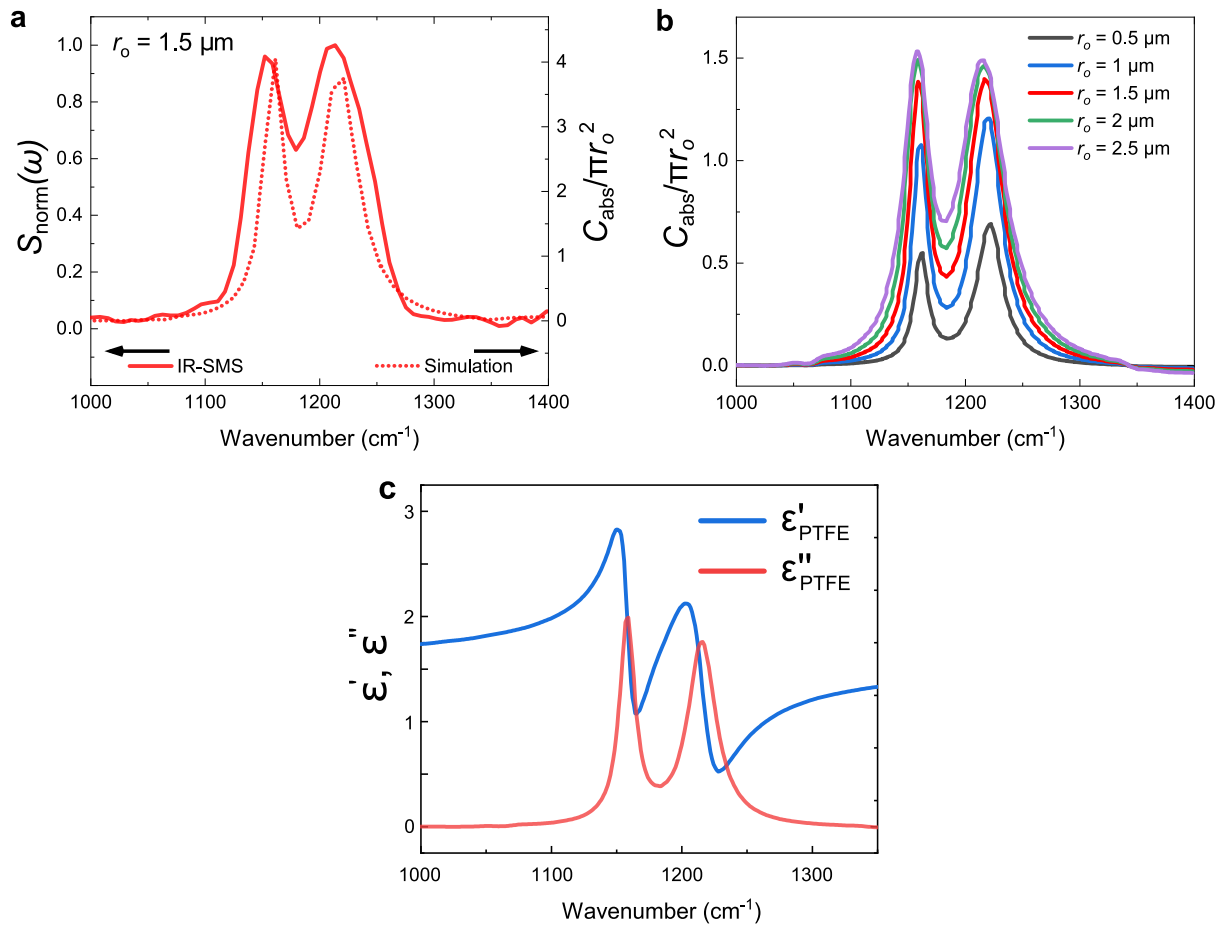


Figure 3.26: (a) Measured thermal radiation spectrum of a single PTFE sphere with $r_o = 1.5 \mu\text{m}$ on a gold substrate (solid curve, left axis) and its corresponding simulated absorption efficiency ($C_{\text{abs}}/\pi r_o^2$, dotted curve, right axis) for unpolarized light averaged over various angles of incidence from 10 to 30° from the normal. (b) Mie theory calculation of the absorption efficiency of PTFE spheres, in vacuum, of various radii r_o . (c) Real (ϵ'_{PTFE}) and imaginary (ϵ''_{PTFE}) parts of the dielectric function of PTFE, taken from ref. [56].

absorption length of $\sim 0.4 \mu\text{m}$ near the surface mode frequency.

It has been shown that the absorption efficiency ($C_{\text{abs}}/\pi r_o^2$) of lossy spheres, such as the PTFE spheres considered here, is limited to $\sim 3/2$ for large radii [57]. This is consistent with our calculations of the absorption efficiency of large PTFE spheres in vacuum based on Mie theory (see Fig. 3.26 (b), green and magenta curves). For a PTFE sphere on a gold substrate (Fig. 3.26 (a)), the absorption efficiency reaches more than twice this value due to the presence of the image sphere.

3.4 Conclusion

Near-field detection techniques were thoroughly discussed and presented. Special focus was given to scattering-type near-field techniques, such as s-SNOM. We have presented near-field spectroscopy measurements of typical polaritonic materials using s-SNOM (nano-FTIR) and

illustrated the modeling involved in these types of measurements. We then applied these measurement and modeling procedures to measure the local thickness and dielectric properties of hBN flakes. We also presented a novel near-field spectroscopy technique, in which sub- λ scatterers that were fabricated on the surface of a polaritonic material, were used to couple the sample's near-field signal to the far-field where it could be detected. Lastly, we illustrated the first measurements of the far-field thermal radiation of single sub- λ spheres on a gold substrate via IR-SMS [35]. This study revealed that a sub- λ SiO₂ sphere on gold undergoes a transition from a phonon-mode-dominated to a Mie-mode dominated emission (or absorption) spectrum, as its radius is increased from 1 to 2.5 μm .

References

- [1] E Abbe. “Beiträge zur Theorie des Mikroskops und der mikroskopischen Wahrnehmung”. *Arch. Mikroskop. Anat.* 9.1 (1873), pp. 413–468.
- [2] L Rayleigh. “Investigations in optics, with special reference to the spectroscope”. *Lond. Edinb. Dublin philos. mag.* 8.49 (1879), pp. 261–274.
- [3] EH Synge. “XXXVIII. A suggested method for extending microscopic resolution into the ultra-microscopic region”. *Lond. Edinb. Dublin Philos. Mag.* 6.35 (1928), pp. 356–362.
- [4] EH Synge. “XXIII. An application of piezo-electricity to microscopy”. *Lond. Edinb. Dublin Philos. Mag.* 13.83 (1932), pp. 297–300.
- [5] EA Ash and G Nicholls. “Super-resolution aperture scanning microscope”. *Nature* 237.5357 (1972), pp. 510–512.
- [6] ZM Zhang, ZM Zhang, and Luby. *Nano/microscale heat transfer*. Vol. 410. Springer, 2007.
- [7] L Novotny and B Hecht. *Principles of nano-optics*. Cambridge University Press, 2012.
- [8] M Born and E Wolf. *Principles of optics: electromagnetic theory of propagation, interference and diffraction of light*. Elsevier, 2013.
- [9] LD Landau, EM Lifšic, EM Lifshitz, AM Kosevich, and LP Pitaevskii. *Theory of elasticity: volume 7*. Vol. 7. Oxford: Pergamon Press, 1986.
- [10] G Wurtz, R Bachelot, and P Royer. “A reflection-mode apertureless scanning near-field optical microscope developed from a commercial scanning probe microscope”. *Rev. Sci. Instrum.* 69.4 (1998), pp. 1735–1743.
- [11] M Labardi, S Patane, and M Allegrini. “Artifact-free near-field optical imaging by apertureless microscopy”. *Appl. Phys. Lett.* 77.5 (2000), pp. 621–623.
- [12] B Knoll and F Keilmann. “Enhanced dielectric contrast in scattering-type scanning near-field optical microscopy”. *Opt. Commun.* 182.4-6 (2000), pp. 321–328.
- [13] F Keilmann and R Hillenbrand. “Near-field microscopy by elastic light scattering from a tip”. *Philos. Trans. Royal Soc. A* 362.1817 (2004), pp. 787–805.
- [14] F Huth, A Govyadinov, S Amarie, W Nuansing, F Keilmann, and R Hillenbrand. “Nano-FTIR absorption spectroscopy of molecular fingerprints at 20 nm spatial resolution”. *Nano Lett.* 12.8 (2012), pp. 3973–3978.
- [15] R Hillenbrand, T Taubner, and F Keilmann. “Phonon-enhanced light–matter interaction at the nanometre scale”. *Nature* 418.6894 (2002), pp. 159–162.
- [16] AA Govyadinov, I Amenabar, F Huth, PS Carney, and R Hillenbrand. “Quantitative measurement of local infrared absorption and dielectric function with tip-enhanced near-field microscopy”. *J. Phys. Chem. Lett.* 4.9 (2013), pp. 1526–1531.
- [17] A Cvitkovic, N Ocelic, and R Hillenbrand. “Analytical model for quantitative prediction of material contrasts in scattering-type near-field optical microscopy”. *Opt. Express* 15.14 (2007), pp. 8550–8565.

- [18] A Babuty, K Joulain, PO Chapuis, JJ Greffet, and Y De Wilde. “Blackbody spectrum revisited in the near field”. *Phys. Rev. Lett.* 110.14 (2013), p. 146103.
- [19] LM Zhang, GO Andreev, Z Fei, AS McLeod, G Dominguez, M Thiemens, AH Castro-Neto, DN Basov, and MM Fogler. “Near-field spectroscopy of silicon dioxide thin films”. *Phys. Rev. B* 85.7 (2012), p. 075419.
- [20] CF Bohren and DR Huffman. *Absorption and scattering of light by small particles*. John Wiley & Sons, 2008.
- [21] B Hauer, AP Engelhardt, and T Taubner. “Quasi-analytical model for scattering infrared near-field microscopy on layered systems”. *Opt. Express* 20.12 (2012), pp. 13173–13188.
- [22] A Röseler and EH Korte. “Infrared spectroscopic ellipsometry”. *Handbook of Vib. Spectrosc.* (2006).
- [23] S Dai, Q Ma, MK Liu, T Andersen, Z Fei, MD Goldflam, M Wagner, K Watanabe, T Taniguchi, M Thiemens, et al. “Graphene on hexagonal boron nitride as a tunable hyperbolic metamaterial”. *Nat. Nanotechnol.* 10.8 (2015), pp. 682–686.
- [24] ED Palik. *Handbook of optical constants of solids*. Vol. 3. Academic press, 1998.
- [25] Y Cai, L Zhang, Q Zeng, L Cheng, and Y Xu. “Infrared reflectance spectrum of BN calculated from first principles”. *Solid State Commun.* 141.5 (2007), pp. 262–266.
- [26] JD Caldwell, AV Kretinin, Y Chen, V Giannini, MM Fogler, Y Francescato, CT Ellis, JG Tischler, CR Woods, AJ Giles, et al. “Sub-diffractive volume-confined polaritons in the natural hyperbolic material hexagonal boron nitride”. *Nat. Commun.* 5.1 (2014), pp. 1–9.
- [27] A Arbouet, D Christofilos, N Del Fatti, F Vallée, JR Huntzinger, L Arnaud, P Billaud, and M Broyer. “Direct measurement of the single-metal-cluster optical absorption”. *Phys. Rev. Lett.* 93.12 (2004), p. 127401.
- [28] C Li, V Krachmalnicoff, P Bouchon, J Jaeck, N Bardou, R Haidar, and Y De Wilde. “Near-field and far-field thermal emission of an individual patch nanoantenna”. *Phys. Rev. Lett.* 121.24 (2018), p. 243901.
- [29] Y De Wilde, F Formanek, R Carminati, B Gralak, PA Lemoine, K Joulain, JP Mulet, Y Chen, and JJ Greffet. “Thermal radiation scanning tunnelling microscopy”. *Nature* 444.7120 (2006), pp. 740–743.
- [30] AC Jones and MB Raschke. “Thermal infrared near-field spectroscopy”. *Nano Lett.* 12.3 (2012), pp. 1475–1481.
- [31] JH Lambert. *Photometria sive de mensura et gradibus luminis, colorum et umbrae*. Klett, 1760.
- [32] G Kirchhoff. “I. On the relation between the radiating and absorbing powers of different bodies for light and heat”. *Lond. Edinb. Dublin Philos. Mag. J. Sci.* 20.130 (1860), pp. 1–21.
- [33] JJ Greffet, P Bouchon, G Brucoli, and F Marquier. “Light emission by nonequilibrium bodies: local Kirchhoff law”. *Phys. Rev. X* 8.2 (2018), p. 021008.
- [34] HE Revercomb, H Buijs, HB Howell, DD LaPorte, WL Smith, and LA Sromovsky. “Radiometric calibration of IR Fourier transform spectrometers: solution to a problem with the High-Resolution Interferometer Sounder”. *Appl. Opt.* 27.15 (1988), pp. 3210–3218.
- [35] L Abou-Hamdan, L Coudrat, S Bidault, V Krachmalnicoff, R Haidar, P Bouchon, and Y De Wilde. “Transition from Phononic to Geometrical Mie Modes Measured in Single Subwavelength Polar Dielectric Spheres”. *ACS Photonics* 9.7 (2022), pp. 2295–2303.
- [36] Y Zhai, Y Ma, SN David, D Zhao, R Lou, G Tan, R Yang, and X Yin. “Scalable-manufactured randomized glass-polymer hybrid metamaterial for daytime radiative cooling”. *Science* 355.6329 (2017), pp. 1062–1066.
- [37] CM Liu, NZ Hu, Q Li, and M Qiu. “Metal-dielectric hybrid structure for radiative cooling”. *J. Phys. Conf. Ser.* Vol. 1077. 1. IOP Publishing. 2018, p. 012003.
- [38] J Jaramillo-Fernandez, GL Whitworth, JA Pariente, A Blanco, PD Garcia, C Lopez, and CM Sotomayor-Torres. “A Self-Assembled 2D Thermofunctional Material for Radiative Cooling”. *Small* 15.52 (2019), p. 1905290.

-
- [39] J Doumouro, E Perros, A Dodu, N Rahbany, D Leprat, V Krachmalnicoff, R Carminati, W Poirier, and Y De Wilde. “Quantitative measurement of the thermal contact resistance between a glass microsphere and a plate”. *Phys. Rev. Appl.* 15.1 (2021), p. 014063.
- [40] K Joulain, P Ben-Abdallah, P-O Chapuis, Y De Wilde, A Babuty, and C Henkel. “Strong tip-sample coupling in thermal radiation scanning tunneling microscopy”. *J. Quant. Spectrosc. Radiat. Transf.* 136 (2014), pp. 1–15.
- [41] AE Miroshnichenko, AB Evlyukhin, YS Kivshar, and BN Chichkov. “Substrate-induced resonant magnetoelectric effects for dielectric nanoparticles”. *ACS Photonics* 2.10 (2015), pp. 1423–1428.
- [42] F Herz and SA Biehs. “Dipole model for far-field thermal emission of a nanoparticle above a planar substrate”. *J. Quant. Spectrosc. Radiat. Transf.* 266 (2021), p. 107572.
- [43] PA Bobbert and J Vlieger. “Light scattering by a sphere on a substrate”. *Phys. A: Stat. Mech. Appl.* 137.1-2 (1986), pp. 209–242.
- [44] G Videen. “Light scattering from a sphere on or near a surface”. *J. Opt. Soc. Am. A: Opt. Image Sci. Vis.* 8.3 (1991), pp. 483–489.
- [45] F Herz and SA Biehs. “Generalized coupled dipole method for thermal far-field radiation”. *Phys. Rev. B* 105 (20 May 2022), p. 205422. DOI: [10.1103/PhysRevB.105.205422](https://doi.org/10.1103/PhysRevB.105.205422). URL: <https://link.aps.org/doi/10.1103/PhysRevB.105.205422>.
- [46] G Mie. “Beiträge zur Optik trüber Medien, speziell kolloidaler Metallösungen”. *Ann. Phys.* 330.3 (1908), pp. 377–445.
- [47] S Hayashi. “Optical study of electromagnetic surface modes in microcrystals”. *Jpn. J. Appl. Phys.* 23.6R (1984), p. 665.
- [48] R Fuchs and KL Kliewer. “Optical modes of vibration in an ionic crystal sphere”. *J. Opt. Soc. Am.* 58.3 (1968), pp. 319–330.
- [49] M Striebel, J Wrachtrup, and I Gerhardt. “Absorption and extinction cross sections and photon streamlines in the optical near-field”. *Sci. Rep.* 7.1 (2017), pp. 1–13.
- [50] AI Kuznetsov, AE Miroshnichenko, ML Brongersma, YS Kivshar, and B Luk’yanchuk. “Optically resonant dielectric nanostructures”. *Science* 354.6314 (2016).
- [51] PG Klemens. “Anharmonic decay of optical phonons”. *Phys. Rev.* 148.2 (1966), p. 845.
- [52] R Ruppin. “Surface modes and optical absorption of a small sphere above a substrate”. *Surf. Sci.* 127.1 (1983), pp. 108–118.
- [53] T Takemori, M Inoue, and K Ohtaka. “Optical response of a sphere coupled to a metal substrate”. *J. Phys. Soc. Japan* 56.4 (1987), pp. 1587–1602.
- [54] R Ruppin. “Optical absorption by a small sphere above a substrate with inclusion of nonlocal effects”. *Phys. Rev. B* 45.19 (1992), p. 11209.
- [55] J Lermé, C Bonnet, M Broyer, E Cottancin, D Manchon, and M Pellarin. “Optical properties of a particle above a dielectric interface: cross sections, benchmark calculations, and analysis of the intrinsic substrate effects”. *J. Phys. Chem. C* 117.12 (2013), pp. 6383–6398.
- [56] EH Korte and A Röseler. “Infrared reststrahlen revisited: commonly disregarded optical details related to $n < 1$ ”. *Anal. Bioanal. Chem.* 382.8 (2005), pp. 1987–1992.
- [57] MI Tribelsky and AE Miroshnichenko. “Giant in-particle field concentration and Fano resonances at light scattering by high-refractive-index particles”. *Phys. Rev. A* 93.5 (2016), p. 053837.

Chapter 4

Properties of mid-infrared plasmonic antennas: from single to multi-element subwavelength cavity antennas

In the previous chapters, we have dealt exclusively with surface optical excitations in dielectric media. We will now turn our attention to metallic nanostructures in which *plasmonic* resonances occur. In particular, we will be interested in metal-insulator-metal (MIM) cavities where one of the metallic layers is of sub- λ dimensions. MIM resonators have been studied in a wide variety of configurations, ranging from nanoribbons [1, 2] to coated spherical nanoparticles [3], and have been shown to be spectrally tunable and angularly independent [1, 2, 4]. So far, these studies have mainly considered periodic arrays of antennas. However, diffraction orders as well as coupling effects between neighboring antennas take place, which affects the overall electromagnetic response of such arrays [5]. In addition, when two plasmonic resonators are in near-field interaction, the *dimer*¹ structure may exhibit hybrid plasmonic resonances [6–12]. Diffractive coupling between neighboring dimers placed in an array has also been shown to alter optical behavior [13].

Here, we will use IR-SMS and s-SNOM, among other techniques, to probe the intrinsic electromagnetic radiation of few-element sub- λ MIM antennas. Starting from a single square-patch MIM antenna, we will gradually increase the number of elements of the antenna, thereby increasing the complexity of the near-field interaction. The fundamental interactions arising in each case will be illustrated and their influence on the near- and far-field response of the antenna will be examined.

4.1 Metal-insulator-metal (MIM) cavities

Let us consider the metal-insulator-metal (MIM) cavity of Fig. 4.1 (a), consisting of a dielectric (insulator) layer of thickness t_d and metallic layers that are thicker than the skin depth (see

¹A dimer refers to a pair of antennas coupled by near-field interaction.

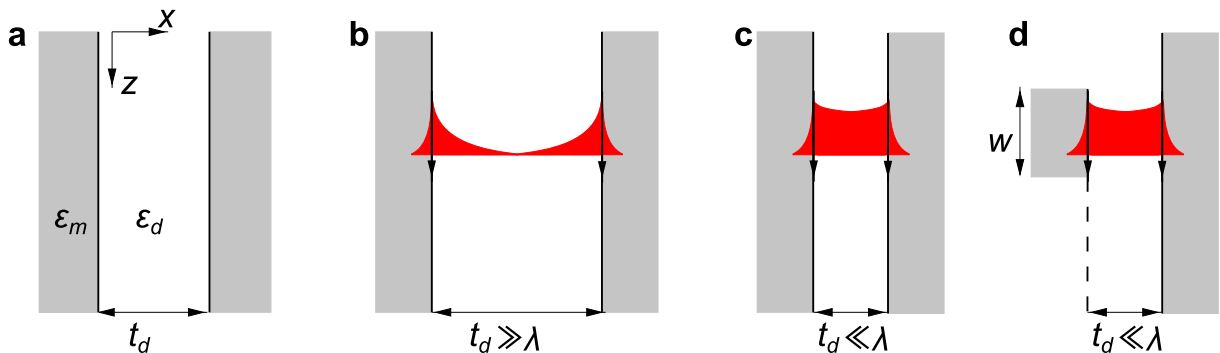


Figure 4.1: (a) Sketch of a one-dimensional metal-insulator-metal cavity. The surface plasmon-polariton modes propagating at each interface (drawn in red) are weakly coupled for a thick cavity ($t_d \gg \lambda$, panel (b)) and are strongly coupled for a narrow cavity ($t_d \ll \lambda$, panel (c)). (d) Same as panel (c) except that one of the metallic layers has a finite length w . Reproduced from ref. [14].

subsection 2.1.2). In the spirit of Fig. 2.9, the MIM cavity shown in Fig. 4.1 (a), forms a one-dimensional (1D) wave-guide for surface plasmon-polaritons (SPPs) propagating at the two metal/dielectric interfaces. The 1D mode equation for p -polarized modes in the wave-guide is given by [14]

$$\frac{\alpha_d}{\epsilon_d} \left\{ \frac{1 - e^{i\alpha_d t_d}}{1 + e^{i\alpha_d t_d}} \right\} + \frac{\alpha_m}{\epsilon_m} = 0, \quad (4.1)$$

where $\alpha_j = (\epsilon_j \omega^2 / c^2 - k^2)^{1/2}$, with $j = d$ or m , gives the wavevector components along the x -direction in the dielectric and metallic layers of permittivities, ϵ_d and ϵ_m , respectively.

For a thick wave-guide ($t_d \gg \lambda$) in which $\text{Im}(\alpha_d t_d) \gg 1$, Eq. (4.1) reduces to $\alpha_d / \epsilon_d + \alpha_m / \epsilon_m = 0$, which is the dispersion relation of SPPs at a single semi-infinite dielectric/metal interface (cf. Eq. (2.37)). The effective index of refraction for this mode is given by

$$n_{\text{eff}}^{t_d \gg \lambda} = \frac{ck}{\omega} = \frac{1}{\sqrt{\frac{1}{\epsilon_d} + \frac{1}{\epsilon_m}}}. \quad (4.2)$$

In this case, the fundamental TM mode of the wave-guide is composed of two uncoupled SPPs propagating along both dielectric/metal interfaces (see Fig. 4.1 (b)).

For a sub- λ wave-guide such that $|\alpha_d t_d| \ll \lambda$, the SPPs propagating at the two interfaces are coupled (Fig. 4.1 (c)), and we get $(1 - e^{i\alpha_d t_d}) / (1 + e^{i\alpha_d t_d}) \approx -i\alpha_d t_d / 2$, so that Eq. (4.1) becomes

$$\frac{\alpha_m}{\epsilon_m} = \frac{\alpha_d}{\epsilon_d} \left(\frac{i\alpha_d t_d}{2} \right). \quad (4.3)$$

Since $\alpha_d^2 - \alpha_m^2 = (\epsilon_d - \epsilon_m)\omega^2 / c^2$, then the above mode equation can be rewritten as

$$\alpha_d^2 \left\{ 1 + \alpha_d^2 \left(\frac{\epsilon_m}{\epsilon_d} \right)^2 \frac{t_d^2}{4} \right\} = (\epsilon_d - \epsilon_m) \frac{\omega^2}{c^2}. \quad (4.4)$$

The effective index of refraction is therefore given by

$$n_{\text{eff}}^{t_d \ll \lambda} = \varepsilon_d^{1/2} \left(1 - \frac{i\lambda}{\pi t_d \varepsilon_m^{1/2}} \sqrt{1 - \frac{\varepsilon_d}{\varepsilon_m}} \right)^{1/2}. \quad (4.5)$$

As we will only discuss sub- λ cavities, we will henceforth omit the superscript $t_d \ll \lambda$, *i.e.*, the effective index will be written as $n_{\text{eff}} = \tilde{n}_{\text{eff}} + i\tilde{k}_{\text{eff}}$.

If one of the metallic layers has a finite length w (Fig. 4.1 (d)), then the sub- λ cavity can become resonant at a resonance wavelength, λ^{res} , provided that the following Fabry-Perot phase-matching condition is satisfied:

$$\lambda_m^{\text{res}} = \frac{2w\tilde{n}_{\text{eff}}}{m - \frac{\phi_r}{\pi}}, \quad (4.6)$$

in which, $m = 1, 2, 3, \dots$ is the mode number, and ϕ_r is the phase of the modal reflection coefficient r_p . For $m = 1$, Eq. (4.6) gives the resonance condition of the fundamental resonant mode of the MIM cavity. Typically, the phase ϕ_r varies between $-\pi/20$ and $\pi/8$ depending on the dimensions of the cavity [15]. For the MIM cavities that will be discussed here, we have $\phi_r \approx \pi/6$. Within the Fabry-Perot picture, the resonance is described as a standing wave pattern along the z -direction, created by the bouncing of the propagating SPP modes between the two ends of the metallic layer of finite length.

4.2 Single MIM antennas in the near- and far-field

Consider the MIM antenna sketched in Figs. 4.2 (a) and (b), in which the top metallic layer consists of a 40 nm-thick Au square patch of width w . For $w = 1.65 \mu\text{m}$, Eq. (4.6) rules that the MIM cavity becomes resonant at a wavelength $\lambda_1^{\text{res}} = 8.88 \mu\text{m}$ (see Fig. 4.2 (d)). At this wavelength, the MIM cavity resonantly absorbs incoming light. This means that an electric field that is incident upon the MIM antenna, as depicted in Fig. 4.2 (a), gets funneled and absorbed into the cavity underneath the patch, yielding a large field enhancement in this region (see Fig. 4.2 (e)). The largest field enhancement actually occurs at the vertices of the patch (over 70 times the incident field, Fig. 4.2 (e)), due to the fact that the field gets "squeezed" into the cavity at the edges of the patch, resulting in a lightning-rod effect at its vertices. This behavior becomes more apparent when examining the field enhancement in the xy -plane above the square patch (Fig. 4.2 (f)).

The fact that the cavity is sub- λ in all directions, means that at resonance, the MIM cavity results in sub- λ *confinement* of the electric field. The sub- λ confinement and high field enhancement achieved by the MIM antenna can be understood as follows. The total power removed from the incident field by the antenna is proportional to its extinction cross-section (C_{ext}). As shown in Figs. 4.3 (a) and (b), the extinction cross-section is several times the geometrical cross-section of the patch at resonance (over 18 times for $\theta = 0^\circ$ and over 3 times for $\theta = 60^\circ$). As a result, the portion of the field that is absorbed (or scattered) by the antenna is equivalent to that of a much larger surface whose area is given by C_{ext} , but ultimately this field is confined to the sub- λ region defined by the geometrical cross-section of the patch, leading to the previously mentioned

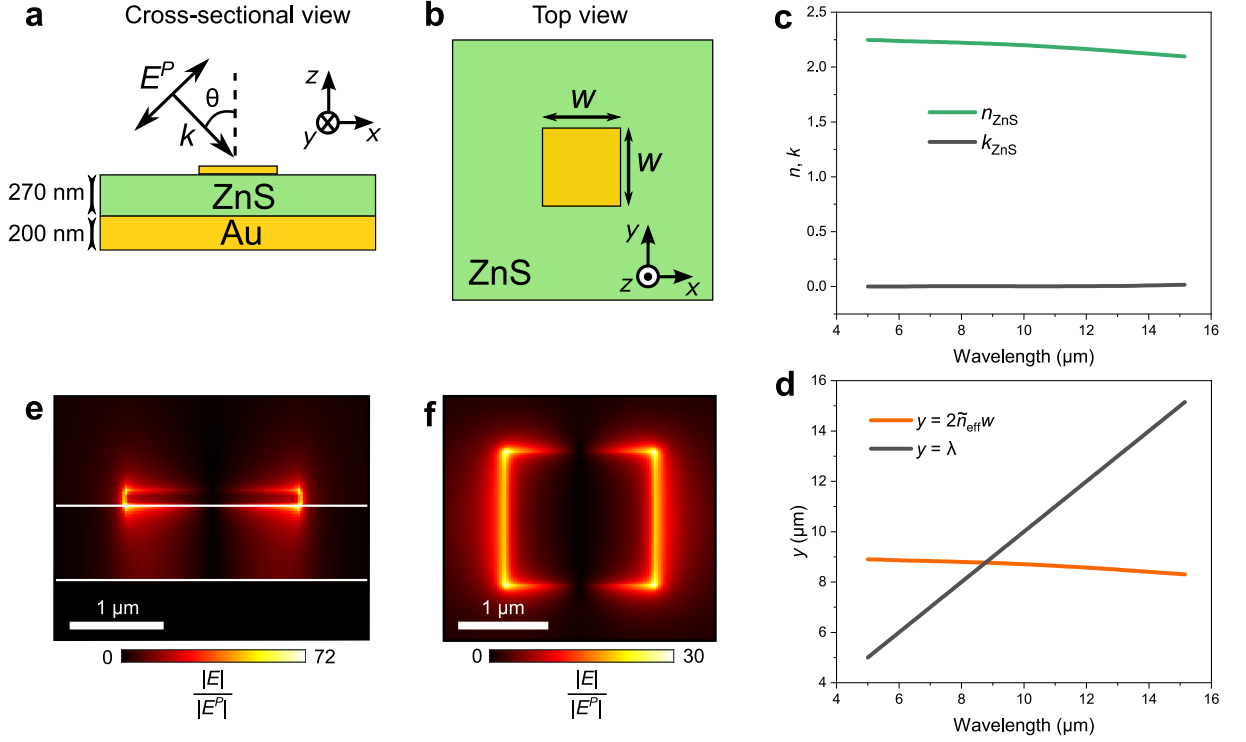


Figure 4.2: (a) Cross-sectional view of a square-patch MIM antenna, showing a p -polarized electric field of amplitude $|E^P|$, that is incident from the top at an angle θ . (b) Top view of the antenna. (c) Real (n_{ZnS}) and imaginary (k_{ZnS}) parts of the index of refraction of the insulator layer of the antenna, which consists of zinc sulfide (ZnS). The average value of the index of refraction of ZnS in the spectral range considered here is $\bar{n}_{\text{ZnS}} = 2.21 + 0.003i$. Optical constants taken from ref. [16]. (d) Fabry-Perot phase matching condition for the fundamental resonant mode ($m = 1$), $\lambda_1^{\text{res}} = 2\tilde{n}_{\text{eff}}w$ ($n_{\text{eff}} = \tilde{n}_{\text{eff}} + i\tilde{k}_{\text{eff}}$), of the antenna sketched in panels (a) and (b) with $w = 1.65 \mu\text{m}$. The fundamental resonance mode occurs at $\lambda_1^{\text{res}} = 8.88 \mu\text{m}$. (e) Finite-difference time-domain simulation of the electric field enhancement ($|E|/|E^P|$) in the near-field of the square patch MIM antenna with $w = 1.65 \mu\text{m}$, computed at one of the ends of the patch in the xz -plane at $\lambda = 8.88 \mu\text{m}$ for normal incidence ($\theta = 0^\circ$). (f) Electric field enhancement of the antenna in the xy -plane 30 nm above the patch at $\lambda = 8.88 \mu\text{m}$. Further details on the FDTD simulations presented here can be found in Appendix B.

funneling of the field.

Figures 4.3 (a) and (b) also show that the fundamental resonant mode of the MIM cavity is spectrally invariant with respect to the angle of incidence of the electric field, that is, λ_1^{res} is constant with respect to the angle θ in Fig. 4.2 (a). Nonetheless, the amplitude of the antenna's cross-sections decreases with increasing angle. By examining the values of the antenna cross-sections at λ_1^{res} as a function of the incidence angle θ , one can therefore construct a "radiation pattern"² of the MIM antenna (Figs. 4.3 (c) and (d)). This calculation shows that for p -polarized light, the antenna cross-sections are almost constant up to 20° , after which they start to decrease with a total drop of $\sim 40\%$ from $\theta = 0^\circ$ to $\theta = 70^\circ$ (see Fig. 4.3 (c)). For s -polarized light, the decrease in the antenna cross-sections as a function of increasing angle is much more drastic,

²The double quotations are added here since the term *radiation pattern* usually refers to the scattered field of the antenna.

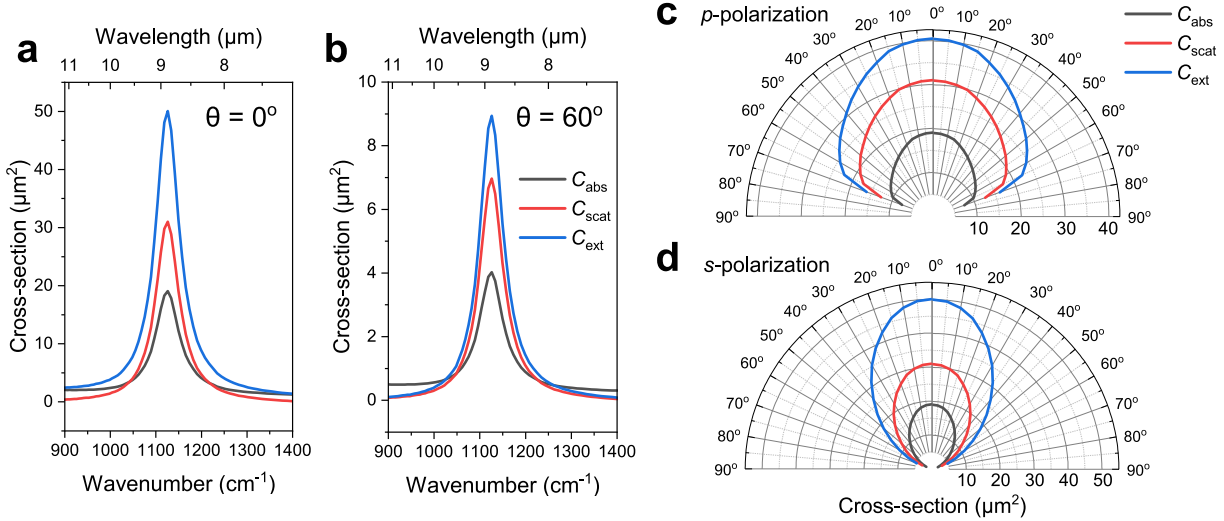


Figure 4.3: (a) & (b) Finite-element method simulations of the cross-sections of the MIM antenna of Figs. 4.2 (a) and (b) with $w = 1.65 \mu\text{m}$, for $\theta = 0$ and 60° . (c) & (d) Radiation pattern of the MIM antenna at resonance ($\lambda = 8.88 \mu\text{m}$) for p - and s -polarized light. Further details of the simulation methods used here can be found in Appendix A. Legend: black, absorption cross-section (C_{abs}); red, scattering cross-section (C_{scat}); blue, extinction cross-section (C_{ext}).

with a total decrease of $\sim 95\%$ from $\theta = 0^\circ$ to $\theta = 70^\circ$ (see Fig. 4.3 (d)). By the principle of reciprocity, the behavior of the MIM antenna in emission is required to be equivalent to that in which an external electric field is present. The patterns shown in Figs. 4.3 (c) and (d) can, therefore, also be thought of as *emission patterns*.

In order to experimentally probe the response of MIM cavities, we patterned, via electron-beam (e -beam) lithography, sub- λ gold square patches ($w = 1.65 \mu\text{m}$) in various configurations³, on a substrate consisting of the following stack, from top to bottom: ZnS(270 nm)/Au(200 nm)/Si(300 μm), in which the values between parenthesis indicate the thickness of each layer.

To map the near-field of a single square patch MIM antenna, we performed near-field imaging using the s -SNOM setup of Fig. 3.4. A p -polarized quantum-cascade laser (QCL) source is tuned to the fundamental resonance frequency of the MIM antenna, *i.e.*, $\omega_{\text{QCL}} = 1126 \text{ cm}^{-1}$ ($\lambda_{\text{QCL}} = 8.88 \mu\text{m}$), and focused onto the tip/antenna region with an angle of 60° with respect to the normal to the sample surface (see Fig. 4.4 (d)). As illustrated in subsection 3.1.1, the s -SNOM setup used here utilizes a pseudo-heterodyne detection scheme, which enables the simultaneous measurement of both amplitude and phase of the electric near-field. The measured amplitude and phase of the near-field optical signal of the MIM antenna are shown in Figs. 4.4 (b) and (c), respectively. As the field probed by the tip is dominated by the out-of-plane electric field component⁴ (see subsection 3.1.2), and since the local electric field of a MIM antenna is

³These antennas were fabricated by Nathalie Bardou and Christophe Dupuis at Centre de Nanosciences et de Nanotechnologies (C2N). See Appendix G for details on the e -beam lithography procedure used.

⁴The illumination is p -polarized with an incidence angle of 60° with respect to the normal to the sample surface (z -direction). Thus, the electric field has an in-plane and an out-of-plane component. The latter component is polarized along the long axis of the tip (z -direction) and thus dominates the near-field signal scattered by the tip.

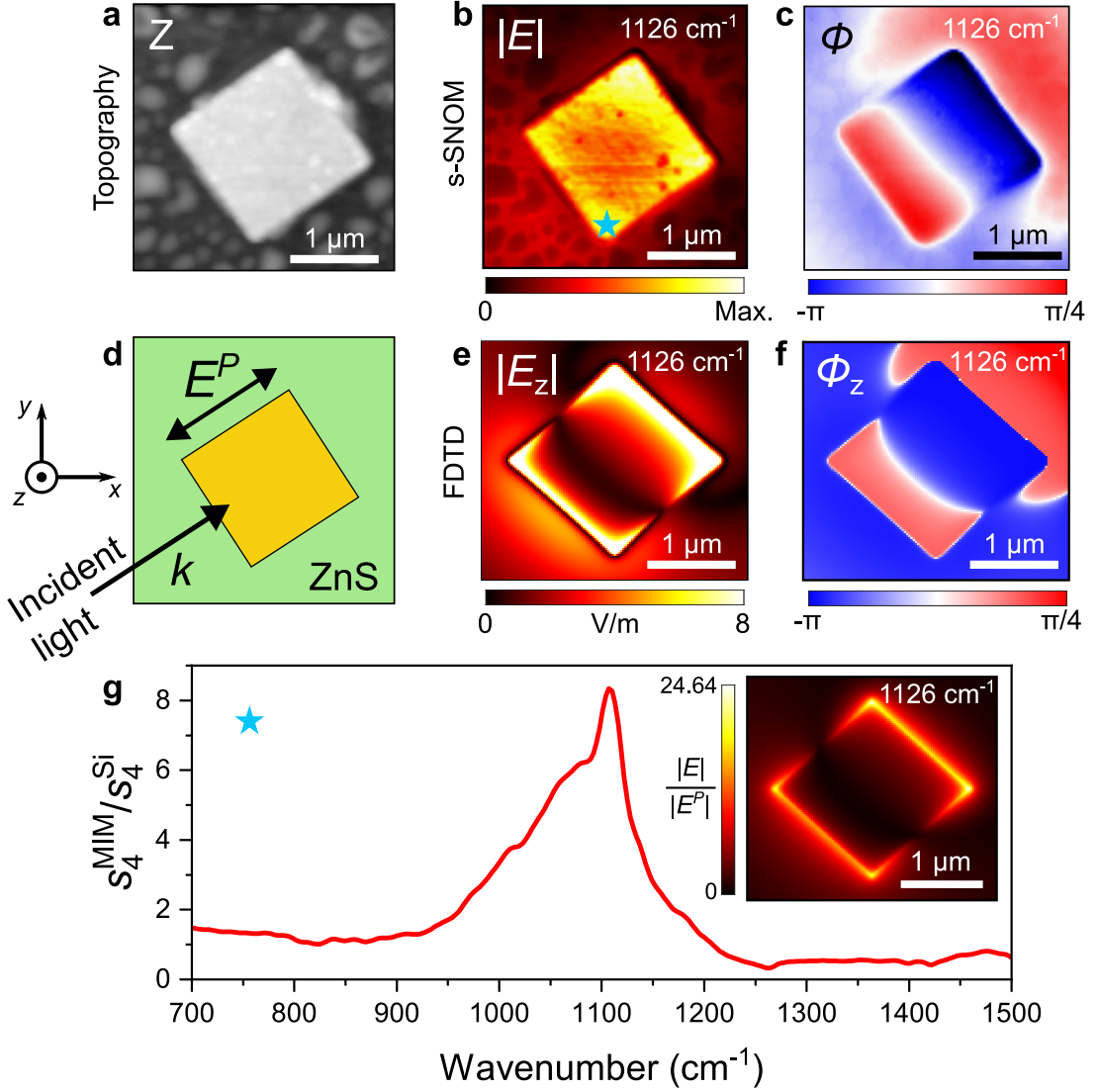


Figure 4.4: (a) Topography of a $1.65 \times 1.65 \mu\text{m}^2$ square-patch MIM antenna. (b) Amplitude ($|E|$) and (c) phase (ϕ) images of the near-field optical signal of the patch antenna of panel (a), demodulated at the 3rd harmonic of the tip oscillation frequency. The slight asymmetry in the field distribution arises from the oblique illumination used in the measurements. (d) Sketch illustrating the illumination configuration used in panels (b) and (c). A p -polarized quantum cascade laser source ($\omega = 1126 \text{ cm}^{-1}$) is used with an incidence angle of 60° . The projection of the incident electric field onto the antenna in the xy -plane is indicated by the double arrow marked by E^P . (e) Amplitude and (f) phase from the finite-difference time-domain simulations corresponding to the measurements in panels (b) and (c), computed in the xy -plane 30 nm above the antenna. The color bar in panel (e) is scaled for better agreement with panel (b). The maximal values of the amplitudes of the electric field components in the x , y , and z -directions were found at the vertices of the patch and are given by: $\max(|E_x|) = \max(|E_y|) = 16.44 \text{ V/m}$ and $\max(|E_z|) = 20.23 \text{ V/m}$. (g) Normalized amplitude of the nano-FTIR spectrum measured at the vertex of the patch marked with a star in panel (b). The spectrum is normalized to that of a reference Si sample and the result is shown for the 4th harmonic. The inset shows the simulated electric field enhancement at resonance in the xy -plane 30 nm above the antenna. The far-field absorption spectrum of the same antenna is shown in Fig. A8 of the appendix.

such that: $|E_x| = |E_y| < |E_z|$ (see Fig. 4.4), we compare the measurements in Figs. 4.4 (b) and (c) to the FDTD-simulated z -component of the MIM antenna electric field (Figs. 4.4 (e) and (f)). The complex electric field components, E_x , E_y , and, E_z are calculated using a monitor placed in the xy -plane 30 nm above the MIM patch so that the field is computed at the average height of the tip used in the measurement, which undergoes oscillations with an amplitude $\Delta z \approx 60$ nm. The amplitude and phase of E_z are subsequently plotted in Figs. 4.4 (e) and (f).

As shown in Figs. 4.4 (b) and (e), the near-field of the MIM antenna is mostly localized at the two opposing edges of the square patch in the top right and bottom left corners of the panels. Since the incident field is p -polarized, it is projected onto the Au patch of the antenna in such a way that these two aforementioned edges are polarized (see Fig. 4.4 (d)). This is further corroborated by the fact that the phase of the field undergoes a shift from $-\pi$ to $\pi/4$ between these two edges (see Figs. 4.4 (c) and (f)). The incident field is then resonantly absorbed at these two edges into the cavity underneath the patch. The field observed at the surface of the patch is simply the field that leaks out from the cavity, as the back-scattered incident field is suppressed by the demodulation process. We reiterate here the fact that the local field of a MIM antenna is mostly located in its cavity and thus hidden from the surface, emphasizing the difficulty of experimentally probing its near-field.

Using nano-FTIR, we also measured the near-field spectral response of the MIM antenna at one of the vertices of the square patch (marked with a star in Fig. 4.4 (b)). The normalized amplitude of the measured spectral signal, $s_4^{\text{MIM}}/s_4^{\text{Si}}$, is plotted in Fig. 4.4 (g). The normalized amplitude, in this case, corresponds to the electric field enhancement in the near-field of the antenna (see subsection 3.1.1). The shown spectrum exhibits a solitary peak at 1110 cm^{-1} , at which a field enhancement of 8.34 is measured, demonstrating the large near-field enhancement close to the fundamental resonance of the cavity (see Fig. 4.4 (g), inset).

The thermal emission of a single sub- λ square-patch MIM antenna has previously been characterized both in the near- and far-field [17]. The far-field thermal emission spectra of a single MIM antenna of varying width w (see Fig. 4.5 (a)), measured via IR-SMS, are shown in Fig. 4.5 (b) (corresponding simulations in Fig. 4.5 (c)). In this particular case, the spectra consist of two peaks both of which corresponding to the antenna's fundamental resonance mode. This peculiar behavior arises due to the dielectric properties of the SiO_2 layer used as the insulator in the MIM cavity. We have already seen in Fig. 2.1 (b) that the real part of the dielectric function of SiO_2 undergoes significant variations in the spectral range considered here. As a consequence, the real part of the effective index of refraction of the cavity, \tilde{n}_{eff} follows the same trend. This enables the fundamental resonance condition to be satisfied at two different wavelengths, in this case around $7 \mu\text{m}$ and $11 \mu\text{m}$ (see Fig. 4.5 (d)). The field intensity plots of Fig. 4.5 (e) further show that these two resonance peaks correspond to the same mode, as they both have the same spatial distribution. Actually, the Fabry-Perot resonance condition for the fundamental MIM resonance is also satisfied at an intermediate wavelength (close to $9 \mu\text{m}$). However, at this wavelength, the cavity is extremely lossy (see Fig. 4.5 (d), orange curve) resulting in the suppression of this mode in the far-field spectrum.

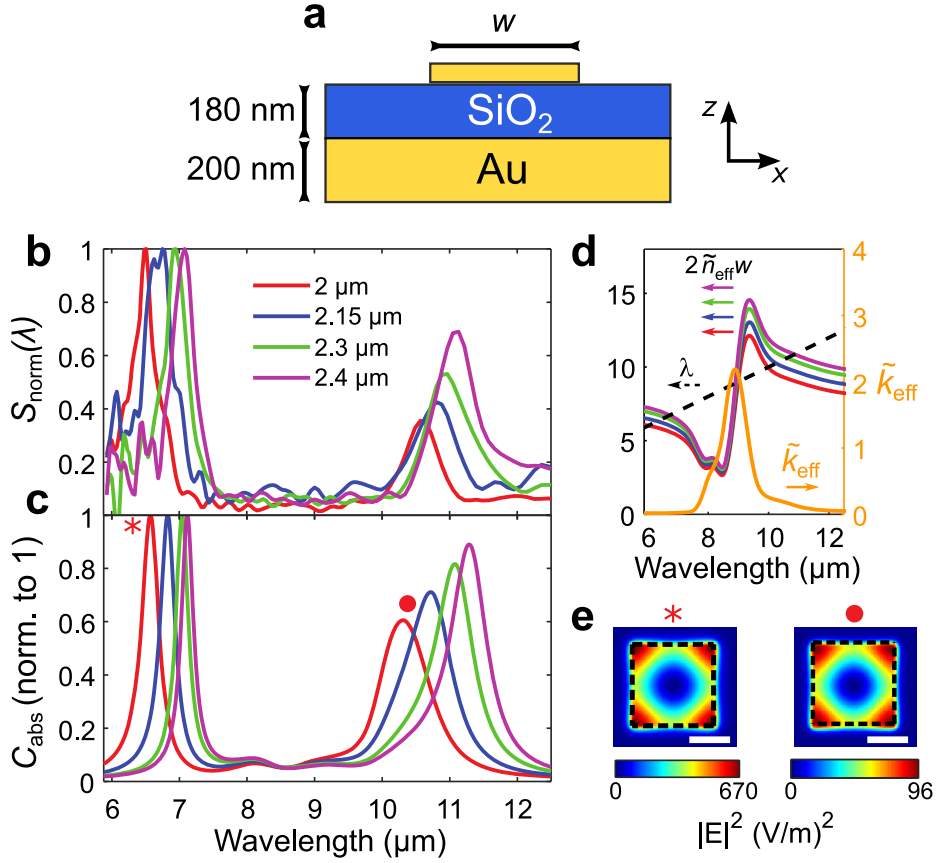


Figure 4.5: (a) Sketch of a MIM stack consisting of the following layers from top to bottom: Au(50 nm)/SiO₂(180 nm)/Au(200 nm), where the layer thickness is indicated between parenthesis. The top Au layer is a sub- λ square patch of side w . (b) Normalized IR-SMS spectra of the single nanoantenna sketched in panel (a) for different widths w . (c) FDTD simulations of the absorption cross-section (normalized by the maximal value) corresponding to the measurements of panel (b). (d) Phase-matching condition for the MIM antenna fundamental resonance mode (λ_1^{res}) and effective extinction coefficient \tilde{k}_{eff} . (e) Calculated intensity maps inside the cavity of a MIM nanoantenna (dashed outline) for the two resonances denoted by the markers in (c). The white scale bars correspond to 1 μm . Reproduced from ref. [17].

4.3 Far-field thermal radiation of a coupled patch MIM antenna pair: thermally excited hybrid plasmonic modes

In this section, we demonstrate simultaneous probing of the bonding and anti-bonding modes of an isolated dimer of MIM antennas by thermal excitation [18]. This striking result, which is confirmed by FDTD simulations and polarization analysis, shows that various coupled modes of a single nano-antenna can be simultaneously excited by thermal fluctuations, an essentially incoherent process arising from fluctuating thermal currents.

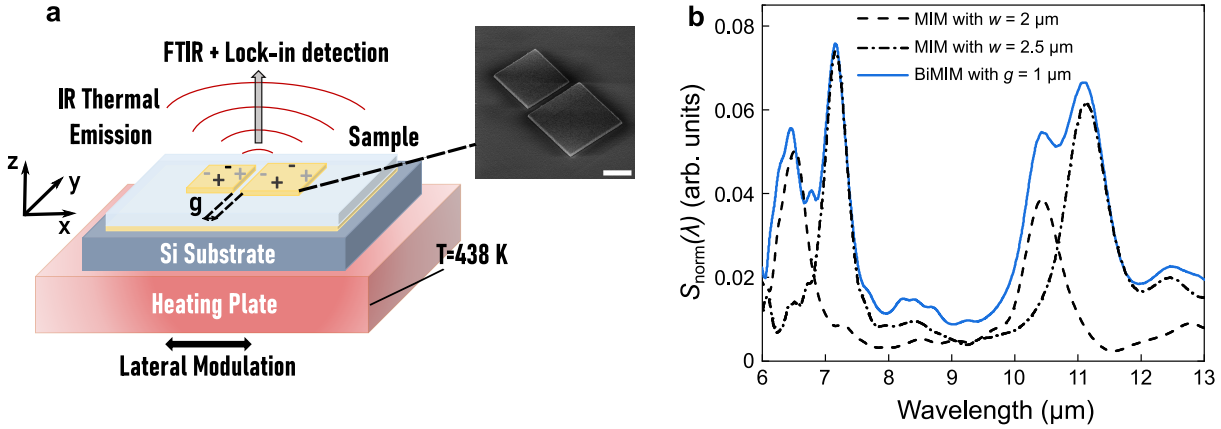


Figure 4.6: (a) Schematic illustration of the BiMIM geometry and IR-SMS technique. The sample consists of a transparent Si substrate on top of which a 200 nm-thick layer of gold is evaporated, then a 300 nm spacer layer of SiO₂ is deposited, and a final top layer consisting of two 100 nm-thick sub- λ gold square patches, and sides $w_1 = 2 \mu\text{m}$ and $w_2 = 2.5 \mu\text{m}$, separated by a gap g . An SEM image of the investigated sample is shown in the top right corner. The scale bar is $1 \mu\text{m}$. (b) Measured IR-SMS far-field thermal emission spectrum of a BiMIM with a $1 \mu\text{m}$ gap compared to that of its constituent MIM antennas. The antennas resonate near $(6.5 \mu\text{m}, 10.5 \mu\text{m})$ and $(7.2 \mu\text{m}, 11.2 \mu\text{m})$, for $w = 2 \mu\text{m}$ and $2.5 \mu\text{m}$, respectively.

4.3.1 Far-field thermal radiation of a single asymmetric dimer MIM antenna

The samples that we investigate here consist of a homogeneous substrate supporting two coupled sub- λ gold square patch MIM antennas of different widths with an SiO₂ spacer layer, separated by a nanometric gap g . This geometry will hereafter be referred to as a BiMIM structure (see Fig. 4.6 (a) for sample geometry). The sample is placed on a flat heating plate (see Fig. 3.14 (a)) in order to raise its temperature and in this way stimulate the excitation of its electromagnetic modes by thermal fluctuations [19]. The far-field thermal radiation spectrum of the coupled MIM antennas is then extracted from the overwhelming background thermal radiation via IR-SMS [17] in the spectral range between $6 - 13 \mu\text{m}$. As sketched in Fig. 4.6 (a), the temperature of the BiMIM and the substrate, in this case, is raised to 438 K by means of the hot sample stage, and the measurements are carried out as outlined in subsection 3.2.1.

As we have seen in the previous sections, a single MIM antenna with a patch of width w acts as a Fabry-Perot resonator for the gap plasmons below the patch. By thermally exciting the MIM antennas, all their electromagnetic modes are excited in the spectral range considered and are populated according to Bose-Einstein statistics [19–21]. As illustrated previously, the resonance wavelength of the modes can be found from the phase matching condition given in Eq. (4.6). Figure 4.6 (b) shows the measured thermal emission spectrum of a BiMIM structure with a $1 \mu\text{m}$ gap (blue curve). As a reference, we also show measured spectra of the single MIM antennas making up the structure (respective widths $w = 2 \mu\text{m}$ and $2.5 \mu\text{m}$, dashed and dash-dotted curves) each consisting of two resonance peaks, which are a signature of the excitation of the MIM fundamental mode at two different wavelengths (see section 4.2). We have seen in the previous section that the peak at the largest wavelength results from the peculiar dispersion

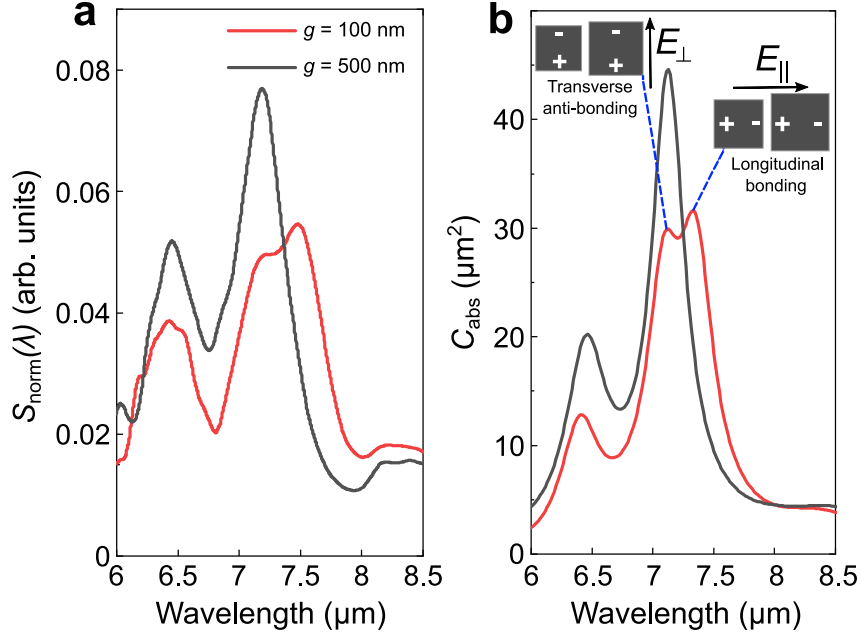


Figure 4.7: (a) Measured thermal emission spectra of the BiMIM structure for different gap size g . (b) FDTD calculations of absorption cross-sections for normally incident, unpolarized illumination, corresponding to the measurements. The inset shows a sketch of the dimer geometry showing two of the hybrid modes of the BiMIM, for electric field polarizations parallel (E_{\parallel}) and perpendicular (E_{\perp}) to the dimer axis. The positive and negative signs indicate the surface charge distribution.

of the SiO_2 spacer layer but it also occurs in a region where the cavity is slightly lossy (see Appendix F for more details). We, therefore, choose to exclude it from the following and focus the remainder of our discussion on spectral features below 8.5 μm .

As can be seen from Fig. 4.6 (b), for such a large gap, the thermal emission spectrum of the BiMIM structure simply overlaps with that of the two individual antennas, meaning that the two MIM antennas behave independently. However, when the MIM antennas are separated by a smaller gap, their two gold patches form a plasmonic dimer pair that exhibits bonding and anti-bonding hybrid modes [7]. If an external illumination is used, the latter modes can be selectively excited by varying the polarization of the electromagnetic excitation with respect to the dimer common axis (see Fig. 4.7 (b), inset). These hybrid modes can be studied using a plasmon hybridization model [7, 22, 23], in which the conduction electrons in the metal are modeled as a charged incompressible liquid, whose deformations lead to the formation of a surface charge.

In our experiment, a thermal excitation of the BiMIM structure is instead produced *in situ* by raising the overall temperature of the sample, inducing a superposition between the longitudinal and the transverse bonding and anti-bonding modes, which modifies the observed far-field response. In particular, when the gap size is reduced to 100 nm (red curve in Fig. 4.7) a splitting begins to form in the resonance peak between 7 and 8 μm , while an overall red-shift in the peaks is also observed. It has been shown that the bonding hybrid modes lead to a red-shift in the spectrum, while the anti-bonding modes result in a slight blue-shift [6, 9, 10, 24]. The observed splitting is thus, a hallmark of the simultaneous excitation of the longitudinal

bonding and transverse anti-bonding modes due to thermal fluctuations. FDTD calculations of the emission cross-section of the BiMIM structure (Fig. 4.7 (b)) confirm this effect. For a larger gap size ($g = 500$ nm, black curve in Fig. 4.7) the splitting and red-shift disappear.

It should be noted that the thermal radiation emitted by the BiMIM structure is collected by a reflective objective ($\text{NA} = 0.5$), which collects radiation from a solid angle between 10 and 30° . By reciprocity, this means that the BiMIM's hybrid modes can be excited by an external source at non-normal incidence. The agreement of our off-axis measurements with simulations at normal incidence suggests that the emission spectra of the hybrid modes of the considered BiMIM structure are angularly independent up to at least 30° .

4.3.2 Polarized thermal emission measurements of a single MIM antenna pair

It is possible to distinguish between the various hybrid modes of the BiMIM antennas, that are thermally excited, by performing polarized thermal emission measurements. This is done by placing a wire-grid analyzer (polarizer) before the detector in order to select the E_{\parallel} and E_{\perp} polarizations of Fig. 4.7 (b). The experimental results and the corresponding cross-section calculations are shown in Fig. 4.8 (a) and (b), respectively.

For the parallel polarization, FDTD simulations show that the longitudinal anti-bonding and bonding modes are excited at the resonance positions (i) and (ii), respectively (see Fig. 4.8 (b)). At these resonance positions, charges accumulate on the left and right edges of the square patches. This produces a strong enhancement of the amplitude $|E_z|$ of the z -component of the electric field, at the edges of the squares, as shown in Fig. 4.8 (c) (i-ii). The plots of the electric field component E_z in Fig. 4.8 (c) provide a qualitative picture of the surface charge distribution of the BiMIM antenna. This enables one to identify the influence of near-field interaction on the observed far-field modes. In particular, the opposite charges, found at the edges near the gap, lead to the observed red-shift in the longitudinal bonding mode (position (ii) in Fig. 4.8 (b)), due to attraction. On the other hand, charges of the same sign are found at the edges near the gap for the longitudinal anti-bonding mode (Fig. 4.8 (c) (i)). This latter mode appears as a small peak at position (i) in Fig. 4.8 (b). Note that the asymmetry of the BiMIM structure is essential for the observation of this mode. If the square patches were identical in size the net dipole moment for this mode would be zero, and it would be inaccessible by far-field illumination, as it constitutes a dark mode [22]. By reciprocity, it would not produce any measurable thermal radiation to the far-field as well.

For the E_{\perp} polarization, charges accumulate at the top and bottom edges of the patches, leading to the weakly interacting transverse bonding and anti-bonding modes at positions (iii) and (iv), respectively (Fig. 4.8 (c) (iii-iv)). In the measured spectra (Fig. 4.7 (a)), the thermally induced splitting is thus the result of the combined response of the longitudinal and transverse bonding and anti-bonding modes. In contrast, the longitudinal anti-bonding and the transverse bonding modes (i and iii, respectively) are degenerate and do not produce a splitting in the unpolarized thermal emission spectrum.

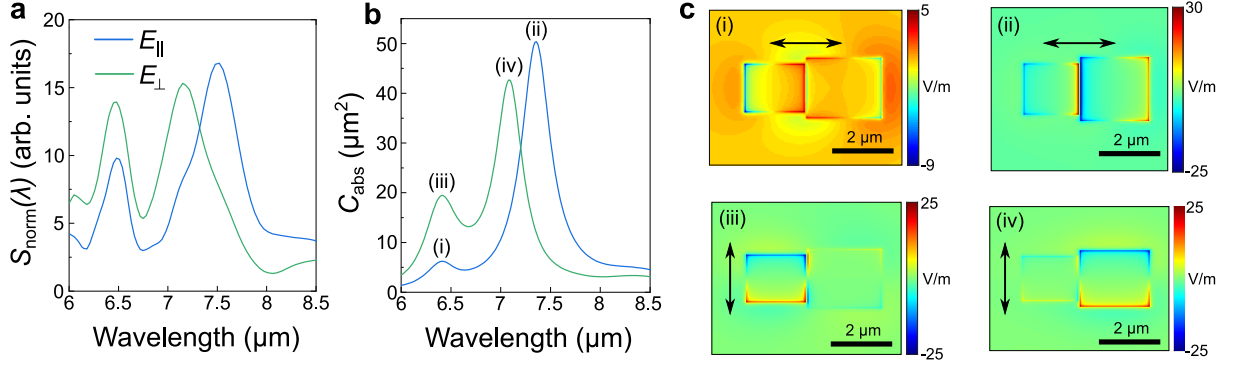


Figure 4.8: (a) Measured thermal emission and (b) calculated emission cross-section of the BiMIM structure with $g = 100$ nm for polarized thermal emission. (c) Plots of the z -component E_z of the electric field in the xy -plane at the top of the square metal patches, at the resonance peaks indicated by the markers (i), (ii), (iii), and (iv) in panel (b). The double arrow indicates the electric field polarization in each case.

4.3.3 Asymmetric vs symmetric MIM antenna pair

If a symmetric BiMIM structure is considered, where both MIM antennas of the structure resonate near $6.5 \mu\text{m}$ (Fig. 4.9, black simulated curve), the spectral overlap of the resonances near $6.5 \mu\text{m}$ precludes the excitation of the dark mode, while a splitting due to the longitudinal bonding and transverse anti-bonding modes still occurs—as indicated by the splitting between 6 and $7.5 \mu\text{m}$. An interesting effect is also observed in the considered BiMIM structure, when examining the simulated electric field enhancement plots, for unpolarized emission, at the resonance positions A1 and A2 (Fig. 4.9 (b)). The plots reveal emission hot spots from the BiMIM structure, showing that the two MIM antennas emit independently at these resonance positions, even though they are effectively in near-field interaction.

On the other hand, at the resonance peak A3 the two MIM antennas act as a coupled system, and a larger field enhancement is found in the gap (Fig. 4.9 (b), A3). The observed behavior at positions A1 and A2 is a direct result of the nature of the weakly interacting transverse hybrid modes, and the asymmetry of the BiMIM structure under study. In fact, since the resonance wavelength of a MIM antenna scales with its width (cf. Eq. (4.6)), the size difference between the two MIM antennas allows for independent emission at two different wavelengths. To illustrate this point, we also show field enhancement plots at the resonance positions S1 and S2 for the symmetric BiMIM case (Fig 4.9 (b) bottom two panels). In this case, the two MIM antennas cannot emit independently, and emission hot spots are either found at the edges of the two gold patches (position S1) or in the gap (position S2).

The equivalence between emission and absorption suggests that if an external electric field is incident on the considered asymmetric BiMIM structure, it will be routed to, and resonantly absorbed by each MIM antenna at the resonance positions A1 and A2. Such an attribute could be beneficial for IR photo-detection applications [2].

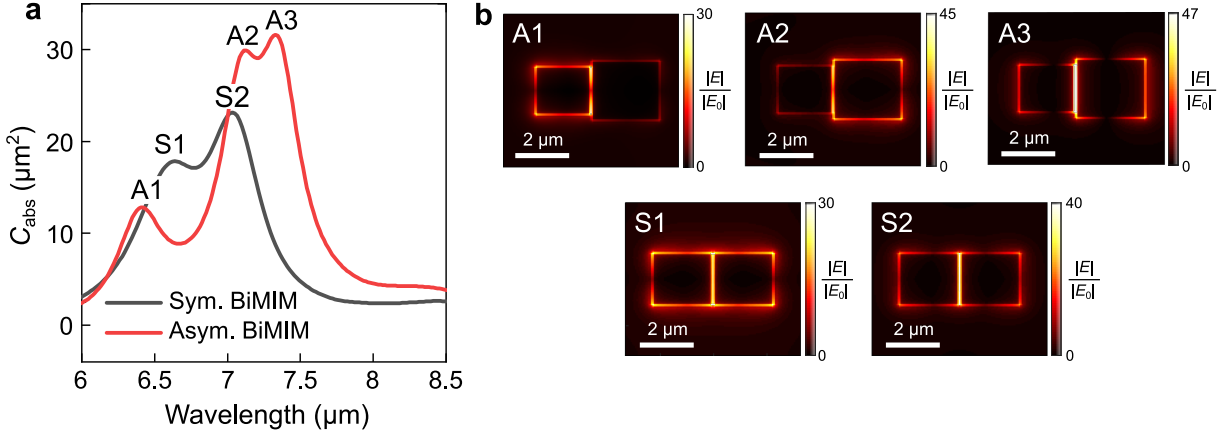


Figure 4.9: (a) Simulated absorption cross-section for unpolarized light for the considered BiMIM structure with $g = 100$ nm compared with that of a symmetric BiMIM whose patches have widths $w_1 = w_2 = 2$ μm . (b) Electric field enhancement plots showing field hot spots in the xy -plane at the top of the metal patches, recorded at the resonance positions in panel (a).

4.4 Shaping the optical properties of MIM cavities through multi-element surface patterning: the case of a 3×3 -patch MIM cavity antenna

In this section, we illustrate how the near- and far-field response of MIM antennas can be tailored by the shaping of the cavity's top metallic layer [25]. In particular, we consider the case in which the top metallic layer consists of nine square patches in total, each of side $w = 1.65$ μm , placed in a 3×3 configuration (see Figs. 4.10 (a), (b), and (e)). The patches are separated from one another by a gap $g = 100$ nm so that they are effectively in near-field interaction. We show through s-SNOM and focused microscope reflectivity measurements that the near-field interaction among the antenna elements (*i.e.*, the square patches) leads to a spatial confinement of the local near-field of the antenna and an angularly-dependent near- and far-field optical response. The results presented hereafter may be of interest to photo-detector applications in which MIM cavities are used [26], as they show that the spectral response of such detectors may be tuned by appropriately engineering the cavity layers.

4.4.1 Mapping the near-field of a 3×3 -patch MIM antenna

We begin by mapping the near-field of the 3×3 antenna via s-SNOM imaging. As shown in Fig. 4.10 (a), a silicon (Si) tip is utilized here in order to minimally perturb the intrinsic near-field of the antenna. Previous studies have revealed that the use of dielectric tips is more advantageous compared to metallic tips when mapping the near-field of a plasmonic nanostructure with s-SNOM [27–31]. This is due to the tip/nanostructure coupling which is the dominant effect in the near-field when a metallic tip is used.

As we have seen in subsection 3.1.2, dielectric tips are less scattering than their metallic counterparts, therefore, leading to significantly lower s-SNOM signals. It has been recently

4.4. Shaping the optical properties of MIM cavities through multi-element surface patterning:
the case of a 3×3 -patch MIM cavity antenna

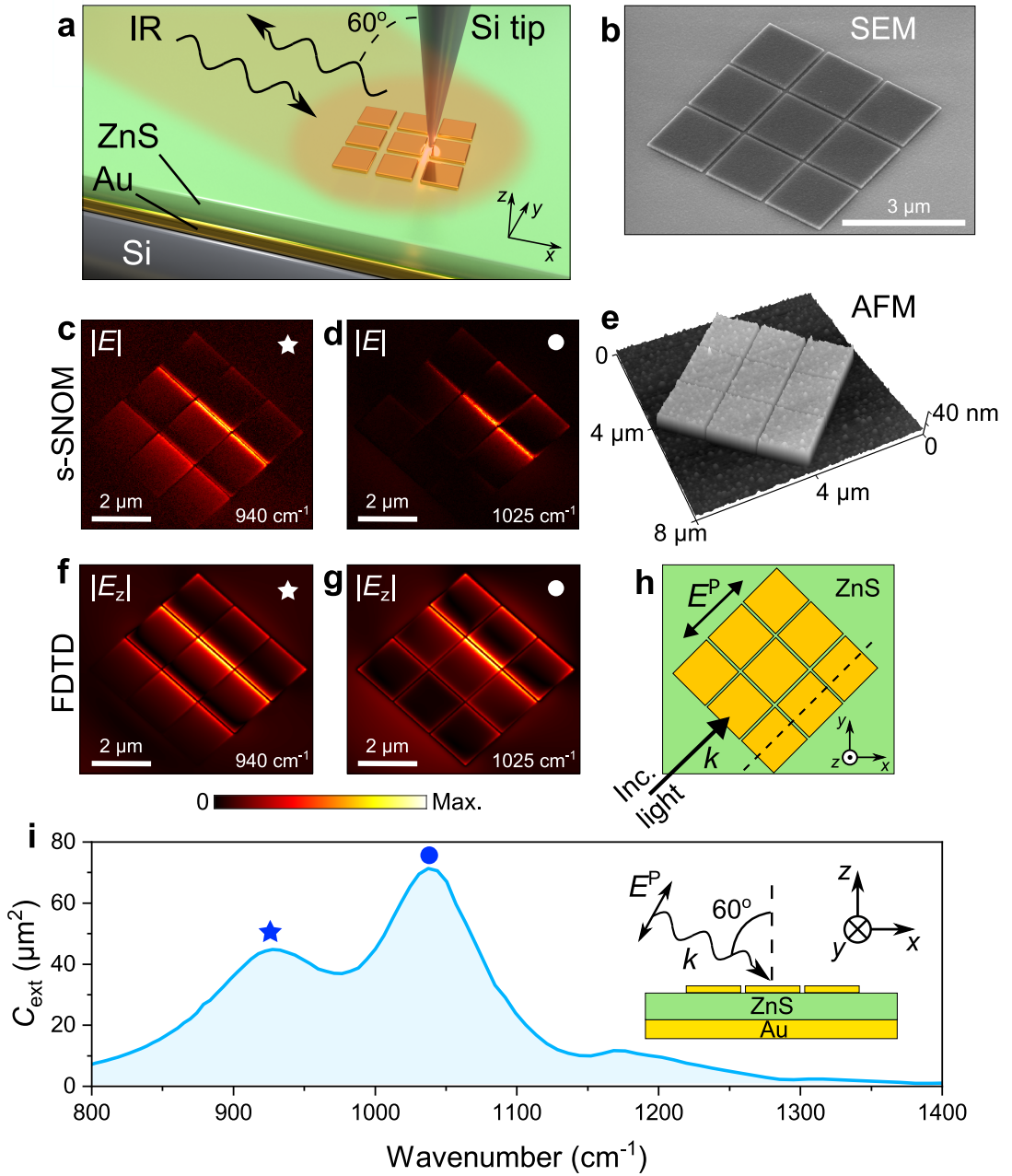


Figure 4.10: (a) Sketch of the s-SNOM configuration used for the mapping of the near-field of a 3×3 -patch MIM antenna. The antenna consists of a stack with the following layers from top to bottom: Au (40 nm)/ZnS (270 nm)/Au (200 nm), where the top layer comprises nine patches of width $w = 1.65 \mu\text{m}$, placed in a 3×3 configuration with a gap of 100 nm (see Appendix G for details on sample fabrication). (b) Scanning electron microscope (SEM) image of the 3×3 -patch MIM antenna. Courtesy of Christophe Dupuis from C2N. See Fig. A6 for more details. (c-g) Near-field images of the measured amplitude of the s-SNOM signal demodulated at the 3rd harmonic and their corresponding FDTD simulations at the resonance frequencies indicated by the markers in panel (i). The simulation results were computed in the xy -plane 30 nm above the Au patches of the antenna, *i.e.*, at the average height of the tip in our experiment ($\Delta z \approx 60$ nm). (e) Atomic force microscope (AFM) image showing the topography of the 3×3 -patch antenna. (h) Projection of the p -polarized incident field onto the antenna in the xy -plane. (i) FEM simulation of the extinction cross-section of the antenna for a p -polarized field incident as sketched in the inset.

shown that changing the orientation of a nanorod antenna with respect to the illuminating field allows one to map its local near-field with s-SNOM operated with a metallic tip [32]. This approach suggests that it is possible to benefit from the comparatively higher signals of the highly scattering metallic tip while preserving the antenna's near-field distribution. Nevertheless, in the current case, the symmetry of the antenna precludes the use of this method, which is why we have opted for the use of an Si tip. We stress here the difficulty of extracting the near-field signal of a sub- λ antenna using this approach due to the intrinsically low scattering cross-section of the Si tip, a feat that requires optimal alignment of the optical setup. This is compounded by the fact that the local field of a MIM antenna is buried in its cavity so that one may only probe the portion of the field that leaks out (see section 4.2). To make matters worse, approach curves measured on a large Au pattern ($\sim 30 \times 30 \mu\text{m}^2$ in size), revealed that in this configuration, it is necessary to demodulate the detected signal at the 3rd-harmonic of the tip oscillation frequency to adequately isolate the near-field signal (see Fig. A10). As the detected signal systematically decreases with demodulation at higher harmonics, this further exacerbates the complexity of such near-field measurements. Typically each measurement is preceded by the measurement of an approach curve as a verification of the optical alignment of the setup.

The measured near-field images of the 3×3 antenna mapped at its two resonance modes, which are indicated by the markers in Fig. 4.10 (i), are shown in Figs. 4.10 (c) and (d). Using the same arguments presented in section 4.2 when comparing s-SNOM images of a single patch MIM antenna with simulations (see also Fig. A9), we compare the measurements of Figs. 4.10 (c) and (d) to FDTD simulations of the z -component of the antenna near-field (Figs. 4.10 (f) and (g)). It should be mentioned here that one may place an analyzer before the detector selecting only p -polarized light so that the comparison between the measured signal and the simulated z -component of the electric field is exact. However, this severely reduces the signal-to-noise ratio of the experiment and we have found that, for this particular antenna configuration, the resulting field distribution is essentially identical to what is obtained without an analyzer.

It is clear that at its two resonance modes ($\omega = 940 \text{ cm}^{-1}$ and 1025 cm^{-1}), the near-field of the antenna is highly asymmetrical. Namely, the large field enhancement and confinement are found solely in the gaps in the top right corners of Figs. 4.10 (c) and (d). This is quite striking, as, for such a geometrically symmetric antenna, one would intuitively expect a more symmetrical field distribution, in which the field is evenly distributed among the gaps. The observed asymmetrical field distribution is a consequence of the near-field interaction among the antenna patches as well as the oblique illumination of our experiment (see Fig. 4.10 (a)). In particular, the large field enhancement in the gaps arises from the presence of charges of opposite sign at the patch edges which are separated by a nanometric gap as discussed in subsection 4.3.2 (see Figs. 4.11 (c) and (f)). Concordantly, the observed field confinement is a result of the oblique incident field being funneled into the gaps in the top right corners of the panels in Figs. 4.10 (c-g). The phase images of Figs. 4.11 (b) and (e) show that the electric field phase undergoes a shift from $-\pi$ to π between the patches at either side of the aforementioned gaps, indicating that these patches are coupled. If the patches were uncoupled, such a phase shift would be expected to occur at the surface of each patch individually (see Figs. 4.4 (c) and (f)).

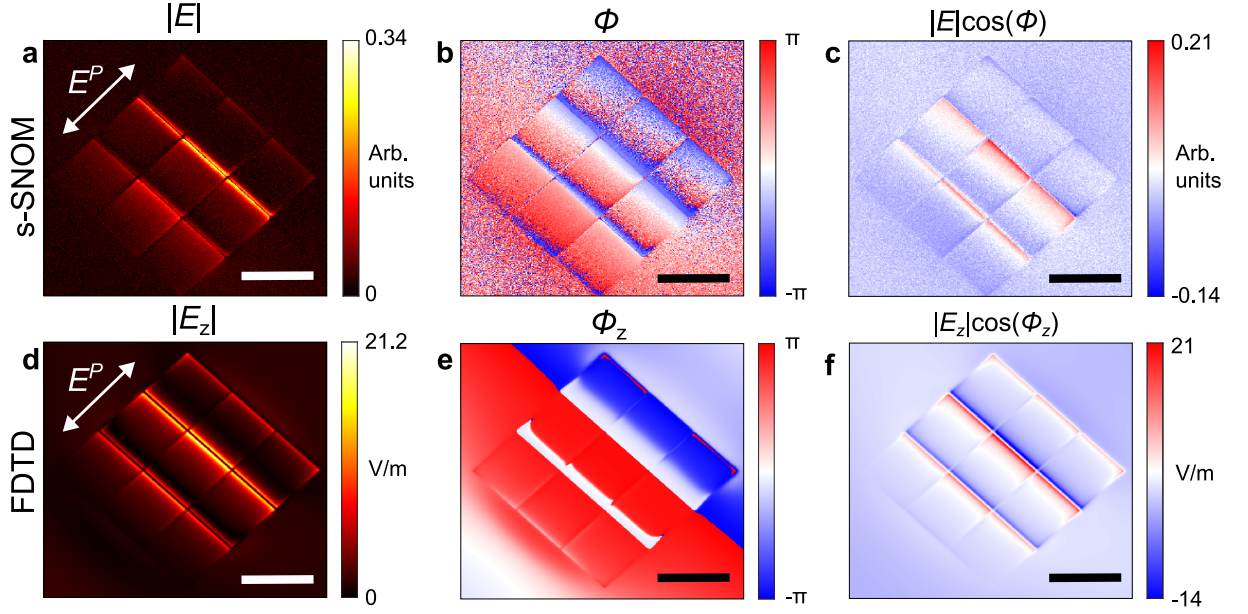


Figure 4.11: (a) Amplitude ($|E|$), (b) phase (ϕ), and (c) real part ($\text{Re}\{E\} = |E| \cos \phi$) of the near-field of the antenna, mapped at 940 cm^{-1} . The real part of the electric field shows that charges of opposite sign are present at the patch edges separated by the nanometric gap (100 nm). (d-f) FDTD simulations corresponding to panels (a-c). The antenna is illuminated from the bottom left corner of the panels with p -polarized light incident at 60° from the normal to the surface. The projection of the incident field onto the antenna is indicated by the double arrows in panels (a) and (d). The scale bars correspond to $2 \mu\text{m}$.

The behavior of the antenna at the two modes introduced here will be discussed in greater detail in the next subsection.

Finally, we comment on the influence of using a dielectric tip versus a metallic tip. In addition to the near-field images presented in Figs. 4.10 (c) and (d), which were measured using an Si tip, we also performed the same measurements with a platinum (Pt) coated tip (see Fig. A10). In contrast to the Si tip, it is found that the Pt tip produces an image that poorly matches the simulated near-field distribution of the antenna without the tip. As shown in Fig. A11 (b), the maps measured with a Pt tip reveal a uniform field with minimal contrast between the field on the top of the patches and that of the substrate, thus, concealing the expected field enhancement and confinement in the gaps. This comparison plainly illustrates that the use of dielectric tips facilitates the interpretation of near-field images of plasmonic nanostructures.

4.4.2 Microscope reflectivity measurements of a 3×3 -patch MIM antenna: angularly dependent antenna response

In order to more closely examine the angular dependence of the antenna response, we performed focused far-field microscope reflectivity measurements of the 3×3 -patch MIM antenna (Figs. 4.12 (a) and (b)). Two measurements were performed separately, each with a different Cassegrain objective focusing and collecting light from the antenna at a different angular interval (see Figs. 4.12 (a-c)). The measurements and corresponding FEM simulations show that for

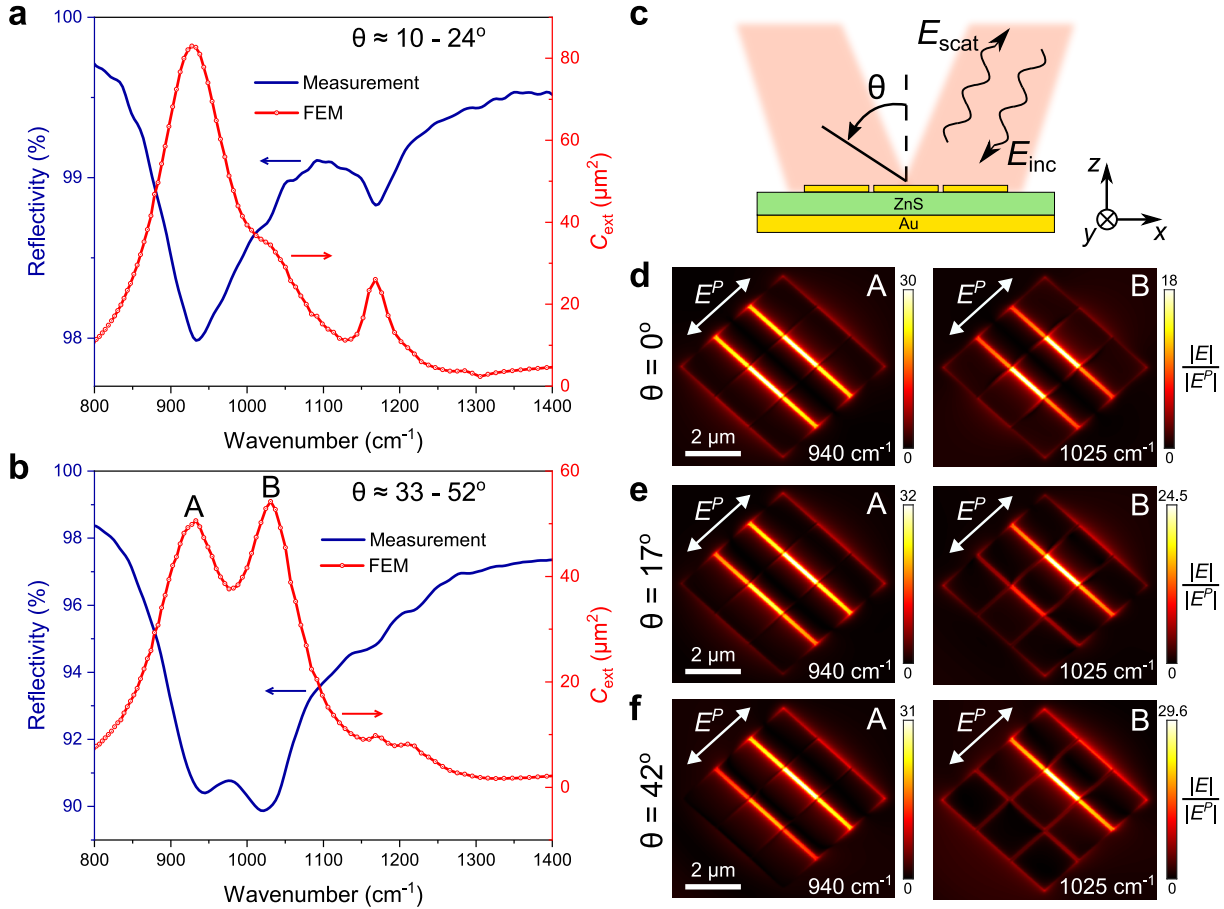


Figure 4.12: (a) & (b) Far-field response of the 3×3 -patch MIM antenna versus angle of incidence θ sketched in panel (c). The blue curves correspond to focused microscope reflectivity (*Bruker Hyperion*) spectra of the antenna, each measured with a Cassegrain objective with a different angular collection interval ($\theta \approx 10 - 24^\circ$ for (a) and $\theta \approx 33 - 52^\circ$ for (b)). The red curves are FEM simulations of the extinction cross-section (C_{ext}) of the antenna averaged at three different values of θ within the collection interval of the objective. The two resonance modes of the antenna are marked with the letters "A" and "B" in panel (b). The dips in the reflectivity spectra correspond to the maxima of C_{ext} . (c) Sketch depicting the incident (E_{inc}) and scattered (reflected, E_{scat}) fields in the experiment. A broadband unpolarized global source is used as the illumination. The same objective is used to focus the incident field onto the antenna and collect its scattered field. A diaphragm is also employed to restrict the field of view of the detector to a $50 \times 50 \mu\text{m}^2$ region of the sample. A reference measurement is first performed on a part of the sample with no patterns, giving the intensity of the incident field I_{inc} . This is followed by a measurement with the antenna in the focus of the objective, giving the intensity I_{scat} . The reflectivity is then found from the ratio $R = I_{\text{inc}}/I_{\text{scat}}$. (d-f) FDTD simulations of the electric field enhancement $|E|/|E^P|$, where E^P is the p -polarized incident field sketched in Figs. 4.10 (h) and (i), calculated in xy -plane 30 nm above the patches for the two modes A and B as a function of increasing angle θ .

angles near normal incidence ($\theta \leq 24^\circ$), the antenna exhibits one predominant resonance mode at 940 cm^{-1} , while for larger angles ($\theta \geq 33^\circ$), this mode is supplemented by another at 1025 cm^{-1} . In other words, the 3×3 -patch antenna exhibits an angularly-dependent spectral response. This is quite remarkable given the fact that an individual square-patch MIM antenna has an angularly-

independent spectral response (see section 4.2). The two modes of the 3×3 -patch antenna will henceforth be referred to as mode "A" and "B", respectively (see Fig. 4.12 (b)).

The angularly-dependent spectral response of the 3×3 -patch MIM antenna originates from the near-field interaction between its patches discussed in the previous subsection. Although the near-field distributions of the two modes A and B, presented in Figs. 4.10 (c-g), seem similar, there exist a few subtle differences in the behavior of the antenna at the two modes. To elucidate this point and to detail the near-field angular response of the antenna, we performed FDTD simulations of the electric field enhancement of the antenna at the modes A and B for normal incidence and at angles mid-way through the two experimentally probed angular intervals (Figs. 4.12 (d-f)). For normal incidence, the near-field is evenly distributed among the gaps orthogonal to the incident electric field polarization for both modes. However, for mode B the field is more confined to the gaps adjacent to the central patch (see Fig. 4.12 (d), B), leading to a weaker contribution to the overall far-field response (cf. Fig. 4.12 (a)). As the angle increases, the local field undergoes a shift toward the gaps to the opposite side of the incident field, *i.e.*, to the gaps in the top right corners of the panels in Figs. 4.12 (e) and (f)⁵. This shift is more drastic for mode B as the field, in this case, is almost totally confined in the aforementioned gaps, while for mode A, a portion of the field remains in the bottom left gaps, mostly in the central gap (see Figs. (e) and (f), A). Additionally, the field enhancement in the gaps increases with increasing angle for mode B, whereas that of mode A is almost angularly independent. These observations suggest that mode A can be classified as an *aggregate or collective mode* arising from the collective near-field coupling of all the elements of the antenna. On the other hand, mode B is a *gap mode*, which results from the coupling of two adjacent patches as in gap antennas [33].

As a verification of this mode classification, we performed simulations of a BiMIM structure with the same layers as in Fig. 4.10 (a) but with a top metallic part consisting of only two square patches of side $w = 1.65 \mu\text{m}$, separated by a gap of 100 nm. This simulation shows that the considered BiMIM structure has two resonance modes, one at 1037 cm^{-1} and one at 1184 cm^{-1} (see Fig. 4.13 (a)), in which the field is confined to the gap (Figs. 4.13 (b) and (c)). These two modes are a result of the mode hybridization discussed in section 4.3. Both BiMIM modes appear in the far-field spectra of the 3×3 -patch MIM antenna (see Fig. 4.12 (a) and (b)), with the one at 1037 cm^{-1} corresponding to the gap mode B of the 3×3 -patch MIM antenna.

The absence of the aggregate mode A in the spectra of Fig. 4.13 (a) indicates that this mode is a result of the near-field coupling unique to the 3×3 antenna. This point is further corroborated by the fact that mode A is also the most red-shifted mode compared to the fundamental resonance of the single square patch MIM antenna with which the 3×3 antenna is constructed. As the resonance of a plasmonic nanostructure is expected to red-shift as the near-field interaction is enhanced⁶, it is clear that the strongest near-field interaction occurs at the aggregate mode A, in which all the patches of the 3×3 antenna are coupled through near-field interaction.

⁵The antenna is illuminated from the bottom left corner of the panels in Figs. 4.12 (d-f).

⁶The near-field interaction can be enhanced, leading to a red-shift of the antenna's plasmonic resonances, by decreasing the gap size (see, for instance, ref. [13]) or by increasing the number of interacting elements as in the case of a 3×3 antenna.

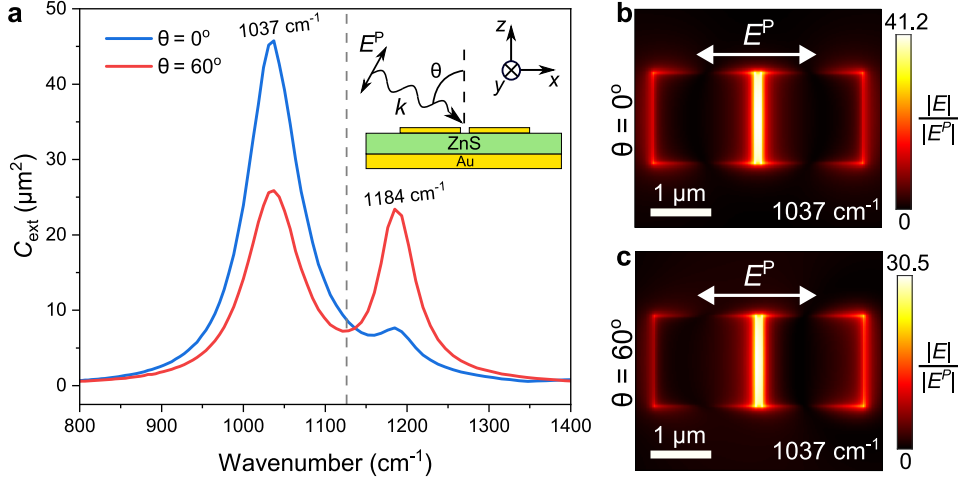


Figure 4.13: Simulations of the MIM antenna of Fig. 4.10 (a) but with a top layer consisting of only two patches separated by a gap of 100 nm (BiMIM geometry). (a) FEM simulations of the extinction cross-section of the BiMIM structure for two angles of incidence ($\theta = 0^\circ$ and 60° .) as sketched in the inset. The dashed vertical line marks the spectral position of the fundamental resonance mode of a single square patch of the shown BiMIM structure. (b) & (c) FDTD simulations of the electric field enhancement, $|E|/|E^P|$, computed in the xy -plane 30 nm above the BiMIM structure at the resonance frequency $\omega = 1037 \text{ cm}^{-1}$.

Thus it appears from our experimental observations that the field distribution of this mode is only weakly altered with increasing angle (see Fig. 4.12 (d-f), A).

To conclude this subsection, we will briefly touch upon the influence of gap size on the response of the 3×3 antenna. Apropos, we measured via microscope reflectivity the far-field response of the 3×3 antenna as a function of gap size g (see Fig. A12). The measurements show that beyond a gap $g = 2 \mu\text{m}$, the extinction of the incident field by the 3×3 antenna exhibits a single resonance peak corresponding to an additive response of its constituent patch MIM antennas (Fig. A12, turquoise curve). For a single square-patch MIM antenna of side width $w = 1.65 \mu\text{m}$, FEM simulations yield an extinction cross-section of $39.5 \mu\text{m}^2$ (for unpolarized light incident at 20° with respect to the normal). This corresponds to a circular area with a radius of $3.55 \mu\text{m}$. Taking into account the width of the patches ($1.65 \mu\text{m}$), the patch MIM antennas placed in a 3×3 configuration would then be independent if $g > g_{th} \approx 2.73 \mu\text{m}$, where g_{th} is a threshold gap size. This is consistent with the experimental observation reported above.

4.4.3 3×3 -patch MIM antenna with a missing element

We now ask ourselves the following question: how would the response of the 3×3 -patch antenna be affected if one of its patches were to be removed? To shed some light on this line of inquiry, we performed s-SNOM imaging of 3×3 -patch antennas with a missing patch (Figs. 4.14 (a-c)). Three cases were considered: a 3×3 antenna with (i) a patch missing from one of its corners, (ii) one of its mid-outer patches removed, or (iii) its central patch removed (see Fig. 4.14 (a)). Interestingly, the removal of one of the patches has almost no effect on the antenna's near-field distribution. Save for the fact that the field is now distributed among two gaps instead

4.4. Shaping the optical properties of MIM cavities through multi-element surface patterning: the case of a 3×3 -patch MIM cavity antenna

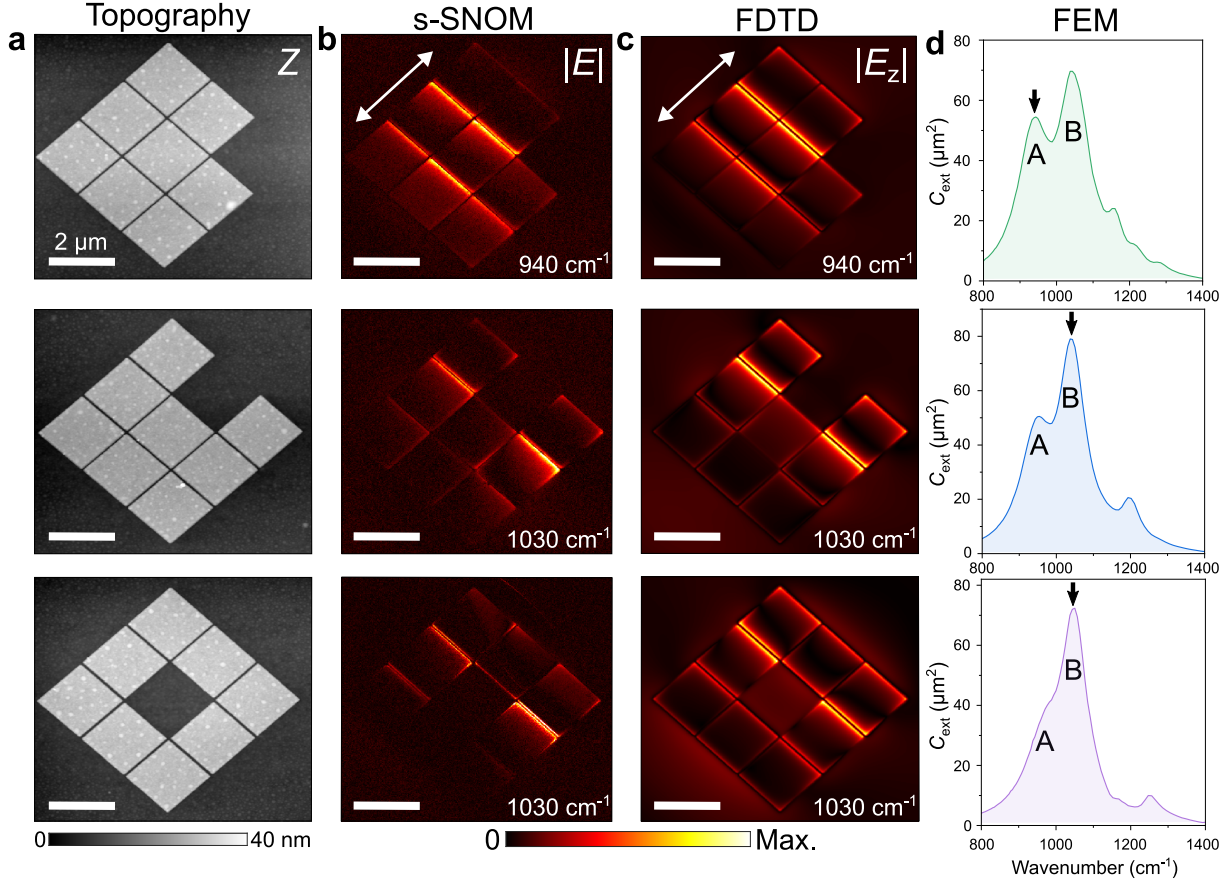


Figure 4.14: (a) Topography of 3×3 -patch antennas with a missing element. (b) Measured and (c) computed near-field images of the antennas, mapped at the resonances indicated by arrows in panel (d), and their corresponding FDTD simulations. The antenna is illuminated by p -polarized light from the bottom left corner of the panels with an incidence angle of 60° with respect to the normal to the surface. The double arrow in the top panels of columns (b) and (c) indicates the projection of the incident field polarization onto the antenna. (d) FEM simulations of extinction cross-section spectra of the antennas for p -polarized light incident at 60° with respect to the normal to the surface. The corresponding extinction spectra at smaller angles are shown in Fig. A13.

of three, the near-field images of Figs. 4.14 (b) and (c) show the same asymmetrical near-field distribution as that of the straight 3×3 antenna (see subsection 4.4.1). This behavior becomes more comprehensible if one considers the large field enhancement that occurs between the two edges of two metal patches when brought close to one another (see Figs. 4.13 (b) and (c)). In other words, the field in the gaps is expected to be predominant regardless of the number of interacting elements.

It is also interesting to examine the spectral response of the antenna when it is devoid of one of its patches. In particular, if the elimination of one of the patches results in an asymmetric antenna configuration (cases (i) and (ii)), the two modes A and B of the straight 3×3 antenna remain intact (see Fig. 4.14 (d), green and blue curves). On the other hand, the elimination that preserves the antenna symmetry, that is, removing the central patch (case (iii)), suppresses mode A (Fig. 4.14, magenta). This suggests that the central patch plays a critical role in

the near-field coupling associated with mode A of the 3×3 antenna, further validating its classification as an aggregate or collective mode (see subsection 4.4.2). Further, microscope reflectivity measurements showed that for cases (i) and (ii) the spectral response near normal incidence is essentially the same as that of the straight 3×3 antenna, *i.e.*, displaying only one main resonance corresponding to mode A (see Fig. A13, green and blue curves). In contrast, case (iii) showed a peak corresponding to mode B instead of mode A (Fig. A13, magenta curve).

4.5 Conclusion

We have illustrated in this chapter how the optical properties of a surface may be tuned by sandwiching a dielectric layer between two metallic layers, forming a sub- λ MIM cavity. The cavity was shown to act as a waveguide for surface plasmon-polaritons propagating at its two metal/dielectric interfaces, leading to plasmonic Fabry-Perot resonances. We began our treatment of the problem by discussing both, theoretically and experimentally, the properties of a single sub- λ square-patch MIM antenna. Special attention was given to the fundamental resonance mode of the MIM cavity, whose frequency was shown to be angle-independent for the case of a square-patch MIM antenna. We also revealed that incoming light whose frequency matches that of the fundamental resonance mode of a patch-MIM antenna gets funneled into the cavity underneath the patch, resulting in a large field enhancement and sub- λ confinement. This behavior stems from the fact that the optical cross-sections of a resonant MIM antenna are several times the antenna's geometrical cross-section.

To demonstrate the tunability of MIM cavities, two examples were considered, in which two or more square-patch MIM antennas were combined. In the first example, we considered a single asymmetric BiMIM structure consisting of two coupled sub- λ square-patch MIM antennas of different widths. Using IR-SMS, simultaneous excitation of the various hybrid modes of the BiMIM structure due to thermal fluctuations was established. Further, simulated electric field enhancement plots revealed that due to the nature of the transverse hybrid modes, and the asymmetry of the system considered, the two MIM antennas making up the structure can emit (equivalently, absorb) radiation independently. In the second example, we presented a more complex MIM antenna combining 9 sub- λ square patches, placed in a 3×3 configuration. The near-field distribution of this antenna was mapped via s-SNOM and its far-field spectral response was determined from angle-resolved microscope reflectivity measurements. In contrast to an individual patch-MIM antenna, the measurements showed that the 3×3 antenna exhibits an angularly-dependent response both in the near- and far-field, arising from the near-field interaction among the antenna's multiple patches. We also commented on the influence of gap size and the removal of one of the interacting patches on the antenna's behavior.

The tunability of MIM cavities, along with the fact that the absorbed radiation is mainly concentrated in the insulator layer in a MIM antenna, could be of use for realizing IR photodetectors with improved responsivity at room temperature. The absorbed radiation may be harnessed by replacing the insulating layer considered here by a semi-conductor like HgCdTe [2, 34] or a quantum well material [26].

References

- [1] Y Todorov, L Tosetto, J Teissier, AM Andrews, P Klang, R Colombelli, I Sagnes, G Strasser, and C Sirtori. “Optical properties of metal-dielectric-metal microcavities in the THz frequency range”. *Opt. Express* 18.13 (2010), pp. 13886–13907.
- [2] C Koechlin, P Bouchon, F Pardo, J Jaeck, X Lafosse, JL Pelouard, and R Haidar. “Total routing and absorption of photons in dual color plasmonic antennas”. *Appl. Phys. Lett.* 99.24 (2011), p. 241104.
- [3] W Yu, Y Lu, X Chen, H Xu, J Shao, X Chen, Y Sun, J Hao, and N Dai. “Large-Area, Broadband, Wide-Angle Plasmonic Metasurface Absorber for Midwavelength Infrared Atmospheric Transparency Window”. *Adv. Opt. Mater.* 7.20 (2019), p. 1900841.
- [4] J Hao, J Wang, X Liu, WJ Padilla, L Zhou, and M Qiu. “High performance optical absorber based on a plasmonic metamaterial”. *Appl. Phys. Lett.* 96.25 (2010), p. 251104.
- [5] P Chevalier, P Bouchon, J Jaeck, D Lauwick, N Bardou, A Kattnig, F Pardo, and R Haidar. “Absorbing metasurface created by diffractionless disordered arrays of nanoantennas”. *Appl. Phys. Lett.* 107.25 (2015), p. 251108.
- [6] W Rechberger, A Hohenau, A Leitner, JR Krenn, B Lamprecht, and FR Aussenegg. “Optical properties of two interacting gold nanoparticles”. *Opt. Commun.* 220.1-3 (2003), pp. 137–141.
- [7] P Nordlander, C Oubre, E Prodan, K Li, and MI Stockman. “Plasmon hybridization in nanoparticle dimers”. *Nano Lett.* 4.5 (2004), pp. 899–903.
- [8] NJ Halas, S Lal, WS Chang, S Link, and P Nordlander. “Plasmons in strongly coupled metallic nanostructures”. *Chem. Rev.* 111.6 (2011), pp. 3913–3961.
- [9] L Gunnarsson, T Rindzevicius, J Prikulis, B Kasemo, M Käll, S Zou, and GC Schatz. “Confined plasmons in nanofabricated single silver particle pairs: experimental observations of strong interparticle interactions”. *J. Phys. Chem. B* 109.3 (2005), pp. 1079–1087.
- [10] PK Jain, W Huang, and MA El-Sayed. “On the universal scaling behavior of the distance decay of plasmon coupling in metal nanoparticle pairs: a plasmon ruler equation”. *Nano Lett.* 7.7 (2007), pp. 2080–2088.
- [11] LV Brown, H Sobhani, JB Lassiter, P Nordlander, and NJ Halas. “Heterodimers: plasmonic properties of mismatched nanoparticle pairs”. *ACS Nano* 4.2 (2010), pp. 819–832.
- [12] EP Bellido, Y Zhang, A Manjavacas, P Nordlander, and GA Botton. “Plasmonic coupling of multipolar edge modes and the formation of gap modes”. *ACS Photonics* 4.6 (2017), pp. 1558–1565.
- [13] P Zilio, M Malerba, A Toma, RP Zaccaria, A Jacassi, and FD Angelis. “Hybridization in three dimensions: a novel route toward plasmonic metamolecules”. *Nano Lett.* 15.8 (2015), pp. 5200–5207.
- [14] S Collin, F Pardo, and JL Pelouard. “Waveguiding in nanoscale metallic apertures”. *Opt. Express* 15.7 (2007), pp. 4310–4320.
- [15] J Yang, C Sauvan, A Jouanin, S Collin, JL Pelouard, and P Lalanne. “Ultrasmall metal-insulator-metal nanoresonators: impact of slow-wave effects on the quality factor”. *Opt. Express* 20.15 (2012), pp. 16880–16891.

- [16] MR Query. *Optical constants of minerals and other materials from the millimeter to the ultraviolet*. Chemical Research, Development & Engineering Center, US Army Armament, 1998.
- [17] C Li, V Krachmalnicoff, P Bouchon, J Jaeck, N Bardou, R Haidar, and Y De Wilde. “Near-field and far-field thermal emission of an individual patch nanoantenna”. *Phys. Rev. Lett.* 121.24 (2018), p. 243901.
- [18] L Abou-Hamdan, C Li, R Haidar, V Krachmalnicoff, P Bouchon, and Y De Wilde. “Hybrid modes in a single thermally excited asymmetric dimer antenna”. *Opt. Lett.* 46.5 (2021), pp. 981–984.
- [19] R Carminati, A Cazé, D Cao, F Peragut, V Krachmalnicoff, R Pierrat, and Y De Wilde. “Electromagnetic density of states in complex plasmonic systems”. *Surf. Sci. Rep.* 70.1 (2015), pp. 1–41.
- [20] Y De Wilde, F Formanek, R Carminati, B Gralak, PA Lemoine, K Joulain, JP Mulet, Y Chen, and JJ Greffet. “Thermal radiation scanning tunnelling microscopy”. *Nature* 444.7120 (2006), pp. 740–743.
- [21] A Babuty, K Joulain, PO Chapuis, JJ Greffet, and Y De Wilde. “Blackbody spectrum revisited in the near field”. *Phys. Rev. Lett.* 110.14 (2013), p. 146103.
- [22] E Prodan and PJCP Nordlander. “Plasmon hybridization in spherical nanoparticles”. *J. Chem. Phys.* 120.11 (2004), pp. 5444–5454.
- [23] E Prodan, C Radloff, NJ Halas, and P Nordlander. “A hybridization model for the plasmon response of complex nanostructures”. *Science* 302.5644 (2003), pp. 419–422.
- [24] M Gluodenis and CA Foss. “The effect of mutual orientation on the spectra of metal nanoparticle rod-rod and rod-sphere pairs”. *J. Phys. Chem. B* 106.37 (2002), pp. 9484–9489.
- [25] L Abou-Hamdan et al. (*in preparation*) (2023).
- [26] D Palaferri, Y Todorov, A Bigioli, A Mottaghizadeh, D Gacemi, A Calabrese, A Vasanelli, L Li, AG Davies, EH Linfield, et al. “Room-temperature nine- μm -wavelength photodetectors and GHz-frequency heterodyne receivers”. *Nature* 556.7699 (2018), pp. 85–88.
- [27] R Esteban, R Vogelgesang, J Dorfmueller, A Dmitriev, C Rockstuhl, C Etrich, and K Kern. “Direct near-field optical imaging of higher order plasmonic resonances”. *Nano Lett.* 8.10 (2008), pp. 3155–3159.
- [28] M Rang, AC Jones, F Zhou, Z Li, BJ Wiley, Y Xia, and MB Raschke. “Optical near-field mapping of plasmonic nanoprisms”. *Nano Lett.* 8.10 (2008), pp. 3357–3363.
- [29] M Schnell, A Garcia-Etxarri, AJ Huber, K Crozier, J Aizpurua, and R Hillenbrand. “Controlling the near-field oscillations of loaded plasmonic nanoantennas”. *Nat. Photon.* 3.5 (2009), pp. 287–291.
- [30] A Garcia-Etxarri, I Romero, FJG de Abajo, R Hillenbrand, and J Aizpurua. “Influence of the tip in near-field imaging of nanoparticle plasmonic modes: Weak and strong coupling regimes”. *Phys. Rev. B* 79.12 (2009), p. 125439.
- [31] M Schnell, P Alonso-Gonzalez, L Arzubia, F Casanova, L El Hueso, A Chuvilin, and R Hillenbrand. “Nanofocusing of mid-infrared energy with tapered transmission lines”. *Nat. Photon.* 5.5 (2011), pp. 283–287.
- [32] R Buuchner, T Weber, L Kühner, SA Maier, and A Tittl. “Tip Coupling and Array Effects of Gold Nanoantennas in Near-Field Microscopy”. *ACS Photonics* 8.12 (2021), pp. 3486–3494.
- [33] T Neuman, P Alonso-González, A Garcia-Etxarri, M Schnell, R Hillenbrand, and J Aizpurua. “Mapping the near fields of plasmonic nanoantennas by scattering-type scanning near-field optical microscopy”. *Laser Photonics Rev.* 9.6 (2015), pp. 637–649.
- [34] J Le Perchec, Y Desieres, and R Espiau de Lamaestre. “Plasmon-based photosensors comprising a very thin semiconducting region”. *Appl. Phys. Lett.* 94.18 (2009), p. 181104.

Chapter 5

Mid-infrared emission of high-mobility hBN/graphene/hBN field-effect transistors under large bias: electroluminescence and radiative cooling

So far, we have mainly discussed light-matter interaction in semi-conductors and metals in the form of passive devices which were either excited thermally or optically. In this last chapter, we will shift our focus to the study of the infrared radiation produced by active graphene-based devices. Graphene has the band structure of a semi-metal (between a metal and semi-conductor) with a vanishing electronic density of states at the charge-neutral point (*i.e.*, at $E_F = 0$) [1]. The study that will be presented here is dedicated to a novel process of infrared electroluminescence in transistors made of hexagonal boron nitride (hBN)-encapsulated graphene. While this subject warrants a more extended discussion than what can be presented in a solitary chapter, we will nevertheless try to introduce the reader to the main aspects that are required for a proper understanding of the physical phenomenon at the origin of the observed luminescence in the investigated devices¹.

Since its discovery in 2005 [2], graphene has been subject to numerous studies, investigating its peculiar thermal² [3, 4] and electronic properties [1]. In particular, electrons propagating through graphene's honeycomb lattice have no effective mass, which results in quasi-particles that are described by a Dirac-like equation rather than a Schrödinger equation (see Fig. 5.1). As a result of its massless charge carriers and little scattering, quantum effects are discernible at room temperature in graphene, making it the quintessential playground for the experimental verification of various exotic physical phenomena [5–8].

¹The body of work presented in this chapter was conducted in close collaboration with the group of Emmanuel Baudin at LPENS. The studied graphene transistors were prepared and electrically characterized by Aurélien Schmitt, while the optical characterization of their infrared emission was carried out at Institut Langevin using the far-field techniques described in chapter 3.

²See, *e.g.*, Table 5.1.

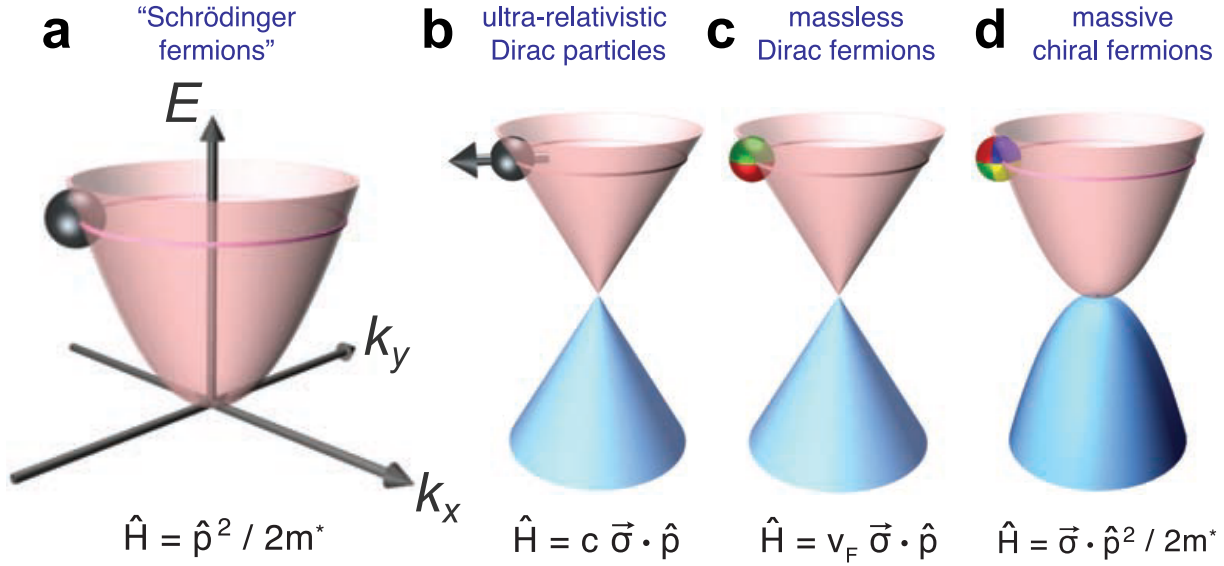


Figure 5.1: Depiction of the density of states for various quasi-particles (reproduced from ref. [13]). (a) Charge carriers in condensed matter physics are usually described by the Schrödinger equation with an effective mass m^* that is different from the free electron mass (\hat{H} and \hat{p} are the Hamiltonian and momentum operators, respectively). The effective mass approximates the effect of the particle’s potential, which in general may take a very complicated form. (b) Relativistic particles in the limit of zero rest mass follow the Dirac equation, where c is the speed of light and $\vec{\sigma}$ is the Pauli matrix. (c) Charge carriers in graphene are called massless Dirac fermions and are described by a 2D analog of the Dirac equation, with the Fermi velocity $v_F \approx 10^6$ m/s playing the role of the speed of light and a 2D pseudo-spin matrix describing two sub-lattices of the honeycomb lattice. Similar to the real spin that can change its direction between, say, left and right, the pseudo-spin is an index that indicates on which of the two sub-lattices a quasi-particle is located. The pseudo-spin can be indicated by color (*e.g.* red and green). (d) Bi-layer graphene provides us with yet another type of quasi-particles that have no analog. They are massive Dirac fermions described by a rather bizarre Hamiltonian that combines features of both Dirac and Schrödinger equations. The pseudo-spin changes its color index four times as it moves among four carbon sub-lattices.

The minimal scattering in graphene results in electron scattering mean-free paths that cover sub-micrometer distances, even in samples placed on an atomically rough substrate, covered with adsorbates and at room temperature. This endows suspended graphene with substantially high electron mobility, which can reach up to $250,000 \text{ cm}^2/\text{V.s}$ in some cases [9, 10]. When deposited on an hBN substrate, electron mobilities of $\sim 25,000 \text{ cm}^2/\text{V.s}$ for mono-layer graphene and $\sim 40,000 \text{ cm}^2/\text{V.s}$ for bi-layer graphene can be achieved at room temperature [11]. The large electron mobility of the graphene/hBN heterostructure results from an enhancement of the flatness of the graphene layer (in comparison to when it is placed on other substrates), brought upon by its adhesion with the atomically flat hBN substrate, through van der Waals interaction [12]. Introducing a second hBN capping layer to fully encapsulate graphene, further improves its flatness, yielding electron mobilities as high as $200,000 \text{ cm}^2/\text{V.s}$. This is 100 times larger than the electron mobility of silicon, which is the material of choice in logic transistors.

As a light emitter, low-mobility graphene has well-understood incandescent properties sim-

Material	κ (W/m.K)	C_p (J/kg.K)	ρ (kg/m ³)	$\alpha_D = \kappa/\rho C_p$ (m ² /s)	Refs.
Graphene	4840 – 5300	700*	2250	$(3.1 - 3.4) \times 10^{-3}$	[3, 4]
Si	124	714.5	2329	7.45×10^{-5}	[14, 15]
Ag	436	231.8	10490	1.79×10^{-4}	[16, 17]
Au	318	134.5	19320	1.23×10^{-4}	[18, 19]
Cu	402	377	8960	1.19×10^{-4}	[17, 20]
W	183	185.9	19300	5.1×10^{-5}	[20, 21]

Table 5.1: Room temperature thermal properties of suspended graphene compared to those of silicon (Si) and typical metals. The listed thermal properties correspond to the thermal conductivity (κ), specific heat capacity at constant pressure (C_p), and thermal diffusivity (α_D). More comprehensive lists of thermal properties of materials can be found in the literature (*e.g.*, ref. [22]). *This includes both the lattice and electron gas contributions to the specific heat.

ilar to those of graphite. On the other hand, light emission from high-mobility graphene is fundamentally different. This is because the electron gas in high-mobility graphene is almost completely decoupled from its lattice, a situation with no precedent among the known natural materials. While this has many implications on the material’s transport properties, in the domain of radiative emission, which is our focus here, there are two obvious consequences:

- (i) The electron gas temperature is independent of that of the lattice. This results in an ultra-small electron gas heat capacity in graphene devices, that is only limited by the number of degrees of freedom corresponding to the small number of free electrons in graphene ($\sim 10^6$), which is much smaller than the number of atoms ($\sim 10^{23}$). In principle, this allows ultra-fast incandescence switching (> 200 GHz) and the possibility of reaching ultra-large electronic temperatures comparable to that of plasma incandescent light sources used as visible or UV emitters, without being limited by the material sublimation temperature.
- (ii) At large electrical bias, a non-thermal, out-of-equilibrium electronic state develops in hBN-encapsulated graphene transistors below the optical phonon energy, which leads to electroluminescence in the mid-infrared (mid-IR) [23].

The second consequence is particularly striking, as one may remark, with reasonable certainty, that this is the first time a metal is found to be electroluminescent. This indeed opens the door for many questions from a fundamental point of view, but it also has strong implications for lighting devices and spectroscopy.

In this chapter, we will report the first experimentally observed signatures of graphene electroluminescence in the mid-IR. In a series of test experiments³, designed to unequivocally identify the electroluminescent nature of the detected signal, we reveal hallmarks of radiative cooling and emission due to electroluminescence in high-mobility hBN/graphene/hBN field-effect transistors [24].

³The experiments rely on the optical detection techniques presented in the previous chapters.

5.1 Ultra-fast and ultra-hot incandescent graphene in the visible to ultra-violet spectral range

Solid-state incandescent emitters are widely used for broadband optical spectroscopy but are intrinsically limited by the sublimation temperature of the material. Among metals, tungsten is commonly used with a record 3200 K temperature limit, far exceeding that of plasma sources, which are complex and costly. Nevertheless, switching incandescence is inherently slow due to the large heat capacity of metals (see Table 5.1). Indeed, the switching frequency cut-off of a common light bulb is only a few Hertz, while state-of-the-art switching frequencies, as high as 10 MHz, can only be achieved using complex micro-hot-plates structures [25].

The ultra-small heat capacity of high-mobility graphene has been readily recognized and several experiments have already demonstrated bright visible light emission with suspended graphene [26], and hBN-encapsulated graphene [27, 28] under extreme bias (Fig. 5.2). In particular, it has been shown that, under ultra-fast pulsed excitation, switching frequencies up to 10 GHz could be reached, which is significantly larger than that of the state-of-the-art micro-hot-plates [27]. Although this result represents a substantial leap forward in the quest for ultra-fast light sources, there is strong evidence suggesting that ultimate performance is yet to be reached. According to experiments on the cooling of graphene [29, 30], much faster operation – on the order of 200 GHz – should be possible. It is also important to reiterate here that the studies cited above (refs. [26–28]) applied excessively large bias, up to 6.6 V per micrometer of graphene channel length (see Fig. 5.2), which is over 6 times larger than that of the graphene transistors under study here. At such a large bias, the electron gas decoupling is lost and the lattice is almost completely thermalized to the electron gas temperature T_e . This behavior has been well-established by Raman thermometry measurements and further confirmed by a limitation in operation temperature to 2000 K, corresponding to the sublimation temperature of graphene [31].

5.2. Transport properties of high-mobility graphene field-effect transistors (HGFETs) under large bias

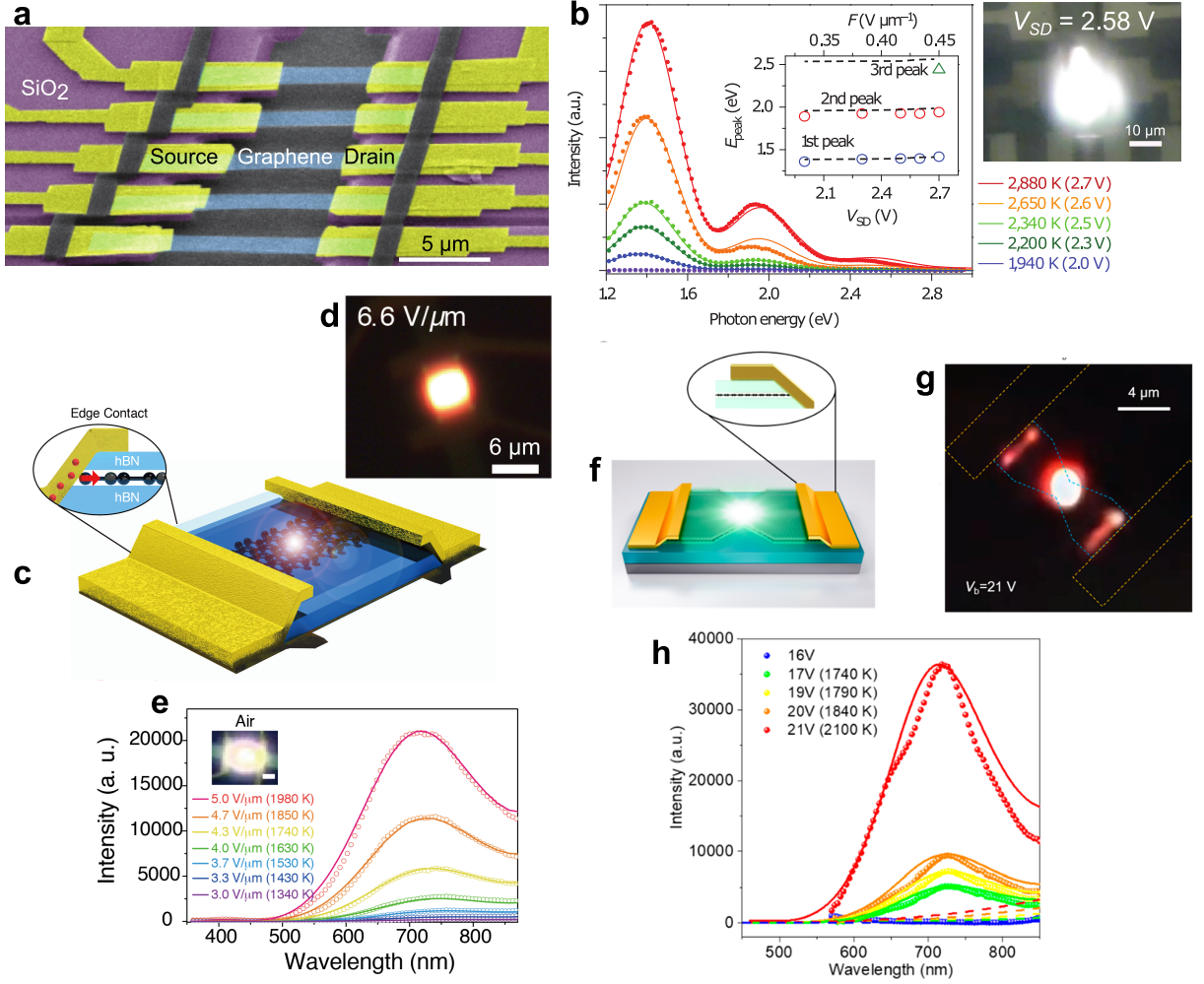


Figure 5.2: Examples of visible light incandescent emission from graphene devices under bias: (a-b) suspended graphene (ref. [26]), (c-e) hBN encapsulated graphene (ref. [27]), and (f-h) hBN-encapsulated graphene with a constriction in the center of the channel (ref. [28]). The images in (b), (d), and (g) are microscope images of the visible light emission of the device under bias. Panels (b), (e), and (h) show the visible light emission spectra of the device under bias (dots), which are fitted by appropriately modeling the Planck blackbody emission of the device (solid curves). The fits provide estimates of the electron gas temperature T_e (legend keys). Notice that a significantly large electric field must be applied across the channel to bring about the visible light emission from these devices. In panel (d), for instance, the applied electric field is as large as $6.6 \text{ V}/\mu\text{m}$ for a channel that is $6 \mu\text{m}$ in length and $3 \mu\text{m}$ in width.

5.2 Transport properties of high-mobility graphene field-effect transistors (HGFETs) under large bias

Under the application of large electric fields, the high mobility of graphene's electrons enables exotic transport regimes. This section introduces the fundamental transport properties that are essential for understanding the origin of the electroluminescent behavior of high-mobility

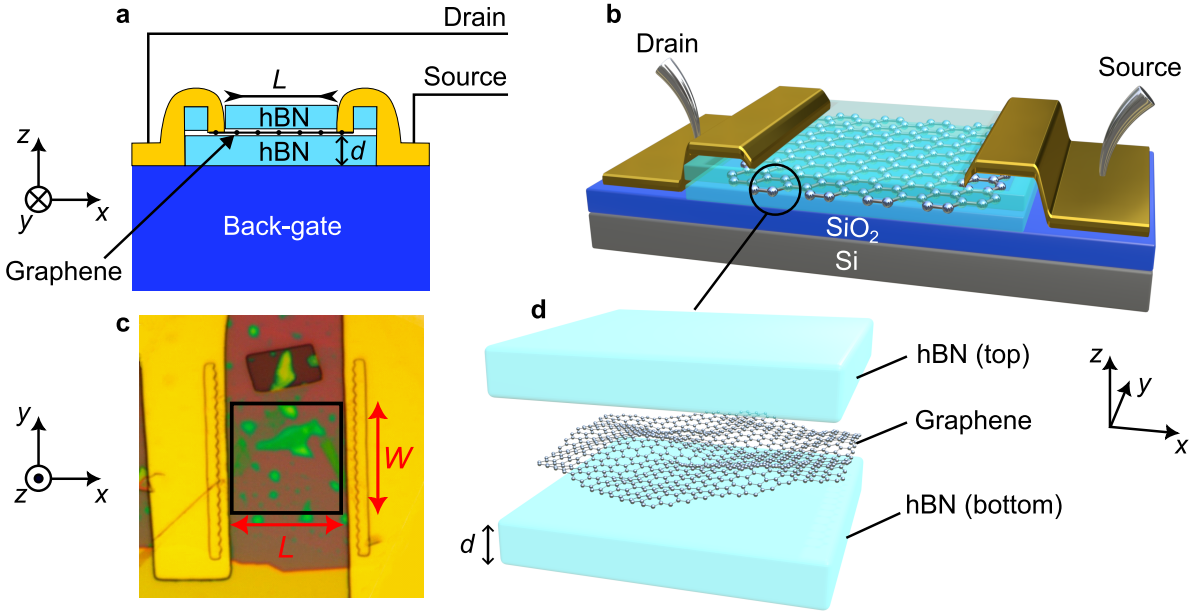


Figure 5.3: (a) Schematic illustration of the geometry of a high-mobility field-effect transistor (HGFET). A mono-layer graphene is encapsulated between two hBN layers, that are placed on a back-gate layer. The top hBN layer is etched, revealing the two ends of the graphene layer. Gold/chromium pads are then evaporated onto the etched regions, creating the source and drain electrodes of the transistor. The region between the two electrodes forms the transistor's channel with an area given by $A = L \times W$, where L and W are the channel length and width, respectively. See Appendix K for more details on the device fabrication process. (b) Three-dimensional sketch of a typical HGFET with a back-gate consisting of an SiO_2/Si substrate. (c) Microscope image of an hBN-encapsulated HGFET with a channel area $A = L \times W \sim 35 \mu\text{m} \times 35 \mu\text{m}$ on an SiO_2/Si back-gate (the transistor's graphene channel is indicated by a black box). The mono-layer graphene is encapsulated between a 65 nm-thick hBN layer from the bottom and an 82-nm-thick hBN layer from the top. The estimated electron mobility of this transistor is $60,000 \text{ cm}^2/\text{V}\cdot\text{s}$ at room temperature with a contact resistance of 250Ω . (d) Zoom of the layers forming the encapsulated graphene transistor of panel (b).

graphene field-effect transistors (HGFETs)⁴.

5.2.1 Electrostatic doping

In a typical HGFET geometry (Fig. 5.3), the graphene channel and the back-gate form a parallel plate capacitor of capacitance per unit area $C_g = \epsilon_0 \epsilon_r / d$, where ϵ_r is the capacitor dielectric constant, ϵ_0 is the permittivity of free space and d is the thickness of the bottom hBN layer (see Fig. 5.3 (a)). The capacitance enables electrostatic control of the channel's charge carrier density. For the transistor shown in Fig. 5.3 (c), the bottom hBN layer is 65 nm-thick and has a dielectric constant $\epsilon_r \simeq 3.2$ so that its capacitance per unit area is $C_g \simeq 0.44 \text{ mF}/\text{m}^2$. By applying a gate voltage V_g , the charge carrier density is modified by $C_g V_g$. Taking into account the residual doping of graphene, $n_0 = C_g V_{CNP}$, in which V_{CNP} corresponds to the

⁴All the HGFETs investigated in this chapter were designed and fabricated by Aurélien Schmitt at Laboratoire de Physique de l'Ecole Normale Supérieure (LPENS).

applied voltage for which charge neutrality is reached, the complete expression for the doping concentration in a realistic device is given by

$$n = C_g(V_g - V_{CNP}). \quad (5.1)$$

Electrostatic doping is limited by the breakdown voltage of the hBN dielectric, which has been estimated to be ~ 0.5 V/nm [32]. For the example given above, this implies a maximal doping voltage interval $[-32.5 \text{ V}, 32.5 \text{ V}]$ corresponding to a charge density span of $[-9 \times 10^{12} \text{ cm}^{-2}, 9 \times 10^{12} \text{ cm}^{-2}]$. The electrostatic modulation of the charge density corresponds to an effective doping modulation of the corresponding Fermi energy E_F since the two quantities are related by the electronic density of states at low temperature through $n = \int_0^{E_F} D(E)dE$, where $D(E)$ is the density of states. For monolayer graphene near the charge neutral point⁵, the density of states is given by [1]: $D(E) = 2|E|/\pi\hbar^2v_F^2$, where $v_F \approx 10^6$ m/s is the Fermi velocity. Therefore, the range of Fermi energies which can in principle be explored in the example that we have taken is $E_F = \hbar v_F \sqrt{\pi n} \in [-0.35 \text{ eV}, 0.35 \text{ eV}]$. In practice, we limit our study to $|V_g| \leq 15 \text{ V}$ and $|E_F| \leq 0.3 \text{ eV}$, depending on the size of the transistor.

5.2.2 Electron mobility

The application of a drain-source bias, V_{ds} , results in a uniform longitudinal electric field $E = V_{ds}/L$ across the graphene channel of the transistor, where L is the channel length. Locally, Ohm's law implies that the current density is simply given by $j = -env_d$, where n is the charge carrier density (see Eq. (5.1)), $-e$ is the electron charge, and v_d is the average drift velocity of charge carriers. The drift velocity is directly proportional to the applied electric field, with the constant of proportionality being the electron mobility μ , that is, $v_d = \mu E$. Electron mobility is an intensive quantity that is independent of the channel dimensions. As such, it is a good indicator of the material's electronic transport quality. In terms of electron mobility, graphene is superior to most state-of-the-art materials, such as the widely used Si and GaAs (see Table 5.2).

Another interesting property of graphene can be inferred from Table 5.2, namely, its mobility is strongly dependent on the substrate it lies upon. This substrate dependence is a direct consequence of the two-dimensional nature of graphene, which is extremely sensitive to its environment. In particular, nearby charges and surface roughness lead to increased electron scattering thereby decreasing electron mobility. In this regard, hBN has emerged as an ideal substrate for graphene due to the fact that it is an atomically flat insulator, can adhere to graphene via van der Waals forces, and has good dielectric properties [11].

The hBN-encapsulated graphene transistors studied here are routinely produced with electron mobility ranging from $50,000 \text{ cm}^2 \cdot \text{V}^{-1} \cdot \text{s}^{-1}$ to $170,000 \text{ cm}^2 \cdot \text{V}^{-1} \cdot \text{s}^{-1}$ at room temperature (see Appendix K for details on device fabrication). At low bias, the electron mobility in graphene on hBN is mainly limited by electron scattering with acoustic phonons. At low temperatures, this scattering mechanism becomes less efficient, which results in an enhancement in electron mobility below room temperature (cf. Table 5.2).

⁵Also referred to as the *Dirac point*.

Material/substrate	μ (cm ² .V ⁻¹ .s ⁻¹)
Graphene/hBN	$\sim 10^5$ (300 K) – $\sim 10^6$ (4.2 K)
Graphene/Al ₂ O ₃	$\sim 10^4$ (300 K)
Graphene/SiO ₂	$\sim 10^3$ (300 K)
2DEG/-	6000 (300 K) – 3×10^7 (4.2 K)
GaAs/-	9000 (300 K)
Si/-	1400 (300 K)

Table 5.2: Electron mobility (μ) of graphene on various substrates compared to that of state-of-the-art materials. Graphene mobility strongly depends on its substrate, the best yet being hBN. At room temperature, the electron mobility of graphene is superior to that of state-of-the-art transport materials, however, at low temperatures, the mobility of the two-dimensional electron gas (2DEG) in AlGaAs/GaAs quantum wells is still 10 times better.

5.2.3 Contact resistance

The transistor resistance is the sum of the channel resistance and the drain and source contact resistances. For large electric field operation, it is crucially important to minimize contact resistances for two main reasons. (i) The voltage drop at the contacts lowers the effective electric field in the graphene channel, preventing the transistor from reaching the transport regimes of interest. (ii) A contact resistance larger than the channel resistance can lead to significant Joule heating during large current transistor operation. This can bring heat to the channel’s electrons independently from the intrinsic transport mechanisms of graphene, and in some cases completely destroy the device.

It is widely recognized that contact resistance in graphene transistors depends solely on the contact width. This is a consequence of the atomic thickness of graphene which possesses a finite number of transverse modes that can be accessed by the metallic contact. Usual metal-metal contact theory suggests that the largest contact conductance is reached for the largest possible effective contact surface area between the two electrodes⁶. In practice, approaching this limit necessitates the use of ultra-pure materials and increasing the contact length by using a wiggled line (see Fig. 5.3 (c)). The contacts of the hBN-encapsulated graphene transistors discussed here are made of gold and chromium and are in contact with the graphene mono-layer through etches in the top hBN capping layer (see Fig. 5.3). Typical values for the contact resistance of these transistors lie between 50 Ω and 1000 Ω .

5.2.4 I-V Transfer Curve

Figure 5.4 (a) represents the transfer curve of the HGFET of Fig. 5.3 (c) under low drain-source bias ($V_{ds} = 10$ mV). The charge neutrality point is reached for $V_g = V_{CNP} \approx 0$ V. Since the number of charge carriers scales with the gate voltage (see Eq. (5.1)), increasing the gate voltage increases the number of charge carriers, leading to a drop in the channel resistivity R_{channel} . We can therefore extract the contact resistance (R_{contact}) from the asymptotic behavior of the transfer curve. Mono-, bi-, and tri-layer graphene all present a resistivity peak near neutrality

⁶This area is usually referred to as an A-zone.

5.2. Transport properties of high-mobility graphene field-effect transistors (HGFETs) under large bias

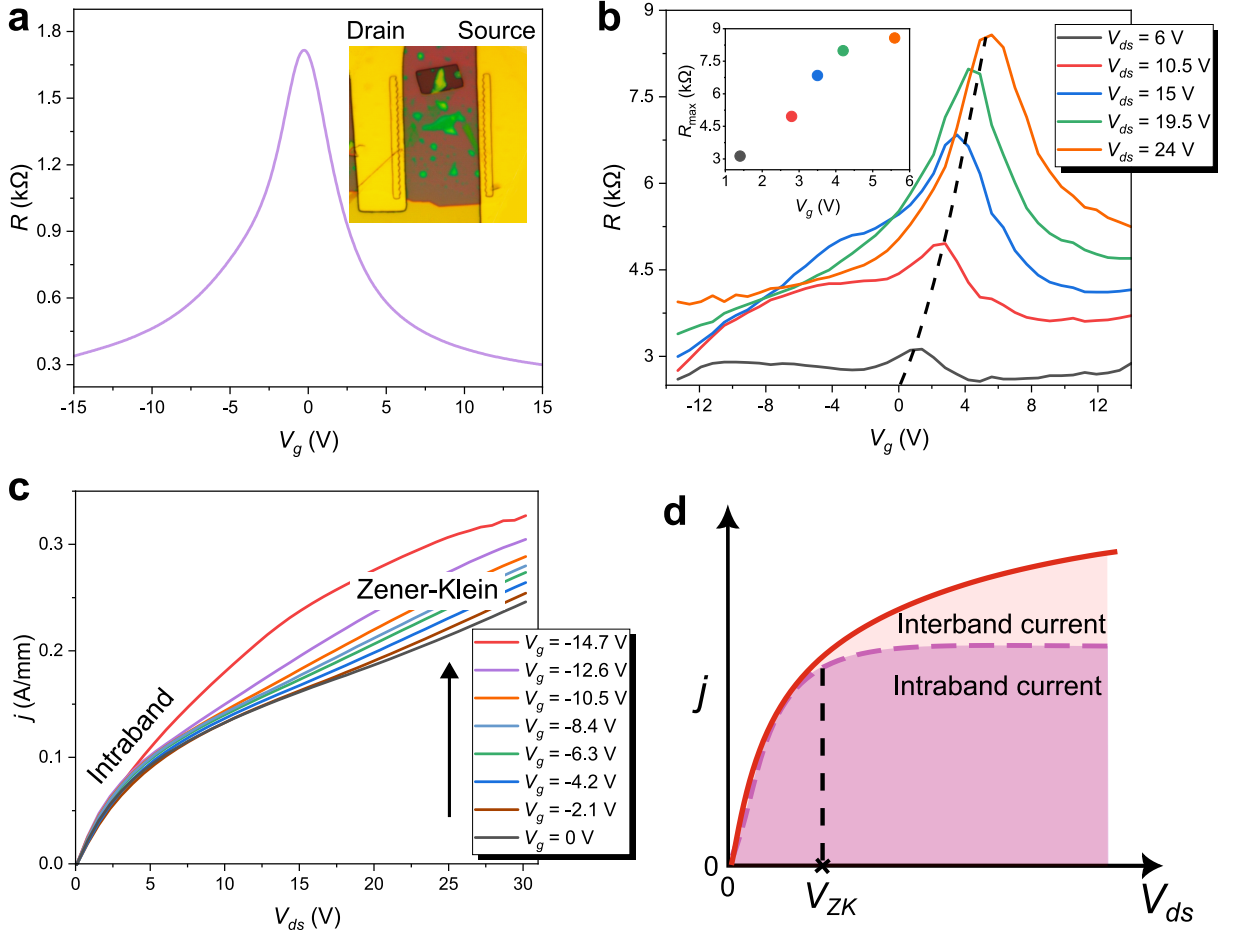


Figure 5.4: (a) Low-bias transfer curve of an HGFET measured at 300 K and $V_{ds} = 10$ mV. Right inset: Optical image of the transistor. (b) Transfer curves of the transistor as a function of increasing bias voltage V_{ds} . The dashed line is a guide for the eye. The inset shows the evolution of the maximal channel resistance R_{\max} as a function of increasing V_{ds} . This indicates the evolution of the gate voltage V_g , at which charge neutrality is reached, as a function of increasing V_{ds} . (c) Non-linear current density to voltage transfer curve ($j = I_{ds}/L$ vs V_{ds}) for the hole-doped regime. The gate voltage (and hence carrier density and Fermi energy) increases linearly in the range $V_g = [0, -14.7]$ V (shown in colors, black to red) so that the hole density range is $p = [0, 4.05] \times 10^{12} \text{ cm}^{-2}$, and $E_F = [0, 0.24]$ eV. (d) Schematic representation of the non-linear interband current (red curve, constant doping) and the intraband current (dashed curve). The intraband current saturates rapidly due to the high electron mobility. However, beyond a threshold bias V_{ZK} , the interband current originating from Zener-Klein tunneling processes (see main text) becomes predominant so that the current saturation is compensated for and an overall non-linear current behavior is observed as in panel (c).

due to the reduced number of charge carriers. In practice, the charge carrier density is slightly larger than zero at neutrality because of small doping inhomogeneities along the channel, which give rise to a charge density n_s . To model the transfer curve it is thus necessary to account for this residual charge density in the channel resistance as follows

$$R_{\text{channel}} = R_{\text{contact}} + \frac{\frac{L}{eW}}{\mu^* \sqrt{n_s^2 + \frac{1}{e^2} [C_g(V_g - V_{CNP})]^2}}, \quad (5.2)$$

where μ^* is the electron mobility of the transistor. For the transistor under consideration here (Fig. 5.4 (a), inset), we have $R_{\text{contact}} = 250 \Omega$ so that Eq. (5.2) estimates the transistor's mobility to be $\mu^* = 55,000 \text{ cm}^2 \cdot \text{V}^{-1} \cdot \text{s}^{-1}$.

5.2.5 Bias doping

As we have seen in the previous subsection, the charge neutrality point corresponds to minimal channel conductance (inversely, maximal channel resistance). In practice, the null channel conductance locus drifts linearly with bias voltage V_{ds} . This phenomenon is called drain doping, which is caused by the inhomogeneity of the electrostatic potential along the channel. Considering a linear voltage drop along the channel, the average voltage drop between the gate electrode and the channel electrode would be $\langle V_{gc} \rangle = \frac{1}{2}(V_d + V_s) - V_g$. In reality, however, we have $\langle V_{gc} \rangle = V_{gc}$ for low bias, and $\langle V_{gc} \rangle = V_{gs} + \eta V_{ds}$ with $\eta = 0.5$ for large bias, which results in a shift of the charge neutral point with applied bias. Experimental data indicate a slightly weaker dependence given by $\eta \simeq 0.2 - 0.4$. This can be inferred from measurements of the transistor's resistance as a function of increasing bias voltage V_{ds} , as in Fig. 5.4 (b). As stated in the previous subsection, the channel resistance is maximal near the charge-neutral point so that the value of V_g at which maximum resistance is reached corresponds to V_{CNP} . The points corresponding to maximal resistance are plotted in the inset of Fig. 5.4 (b) as a function of increasing V_{ds} , from which we get $\eta = 0.2$.

From a practical point of view, it is more convenient to study the electronic response of a transistor at constant electron density rather than at constant gate voltage. Therefore, all the measurements reported in this chapter were performed at constant electron density by taking bias doping into account, as represented in Fig. 5.4 (c). Interestingly, the transistor current exhibits highly non-linear behavior, whose origin will be discussed in the next subsection.

5.2.6 Zener-Klein tunneling

To illustrate the current profiles of Fig. 5.4 (c), we outline in Fig. 5.4 (d) the two regimes involved in the transistor's overall current behavior, namely the transistor's *intragand* and *interband* currents. At low bias, the transistor shows linear Ohmic behavior, with a strong increase of the intragand current with doping. Due to the transistor's high mobility, the current rapidly attains large values and saturates for $V_{ds} > V_{sat}$, where V_{sat} is the saturation voltage. The saturation of intragand current can be consistently attributed to the scattering of graphene's electrons with optical phonons of the lower *Reststrahlen* band (type I) of hBN ($\hbar\omega_{\parallel} \simeq 90 - 100 \text{ meV}$, cf. Fig. 2.13 (a)) [23, 33]. This velocity saturation regime is followed at high bias by the onset of an interband conduction regime, characterized by a constant bias- and doping-independent differential conductivity⁷ $\sigma_{ZK} \lesssim 2 \text{ mS}$. This behavior is systematically observed with all high-

⁷The differential conductivity σ_{ZK} is determined from the slopes of the curves in Fig. 5.4 (c).

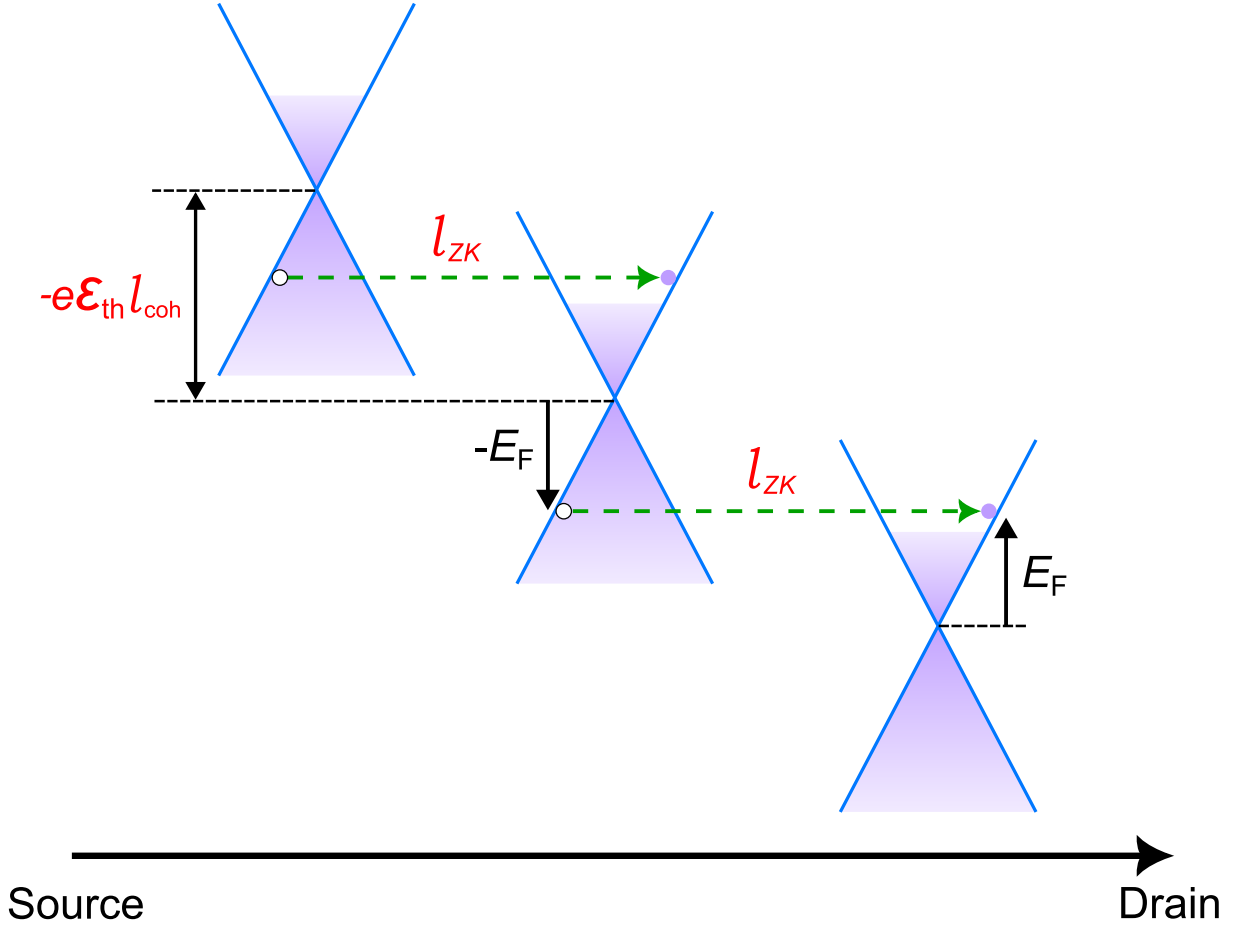


Figure 5.5: Depiction of electronic distribution along a mono-layer graphene channel under large bias. For a tunneling process with a characteristic coherence length, l_{coh} , a threshold electric field $\mathcal{E}_{\text{th}} = |\Delta E_{\text{tun}}|/el_{\text{coh}}$ is required for tunneling to occur, where ΔE_{tun} is the energy difference between the initial and final state. Zener-Klein tunneling processes in graphene (represented by dashed green arrows) occur with a coherence length $l_{\text{coh}} \equiv l_{\text{ZK}}$ and $|\Delta E_{\text{tun}}| = 2E_F$.

mobility graphene transistors, regardless of hBN thickness and graphene number of layers. The observed increase in current beyond the current saturation limit is a direct consequence of *Zener-Klein* tunneling that is contemporaneous with the start of current saturation.

Zener tunneling is a well-known phenomenon in solid-state physics that was first theorized in 1931 [34]. It has since been suggested that this exotic tunneling process can occur in graphene [35] and was subsequently observed experimentally [7, 8]. Briefly, Zener-Klein⁸ tunneling refers to the tunneling of charge carriers from one band to another through a forbidden energy gap, for example, from the valence band to the conduction band. In usual materials, Zener tunneling is a minor effect since the probability of this tunneling process decreases exponentially with the barrier height. On the other hand, since electrons in graphene possess properties characteristic of Dirac particles, this type of tunneling is much more likely in the current case.

Figure 5.5 represents the Zener-Klein tunneling process along the channel of mono-layer

⁸The term *Zener-Klein* refers to an analogy with the *Klein Paradox* [36] in high-energy physics and hence to the Dirac nature of electrons in graphene.

graphene. For a ballistic device, tunneling processes can occur at any distance within the channel and can be described by the so-called *Landauer approach*⁹. We suppose that Zener-Klein tunneling occurs on a characteristic distance l_{ZK} which can be interpreted as the coherence length of a tunneling event (see Fig. 5.5). Due to the Pauli exclusion principle, an electron can tunnel out of the valence band only if there is an available state in the conduction band¹⁰. Since the available states in the conduction band lie at energy E_F , conservation of momentum imposes that the electron tunneling from the valence band can have at most an energy $-E_F$. The coherence length then corresponds to a characteristic Zener-Klein electric field given by $\mathcal{E}_{ZK} = 2E_F/el_{ZK}$, which is the threshold electric field for Zener-Klein tunneling [37]. Therefore, the threshold Zener-Klein voltage is given by

$$V_{ZK} = \frac{2LE_F}{el_{ZK}}. \quad (5.3)$$

To determine the threshold voltage V_{ZK} that is necessary to achieve Zener-Klein tunneling experimentally, we go back to the total differential conductivity of the transistor, which can be fitted using the following voltage dependence [33, 38]

$$\sigma_{ds}(V) = \frac{ne\mu_0}{(1 + V/V_{sat})^2} + \sigma_{ZK}, \quad (5.4)$$

where μ_0 is the electronic mobility at zero bias and n is the charge carrier density. The first term on the right-hand side of Eq. (5.4) corresponds to the conductance of the saturation current and σ_{ZK} corresponds to the Zener-Klein current conductance as before. Fits of the differential conductivity are presented in Figs. A14 (b) and (e) for two HGFETs, showing good agreement with experimental data. Nevertheless, Eq. (5.4) precludes the existence of a doping-dependent threshold for the onset of interband Zener-Klein conduction due to Pauli blocking. A better description relies on an optical conductivity-like formula for the interband conductivity as a function of bias

$$\sigma_{ds,inter} = \frac{\sigma_{KZ}}{2} \left\{ 1 + \tanh \left[\frac{e(V_{ds} - V_{ZK})}{2k_B T_e} \right] \right\}, \quad (5.5)$$

where T_e is the electronic temperature and σ_{ZK} is again extracted from the slope of the current-voltage curves at high bias. Combining this equation for interband conduction with the intraband part of Eq. (5.4) yields the following formula for the total bias current

$$I_{ds} = I_{intra} + I_{inter}, \quad (5.6)$$

⁹The Landauer approach is usually used in the mesoscopic transport regime in which elastic scattering dominates the transport properties of nearly unperturbed electronic waves. While the conditions for mesoscopic transport are not fully reached in graphene in our experimental situation, it is nevertheless appropriate to use this approach as the tunneling events studied here involve the elastic scattering of an electronic wave. Note that Zener-Klein tunneling cannot lead to Joule heating by itself since energy is conserved during tunneling, however, the Zener-Klein-injected electrons in the conduction band release energy due to friction with the drifting electron gas once tunneling has occurred.

¹⁰This phenomenon can be referred to as *Pauli blocking*.

with

$$I_{\text{intra}} = ne\mu_0 \frac{W}{L} \frac{V_{\text{sat}} V_{\text{ds}}}{V_{\text{sat}} + V_{\text{ds}}}, \quad (5.7)$$

and

$$I_{\text{inter}} = \frac{\sigma_{\text{ZK}} k_B T_e W}{eL} \left\{ \frac{e(V_{\text{ds}} - V_{\text{ZK}})}{2k_B T_e} + \ln \left[\cosh \left(e \frac{V_{\text{ds}} - V_{\text{ZK}}}{2k_B T_e} \right) \right] + \frac{eV_{\text{ZK}}}{2k_B T_e} - \ln \left[\cosh \left(\frac{eV_{\text{ZK}}}{2k_B T_e} \right) \right] \right\}. \quad (5.8)$$

Eqs. (5.4)-(5.8) are used to perform fits of the current-voltage curves of various HGFETs (see Appendix L). Due to the fair agreement of the σ -fits with Eq. (5.4), the values of V_{sat} , μ and σ_{ZK} are set, and only V_{ZK} and T_e are left as adjustable parameters. The resulting fits for two HGFETs are presented in the Figs. A14 (c) and (f) (orange curves), showing excellent agreement with experimental data, with values for $T_e \sim 600$ K and $V_{\text{ZK}} \lesssim 0.5$ V, which are compatible with optical measurements in the near-infrared and mid-infrared spectral ranges. The intraband part of the current (Figs. A14 (c) and (f), green curves) shows a quasi-complete saturation for $V_{\text{ds}} \gg V_{\text{sat}}$, resulting in a linear increase of interband current at large bias.

5.3 Electron gas cooling in graphene under large bias

In this section, we illustrate the main mechanisms involved in the cooling of the electron gas in HGFETs. In particular, we discuss the consequences of the transport behavior presented in the previous section on cooling in graphene and put forth evidence of radiative cooling due to electroluminescence in HGFETs under large bias.

5.3.1 In-plane and out-of-plane heat transfer

The physics of cooling in usual materials is rather well-understood. Nevertheless, in graphene, which is characterized by the decoupling of the electron gas from the lattice, usual cooling mechanisms give way to new exotic cooling regimes. This has led to intense research aimed at exploring the various cooling mechanisms of graphene [39, 40]. We will restrict our discussion here, however, to the case of HGFETs. Apropos, in an HGFET an important distinction has to be made between *in-plane heat transfer* and *out-of-plane heat transfer*.

In-plane heat transfer in graphene is dominated by a thermal conductance that is directly proportional to its electrical conductance and is given by the *Wiedemann-Franz law*¹¹, which describes the usual transport behavior in metals and other two-dimensional electron gas systems [42]. In high-mobility graphene, in-plane heat transfer prevails at low bias but becomes negligible at large bias as the electrical differential conductance vanishes at current saturation. Therefore, at large bias, the only viable cooling mechanism is through out-of-plane heat transfer.

¹¹The Wiedemann-Franz law states that the ratio of the electronic contribution of the thermal conductivity (κ) to the electrical conductivity (σ) of a metal is proportional to the temperature (T) [41]: $\kappa/\sigma = \mathcal{L}T$, with the constant of proportionality \mathcal{L} , the *Lorenz number*, given by $\mathcal{L} = \pi^2 k_B^2 / 3e^2 = 2.44 \times 10^{-8} \text{ V}^2 \cdot \text{K}^{-2}$, where k_B is the Boltzmann constant.

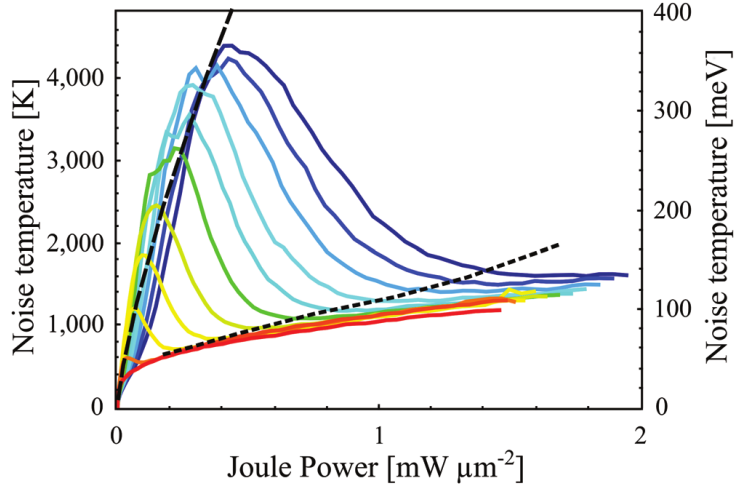


Figure 5.6: Noise temperature versus Joule heating at various doping concentrations in a bi-layer HGFET. Colors represent doping with respective carrier densities $n = 0$ (red), 0.18 (tangerine), 0.35 (orange), 0.53 (amber), 0.70 (yellow), 0.88 (chartreuse), 1.05 (green), 1.23 (turquoise), 1.40 (cyan), 1.58 (cerulean), 1.75 (blue), $1.93 \times 10^{12} \text{ cm}^{-1}$ (dark blue). Reproduced from ref. [23].

Due to lattice stiffness and poor electron-intrinsic phonon coupling in graphene, usual cooling channels are almost completely suppressed. Instead, the dominant cooling channel is through radiative heat transfer to the near-field modes of the hBN substrate. This is a very unusual situation as radiative heat transfer is typically a negligible heat transfer channel in condensed matter physics. The relatively poor efficiency of radiative heat exchange originates from the small number of far-field optical modes available to funnel thermal power at a distance. However, if heat exchange occurs on length scales smaller than the thermal wavelength, numerous near-field optical modes become available [43, 44]. This is particularly the case in the near-field of polaritonic materials, as we have seen in numerous examples in the previous chapters.

In Fig. 5.6, the steady-state electronic temperature of a bi-layer graphene transistor¹² is monitored (by means of noise thermometry¹³) as a function of injected Joule power. The outstanding observation to remark on here is the drop in temperature with increasing injected power above a certain threshold. As mentioned above, the only cooling mechanism available at large bias is through radiative cooling to the sample's near-field modes. The observed cooling, therefore, can be attributed to the ignition of HPhP electroluminescence in the hyperbolic hBN substrate. We will elaborate in greater detail on this radiative cooling mechanism in the following subsections.

5.3.2 Radiative near-field cooling: Planckian emission of hyperbolic phonon-polaritons

As we have seen in subsection 2.3.1, the hyperbolic nature of hBN stems from its hyperbolic iso-frequency curve given by $k_{\parallel}^2/\varepsilon_{\perp} + k_{\perp}^2/\varepsilon_{\parallel} = \omega^2/c^2$, where the subscripts \perp and \parallel correspond to

¹²Although we consider a bi-layer graphene transistor here, the behavior that will be presented and discussed in this section is valid for all HGFETs regardless of the number of graphene layers.

¹³Details on noise thermometry are outlined elsewhere in ref. [33].

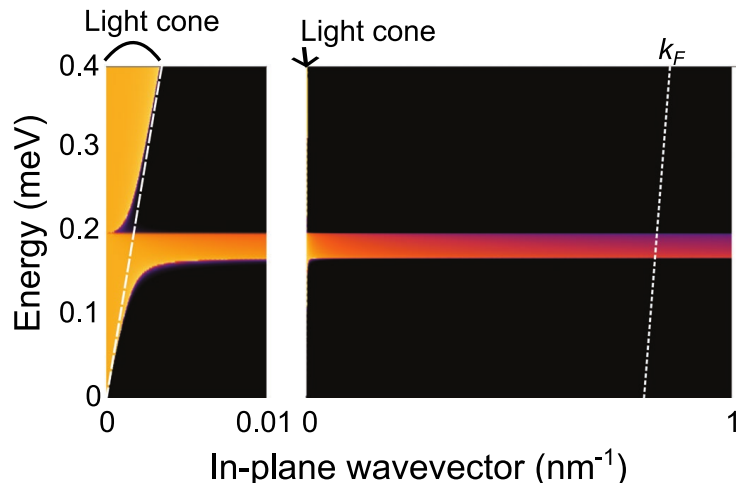


Figure 5.7: Real part of the optical admittance (Z^{-1}) of hBN (omitting the type I *Reststrahlen* band) on two in-plane wavevector scales to illustrate the far field and HPhP extension of radiation phase space. The impedance matching window in the *Reststrahlen* has an upper bound at $2k_F$. Reproduced from ref. [23].

the in-plane and out-of-plane directions, respectively¹⁴. We have also seen that hBN possesses two *Reststrahlen* bands in which $\varepsilon_{\perp}\varepsilon_{\parallel} < 0$: the type I *Reststrahlen* band (corresponding photon energy $\hbar\omega_{\parallel} \in [91.7, 101.7]$ meV) and the type II *Reststrahlen* band (corresponding photon energy $\hbar\omega_{\perp} \in [169, 198.4]$ meV)¹⁵. The *Reststrahlen* band can be characterized by its central frequency $\Omega = (\omega_{\text{LO}} + \omega_{\text{TO}})/2$ and its width $\Delta\omega = \omega_{\text{LO}} - \omega_{\text{TO}}$ so that for hBN we have $\hbar\Omega_{\parallel} = 96.7$ meV, $\hbar\Omega_{\perp} = 183.7$ meV, $\hbar\Delta\omega_{\parallel} = 10$ meV, and $\hbar\Delta\omega_{\perp} = 29.4$ meV. This shows that the *Reststrahlen* bands correspond to a rather narrow energy band.

For an electron gas at temperature T_e , the total radiative power (incandescence) is¹⁶

$$P_{\text{rad}} = \frac{1}{(2\pi)^2} \int_0^{\infty} d\omega \int_0^{\infty} \mathcal{M}(\omega, k) \hbar\omega n_{ph}(T_e, \omega) k dk, \quad (5.9)$$

where $n_{ph} = [\exp(\hbar\omega/k_B T) - 1]^{-1}$ is the *Bose-Einstein distribution function* and $0 < \mathcal{M} < 1$ is the impedance matching factor: $\mathcal{M} = \frac{4\text{Re}(Z^{-1})\text{Re}(\sigma)}{|Z^{-1} + \sigma|^2}$. Here, $Z(\omega, k)$ is the non-local optical impedance of the environment of graphene, and $\sigma(\omega, k)$ is the non-local conductivity of graphene which can be obtained from the electronic density-density response function in the random phase approximation [45]. The impedance matching factor restricts the phase space available for radiative heat exchange. This is due to its dependence on the optical impedance which is given by $Z = \frac{Z_0}{\varepsilon_{\perp}} \frac{k_{\parallel}}{k_0}$, where $Z_0 = 377 \Omega$ is the vacuum impedance (see chapter 2, footnote 6) and $k_0 = \omega/c$.

If the photon energy lies outside of the *Reststrahlen* band, k_{\parallel} can become imaginary when $k > k_0\sqrt{\varepsilon_{\perp}}$ so that $\mathcal{M} = 0$. As a consequence, radiation is limited to the very narrow light cone, as represented in Fig. 5.7, and the emitted power is vanishingly small. For mono-layer graphene

¹⁴The notation that we use here is based on defining the dielectric tensor components with respect to the optical axis, which is taken to be along the normal to the sample surface.

¹⁵See Fig. 2.13.

¹⁶Taking into account summation over positive and negative frequencies.

at 2000 K in vacuum, the radiated power per unit area for $k > k_0\sqrt{\varepsilon_\perp}$ is $P = \overline{\mathcal{M}}\sigma_{SB}T^4 \simeq 2.09 \text{ W.cm}^{-2}$, where $\sigma_{SB} = 5.67 \times 10^{-8} \text{ W.m}^{-2}.\text{K}^{-4}$ is the *Stefan-Boltzmann* constant and $\overline{\mathcal{M}} \sim 2.3\%$ is the average far-field emissivity of graphene. This corresponds to a characteristic thermal conductance $\frac{P}{T} \simeq 10.44 \text{ W.m}^{-2}.\text{K}^{-1}$. In contrast, within the *Reststrahlen* band, k_\perp remains real, and hence \mathcal{M} remains sizeable for much larger k – up to twice the Fermi wavevector k_F (which is 300 times larger than k_0) – thus considerably enhancing radiative cooling efficiency despite the band’s narrow spectral range.

For low bias, below the Zener-Klein threshold, it has been shown that this type of Planckian near-field radiative cooling is the predominant cooling mechanism for graphene devices with channel size on the order of $\sim 15 \times 15 \mu\text{m}^2$ [46, 47]. In smaller devices, electron heat conduction following the Wiedemann-Franz law is the dominant cooling mechanism. Beyond the Zener-Klein threshold, both Planckian radiative cooling and electron heat conduction are insufficient to explain the observed temperature drop in Fig. 5.6 at large bias. Taking only these two cooling mechanisms into account when modeling the temperature evolution of a transistor with applied bias would merely result in a saturation of the temperature at large bias [23]. If one additionally considers the Zener-Klein tunneling-induced pumping of valence band electrons, a more intriguing cooling mechanism emerges, that is, radiative cooling of HPhPs via *electroluminescence*.

5.3.3 Beyond Planckian emission: radiative cooling due to Electroluminescence of HGFETs under large bias

Figure 5.8 shows a side-by-side comparison between the transport (panel (a)) and temperature panel (b)) behavior of an HGFET as a function of applied bias. The comparison reveals that the new cooling mechanism introduced at the end of the previous subsection supersedes electron heat conduction when the applied electric field is slightly larger than the Zener-Klein threshold bias voltage V_{ZK} (indicated by circles in Fig. 5.8 (a)). This suggests that the two events are intimately related: once the Zener-Klein threshold electric field is reached, the tunneling process constantly pumps electrons from the valence band to the conduction band. A steady state is reached when a relaxation mechanism refeeds the electrons back into the valence band. This can happen either via so-called Auger processes or inelastic electron-phonon collisions.

Since the electron-electron intraband relaxation time is extremely short compared to all other scattering processes ($\sim 50 \text{ fs}$), we can assume that a pseudo-temperature and a chemical potential are still well-defined. In addition, assuming that this out-of-equilibrium situation relies simply on the partially independent dynamics of electrons in the valence and conduction bands, each band has its own temperature and chemical potential. The fact that Zener-Klein tunneling naturally promotes electrons from the valence to the conduction band leads to $\mu_c > \mu_v$, where μ_c and μ_v are the chemical potentials of the conduction band and valence band, respectively. This situation is a textbook example of electroluminescence [48], in which an out-of-equilibrium electronic population is built at a pn-junction by the simultaneous injection of electrons on an n-doped electrode and holes on a p-doped electrode. In the region of the junction, the cohabitation of both populations allows the interband radiative process of electron-hole recombination which leads to electroluminescence.

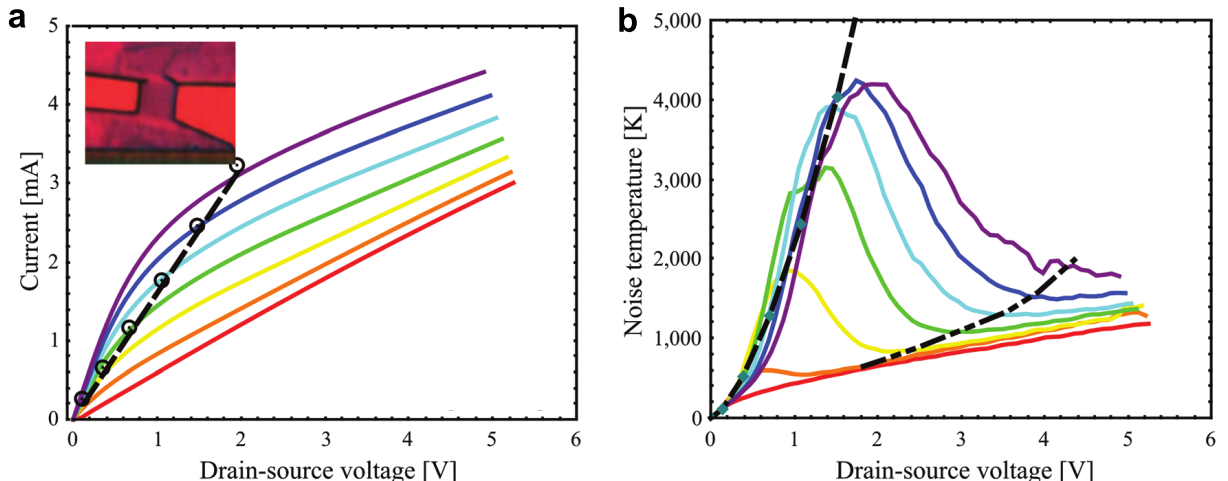


Figure 5.8: Transport and noise temperature of an hBN-supported bi-layer graphene transistor. (a) Current saturation and Zener–Klein regimes in a high-mobility bilayer graphene flake of dimensions $L \times W = 3.6 \mu\text{m} \times 3 \mu\text{m}$. The sample (upper inset) is deposited on a 200 nm-thick hBN flake acting both as a bottom gate dielectric (capacitance per unit area $C_g = 0.14 \text{ mF}\cdot\text{m}^{-2}$) and hyperbolic phonon polariton radiator. Carrier density is tuned in the hole doping range $-n = 0$ (red), 0.35 (orange), 0.70 (yellow), 1.05 (green), 1.40 (cyan), 1.75 (blue), $2.10 \times 10^{12} \text{ cm}^{-2}$ (purple). At low bias, intraband current dominates up to a threshold field $\mathcal{E}_{sat} = v_{sat}/\mu$ set by the saturation velocity $v_{sat} \lesssim 3 \times 10^5 \text{ m/s}$ and mobility $\mu \gtrsim 1 \text{ m}^2\cdot\text{V}^{-1}\cdot\text{s}^{-1}$. At large bias, above a Pauli unblocking voltage V_{ZK} (see Eq. (5.3)), the intraband current is fully saturated, and an additional current arising from interband Zener–Klein tunneling with a constant conductance $\sigma_{ZK} \simeq 0.45 \text{ mS}$ sets in. The boundary between intraband and interband transport regimes follows the theoretically expected behavior given by Eq. (5.7) (black dashed line with the circles corresponding to theoretical values of current). (b) Noise temperature $T_N = S_I/4G_{ds}k_B$ deduced from the microwave excess current noise S_I and the differential conductance G_{ds} . Noise thermometry reveals a striking difference between the intraband and interband regimes with a super-linear bias dependence characteristic of "hot" electrons (black dashed line) in the former, dropping toward a linear dependence characteristic of the "cold" electron regime in the latter. The theoretical value for the threshold between cooling and heating due to electroluminescence is indicated by the staggered-dashed line. Reproduced from ref. [23].

In the case of hBN-encapsulated graphene transistors, electrons and holes are mainly coupled by the dressed electromagnetic modes of the structure, namely, the hyperbolic phonon-polariton modes. Therefore, the electroluminescence of graphene mostly occurs in these extreme near-field modes. The emitted power, in this case, can be computed within the framework of fluctuational electrodynamics [49]. Assuming that the carrier distribution is known, the near-field radiative power can be computed in a fashion similar to Eq. (5.9) as follows

$$dP_{\text{rad}}^L(\omega, \mathbf{k}) = \frac{\text{Re}(Z^{-1})}{|\sigma + Z^{-1}|^2} S_{jj}^L(\omega, \mathbf{k}) d\omega d^2\mathbf{k}, \quad (5.10)$$

where σ is now the non-local optical conductivity of out-of-equilibrium graphene, and S_{jj}^L is the current power spectral density generated by the out-of-equilibrium electrons in graphene.

The out-of-equilibrium current power spectral density is given by the non-local *van Roosbroeck*-

Shockley relation for interband transitions [48, 50, 51], *i.e.*,

$$S_{jj}^L(\omega, \mathbf{k}) = \frac{1}{2\pi^3} \text{Re}(\sigma_{\text{inter}}) \hbar\omega \tilde{n}_{ph}(T, \omega), \quad (5.11)$$

in which, $\tilde{n}_{ph} = [\exp(\hbar\omega - \mu_{ph}/k_B T) - 1]^{-1}$ is the Bose-Einstein distribution function with photon chemical potential $\mu_{ph} = \mu_\zeta - \mu_{\zeta'}$, which corresponds to the difference in chemical potential between the two bands of interest (denoted as ζ and ζ' here). The interband non-local conductivity, $\sigma_{\text{inter}}(\omega, k)$, is evaluated for the interband transitions between the bands of interest. The total radiated power is the sum of power radiated by all intraband and interband transitions. If we consider the case of a pair of valence ($\zeta' \equiv v$) and conduction ($\zeta \equiv c$) bands, the fraction of radiated power cast by electroluminescence can be deduced by using S_{jj}^L as the source. Note that, in this case, the impedance matching coefficient is given by $\mathcal{M}(\omega, k) = \frac{4\text{Re}(Z^{-1})\text{Re}(\sigma_{\text{inter}})}{|Z^{-1} + \sigma_{\text{inter}} + \sigma_{\text{intra}}|^2}$, where σ_{intra} is the intraband conductivity.

In gaped semi-conductors, electroluminescence becomes important when the difference in conduction and valence chemical potentials approaches the band-gap energy E_{bg} ($\mu_c - \mu_v \lesssim E_{\text{bg}}$). In contrast, graphene is characteristically gapless so that in the current context the threshold energy for electroluminescence is determined by the *Reststrahlen* band energy, *i.e.*, $\mu_{ph} = \mu_c - \mu_v \lesssim \hbar\Omega_\perp$. For unbiased graphene, an out-of-equilibrium electronic distribution can be transiently created by optical pumping and has been observed to relax on sub-picosecond timescales via optical pump-probe techniques [47, 52].

It is instructive at this point to draw a parallel with light-emitting diodes (LEDs) in order to better understand why electroluminescence is associated with electron gas cooling. In LEDs, electron-hole pairs are injected from the electrodes and then recombine in the active region. When an LED is used at its designed working point, the injected energy per injected carrier pair (E_{inj}) is slightly larger than the photon energy released at electron-hole pair recombination (which is equivalent to the effective band-gap energy E_{bg}) yielding a slight warming of the device (see Fig. 5.9 (b)). However, it has been reported that for high-quality devices at sub-threshold bias, for which $E_{\text{inj}} < E_{\text{bg}}$, the LED acts as a refrigerator as the missing energy $E_{\text{bg}} - E_{\text{inj}}$ is usually provided by the thermal energy of optical phonons of its active material. Such a situation is depicted schematically in Fig. 5.9 (a), and the corresponding cooling and warming regimes of the LED are outlined in Fig. 5.9 (b).

To date, LED refrigerators are terribly inefficient with a record cooling power of only 8 pW [53]. The graphene transistors considered here operate in the refrigerator mode described above at moderate bias where $E_{\text{inj}} < \hbar\Omega_\perp$, in which the remaining energy required to pass the Zener-Klein tunneling threshold is provided by the thermal energy of graphene's hot electrons. Therefore, the sudden drop in temperature at the Zener-Klein tunneling threshold is a consequence of a competition between intraband heating, and interband HPhP electroluminescence cooling. The cooling power, in this case, can reach ~ 10 mW, *i.e.*, nine orders of magnitude larger than that of conventional LEDs. Nevertheless, since the electron gas temperature is much larger than that of the phonon bath, as a whole a graphene transistor cannot be fully classified as a refrigerator and thus its cooling power is unbound by a Carnot inequality. This is in contrast to LEDs, where the device gets colder than its environment.

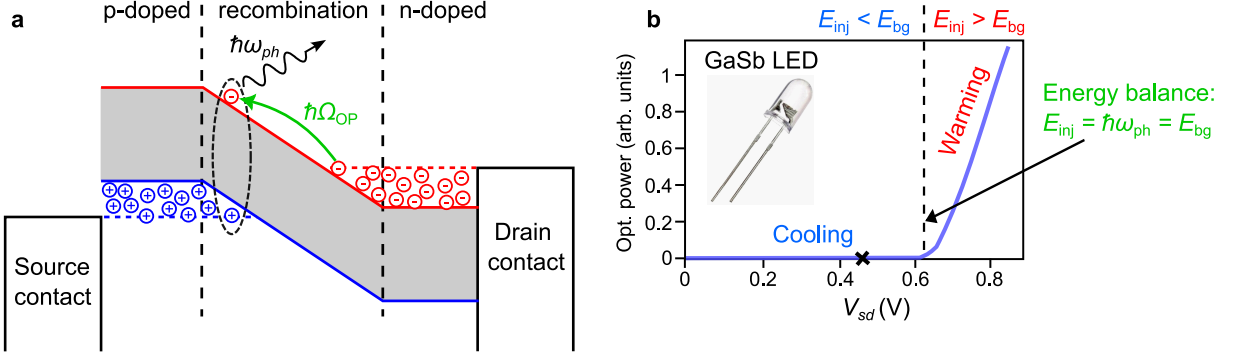


Figure 5.9: (a) Simplified depiction of the phonon-assisted electron-hole recombination process between the source and drain electrodes of a light-emitting diode, which results in the cooling of the diode. (b) Optical power of a GaSb LED as a function of injected bias voltage V_{sd} . Courtesy of the manufacturer. The black cross marks the sub-threshold bias voltage at which cooling due to the recombination process illustrated in panel (a) occurs.

The injected energy per electron-hole pair in an HGFET is the electrical work done by charges during diffusion and is given by $E_{inj} = P_{ZK}/\dot{n}_{ZK}$, where $P_{ZK} = \sigma_{ZK}(\mathcal{E} - \mathcal{E}_{ZK})\mathcal{E}$ is the Joule power associated with Zener-Klein tunneling processes. The electron-hole pair creation rate \dot{n}_{ZK} can be deduced from the Zener-Klein current density $j_{ZK} = \sigma_{ZK}(\mathcal{E} - \mathcal{E}_{ZK}) = e\dot{n}_{ph}l_{ZK}$, which gives $\dot{n}_{ZK} = \frac{\sigma_{ZK}}{el_{ZK}}(\mathcal{E} - \mathcal{E}_{ZK})$. This yields an injection energy per electron-hole pair $E_{inj} = el_{ZK}\mathcal{E}$. We may now obtain the characteristic electric field for which injection energy balances HPhP emission energy $\hbar\Omega_{\perp}$ by electron-hole pair recombination. Formally, this is written as

$$\mathcal{E}_{th} = \frac{\hbar\Omega_{\perp}}{el_{ZK}} = \frac{\hbar\Omega_{\perp}V_{ZK}}{2LE_F}, \quad (5.12)$$

where we have used Eq. (5.3) in the second equality. The threshold electric field in Eq. (5.12) defines the boundary between cooling and heating due to electroluminescence. This boundary is indicated by a staggered-dashed line in Fig. 5.8 (b), which matches well with the voltage for which the minimum temperature is reached.

The chemical potential imbalance between the valence and conduction bands can be estimated from data presented in Fig. 5.6. For a doping concentration $n = 1.25 \times 10^{12} \text{ cm}^{-2}$, the maximum temperature $T_N^{\max} = 3200 \text{ K}$ is reached at the Zener-Klein threshold for an injected Joule power of $0.25 \text{ mW} \cdot \mu\text{m}^{-2}$ and drops to a minimal temperature $T_N^{\min} = 1400 \text{ K}$ at $1 \text{ mW} \cdot \mu\text{m}^{-2}$ of Joule power. Assuming that the variation in cooling power with the electronic bath state is mainly governed by the photon occupation factor, *i.e.*, $P_{\text{rad}} \rightarrow n_{ph}$ (a legitimate assumption because of its singular behavior at the electroluminescence threshold $\hbar\Omega_{\perp} = \mu_c - \mu_v$), we deduce that the chemical potential imbalance $\mu_c - \mu_v \simeq 0.16 \text{ eV} \lesssim \hbar\omega_{\text{TO}}^{\perp}$ reaches the lower boundary of the type II *Reststrahlen* band of hBN. Below the Zener-Klein electric field threshold, the electronic temperature results from a power balance between intraband processes only. For a rather large electric field, where Zener-tunneling and electroluminescence recombination are predominant, the conduction and valence band reach a doping state which is mainly independent of gate-doping, that is, $\mu_c - \mu_v \sim \hbar\Omega_{\perp} \gg (\mu_c - \mu_v)/2 = E_F^0$ where E_F^0 is the Fermi energy at

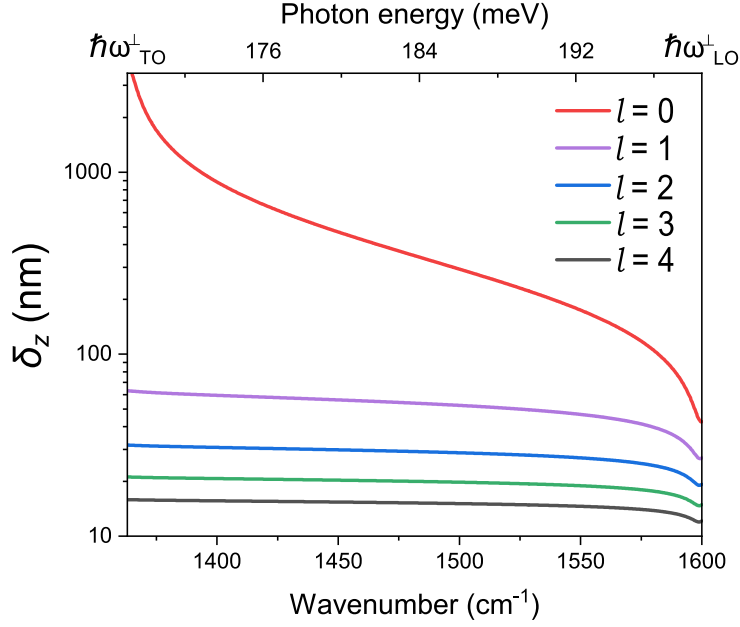


Figure 5.10: Penetration depth of HPhP branches in a 200 nm-thick hBN film for $l \leq 4$.

vanishing bias. As a consequence, the power balance tends to be dominated by Joule heating originating from Zener-Klein tunneling processes, which is independent of doping, and HPhP emission by both intraband thermal emission and interband electroluminescence defined by a similar electronic distribution. Therefore, noise temperature profiles obtained at finite doping tend to line up with the temperature obtained at null doping at large bias as observed in Fig. 5.6.

Finally, we comment here on the spatial dissipation of heat during the electroluminescence cooling process. Heat dissipation due to the radiated power is determined by the penetration depth of HPhPs of the bottom hBN layer of the transistor. As we have seen in chapter 2, the penetration depth of surface polaritons is the inverse of the out-of-plane wavevector component and for an hBN thin film of thickness d on a substrate, which reads $\delta_z^l = \left| \sqrt{\varepsilon_{\perp} \frac{\omega^2}{c^2} - \frac{\varepsilon_{\perp}}{\varepsilon_{\parallel}} k_l^2} \right|^{-1}$, where $l = 0, 1, 2, 3 \dots$ denotes the HPhP branch order (see subsection 2.4.1). For an hBN thin film on an SiO_2 substrate, the in-plane wavevector k_l is given by Eq. (2.79). As shown in Fig. 5.10, the penetration depth of type II HPhPs is maximal near the lower bound of the *Reststrahlen* band and decreases toward the upper bound. Additionally, it is clear that the largest penetration depth corresponds to that of the lowest-order HPhP branch ($l = 0$), at which HPhPs penetrate fully into the hBN thin film at frequencies near $\omega_{\text{TO}}^{\perp}$. As the branch order increases, HPhPs become increasingly localized at the surface (see Fig. 5.10, $l > 0$), reaching a penetration depth as low as 15 nm for $l = 4$. We can conclude that the lowest-order HPhP branch contributes predominantly to electroluminescence cooling as most of the radiated power is channeled across the hBN layer toward the transistor's backgate via this branch.

5.3.4 Mid-infrared signature of electroluminescence cooling in HGFETs by phonon-polaritons

In HGFETs with an SiO₂ back-gate, a direct indication of radiative cooling due to the electroluminescence process described in the previous subsection can be readily obtained by monitoring the far-field mid-IR radiation of the HGFET as a function of electrical bias. At large bias, beyond the threshold for Zener-Klein tunneling, out-of-plane heat transfer due to electroluminescence channels heat, with a power P_{out} , to the transistor's SiO₂ back-gate so that the transistor is cooled via thermal conduction. The local heating of the back-gate is subsequently signaled by the incandescent mid-IR emission of the SiO₂ substrate as depicted schematically in Fig. 5.11 (a). To detect this emission, we utilize the setup shown in Fig. 5.11 (b), which enlists the aid of an optical chopper to dramatically improve the signal-to-noise ratio¹⁷. Using this setup, we first perform spectroscopy of the measured mid-IR signal of a large HGFET with an SiO₂/Si back-gate (see Fig. 5.11 (b), inset) under large bias, which reveals signatures of the emission of the SiO₂ layer. Indeed, as shown in Fig. 5.11 (c), the recorded spectrum possesses two peaks at the transverse and longitudinal optical phonons of SiO₂ (ω_{TO} and ω_{LO} , respectively) and a dip in the middle of the *Reststrahlen* band, which results from enhanced reflectance in this spectral region. Next, we carry out a spatial scan of the detected optical signal (P_{opt} , integrated over the full spectral bandwidth of the detector) of the transistor under electrical bias, over a $50 \times 50 \mu\text{m}^2$ region of the sample centered at the transistor's graphene channel (Fig. 5.11 (d)). One can clearly see from Fig. 5.11 (d) that the detected optical signal is most intense in the transistor channel (between the source and drain electrodes), indicating that the detected signal is a direct consequence of the electric field applied across the channel.

Having established that the detected signal originates from the graphene channel of the transistor, we then execute a scan of the optical signal as a function of electrical bias (Fig. 5.11 (e)). As expected from a transistor undergoing radiative cooling due to electroluminescence, the detected optical signal is maximal at large bias near the charge-neutral point ($V_g = 0$) and falls off away from it. What's more, the onset of this emission almost matches perfectly with the threshold of Zener-Klein tunneling, as indicated by the dashed curve in Fig. 5.11 (e).

We may now obtain an estimate of the contribution of out-of-plane heat transfer on the total cooling power of the transistor. The total thermal energy balance is given by $P_{\text{Joule}} = P_{\text{in}} + P_{\text{out}}$, where $P_{\text{Joule}} = V_{ds}I_{ds}$ is the Joule power (see Fig. 5.11 (g)) and P_{out} (resp. P_{in}) is the out-of-plane (resp. in-plane) cooling power. The out-of-plane cooling power is given by $P_{\text{out}} = \Delta T_{\text{SiO}_2}/R_{\text{th}}$, in which ΔT_{SiO_2} is the temperature increase of the SiO₂/Si back-gate as a function of electrical bias and R_{th} is the equivalent thermal resistance of the back-gate [54] (see Fig. A15 (d)). The temperature increase ΔT_{SiO_2} as a function of electrical bias can be determined from the optical signal presented in Fig. 5.11 (e), as outlined in Appendix M. We first calibrate the temperature dependence of the optical signal by measuring the optical signal of the transistor when heated at various temperatures via a hot plate (see Fig. A15 (a)). This calibration provides a fit of the detected optical signal as a function of temperature (Fig. A15 (b)), which is then used inversely to determine ΔT_{SiO_2} . As a result, we obtain the distribution of the temperature increase as a

¹⁷This optical setup has already been described in chapter 3 (see subsection 3.2.2).

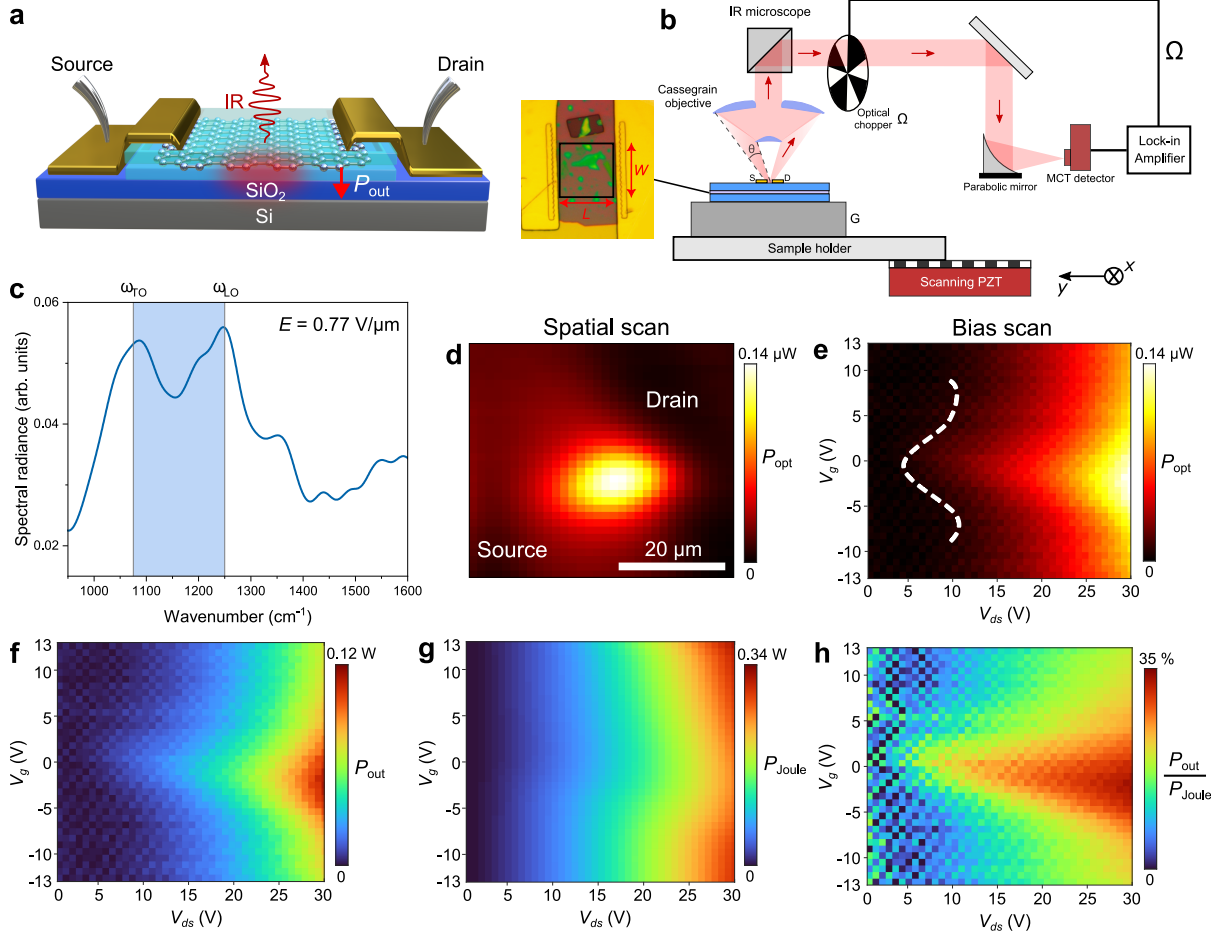


Figure 5.11: (a) Depiction of the out-of-plane heat transfer in an HGFET with an SiO₂ back-gate. The subsequent mid-IR emission is represented by a red wavy arrow. (b) Schematic illustration of the detection technique used for the characterization of the optical signal (P_{opt} , integrated over the full spectral range of the detector) of an HGFET (inset, $L \times W = 35 \times 35 \mu\text{m}^2$) due to the radiative emission of the SiO₂ back-gate. (c) Spectral radiance of the transistor for an applied electric field $E = V_{\text{ds}}/L = 0.77 \text{ V}/\mu\text{m}$ ($V_{\text{g}} = 0 \text{ V}$), measured with the setup of panel (b). The spectrum is subtracted by a reference measurement to remove the contribution of the optical chopper to the detected signal. The spectrum is then normalized by the response function of the setup (see subsection 3.2.1), yielding the spectral radiance of the transistor. The blue-shaded region encloses the *Reststrahlen* band of SiO₂. (d) Spatial scan of the transistor’s optical signal. The signal is most intense between the source and drain electrodes, indicating that the emission originates from the transistor’s channel. (e) Optical signal as a function of electrical bias. The white-dashed curve marks the threshold for Zener-Klein tunneling. (f) Out-of-plane dissipated power (P_{out}) as a function of electrical bias, computed from $P_{\text{out}} = \Delta T_{\text{SiO}_2}/R_{\text{th}}$, where $\Delta T_{\text{SiO}_2} \simeq 20 - 40 \text{ }^\circ\text{C}$ and $R_{\text{th}} \simeq 357 \text{ K}\cdot\text{W}^{-1}$ (see Appendix M). (g) Joule power (P_{Joule}) as a function of electrical bias. (h) Percentage giving the contribution of the out-of-plane cooling mechanism to the total cooling power obtained from the ratio $\frac{P_{\text{out}}}{P_{\text{Joule}}} = \frac{P_{\text{out}}}{(P_{\text{out}} + P_{\text{in}})}$, where P_{in} is the in-plane cooling power.

function of electrical bias, which ranges from $\Delta T_{\text{SiO}_2} \simeq 20 - 40 \text{ }^\circ\text{C}$ (see Fig. A15 (c)).

The out-of-plane cooling power can now be computed as a function of electrical bias and the result is presented in Fig. 5.11 (f). It is clear that P_{out} follows the same trend as the radiated

power (P_{opt}), in which it is maximal at large bias near the charge-neutral point and decays away from this point and at low bias. The envelope of the onset of P_{out} is again given by the Zener-Klein tunneling threshold. In contrast, the Joule power shows a slight decrease near the charge-neutral point at large bias (see Fig. 5.11 (g)). Finally, we may obtain an estimate of the contribution of the out-of-plane heat transfer channel to the total cooling power as in Fig. 5.11 (h). Taking the ratio $P_{\text{out}}/P_{\text{Joule}}$, we find that the contribution of the out-of-plane heat transfer channel reaches at maximum 35 % of the total cooling power. It must be mentioned here that the out-of-plane cooling mechanism is limited by the hBN-SiO₂ interfacial heat conductance, which can be rather poor due to the large surface roughness of SiO₂. Consequently, a fraction of the radiative power carried by the hBN layer is precluded from reaching the SiO₂ substrate and is thus extracted via the in-plane cooling mechanism instead.

5.4 Mid-infrared electroluminescence of graphene

In this section, we will go into further detail about the mid-IR emission due to electroluminescence in HGFETs under large electrical bias. In particular, we will give a clear definition of electroluminescent emission, show experimental proof of electroluminescent emission from an HGFET under large electrical bias, and show how this emission can be tailored.

5.4.1 What is electroluminescence?

By definition, electroluminescence is an optical and electrical phenomenon, in which a material emits light in response to the passage of an electric current or to a large electric field. It should be underscored here that electroluminescence is distinctly different than other forms of radiative emission, such as thermal radiation (incandescence) for instance. Concordantly, emission due to electroluminescence occurs independently from the temperature of the emitter (which may be cold). Although electroluminescent emission typically involves the radiative recombination of an electron-hole pair, which is the case for most radiative processes, the singular nature of electroluminescence lies in the process by which electrons are promoted to the conduction band. Upon thermalization, the band states are occupied according to a Fermi-Dirac distribution both in the conduction and in the valence band. Nonetheless, each band has its own chemical potential, referred to as a quasi-Fermi level, to account for the modification of carrier density. This is possible because the thermalization takes place in typically 1 ps whereas radiative electron-hole recombination takes place in typically 1 ns [51]. This two-quasi-Fermi level situation is the usual regime of electroluminescence for light-emitting diodes, as discussed in subsection 5.3.3. In the same manner as in subsection 5.3.3, the power emitted¹⁸ by a non-equilibrium source within a solid angle $d\Omega$ can be written as follows [51]

$$\frac{dP_e}{d\omega d\Omega} = \frac{\omega^2}{8\pi^3 c^2} \hbar\omega \tilde{n}_{ph}(T, \omega) \int_V C_{\text{inter}}(-\mathbf{u}, \mathbf{r}', \omega) d^3\mathbf{r}', \quad (5.13)$$

where \tilde{n}_{ph} is the Bose-Einstein distribution function with photon chemical potential $\mu_{ph} = \mu_c - \mu_v$

¹⁸For a given polarization.

(see subsection 5.3.3), $\mathcal{C}_{\text{inter}}$ is the local absorption cross-section due to interband transitions, \mathbf{u} is a unit vector pointing outward from the emitting surface, and the integral is computed over the volume V of the radiating object. Although Eq. (5.13) is typically used to describe emission from non-equilibrium semi-conductors, such as in LEDs, it can also be extended to other non-equilibrium systems. This is due to the fact that the only prerequisite to writing Eq. (5.13) is that two different quasi-Fermi levels are defined for the two bands involved in interband transitions. As we have already seen in subsection 5.3.3, this condition is satisfied in the case of graphene electrons in an HGFET.

5.4.2 Can a metal be electroluminescent?

The emission of a non-equilibrium source described by Eq. (5.13) can be split into two contributions. (i) The non-equilibrium excitation of the emitting material, which is accounted for by the temperature and the photon chemical potential (in other words, the interband statistics), and (ii) the efficiency of the coupling between plane waves and local sources mediated by the emitting body (*i.e.*, the absorptivity), which is accounted for by the local absorption cross-section. The first contribution naturally arises in semi-conductors under electrical bias, where interband transitions occur between the valence and conduction bands with a well-defined band-gap so that electron-hole pair recombination occurs when the electrons relax, resulting in electroluminescence. On the other hand, metals lack the band-gap protection required for the creation of an electron-hole pair, and thus electroluminescence is *a priori* forbidden. This should also be the case for graphene, which is characteristically gapless. Nonetheless, as we have seen in the previous subsections, graphene's electrons in HGFETs undergo interband transitions in the form of Zener-Klein tunneling processes that arise at large electrical bias. We mention here that the absorptivity of an HGFET is invariant with respect to the applied electrical bias (see Appendix N). As a result, the variation of electroluminescent emission with electrical bias originates solely from variations in interband statistics due to Zener-Klein tunneling. In the following subsections, we will present experimental evidence of such electroluminescent emission from HGFETs.

5.4.3 Experimental observation of electroluminescent emission from HGFETs under large bias

As previously mentioned in subsection 5.3.3, the electroluminescent emission in HGFETs occurs mainly in the near-field modes of the hBN layers, namely the HPhP modes. Therefore, to detect the electroluminescent emission in a far-field measurement (such as IR-SMS), it is necessary to introduce local scatterers to the transistor, as outlined in subsection 3.2.3. To this end, multiple Au disks (3.5 μm in diameter, 110 nm-thick) were fabricated via optical lithography on the graphene channel¹⁹ of the HGFET discussed in Fig. 5.11 (see Fig. 5.12 (a), star). We then performed spectroscopy of the transistor's emission under electrical bias via IR-SMS as follows. The transistor's graphene channel between its gold electrodes is optically conjugated

¹⁹The disks were randomly distributed across the channel with a separation of 4 μm .

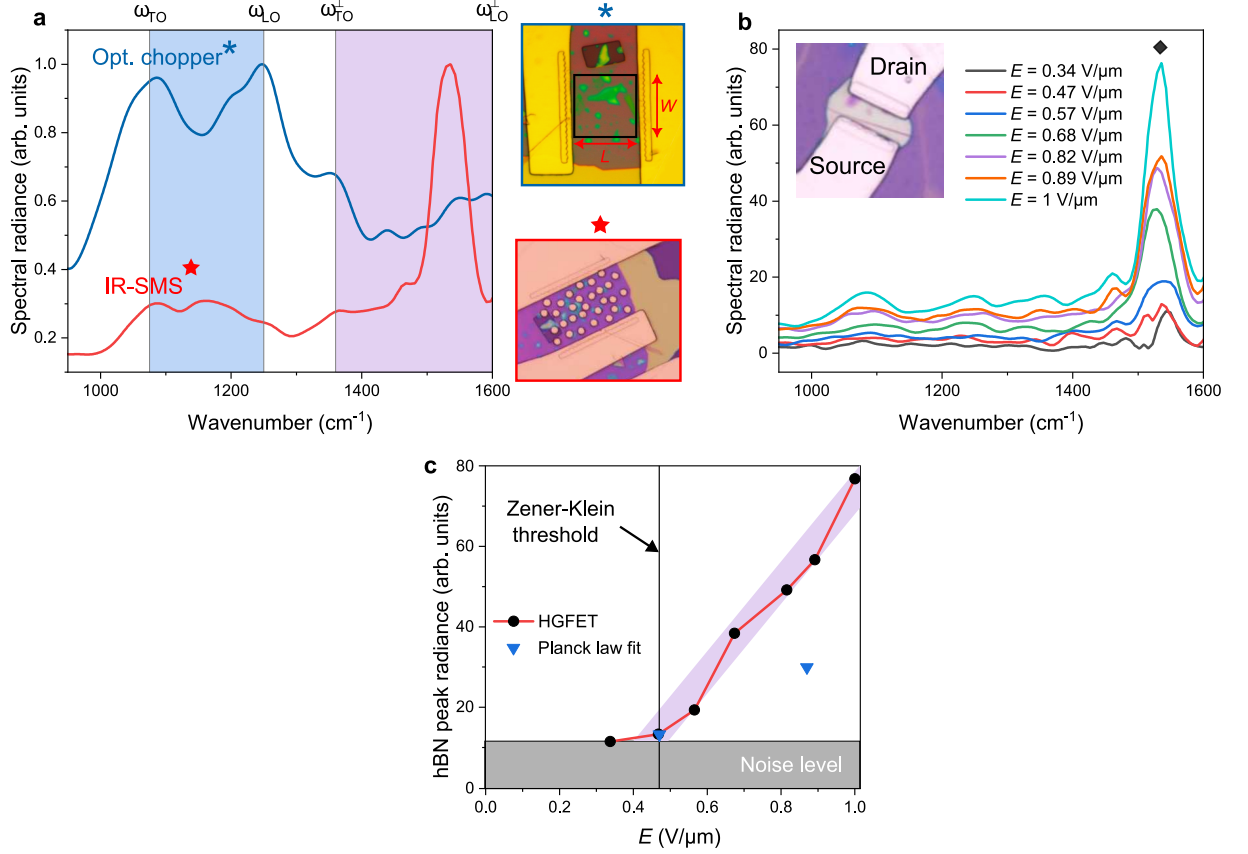


Figure 5.12: (a) Comparison between the spectral radiance of a large HGFET ($L \times W = 35 \mu\text{m} \times 35 \mu\text{m}$) under large electrical bias, before (Fig. 5.11 (c)) and after the addition of scatterers, marked with an asterisk and a star, respectively. (b) Spectral radiance of a smaller HGFET ($L \times W = 9.2 \mu\text{m} \times 15.5 \mu\text{m}$, $\mu = 66,000 \text{ cm}^2/\text{V.s}$, optical image in inset) as a function of increasing electrical bias $E = V_{ds}/L$ ($V_g = 0 \text{ V}$). (c) Evolution of the radiance of the hBN peak, marked by a diamond in panel (b), as a function of the applied electric field E (black circles). The experimental values are fitted to the spectral radiance of a Planck blackbody law (blue triangles), given by $S_P = B(T_e^{\text{NIR}})^4$, where B is a fitting parameter and T_e^{NIR} is the temperature of electrons in graphene under bias. For the two points shown here, we have $(E, T_e^{\text{NIR}}) = (0.47 \text{ V}/\mu\text{m}, 520 \text{ K})$ and $(0.87 \text{ V}/\mu\text{m}, 640 \text{ K})$. B is determined by equating S_P at $E = 0.47 \text{ V}/\mu\text{m}$ to the value of the hBN peak amplitude at the same point. The values for T_e^{NIR} were obtained by characterizing the transistor's thermal radiation in the near-IR spectral range ($\lambda_{\text{NIR}} = 1.4 - 1.6 \mu\text{m}$) as a function of electrical bias using an InGaAs near-IR camera. Courtesy of Marin Tharrault from Laboratoire de Physique de l'École Normale Supérieure (LPENS).

with the active area of the MCT detector. The transistor is then modulated laterally using the piezoelectric translation stage at a frequency Ω , by $\sim 25 \mu\text{m}$, within the field of view of the detector. The optical signal reaching the active area of the detector, thus, varies between that of the graphene channel and the Au electrode. The transistor's near-field electroluminescent signal is scattered by the disks and is captured by the collection optics. The detected signal is demodulated at the frequency Ω , allowing the measurement of a background-free electroluminescence spectrum (see Fig. 5.12 (a), red curve).

In contrast to the spectrum measured in Fig. 5.11 (c), which was dominated by the blackbody

emission of the SiO₂ back-gate, the measured spectrum now shows clear signatures of the HPhPs of the hBN layers. In particular, a predominant contribution to the spectrum comes from a peak at 1532 cm⁻¹, corresponding to the resonance of the lowest order ($l = 0$) HPhP branch (see subsection 3.2.3). As we have seen in subsection 5.3.3, this HPhP branch is also the main channel by which out-of-plane heat transfer in HGFETs occurs.

To test the electroluminescent nature of the detected emission, we consider an HGFET of smaller dimensions than that of Fig. 5.12 (a) (see Fig. 5.12 (b), inset) and a slightly higher mobility. Due to the smaller dimensions of the graphene channel of this transistor, scattering from the Au electrodes is sufficient to obtain an appreciable signal from the graphene channel without the addition of local scatterers, which generally reduce the transistor's mobility. In this transistor specifically, the scattering efficiency is also augmented by the presence of a large crack²⁰ in the top hBN layer (see Fig. 5.12 (b), inset). Using the same measurement technique outlined above, we record spectra of the HGFET as a function of increasing electrical bias (Fig. 5.12 (b)). The amplitude of the hBN peak ($\omega = 1532$ cm⁻¹) systematically increases with increasing bias, with a dramatic increase occurring beyond the Zener-Klein threshold (see Fig. 5.12 (b), $E > 0.47$ V/ μ m). The maximal value of the hBN peak is plotted in Fig. 5.12 (c) as a function of the applied electric field. The observed trend is clearly reminiscent of that of the optical power of an LED as a function of injected electric field (see Fig. 5.9 (b)), namely the optical power is minimal below a threshold electric field beyond which the optical power increases rapidly.

To rule out any contribution to the detected emission from the hot electrons of graphene, the temperature of the graphene electron gas T_e^{NIR} in the HGFET was measured by characterizing the near-IR thermal radiation of the transistor under electrical bias²¹. The electron gas temperature is found to vary from 500 K at low bias to 640 K near the maximal electrical bias considered. Using this temperature, the data points of Fig. 5.12 (c) were fitted to a Planck blackbody law (Fig. 5.12 (c), blue triangles), whose radiance at low bias is assumed to be the same as that detected from the transistor. Following this assumption, we find that, at large bias, the calculated Planck law fit leads to a significant underestimation of the spectral radiance compared to that of the measured spectra. Consequently, thermal emission caused by a thermal excitation of the structure by the hot electrons of graphene is insufficient to account for the observed increase in the transistor's radiance. We can therefore conclude that the measured spectra correspond to the emission due to the electroluminescence of the HGFET.

5.4.4 Shaping the mid-IR emission of electroluminescent HGFETs under large bias

In this subsection, we show how the mid-IR electroluminescence spectrum and intensity as a function of electrical bias in an HGFET can be shaped by engineering the local dielectric environment of the graphene layer, namely, by changing the transistor's back-gate material

²⁰We have already established in subsection 3.2.3 that etches in the hBN layer scatter its near-fields with the same efficiency as scattering disks (see Fig. 3.22 (b)).

²¹These measurements were carried out by Marin Tharrault at Laboratoire de Physique de l'Ecole Normale Supérieure.

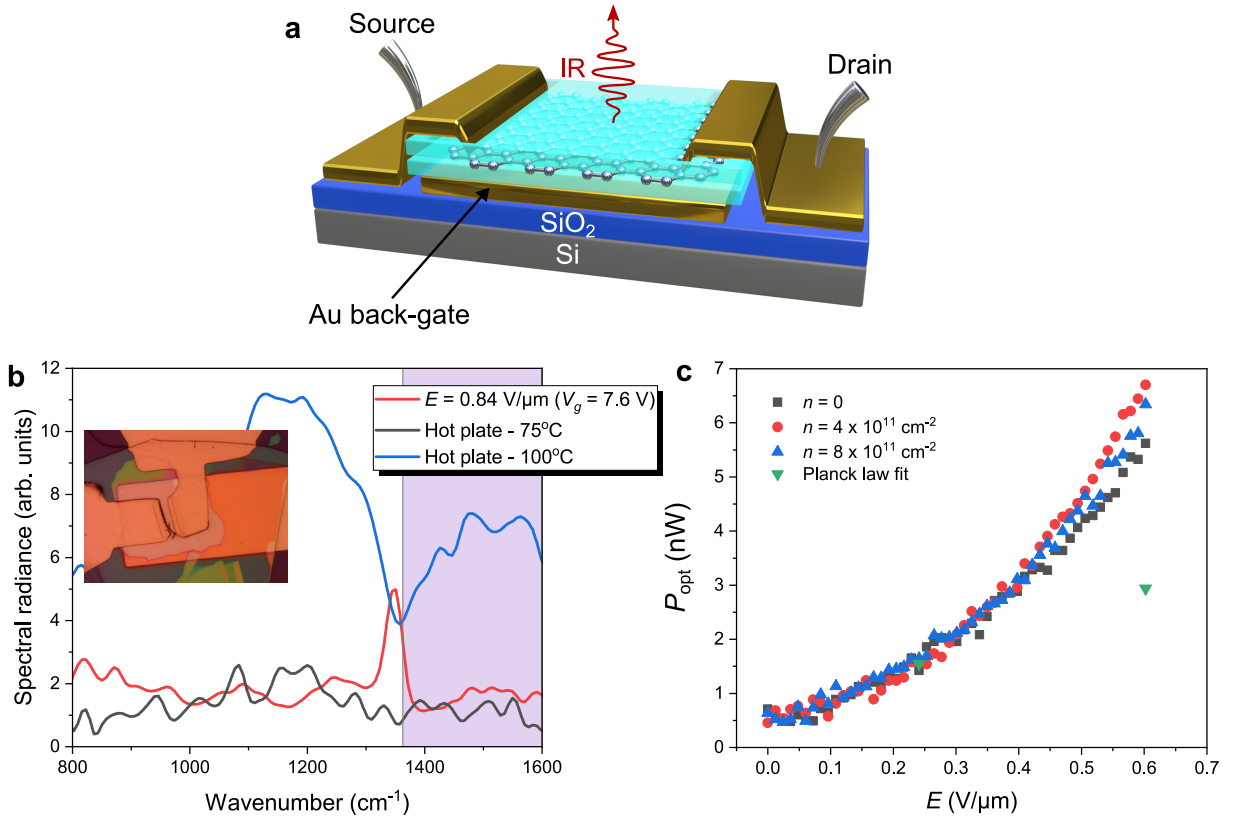


Figure 5.13: Mid-IR emission of an electroluminescent hBN-encapsulated HGFET with a gold back-gate denoted by *Flicker 160* (panel (b), inset). (a) Sketch of an hBN-encapsulated HGFET with a gold back-gate. The dimensions (L , channel length; W , channel width; $t_{\text{hBN}}^{\text{b}}$; thickness of bottom hBN layer, thickness of top hBN layer, $t_{\text{hBN}}^{\text{t}}$) and electron mobility (μ) of the transistor considered here are as follows: $L \times W = 6 \mu\text{m} \times 10 \mu\text{m}$, $t_{\text{hBN}}^{\text{b}} = 160 \text{ nm}$, $t_{\text{hBN}}^{\text{t}} = 45 \text{ nm}$, and $\mu \sim 15 \times 10^4 \text{ cm}^2 \cdot \text{V}^{-1} \cdot \text{s}^{-1}$ (see Appendix L for more details). (b) Spectral radiance of the *Flicker 160* transistor under electrical bias ($E = V_{\text{ds}}/L = 0.84 \text{ V} \mu\text{m}^{-1}$) and by heating the device with a hot plate, measured via IR-SMS. (c) Optical signal (P_{opt} , integrated over the full spectral range of the detector) of *Flicker 160* as a function of increasing electrical bias for three values of the doping concentration. The data points show a super-linear dependence of the optical signal on the applied bias, *i.e.*, $P_{\text{opt}} \propto E^2 = V_{\text{ds}}^2/L^2$. The green triangles correspond to Planck blackbody fits of the experimental data, calculated from near-IR measurements of the electron gas temperature of graphene under electrical bias (courtesy of Marin Tharrault from LPENS).

and channel length. In particular, we will discuss two HGFETs with a gold back-gate (see Fig. 5.13 (a)), each with a different channel length, which we denote as *Flicker 160* and *InOut2*. We begin by characterizing the mid-IR emission of the *Flicker 160* transistor, which has a small channel length ($L = 8.3 \mu\text{m}$).

As shown in Fig. 5.13 (b) (red curve), the emission spectrum of the transistor under electrical bias exhibits a solitary resonance peak at 1350 cm^{-1} . The highly reflecting gold back-gate used here decouples the graphene layer from the far-field over the entire mid-IR spectral range under study, except near the resonances of the refractive index of its direct environment, namely the hBN substrate. As an example, for the *Flicker 160* transistor, maximum coupling

of the graphene layer's emission to the far-field occurs at a wavelength at which a quasi-quarter-wavelength resonance of the equivalent heterostructure arises, *i.e.*, at a wavelength $\lambda = 4nt_{\text{hBN}}^{\text{b}}$, where n is the real part of the refractive index of hBN and $t_{\text{hBN}}^{\text{b}}$ is the thickness of the hBN layer separating the graphene layer from the gold back-gate. Since the hBN layer thickness in this transistor is $0.16 \mu\text{m}$, this condition is satisfied at $\lambda = 7.42 \mu\text{m}$ ($\equiv 1348 \text{ cm}^{-1}$), *i.e.*, just below the type II transverse optical phonon resonance of hBN, at which $n \simeq 11.6$. Therefore, at this precise wavelength, the coupling of the graphene layer to the far-field is optimal, as indicated by the single emission peak, which was observed experimentally around this frequency (see Fig. 5.13 (b), red curve).

Since the emission spectrum measured here is dominated by a resonance near that of the optical phonons of hBN, we assessed the possibility of a thermal emission contribution to the measured spectrum due to a thermal excitation of the optical phonons of hBN by Joule heating. To this end, Stokes-anti-Stokes Raman thermometry was carried out to measure the temperature of the optical phonons of hBN in the transistor as a function of electrical bias (see Appendix O). It is found that the temperature of the optical phonons at large electrical bias is $T_{\text{phonon}} \simeq 75 - 100^\circ\text{C}$. The spectra of the transistor heated via a hot plate sample holder to 75°C and 100°C are plotted in Fig. 5.13 (b) (black and blue curves). Neither spectra reproduce that of the transistor's emission under electrical bias. More specifically, at 75°C , which is the temperature closest to that of the phonons at the electric bias used in Fig. 5.13 (b), corresponds to a much lower detected signal that is almost at the noise level.

We also tracked the evolution of the optical power detected from the transistor as a function of increasing electrical bias at various doping concentrations. Similarly to what was observed in the previous subsection, fitting this optical signal with a Planck blackbody law based on the temperature of graphene's electrons fails to account for the large enhancement of the signal with increasing bias (see Fig. 5.13 (c), green triangles). What stands out in the current transistor, however, is that the optical power exhibits a super-linear behavior as a function of increasing bias, that is, $P_{\text{opt}} \propto E^2 = V_{\text{ds}}^2/L^2$. This super-linear behavior is observed for all the doping concentrations considered in Fig. 5.13 (c). This is due to the fact that the small channel length of the transistor shifts the Zener-Klein threshold voltage to smaller values so that electroluminescence may occur at a much lower bias voltage. We mention that for this transistor P_{opt} is almost invariant with respect to the doping concentration within the range considered here.

We now illustrate the mid-IR emission of the *InOut2* transistor, which has a larger channel length ($L = 20 \mu\text{m}$, Fig. 5.14). Interestingly, at large bias, the mid-IR emission of this transistor is highly localized near the charge-neutral point, exhibiting contrasting behavior with the Joule power (cf. Figs. 5.14 (a) and (b)). In Fig. 5.14 (c), we show line scans of the measured optical power showing the evolution of the emitted signal as a function of the applied electric field for different doping concentrations. In this case, the emission is minimal at low bias and then increases drastically beyond the Zener-Klein tunneling threshold, following a linear dependence on bias. This behavior arises due to the larger graphene channel of the transistor, which results in a Zener-Klein tunneling threshold that occurs at intermediate values of the bias. We also note that the *InOut2* transistor exhibits a much stronger dependence on doping concentration

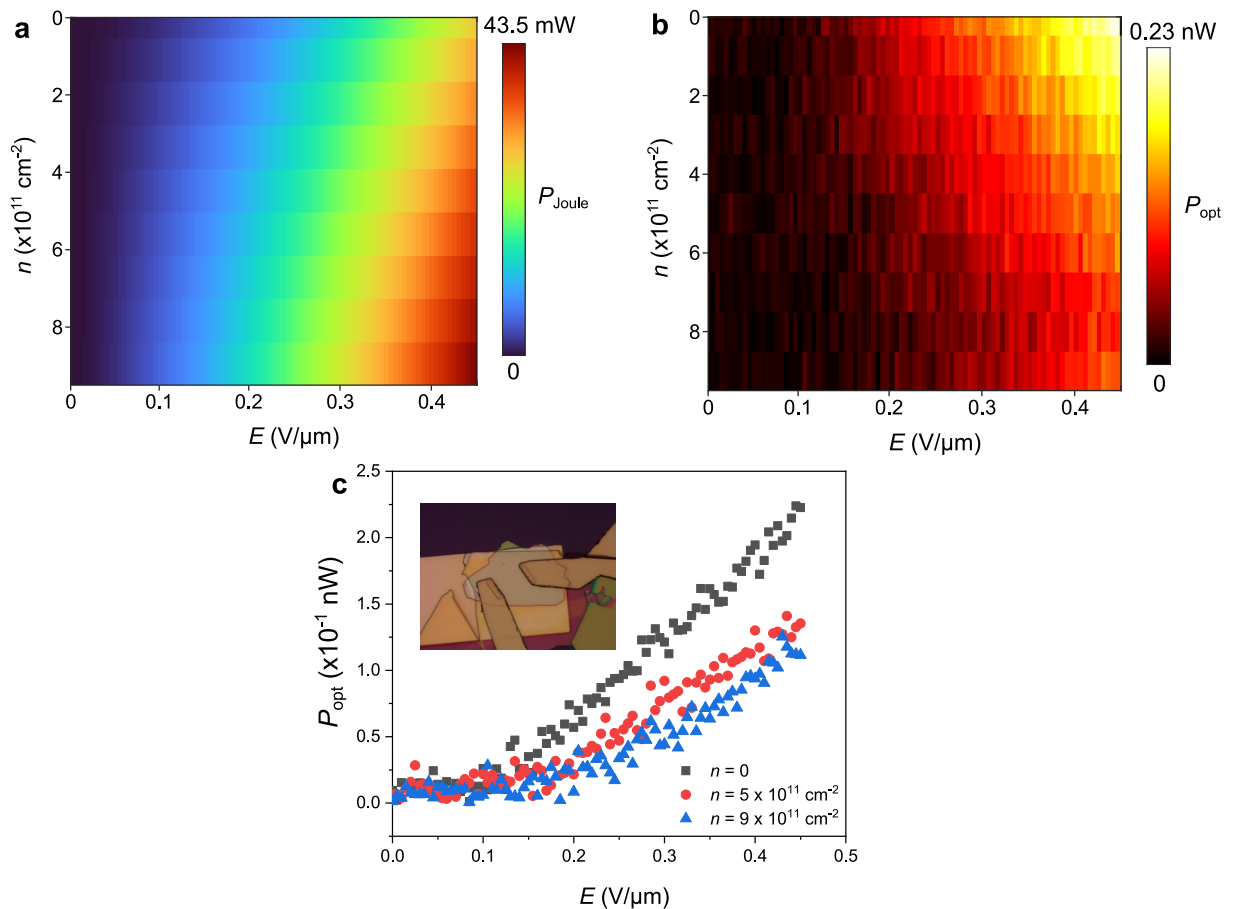


Figure 5.14: Mid-IR emission of an electroluminescent hBN-encapsulated HGFET with a gold back-gate denoted by *InOut2* (panel (c), inset). The dimensions (L , channel length; W , channel width; $t_{\text{hBN}}^{\text{b}}$; thickness of bottom hBN layer, thickness of top hBN layer, $t_{\text{hBN}}^{\text{t}}$) and electron mobility (μ) of this transistor are as follows: $L \times W = 20 \mu\text{m} \times 8.5 \mu\text{m}$, $t_{\text{hBN}}^{\text{b}} = 118 \text{ nm}$, $t_{\text{hBN}}^{\text{t}} = 67 \text{ nm}$, and $\mu \sim 9 \times 10^4 \text{ cm}^2 \cdot \text{V}^{-1} \cdot \text{s}^{-1}$ (see Appendix L for more details). (a) Joule power (P_{Joule}) of the transistor as a function of the applied electrical field $E = V_{ds}/L$. (b) Scan of the optical signal (P_{opt}) of the transistor as a function of doping concentration n and applied electric field. (c) Line scans at constant doping concentration from panel (b).

as compared to the doping-independent emission of *Flicker 160*.

To summarize, the difference in the behavior of the optical signal of the two transistors is mainly due to the larger channel length of the *InOut2* transistor – which results in an increase of the Zener-Klein threshold (see Eq. (5.3)) and a decrease in its mobility – and the super-linear evolution of the transistors’ emission with electrical bias. This can be more clearly seen from the comparison in Fig. 5.15. As shown in Fig. 5.15 (a), the optical power as a function of the applied electric field fits well with a CE^2 dependence (C is a fitting constant), with the optical signal of the *InOut2* transistor showing a steeper slope with increase E . This behavior is reversed when examining the evolution of the transistors’ optical power as a function of applied drain-source voltage V_{ds} (Fig. 5.15 (b)) as a result of the difference in channel length. The contrasting behavior exhibited by these two transistors can be explained with respect to channel length as follows. In short high-mobility transistors at low bias, the drain doping effect is manifested as

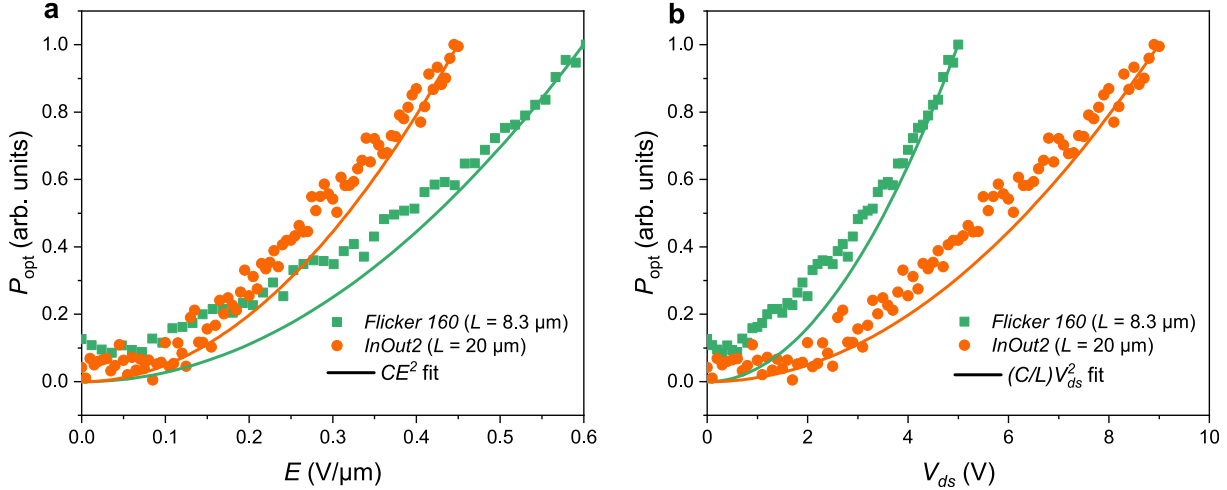


Figure 5.15: Fits of the mid-IR emission of the *Flicker 160* and *InOut2* transistors assuming a super-linear dependence on E (panel (a)) and V_{ds} (panel (b)). Symbols: experimental data, solid lines: fits.

a localization of Zener-Klein tunneling near the drain electrode instead of a mere shift of the charge neutral point. For larger bias, the injection region colonizes the whole channel. For longer/lower-mobility devices, carrier injection occurs across the whole channel starting at the Zener-Klein threshold.

5.5 Conclusion

In this chapter, we drew upon the contents of the previous chapters to investigate the electroluminescence of HGFETs at large electrical bias. We began by introducing the state-of-the-art of graphene devices, which was followed by an illustration of the fundamentals of electron transport and cooling mechanisms in HGFETs. In particular, we showed that at large bias an interband conduction current occurs in HGFETs due to Zener-Klein tunneling processes, which is synonymous with mid-IR electroluminescence in HGFETs. We also distinguished between two cooling mechanisms in HGFETs, in-plane, and out-of-plane heat transfer. The latter was shown to be associated with radiative cooling due to the electroluminescence of the transistor under large electrical bias. The signature of this electroluminescence cooling was observed experimentally by monitoring the far-field emission due to the transistor's SiO_2 back-gate as a function of applied electrical bias. The measurements and corresponding analysis revealed that this cooling mechanism constitutes at least 35% of the transistor's total cooling power.

We capitalized on this by measuring the near-field emission of the HGFETs using detection techniques outlined in chapter 3, such as employing local scatterers to the transistor's graphene channel. The resulting spectra were reported for devices of varying back-gate material, namely SiO_2 and Au. These results emphatically show that a semi-metal, such as graphene, can indeed be electroluminescent.

References

- [1] AH Castro Neto, F Guinea, N MR Peres, Kostya S Novoselov, and AK Geim. “The electronic properties of graphene”. *Rev. Mod. Phys.* 81.1 (2009), p. 109.
- [2] KS Novoselov, D Jiang, F Schedin, TJ Booth, VV Khotkevich, SV Morozov, and AK Geim. “Two-dimensional atomic crystals”. *Proc. Natl. Acad. Sci. U.S.A.* 102.30 (2005), pp. 10451–10453.
- [3] AA Balandin, S Ghosh, W Bao, I Calizo, D Teweldebrhan, F Miao, and CN Lau. “Superior thermal conductivity of single-layer graphene”. *Nano Lett.* 8.3 (2008), pp. 902–907.
- [4] E Pop, V Varshney, and AK Roy. “Thermal properties of graphene: Fundamentals and applications”. *MRS Bull.* 37.12 (2012), pp. 1273–1281.
- [5] Y Zhang, YW Tan, HL Stormer, and P Kim. “Experimental observation of the quantum Hall effect and Berry’s phase in graphene”. *Nature* 438.7065 (2005), pp. 201–204.
- [6] D Allor, TD Cohen, and DA McGady. “Schwinger mechanism and graphene”. *Phys. Rev. D* 78.9 (2008), p. 096009.
- [7] AF Young and P Kim. “Quantum interference and Klein tunnelling in graphene heterojunctions”. *Nat. Phys.* 5.3 (2009), pp. 222–226.
- [8] N Stander, B Huard, and D Goldhaber-Gordon. “Evidence for Klein tunneling in graphene p- n junctions”. *Phys. Rev. Lett.* 102.2 (2009), p. 026807.
- [9] KI Bolotin, KJ Sikes, Z Jiang, M Klima, G Fudenberg, J Hone, P Kim, and HL Stormer. “Ultrahigh electron mobility in suspended graphene”. *Solid State Commun.* 146.9-10 (2008), pp. 351–355.
- [10] M Orlita, C Faugeras, P Plochocka, P Neugebauer, G Martinez, DK Maude, AL Barra, M Sprinkle, C Berger, WA de Heer, et al. “Approaching the Dirac point in high-mobility multilayer epitaxial graphene”. *Phys. Rev. Lett.* 101.26 (2008), p. 267601.
- [11] CR Dean, AF Young, I Meric, C Lee, L Wang, S Sorgenfrei, K Watanabe, T Taniguchi, P Kim, KL Shepard, et al. “Boron nitride substrates for high-quality graphene electronics”. *Nat. Nanotechnol.* 5.10 (2010), pp. 722–726.
- [12] AK Geim and IV Grigorieva. “Van der Waals heterostructures”. *Nature* 499.7459 (2013), pp. 419–425.
- [13] AK Geim. “Graphene: status and prospects”. *Science* 324.5934 (2009), pp. 1530–1534.
- [14] DR Lide. *CRC handbook of chemistry and physics*. Vol. 85. CRC press, 2004.
- [15] P Flubacher, AJ Leadbetter, and JA Morrison. “The heat capacity of pure silicon and germanium and properties of their vibrational frequency spectra”. *Philos. Mag.* 4.39 (1959), pp. 273–294.
- [16] T Matsumura and MJ Laubitz. “Thermal conductivity and electrical resistivity of pure silver between 80 and 350 K”. *Can. J. Phys.* 48.12 (1970), pp. 1499–1503.
- [17] RA MacDonald and WM MacDonald. “Thermodynamic properties of fcc metals at high temperatures”. *Phys. Rev. B* 24.4 (1981), p. 1715.

References

- [18] MJ Laubitz and DL McElroy. “Precise measurement of thermal conductivity at high temperatures (100–1200 K)”. *Metrologia* 7.1 (1971), p. 1.
- [19] Ralph Hultgren. *Selected values of thermodynamic properties of metals and alloys*. Vol. 2. Wiley, 1963.
- [20] JG Hust and AB Lankford. *Thermal conductivity of aluminum, copper, iron, and tungsten for temperatures from 1 K to the melting point*. Tech. rep. National Bureau of Standards, Boulder, CO (USA). Chemical Engineering, 1984.
- [21] YS Touloukian, RW Powell, CY Ho, and MC Nicolaou. *Thermophysical properties of matter-The TPRC data series. Volume 10. Thermal Diffusivity*. Tech. rep. Thermophysical and Electronic Properties Information Analysis Center, 1974.
- [22] TM Tritt. *Thermal conductivity: theory, properties, and applications*. Springer Science & Business Media, 2005.
- [23] E Baudin, C Voisin, and B Plaçais. “Hyperbolic phonon polariton electroluminescence as an electronic cooling pathway”. *Adv. Funct. Mater.* 30.8 (2020), p. 1904783.
- [24] A Schmitt, L Abou-Hamdan, et al. “Electroluminescence of high-mobility graphene transistors”. (*in preparation*) (2023).
- [25] L Wojszwyk, A Nguyen, AL Coutrot, C Zhang, B Vest, and JJ Greffet. “An incandescent metasurface for quasimonochromatic polarized mid-wave infrared emission modulated beyond 10 MHz”. *Nat. Commun.* 12.1 (2021), pp. 1–8.
- [26] YD Kim, H Kim, Y Cho, JH Ryoo, CH Park, P Kim, YS Kim, S Lee, Y Li, SN Park, et al. “Bright visible light emission from graphene”. *Nat. Nanotechnol.* 10.8 (2015), pp. 676–681.
- [27] YD Kim, Y Gao, RJ Shiue, L Wang, B Aslan, MH Bae, H Kim, D Seo, HJ Choi, SH Kim, et al. “Ultrafast graphene light emitters”. *Nano Lett.* 18.2 (2018), pp. 934–940.
- [28] F Luo, Y Fan, G Peng, S Xu, Y Yang, K Yuan, J Liu, W Ma, W Xu, ZH Zhu, et al. “Graphene thermal emitter with enhanced joule heating and localized light emission in air”. *ACS Photonics* 6.8 (2019), pp. 2117–2125.
- [29] L Hamidouche, A Montanaro, M Rosticher, E Grimaldi, B Poupet, T Taniguchi, K Watanabe, B Plaçais, E Baudin, and P Legagneux. “Optoelectronic mixing in high-mobility graphene”. *ACS Photonics* 8.1 (2020), pp. 369–375.
- [30] K Yoshioka, T Wakamura, M Hashisaka, K Watanabe, T Taniguchi, and N Kumada. “Ultrafast intrinsic optical-to-electrical conversion dynamics in graphene photodetector”. *arXiv preprint arXiv:2203.05752* (2022).
- [31] JY Huang, F Ding, BI Yakobson, P Lu, L Qi, and J Li. “In situ observation of graphene sublimation and multi-layer edge reconstructions”. *Proc. Natl. Acad. Sci. U.S.A.* 106.25 (2009), pp. 10103–10108.
- [32] A Pierret, D Mele, H Graef, J Palomo, T Taniguchi, K Watanabe, Y Li, B Toury, C Journet, P Steyer, et al. “Dielectric permittivity, conductivity and breakdown field of hexagonal boron nitride”. *Mater. Res. Express* 9.6 (2022), p. 065901.
- [33] W Yang, S Berthou, X Lu, Q Wilmart, A Denis, M Rosticher, T Taniguchi, K Watanabe, G Fève, JM Berroir, et al. “A graphene Zener–Klein transistor cooled by a hyperbolic substrate”. *Nat. Nanotechnol.* 13.1 (2018), pp. 47–52.
- [34] F Sauter. “Über das Verhalten eines Elektrons im homogenen elektrischen Feld nach der relativistischen Theorie Diracs”. *Z. Phys.* 69.11 (1931), pp. 742–764.
- [35] MI Katsnelson, KS Novoselov, and AK Geim. “Chiral tunnelling and the Klein paradox in graphene”. *Nat. Phys.* 2.9 (2006), pp. 620–625.
- [36] O Klein. “Die Reflexion von Elektronen an einem Potentialsprung nach der relativistischen Dynamik von Dirac”. *Z. Phys.* 53.3 (1929), pp. 157–165.

-
- [37] G Kané, M Lazzeri, and F Mauri. “High-field transport in graphene: the impact of Zener tunneling”. *J. Phys.: Condens. Matter* 27.16 (2015), p. 164205.
- [38] I Meric, MY Han, AF Young, B Ozyilmaz, P Kim, and KL Shepard. “Current saturation in zero-bandgap, top-gated graphene field-effect transistors”. *Nat. Nanotechnol.* 3.11 (2008), pp. 654–659.
- [39] AC Betz, F Vialla, D Brunel, C Voisin, M Picher, A Cavanna, A Madouri, G Fève, JM Berroir, B Plaçais, et al. “Hot electron cooling by acoustic phonons in graphene”. *Phys. Rev. Lett.* 109.5 (2012), p. 056805.
- [40] AC Betz, SH Jhang, E Pallecchi, R Ferreira, G Fève, JM Berroir, and B Plaçais. “Supercollision cooling in undoped graphene”. *Nat. Phys.* 9.2 (2013), pp. 109–112.
- [41] R Franz and G Wiedemann. “Ueber die Wärme-Leitungsfähigkeit der Metalle”. *Ann. Phys.* 165.8 (1853), pp. 497–531.
- [42] L Abou-Hamdan, S Hamyeh, A Iskandar, R Tauk, J Brault, M Tabbal, PM Adam, and M Kazan. “Tuning electrical and thermal conductivities of the two-dimensional electron gas in AlN/GaN heterostructures by piezoelectricity”. *Nanotechnology* 32.11 (2020), p. 115703.
- [43] JJ Greffet, R Carminati, K Joulain, JP Mulet, S Mainguy, and Y Chen. “Coherent emission of light by thermal sources”. *Nature* 416.6876 (2002), pp. 61–64.
- [44] A Babuty, K Joulain, PO Chapuis, JJ Greffet, and Y De Wilde. “Blackbody spectrum revisited in the near field”. *Phys. Rev. Lett.* 110.14 (2013), p. 146103.
- [45] A Principi, M Polini, and G Vignale. “Linear response of doped graphene sheets to vector potentials”. *Phys. Rev. B* 80.7 (2009), p. 075418.
- [46] A Principi, MB Lundberg, N CH Hesp, KJ Tielrooij, F HL Koppens, and M Polini. “Super-Planckian electron cooling in a van der Waals stack”. *Phys. Rev. Lett.* 118.12 (2017), p. 126804.
- [47] KJ Tielrooij, N CH Hesp, A Principi, MB Lundberg, E AA Pogna, L Banszerus, Z Mics, M Massicotte, P Schmidt, D Davydovskaya, et al. “Out-of-plane heat transfer in van der Waals stacks through electron–hyperbolic phonon coupling”. *Nat. Nanotechnol.* 13.1 (2018), pp. 41–46.
- [48] E Rosencher and B Vinter. *Optoelectronics*. Cambridge University Press, 2002.
- [49] AI Volokitin and BNJ Persson. “Near-field radiative heat transfer and noncontact friction”. *Rev. Mod. Phys.* 79.4 (2007), p. 1291.
- [50] P Wurfel. “The chemical potential of radiation”. *J Phys. C: Solid State Phys.* 15.18 (1982), p. 3967.
- [51] JJ Greffet, P Bouchon, G Brucoli, and F Marquier. “Light emission by nonequilibrium bodies: local Kirchhoff law”. *Phys. Rev. X* 8.2 (2018), p. 021008.
- [52] Zhun-Yong Ong and Myung-Ho Bae. “Energy dissipation in van der Waals 2D devices”. *2D Mater.* 6.3 (2019), p. 032005.
- [53] P Santhanam, D Huang, RJ Ram, MA Remennyi, and BA Matveev. “Room temperature thermo-electric pumping in mid-infrared light-emitting diodes”. *Appl. Phys. Lett.* 103.18 (2013), p. 183513.
- [54] E Pop. “Energy dissipation and transport in nanoscale devices”. *Nano Res.* 3.3 (2010), pp. 147–169.

Conclusions and perspectives

In this manuscript, we have seen how the mid-infrared electromagnetic spectrum can be shaped by tailoring the geometrical and material properties of subwavelength (sub- λ) structures. Several examples of sub- λ devices were developed and discussed. The intrinsic mid-infrared radiation of these structures was characterized both in the near- and far-field, using techniques such as infrared spatial modulation spectroscopy (IR-SMS) and scattering-scanning near-field optical microscopy (s-SNOM). Here, we provide a recap of the main results of the studies presented in this manuscript and discuss some perspectives.

In chapter 2, we developed the basic concepts behind surface polaritons, which are surface waves characteristic of the near-field of polar dielectrics and metals. Particularly, we illustrated the *local dielectric continuum theory*, in which the response of a nonmagnetic material to electromagnetic fields is described by the dielectric function $\varepsilon(\omega)$. Conversely, the local dielectric continuum theory shows that one can tune the optical response of a material structure by appropriately engineering $\varepsilon(\omega)$. Another adjustment knob arises due to the presence of boundaries and interfaces in certain material structures, at which surface modes exist. Our approach in this chapter was to define a material structure consisting of polar dielectric materials with varying boundary types and then to compute the normal modes of the structure. Using this approach, we presented a detailed illustration of the properties of surface phonon-polaritons (SPhPs) in a wide array of polar dielectric materials and geometries. We saw that SPhPs arise in the *Reststrahlen* band of polar dielectric materials where the real part of the dielectric function is negative. In the far-field, the effect of having a large negative real part of $\varepsilon(\omega)$ is that the polar dielectric material exhibits an optical response equivalent to that of a metal, that is, the material becomes highly reflecting. On the other hand, in the near-field, this implies that many SPhP modes of large in-plane wavevector exist at the surface.

In chapter 3, we experimentally probed the spectral features associated with surface phonon-polaritons via s-SNOM and IR-SMS. In particular, we experimentally revealed the spectrally coherent near-field response of polar dielectric materials. This spectral coherence arises as a result of resonances corresponding to the substantial number of SPhP modes localized at the surface. Since surface polaritons are confined to the surface, a sub- λ scatterer is necessary to couple them to the far-field where they can be detected. In an s-SNOM experiment, this role is played by a sharp AFM tip, which efficiently scatters a sample's near-fields, making this technique highly beneficial for near-field spectroscopy. Nevertheless, the ill-defined shape of the

tip complicates the modeling of experimental data in certain cases. As an alternative approach, we presented in this chapter a near-field spectroscopy technique based on the combination of a sub- λ local scatterer with the far-field IR-SMS technique. As a proof of concept of this method, we measured the near-field spectral signatures of polar dielectric materials, scattered by individual sub- λ gold discs, which were patterned with optical lithography on the surface. We also showed that etches in the material can also act as efficient scatterers of the sample's near-fields. Having established the validity of this technique, the next step is to perform the appropriate modeling of these experimental data and test out different geometries of scatterers. Additionally, further efforts must be made to determine the optimal size, geometry, and material of the local scatterer to be utilized for near-field spectroscopy. In general, the guiding principle for choosing an optical near-field probe is that the probe must have a large scattering efficiency and a flat optical response (*i.e.*, a sub-resonant response). This principle ensures that the probe merely acts as a passive scatterer that minimally perturbs the local field of the sample under study.

We rounded out this chapter with an experimental investigation of surface phonon-polaritons in the sphere geometry, a special case in which surface modes are directly accessible in the far-field. More precisely, we characterized the far-field thermal radiation of single sub- λ SiO₂ spheres on a gold substrate, using IR-SMS. The measurements, and corresponding analysis based on finite-element method (FEM) simulations and rigorous Mie theory calculations, revealed that the dielectric and geometrical properties of the investigated sub- λ SiO₂ spheres allow the excitation of both phononic and geometrical Mie resonances of the electric and magnetic type. The phononic resonance observed in the measured single polar dielectric spheres is a direct analog to plasmonic resonances exhibited by noble metals in the visible spectral range. The geometrical Mie modes, on the other hand, are equivalent to those prevalent in high-refractive-index dielectric spheres, such as silicon nanospheres, in the visible and near-infrared. The observation of both types of resonances is a direct consequence of the fact that SiO₂ is a polar dielectric material, whose real part of its dielectric function can, thus, be either positive, as in dielectric materials, or negative as in metals, depending on the optical frequency. By sweeping the measured sphere size, a transition from a phononic-mode-dominated to a Mie-mode-dominated absorption spectrum was observed. Further, the combination of the resonant dielectric microsphere and the metallic substrate was shown to result in a large enhancement of the sphere's absorption cross-section, above the unitary limit achievable by a resonant dipole in vacuum. This arises due to a substantial enhancement of the local field between the sphere and substrate, as a consequence of the interaction of the sphere with its induced image in the substrate. Lastly, measurement of the far-field thermal radiation of a single sub- λ PTFE sphere on a gold substrate, along with Mie theory calculations of absorption efficiency of PTFE spheres in vacuum, showed that contrary to SiO₂ spheres, the absorption spectrum of such lossy dielectric spheres, which are SPhP-inactive, is dominated by bulk absorption.

This study offers new insights into the geometrical and electromagnetic degrees of freedom that allow the engineering of the mid-infrared absorption and radiation properties of single dielectric spheres. This will allow, for instance, the design and optimization of systems based

on dielectric spheres on a metallic substrate that achieve efficient radiative cooling properties, *i.e.*, a large emissivity only in the infrared atmospheric window (predominantly between 8 and 14 μm). Moreover, the large field confinement and enhancement observed between the resonant dielectric sphere and metallic substrate could be of interest for bio-detection applications, such as surface-enhanced infrared absorption spectroscopy.

Having thoroughly discussed the properties of dielectric resonators, we shifted our attention to plasmonic antennas in chapter 4. Single sub- λ patch metal-insulator-metal (MIM) cavity antennas were first studied in the near- and far-field. In this part, we established that the response of a single patch MIM cavity antenna can be tuned by exploiting its Fabry-Perot resonances, which conveniently scale with cavity width. From there, the near-field interaction between multiple patch MIM antennas was probed experimentally and interpreted with the aid of finite-difference time-domain and FEM simulations. We began by illustrating the coupling between two square-patch MIM antennas that are separated by a nanometric gap. In this study, we revealed signatures of mode hybridization on the far-field spectrum of the antenna pair. This was followed by a study of a more convoluted MIM antenna structure consisting of 9 patch MIM antennas in near-field interaction. The patches were organized in a symmetric 3×3 configuration. The goal of this study was to illustrate how the response of individual MIM cavities can be shaped via surface patterning. Through s-SNOM imaging, we revealed that the local field of the antenna is confined to specific gaps, which constitute a spatial region of $\sim \lambda/100$. We also showed that the field confinement as well as the far-field spectral response of this antenna can be altered depending on the angle of incidence of the optical excitation. This angularly-dependent response is in stark contrast to single square-patch MIM antennas, which are spectrally angle-independent. Having demonstrated how the optical response of MIM cavities can be tuned by appropriately designing one of its metallic layers, future avenues to be explored in this subject must include a thorough investigation of MIM antennas with varying cavity material. For instance, doped semi-conductors or quantum well materials may be used. Such a study would be of particular importance for photo-detector applications.

Finally, in chapter 5 we applied the expertise and the highly sensitive infrared measurement techniques developed in the previous chapters to probe the mid-infrared emission of hBN-encapsulated high-mobility graphene field-effect transistors (HGFETs) in operation. We elaborated in this chapter that due to the unique transport properties possessed by HGFETs, an out-of-equilibrium state can develop when the transistor is subjected to a large electrical bias, leading to electroluminescence. This electroluminescence is a direct consequence of electron pumping initiated by Zener-Klein tunneling processes. Remarkably, we have been able to characterize the mid-infrared emission due to the electroluminescence of the transistors under large electrical bias. The electroluminescent nature of the detected emission was verified by a series of test experiments and analyses. In particular, we revealed two manifestations of electroluminescence in the transistors under study. The first was in the form of radiative cooling of the hot electrons in graphene via electroluminescence, which we probed experimentally by monitoring the far-field mid-infrared emission of an HGFET with an SiO_2 back-gate as a function of applied electrical bias. The second was a characterization of the emission spectrum due

to electroluminescence in HGFETs under large bias. By changing the back-gate material, we demonstrated that the emission spectrum due to electroluminescence can be shaped. We also showed that changing the back-gate material can influence the behavior of the emitted electroluminescence signal as a function of increasing bias. For instance, it was found that HGFETs with a gold back-gate exhibit a super-linear increase of the emitted electroluminescence power with increasing bias.

Having established the electroluminescent nature of the mid-infrared emission of HGFETs under large bias, a subsequent study aimed at uniquely identifying the near-field spatial distribution of the electroluminescent signal must be undertaken. This can be accomplished by near-field imaging (*e.g.*, via s-SNOM) of the transistor's graphene channel as a function of electrical bias. Further investigation is also required to determine the origin of the super-linear behavior observed in HGFETs with a gold back-gate.

List of communications

Journal articles

- Abou-Hamdan, Loubnan, et al. "Transition from Phononic to Geometrical Mie Modes Measured in Single Subwavelength Polar Dielectric Spheres." *ACS Photonics* 9.7 (2022): 2295-2303.
- Abou-Hamdan, Loubnan, et al. "Hybrid modes in a single thermally excited asymmetric dimer antenna." *Optics Letters* 46.5 (2021): 981-984.
- Abou-Hamdan, Loubnan, et al. "Tuning electrical and thermal conductivities of the two-dimensional electron gas in AlN/GaN heterostructures by piezoelectricity." *Nanotechnology* 32.11 (2020): 115703.

Appendix

A Finite-element method simulations

Finite-element method (FEM) simulations using the commercial software Comsol Multiphysics, were carried out in this manuscript to simulate cross-sections and near-field distributions of subwavelength antennas. To simulate a single antenna, *perfectly matched layers* (PMLs) were set for all boundaries as illustrated in Fig. A1. A plane wave port is incident from the top at an angle θ with respect to the normal to the substrate. The simulation is first run without the antenna, then run again with it so that the field is slightly modified by its presence, allowing to take into account the influence of the sub- λ antenna on the large simulation region. The simulation span is typically taken to be 1.5λ or 2λ , where λ is the wavelength of the incident light, in order to reduce stray reflections off the boundaries and to ensure proper convergence of the simulations.

The scattering cross-section of the antenna is calculated by integrating over the surface of the antenna as follows

$$C_{\text{scat}} = \frac{1}{I_0} \int_S \mathbf{n} \cdot \mathbf{S}_{\text{sc}} dS, \quad (14)$$

where \mathbf{n} is the normal vector pointing outward from the antenna, \mathbf{S}_{sc} is the scattered intensity (Poynting) vector, and I_0 is the intensity of the incident light.

The absorption cross-section, on the other hand, is obtained by integrating losses over the volume of the antenna as follows

$$C_{\text{abs}} = \frac{1}{I_0} \int_V Q dV, \quad (15)$$

where Q is the power loss density in the antenna.

The extinction cross-section is then found by summing the scattering and absorption cross-sections:

$$C_{\text{ext}} = C_{\text{abs}} + C_{\text{scat}}. \quad (16)$$

To obtain the electric field distribution in the near-field of the antenna, the electric field is calculated in a slice of the geometry and plotted in a color map.

The dielectric properties of the materials making up the antenna were taken from the literature. For example, data reported in refs. [1] and [2] were used for the dielectric functions of gold and ZnS, respectively.

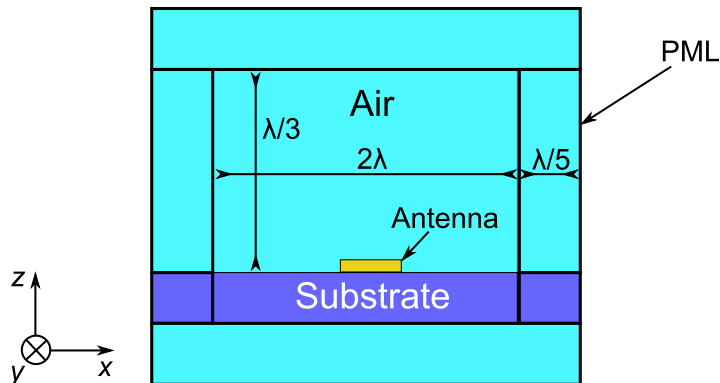


Figure A1: Geometry used to simulate a single sub- λ antenna using the commercial FEM solver of Maxwell's equations, Comsol Multiphysics. The geometry is bounded by perfectly matched layers (PMLs) of thickness $\lambda/5$ in all directions.

B Finite-difference time-domain simulations

The finite-difference time-domain (FDTD) solver Lumerical Solutions is used to simulate the near-field distribution of a single antenna in order to compare with near-field images obtained via s-SNOM. PMLs are set across all boundaries of the antenna structure as described in Fig. A2. To reproduce the conditions of illumination of our experimental setup, a Gaussian beam, focused with a numerical aperture, $NA = 0.46$, is incident from the top onto the antenna at an angle of 60° (measured from the z -axis in Fig. A2). A two-dimensional (2D) monitor placed 30 nm above the antenna structure is used to compute the electric field components E_x , E_y , and E_z , in each mesh cell of the (x, y) -plane.

To calculate the absorption cross-section using this simulation method, a total-field-scattered-field source is used and the antenna is enclosed in all directions with six 2D monitors. The flux of the Poynting vector $\mathbf{\Pi}(\omega) = \mathbf{E}(\omega) \times \mathbf{H}^*(\omega)$, crossing the surface of each monitor is computed. The power passing through each monitor can then be found from

$$P_{ij} = \frac{1}{2} \int_{S_{ij}} \text{Re}(\mathbf{\Pi}(\omega)) \cdot d\mathbf{S}_{ij}, \quad (17)$$

where, $i = x, y, z$ and $j = 1, 2$, and the integration is taken over the surface of the ij -th monitor of surface area S_{ij} .

The total power crossing the monitors is, therefore, given by

$$P_{\text{tot}} = \sum_{i=x,y,z} \sum_{j=1,2} P_{ij}. \quad (18)$$

The absorption cross-section can then be determined by taking the ratio between the total power with the intensity of incident light I_0 , that is

$$C_{\text{abs}} = \frac{P_{\text{tot}}}{I_0}. \quad (19)$$

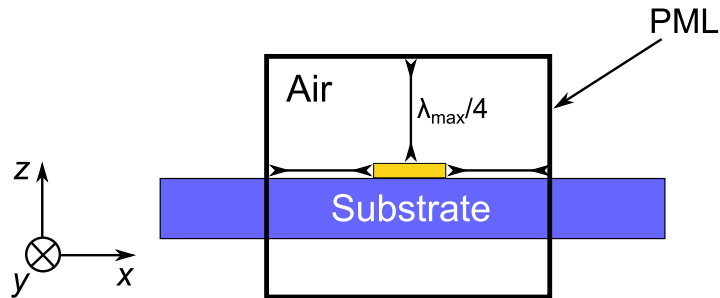


Figure A2: Geometry used to simulate a single sub- λ antenna using the FDTD solver of Maxwell’s equations, Lumerical Solutions. The geometry is bounded by perfectly matched layers PMLs in all directions. The distance between the edges of the antenna and the PML boundaries is taken to be $\lambda_{\max}/4$, where λ_{\max} is the longest wavelength considered.

C Single microspheres on an Au substrate: sample preparation

A $1\ \mu\text{L}$ solution of commercially available microspheres (Sigma Aldrich for SiO_2 and Polysciences for PTFE), of known size, was diluted with $99\ \mu\text{L}$ of solvent (distilled water for SiO_2 and ethanol for PTFE), and sonicated to prevent particle aggregation. The diluted solution was spin-coated on a sample consisting of a $100\ \text{nm}$ thick gold layer on top of a silicon (Si) substrate. The sample was viewed using a microscope with a visible objective ($\times 50$, Numerical aperture $\text{NA} = 0.55$) to determine the positions of single spheres. The spheres were then imaged using a visible camera (Figs. 3.24 (b-e) of the main text, insets) and the thermal radiation of the imaged spheres was characterized using infrared spatial modulation spectroscopy [3–5].

D Heat transfer simulation: sphere on a heated substrate

To assess the possibility of a temperature gradient arising in the measured SiO_2 spheres on the hot substrate, we performed FEM simulations of the temperature distribution in our system using the Comsol Multiphysics Heat Transfer module. A $50 \times 50\ \mu\text{m}^2$ region of the substrate is considered along with a $50\ \mu\text{m}$ thick air layer above it. The substrate is maintained at a temperature of $440\ \text{K}$ while we take into account conductive cooling through air and glass. To simulate the poor contact between the sphere and substrate, the sphere is considered to intersect the substrate at a single point. Under these conditions, we find that the sphere temperature deviates at maximum by $0.35\ \text{K}$ from the substrate temperature (see Fig. A3 (a)).

We note that conduction through the air layer is the main heat transfer channel here [6]. We have verified this by suppressing the solid-solid contact so that the sphere is $1\ \mu\text{m}$ above the substrate (Fig. A3 (b)), for which we find that the temperature deviation is still below $1\ \text{K}$. Thus, temperature variations within the sphere are negligible, showing that the assumption that the sphere is thermalized at the temperature of the substrate ($440\ \text{K}$) is valid under our experimental conditions.

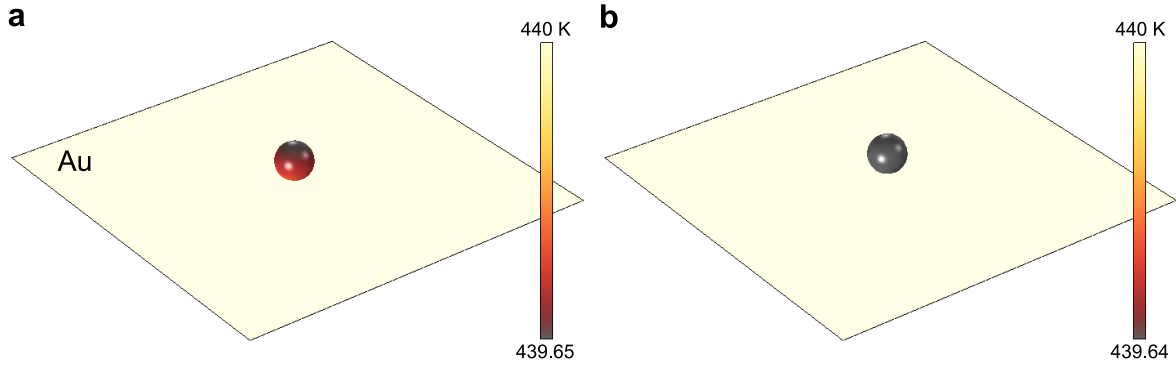


Figure A3: FEM calculations of the temperature distribution in a 2.5 μm radius SiO₂ sphere (a) on and (b) 1 μm above a gold substrate with $T_{\text{substrate}} = 440$ K.

E Angle resolved cross-section spectra of a sphere on an Au substrate

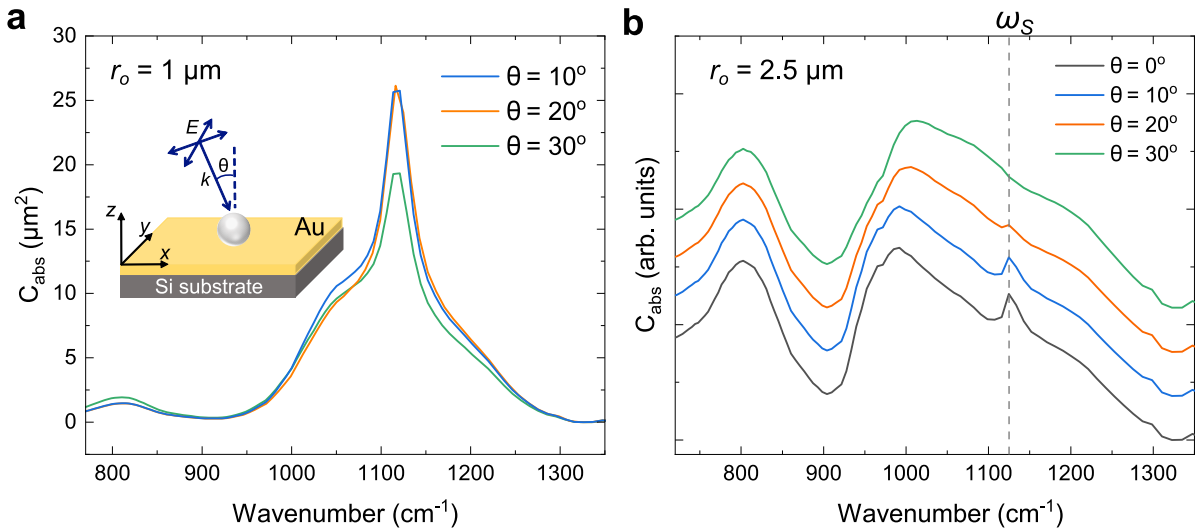


Figure A4: FEM calculations of absorption cross-section (C_{abs}) of an SiO₂ sphere on gold, with (a) $r_o = 1 \mu\text{m}$ and (b) $r_o = 2.5 \mu\text{m}$, for unpolarized light incident at various angles θ , as sketched in the inset of panel (a). The curves in panel (b) are shifted vertically for clarity and the dashed vertical line shows the surface mode peak position (ω_S).

F Absorption in a BiMIM structure with an SiO₂ insulator layer vs absorption in SiO₂ alone

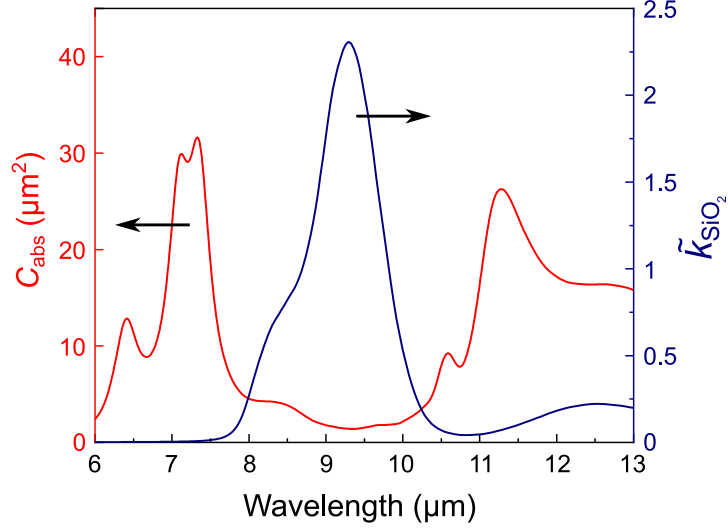


Figure A5: Simulated absorption cross-section (C_{abs}) of a BiMIM structure for gap size $g = 100$ nm (red curve) presented in the main text (red curve in Fig. 4.7 (b) of the main text), along with the imaginary part of the SiO₂ index of refraction (\tilde{k}_{SiO_2} , blue curve). Optical constants taken from ref. [7]. The comparison of the two shows a high absorption due to SiO₂ in the spectral region between 8 and 13 μm , which prevents the formation of a splitting in the BiMIM emission spectrum in this range.

On examining the imaginary part of the index of refraction of SiO₂, we find that due to its high absorption in the spectral range between 8 and 13 μm , a splitting due to the hybrid modes does not occur in this region. Indeed, as illustrated in Fig. A5 the imaginary part of the index of refraction is zero in the spectral range where the splitting occurs (below ~ 7.5 μm), while it is non-zero for higher wavelengths.

G Metal-insulator-metal antennas: sample fabrication

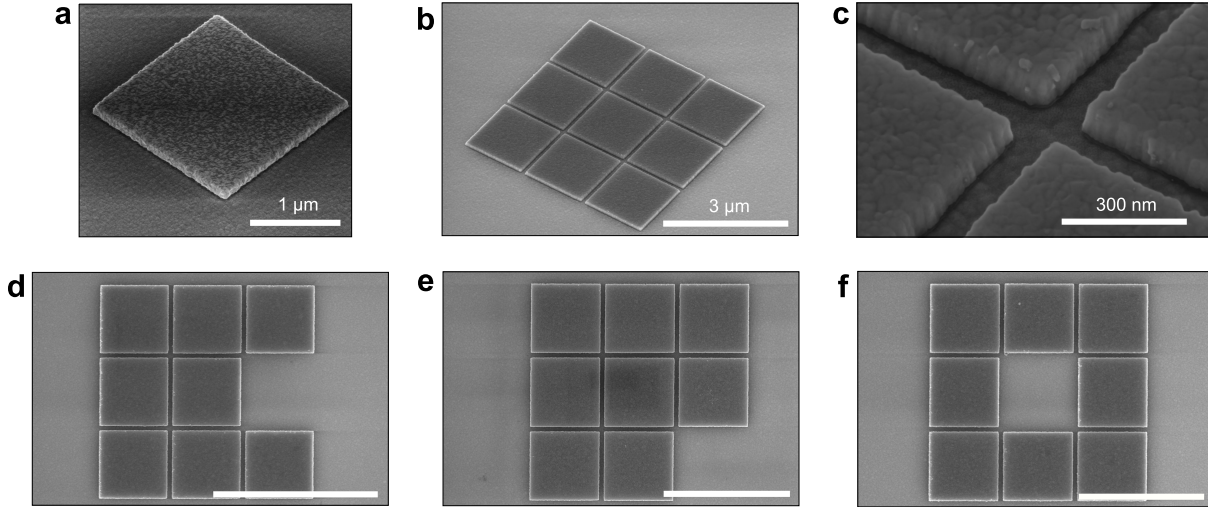


Figure A6: Scanning electron microscope (SEM) images of square-patch metal-insulator-metal (MIM) antennas. (a) A 45° tilted SEM image of a single square-patch MIM antenna of side $w = 1.65 \mu\text{m}$. (b) Tilted SEM image of a 3×3 square-patch MIM antenna with a patch width of $1.65 \mu\text{m}$ and a gap size of 100 nm . (c) Zoom of the gaps in panel (b). (d-f) SEM images of 3×3 square-patch MIM antennas with a missing patch. The scale bars are as follows: (d) $4 \mu\text{m}$, (e) & (f) $3 \mu\text{m}$. Electron beam parameters: High voltage = 10 kV , Current = 0.2 nA , and $30,000 < \text{Magnification} < 350,000$. Courtesy of Christophe Dupuis from C2N (CNRS/University Paris-Sud/Paris-Saclay).

The metal-insulator-metal (MIM) antennas experimentally studied in this manuscript, were fabricated via electron beam (e -beam) lithography²², which we illustrate below.

For the substrate, we used a commercially available stack consisting of the following layers from top to bottom:

ZnS(270 nm)/Au(200 nm)/Si($300 \mu\text{m}$), where the values between parenthesis are the thickness of each layer.

A positive resist consisting of a thin PMMA layer, is spin-coated on top of the ZnS surface and the sample is then placed on a hot plate for 5 minutes (at 170°C). e -beam lithography was then carried out in order to draw the desired antenna patterns. To ensure that each individual pattern is well isolated, only one pattern was drawn within every $100 \times 100 \mu\text{m}^2$ section of the sample surface. The following settings were used for the e -beam: Resolution = 2.5 nm , Dose = $1200 \mu\text{C}/\text{cm}^2$, Intensity = 2.5 nA , and Frequency = 33.5 MHz .

The sample was then developed in a Methyl-isobutyl-ketone (MIK)/Isopropanol (IPA) solution²³. This step was followed by the deposition of a 5 nm chromium (Cr) adhesion layer. Subsequently, a gold layer was evaporated on top of the Cr layer, forming the top gold patches of the MIM antennas. Finally, a lift-off step was executed in order to remove any excess resist from the sample surface.

²²The e -beam lithography was carried out by Nathalie Bardou at Centre de Nanosciences et de Nanotechnologies (C2N).

²³A ratio of 3(MIK):1(IPA) is used.

Some examples of square-patch antennas resulting from the e -beam lithography procedure outlined above are shown in Fig. A6. As can be seen from the SEM images presented in Fig. A6, the e -beam lithography technique yields square patterns of regular shape and highly well-defined gaps (see Fig. A6 (c)). Moreover, the AFM image in Fig. A7 (b) shows that the patches have a thickness of 40 nm, which is thicker than the skin depth of gold.

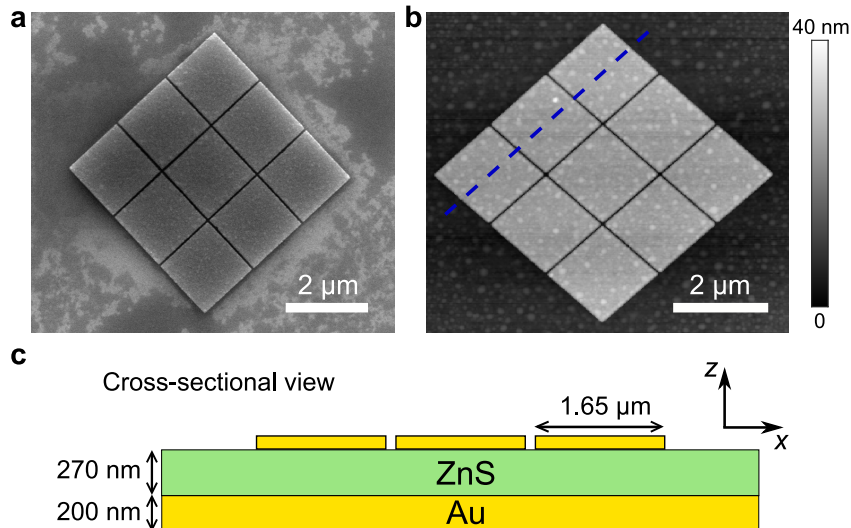


Figure A7: (a) SEM image of 3×3 -patch MIM antenna. (b) Atomic force microscope (AFM) image showing the topography of the antenna. (c) Sketch showing the thicknesses of the various layers of the antenna.

The far-field radiation of a single square-patch MIM antenna is characterized via IR-SMS (see subsection 3.2.1) and is compared to its corresponding FEM-simulated absorption cross-section (Fig. A8). This comparison illustrates the very good agreement obtained between measurement and simulation, both yielding a resonance at 1126 cm^{-1} corresponding to the fundamental Fabry-Perot resonance of the antenna.

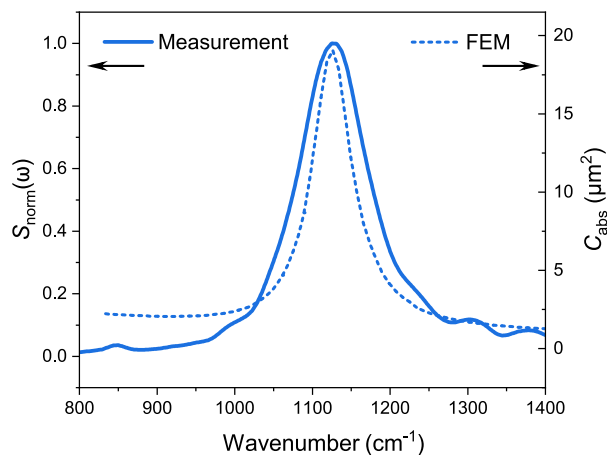


Figure A8: Comparison between the measured IR-SMS and FEM-simulated absorption cross-section spectra of a single square-patch MIM antenna of side $w = 1.65 \mu\text{m}$. The spectra show the fundamental resonance mode of the antenna at 1126 cm^{-1} (cf. Eq. (4.6)).

H Simulations of a 3×3 -patch MIM antenna consisting of the layers sketched in Fig. A7 (c)

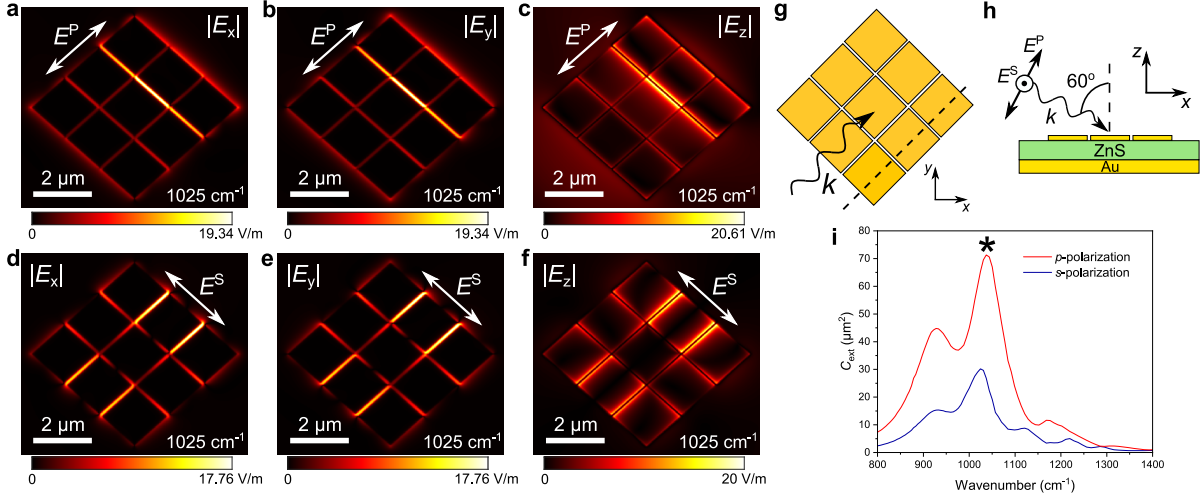


Figure A9: (a-c) (resp. (d-f)) FDTD simulations of the x , y , and z -components of the electric field of a 3×3 -patch antenna for p -polarized light (resp. s -polarized light), calculated at the resonance marked in panel (i). The plots show that just as in the single square-patch case, the near-field of the antenna is such that $|E_x| = |E_y| < |E_z|$. (g) & (h) Sketches of the antenna geometry and illumination configuration. (i) FEM simulations of the extinction cross-section of the antenna for p - and s -polarized light.

I s-SNOM: miscellaneous

i Approach curves

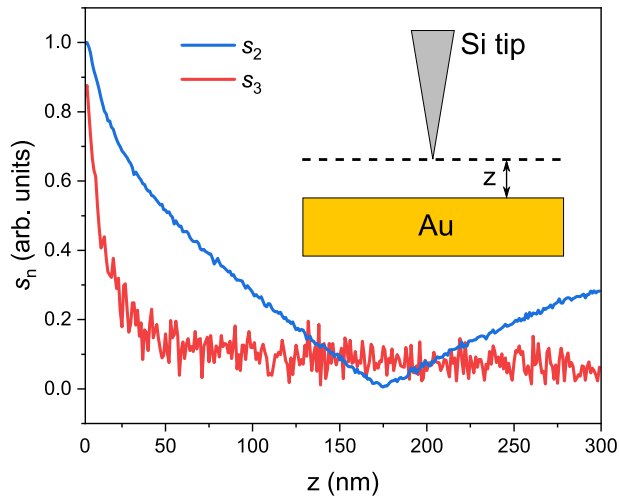


Figure A10: Approach curves measured at the surface of a large gold pattern with a silicon (Si) tip, showing a comparison between the near-field signal demodulated at the 2nd and 3rd harmonic (blue and red curves, respectively). This comparison demonstrates that demodulation at the 3rd harmonic is required in order to adequately isolate the near-field signal. It is clear that the signal s_3 decays exponentially away from the surface and becomes negligible when the tip is 300 nm away from the sample surface (*i.e.*, in a fully retracted position), a behavior characteristic of a near-field signal. On the other hand, s_2 includes a large background contribution as it is non-zero when the tip is fully retracted. The background signal mainly originates from laser light back-scattered off the tip shaft as it oscillates away from the sample.

ii Mapping the near-field of plasmonic nanostructures: metallic vs dielectric tips

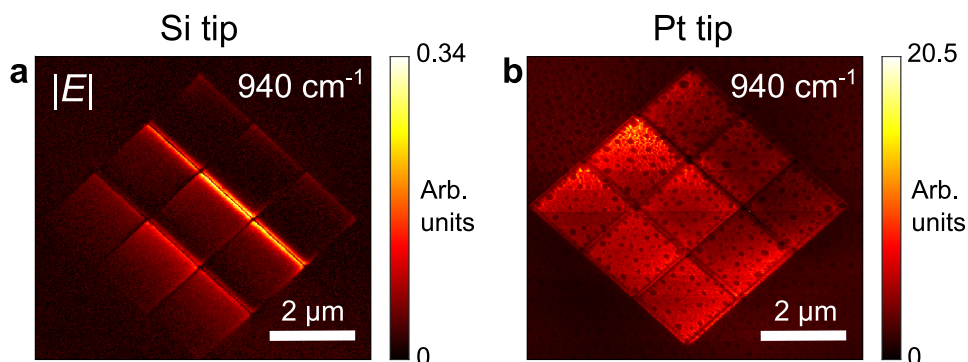


Figure A11: Comparison between near-field images of a 3×3 -patch antenna measured with an Si tip (panel (a)) and a platinum (Pt) coated tip (panel (b)). The image in panel (a) shows a clearly resolved field in the gaps between the patches, while that of panel (b) shows no field in the gaps. This comparison illustrates the fact that a dielectric tip, such as the Si tip used here, minimally perturbs the near-field of a plasmonic nanostructure, whilst a metal-coated tip completely distorts its near-field.

J Microscope reflectivity measurements of 3×3 -patch MIM antennas

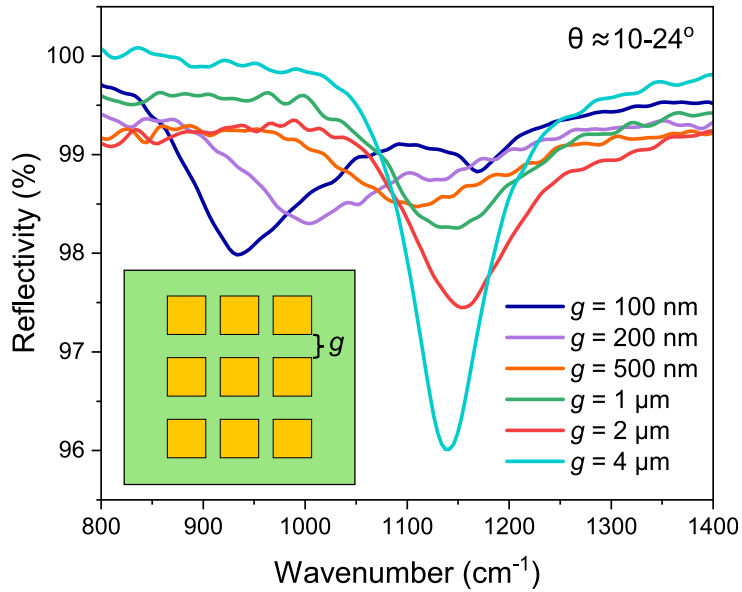


Figure A12: Microscope reflectivity measurements (*Bruker Hyperion*) of a 3×3 -patch MIM antenna as function of gap size g . The measurements were performed using a Cassegrain objective with $\text{NA} = 0.4$ which collects light within an angular interval $\theta \in [10^\circ, 24^\circ]$, where θ is the angle with respect to the normal to the sample surface.

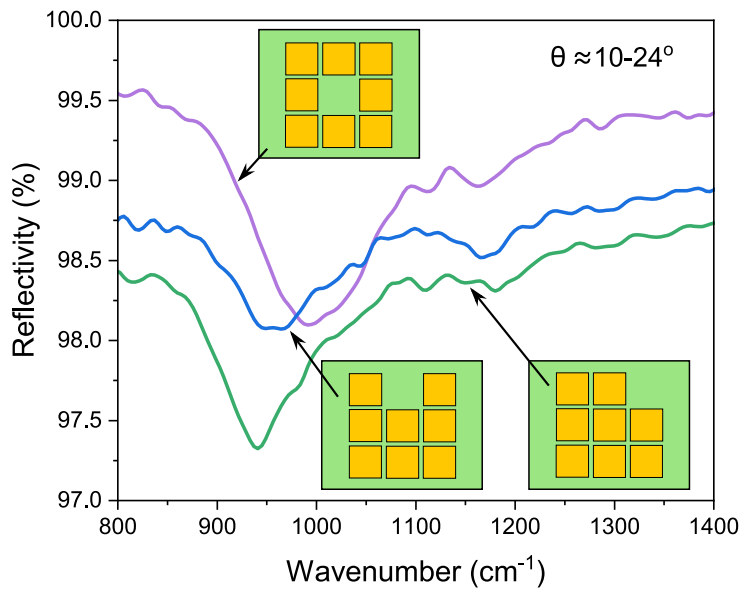


Figure A13: Microscope reflectivity measurements of 3×3 -patch MIM antennas with a missing patch ($g = 100 \text{ nm}$).

K Fabrication of high-mobility graphene field-effect transistors (HGFETs)

The HGFETs studied in chapter 5 of the main text were designed and fabricated by Aurélien Schmitt at Laboratoire de Physique de l'École Normale Supérieure (LPENS). In this section, we briefly describe the fabrication process used.

The hexagonal boron nitride encapsulated graphene heterostructures are fabricated with the standard pick-up and stamping technique, using a polydimethylsiloxane (PDMS)/ polypropylene carbonate (PPC) stamp [8]. The gate electrode is first fabricated on a high-resistivity Si substrate covered by a 285 nm-thick SiO₂ layer. It consists of a pre-patterned gold pad (thickness, 80 nm) designed by laser lithography and Cr/Au metallization. Deposition of the hBN/Graphene/hBN heterostructure on the back-gate is followed by acetone cleaning of the stamp residues, Raman spatial mapping and AFM characterization of the stack. Graphene edge contacts are then defined by means of laser lithography and reactive ion etching, securing low contact resistance $\lesssim 1 \text{ k}\Omega\mu\text{m}$. Finally, metallic contacts to the graphene channel are designed with a Cr/Au Joule evaporation, that also embeds the transistor in a coplanar waveguide geometry suited for microwave and noise characterization. The transistor's dimensions are maximized to get the highest optical signal, while their high mobility $\mu \gtrsim 10 \text{ m}^2\cdot\text{V}^{-1}\cdot\text{s}^{-1}$ at room temperature ensures a moderate channel electric field $E = V/L \gtrsim 10^5 \text{ V/m}$ (L is the graphene channel length) for the threshold of mid-infrared electroluminescence.

L Transport properties of electroluminescent HGFETs

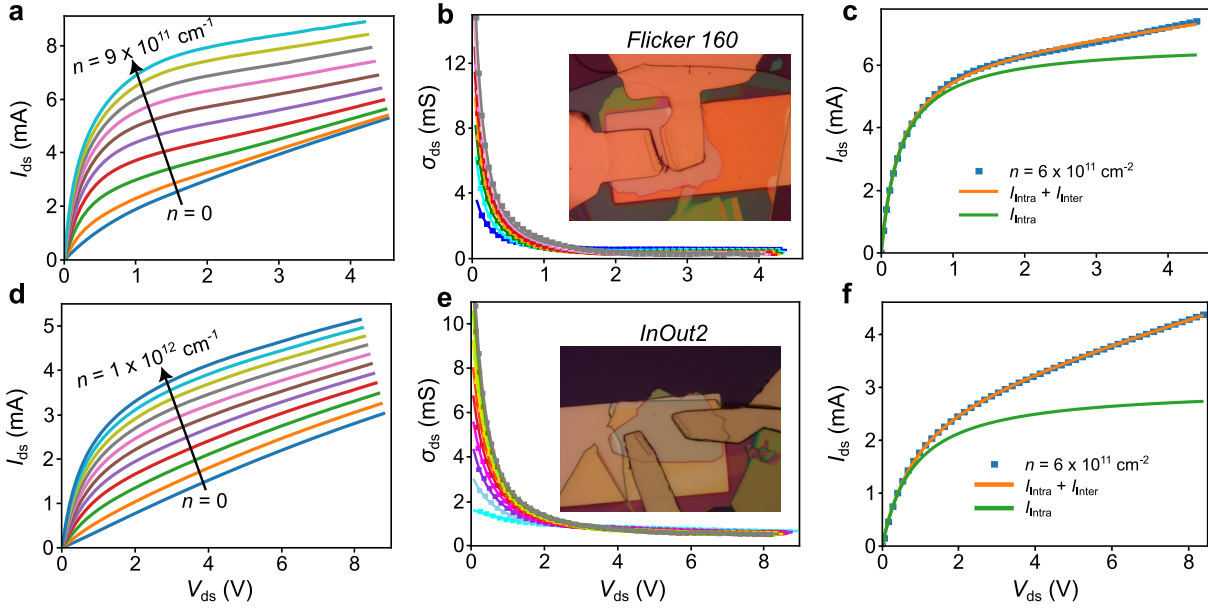


Figure A14: Transport properties of two electroluminescent hBN-encapsulated HGFETs with a gold back-gate (discussed in chapter 5), denoted as *Flicker 160* and *InOut2* (optical images in the insets of panels (b) and (e)). The dimensions (L , channel length; W , channel width; t_{hBN} , thickness of bottom hBN layer) and electron mobility (μ) for these two transistors are as follows: *Flicker 160* (a-c), $L \times W \times t_{\text{hBN}} = 6 \mu\text{m} \times 10 \mu\text{m} \times 160 \text{ nm}$ and $\mu \sim 15 \times 10^4 \text{ cm}^2 \cdot \text{V}^{-1} \cdot \text{s}^{-1}$; *InOut2* (d-f), $L \times W \times t_{\text{hBN}} = 20 \mu\text{m} \times 8.5 \mu\text{m} \times 118 \text{ nm}$ and $\mu \sim 9 \times 10^4 \text{ cm}^2 \cdot \text{V}^{-1} \cdot \text{s}^{-1}$. The plotted transport properties are as follows: (a) & (d) current-voltage curves at fixed charge carrier density (the carrier density is increased linearly from $n = 0$ to the maximal value in steps of $1 \times 10^{11} \text{ cm}^{-2}$), (b) & (e) differential conductivity σ_{ds} as a function of bias (squares) along with the fits (solid lines) using Eq. (5.4) of the main text, (c) & (f) fits of the IV-curves (blue squares) using Eqs. (5.6)-(5.8), where V_{ZK} and T_e are left as adjustable parameters. The total current fit ($I_{\text{intra}} + I_{\text{inter}}$) is plotted in orange, whereas the intraband current (I_{intra}) appears in green and underlines the quasi-linear increase of interband current at large bias. Courtesy of Aurélien Schmitt who designed, fabricated, and characterized these transistors at Laboratoire de Physique de l'Ecole Normale Supérieure (LPENS).

M Determining the temperature increase of an HGFET with an SiO₂ back-gate from mid-infrared measurements

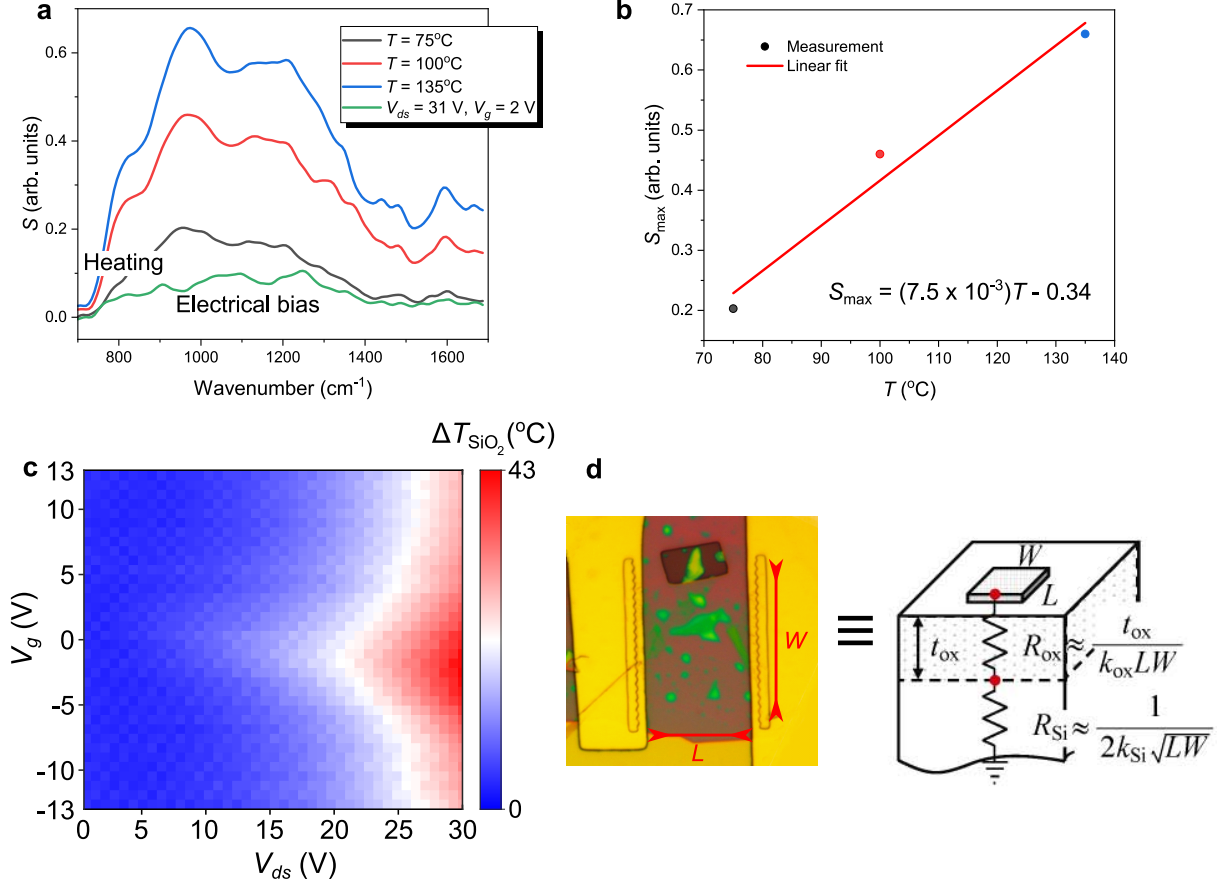


Figure A15: (a) Comparison between the mid-infrared (mid-IR) spectra of the hBN-encapsulated HGFET of panel (d) with an SiO₂ back-gate under electrical bias and by heating the transistor via a hot plate at various temperatures T . The mid-IR signal is measured using an optical chopper (see Fig. 5.11 (a)). The plotted spectra are corrected by a reference measurement, which removes the contribution of the chopper to the detected signal. (b) Linear fit of the maxima of the spectra obtained with the hot plate (S_{\max}) as a function of temperature. From the comparison of panel (a) we find that the temperature of SiO₂ back-gate varies between $T_{\text{SiO}_2} \simeq 50 - 60$ °C when the transistor is electrically biased. (c) Increase in the temperature of the SiO₂ back-gate (ΔT_{SiO_2}) as a function of electrical bias. (d) Left: an optical image of the transistor under study, right: equivalent sketch, in which the heat conduction in the back-gate under the graphene channel ($L \times W = 35 \times 35 \mu\text{m}^2$) of the transistor is modeled via an effective thermal resistance $R_{\text{th}} = R_{\text{ox}} + R_{\text{Si}} = 356.66$ K/W, where R_{ox} and R_{Si} correspond to the thermal resistance in the SiO₂ and Si layers, respectively (see ref. [9] for more details). Here, $t_{\text{ox}} = 285$ nm is the thickness of the SiO₂ layer and $k_{\text{ox}} = 1.4$ W/m.K and $k_{\text{Si}} = 150$ W/m.K are the thermal conductivities of SiO₂ and Si, respectively. Using this model and the result of panel (c), we can compute the power dissipated, P_{out} to the SiO₂ layer via out-of-plane radiative cooling due to the electroluminescence of the transistor. Formally, this is written as $P_{\text{out}} = \Delta T_{\text{SiO}_2} / R_{\text{th}}$. The result of this calculation is plotted in Fig. 5.11 (f) of the main text.

N Measurements of the absorptivity of an HGFET as a function of electrical bias

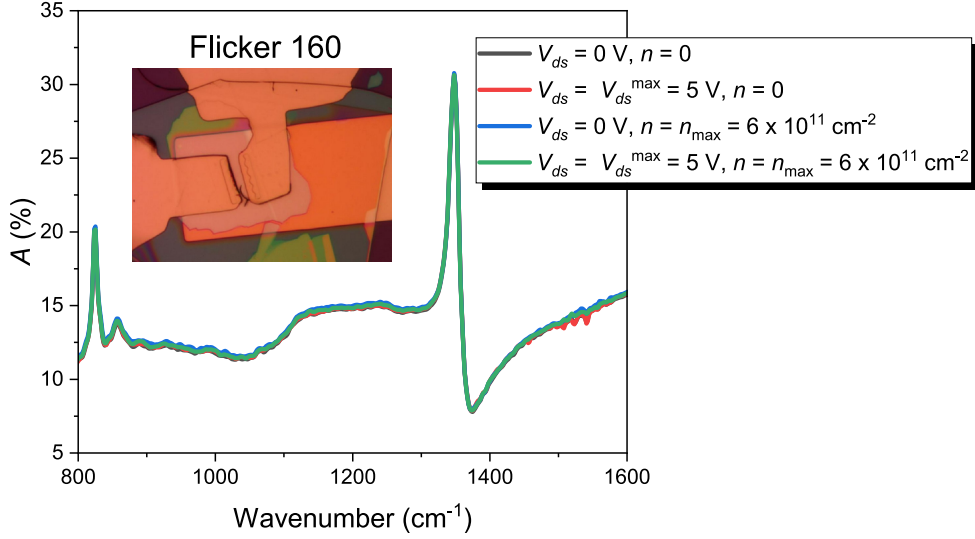


Figure A16: Absorptivity (A) of the *Flicker 160* HGFET (optical image in inset) as a function of electrical bias, determined from microscope reflectivity measurements (*Bruker Hyperion*). Since the transistor is built on a gold back-gate the absorptivity is given by $A = 1 - R$, where R is the measured reflectivity. Measurements for minimal ($V_{ds} = 0$ and $n = 0$) and maximal ($V_{ds} = V_{ds}^{\max} = 5$ V and $n = n_{\max} = 6 \times 10^{11}$ cm $^{-2}$) electrical bias are presented. It is clear that the measured absorptivity spectra are overlapping with a maximal variation of the hBN peak at 1350 cm $^{-1}$ of only $\sim +0.2\%$ between $V_{ds} = 0$ V and $V_{ds} = V_{ds}^{\max}$. We conclude that the transistor's absorptivity varies negligibly as a function of applied electrical bias.

O Stokes-anti-Stokes Raman thermometry of HGFETs

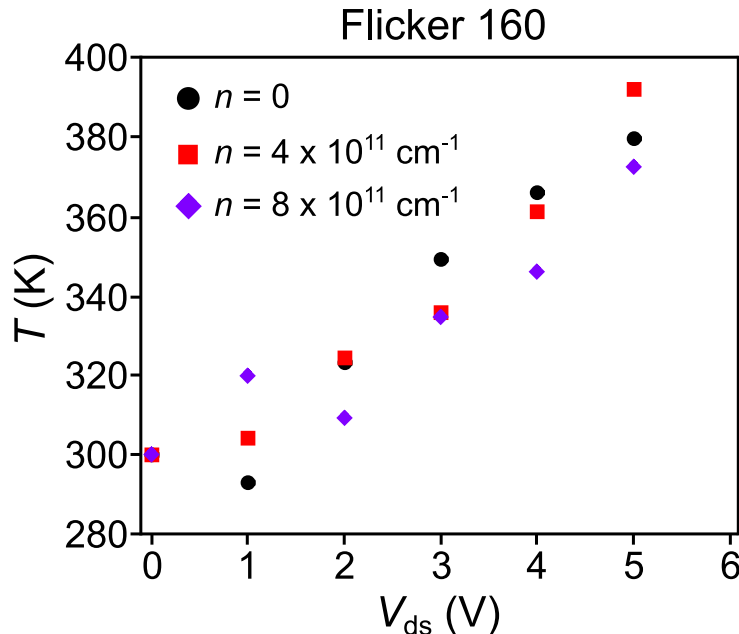


Figure A17: Temperature of optical phonons, deduced from Stokes-anti-Stokes Raman thermometry, as a function of electrical bias (V_{ds}) for the *Flicker 160* HMGFET (see Figs. A14 (a-c)).

Stokes-anti-Stokes Raman thermometry was carried out by Aurélien Schmitt at LPENS for the determination of the temperature of optical phonons in the HGFETs discussed in the main text. This technique enables precise and unequivocal determination of temperature, which relies on the shift of the Stokes peaks. This method is also sensitive to doping and strain. A *Renishaw Raman spectrometer* was used with a notch filter that allows simultaneous measurement of the Stokes and anti-Stokes peaks. The transistor is excited with a $\lambda = 532$ nm laser ($P = 5$ mW).

The ratio between the intensities of the Stokes (I_S) and the anti-Stokes (I_{AS}) peaks is related to the temperature T via $\frac{I_{AS}}{I_S} = e^{-\frac{\hbar\Omega}{k_B T}}$, where $\hbar\Omega$ is the energy of the optical phonon mode. For hBN, the type II transverse optical phonon is $\hbar\Omega^\perp \simeq 169$ meV, which yields a ratio $\frac{I_{AS}}{I_S} \sim 10^{-3}$ at room temperature. By comparing the intensity ratios at zero bias and non-zero bias, the temperature of the optical phonons of hBN can be deduced as a function of doping and bias voltage. The temperature of optical phonons in the *Flicker 160* HGFET obtained from Stokes-anti-Stokes measurements is plotted in Fig. A17. The temperature shows a slight increase as a function of bias, which is insufficient to explain the strong increase of the mid-IR signal measured at the same value of doping and bias (see main text).

References

- [1] RL Olmon, B Slovick, TW Johnson, D Shelton, SH Oh, GD Boreman, and B Raschke. “Optical dielectric function of gold”. *Phys. Rev. B* 86.23 (2012), p. 235147.
- [2] MR Querry. *Optical constants of minerals and other materials from the millimeter to the ultraviolet*. Chemical Research, Development & Engineering Center, US Army Armament, 1998.
- [3] C Li, V Krachmalnicoff, P Bouchon, J Jaeck, N Bardou, R Haidar, and Y De Wilde. “Near-field and far-field thermal emission of an individual patch nanoantenna”. *Phys. Rev. Lett.* 121.24 (2018), p. 243901.
- [4] L Abou-Hamdan, C Li, R Haidar, V Krachmalnicoff, P Bouchon, and Y De Wilde. “Hybrid modes in a single thermally excited asymmetric dimer antenna”. *Opt. Lett.* 46.5 (2021), pp. 981–984.
- [5] L Abou-Hamdan, L Coudrat, S Bidault, V Krachmalnicoff, R Haidar, P Bouchon, and Y De Wilde. “Transition from Phononic to Geometrical Mie Modes Measured in Single Subwavelength Polar Dielectric Spheres”. *ACS Photonics* 9.7 (2022), pp. 2295–2303.
- [6] J Doumouro, E Perros, A Dodu, N Rahbany, D Leprat, V Krachmalnicoff, R Carminati, W Poirier, and Y De Wilde. “Quantitative measurement of the thermal contact resistance between a glass microsphere and a plate”. *Phys. Rev. Appl.* 15.1 (2021), p. 014063.
- [7] J Kischkat, S Peters, B Gruska, M Semtsiv, M Chashnikova, M Klinkmüller, O Fedosenko, S Machulik, A Aleksandrova, G Monastyrskyi, et al. “Mid-infrared optical properties of thin films of aluminum oxide, titanium dioxide, silicon dioxide, aluminum nitride, and silicon nitride”. *Appl. Opt.* 51.28 (2012), pp. 6789–6798.
- [8] M Yankowitz, Q Ma, P Jarillo-Herrero, and BJ LeRoy. “van der Waals heterostructures combining graphene and hexagonal boron nitride”. *Nat. Rev. Phys.* 1.2 (2019), pp. 112–125.
- [9] E Pop. “Energy dissipation and transport in nanoscale devices”. *Nano Res.* 3.3 (2010), pp. 147–169.

RÉSUMÉ

Les métamatériaux infrarouges ont été utilisés dans un large éventail d'applications, telles que le refroidissement radiatif, la photodétection et la conception de cellules solaires. Les éléments constitutifs de ces matériaux sont des structures de taille sub-longueur d'onde qui présentent de nombreux effets d'antenne intéressants, à savoir une émission directionnelle, une sélectivité spectrale, ainsi qu'une exaltation du confinement du champ. L'étude des propriétés radiatives intrinsèques de ces structures sub-longueur d'onde est une étape cruciale vers l'optimisation de la réponse optique des métasurfaces à grande échelle. Traditionnellement, l'étude des propriétés radiatives des structures individuelles sub-longueur d'onde est extrêmement difficile en raison de leur rayonnement électromagnétique intrinsèquement faible. Dans la gamme spectrale du moyen infrarouge, le rayonnement du fond est dominant.

Dans cette thèse, nous repoussons les limites de diverses techniques hautement sensibles, telles que la spectroscopie à modulation spatiale infrarouge et la microscopie optique en champ proche à pointe diffusante, pour sonder le rayonnement électromagnétique intrinsèque dans le moyen infrarouge de structures sub-longueur d'onde composées d'un ou plusieurs éléments. Un pot-pourri de dispositifs sub-longueur d'onde est examiné et discuté, couvrant un large spectre allant, des antennes diélectriques et plasmoniques passives aux transistors à effet de champ en graphène polarisés électriquement. Les propriétés fondamentales et les interactions associées à ces structures sont élaborées, avec un accent particulier mis sur l'influence des propriétés géométriques et des matériaux sur la réponse en champ proche et lointain. Les résultats présentés dans cette thèse et la discussion associée sont d'un intérêt particulier pour les applications photoniques dans lesquelles une adaptation du spectre moyen infrarouge à l'échelle sub-longueur d'onde est requise.

MOTS CLÉS

Sub-longueur d'onde, moyen infrarouge, champ proche, champ lointain, antennes, polaritons de surface

ABSTRACT

Infrared metamaterials have been used in a wide range of applications, such as radiative cooling, photo-detection, and solar cell design. The building blocks of these materials are subwavelength structures that exhibit many interesting antenna effects, namely, directional emission, spectral selectivity, and high field confinement. The study of the intrinsic radiative properties of these subwavelength structures is a crucial step toward the optimization of the optical response of large-scale metasurfaces. Traditionally, investigating the radiative properties of individual subwavelength structures has, for the most part, been rather elusive due to their inherently weak electromagnetic radiation. In the mid-infrared spectral range, one is also met with overwhelming background radiation.

In this thesis, we push the limits of various highly sensitive techniques, such as infrared spatial modulation spectroscopy, and scattering-scanning near-field optical microscopy, to probe the intrinsic mid-infrared electromagnetic radiation of single- or few-element subwavelength structures. A potpourri of subwavelength devices is examined and discussed, spanning a broad continuum, from passive dielectric and plasmonic antennas to electrically biased graphene field-effect transistors. The fundamental properties and interactions associated with these structures are elaborated, with special emphasis being placed on the influence of geometrical and material properties on the near- and far-field response. The results presented in this thesis and the discussion therein are of particular interest to light applications in which a tailoring of the mid-infrared spectrum at the subwavelength scale is required.

KEYWORDS

Subwavelength, mid-infrared, antennas, near-field, far-field, surface polaritons